FORMULATION AND APPLICATION OF A NEW CRITICAL STATE MODEL FOR CLAYS

CHEN JINBO

NATIONAL UNIVERSITY OF SINGAPORE

2013

Formulation and Application of A New Critical State Model for Clays

Chen Jinbo

(*B. Eng., Tongji University*)

A THESIS SUBMITTED

FOR THE DEGREE OF MASTER OF ENGINEERING

DEPARTMENT OF CIVIL AND ENVIRONMENTAL ENGINEERING

NATIONAL UNIVERSITY OF SINGAPORE

2013

Life is somewhat unpredictable; there are so many uncertainties that we humans cannot control everything. What we could do is to plan prudently in advance and make persistent efforts to approach success, if you want.

In discussions with my supervisors

DECLARATION

I hereby declare that the thesis is my original work and it has been written by me in its entirety. I have duly acknowledged all the sources of information which have been used in the thesis.

This thesis has also not been submitted for any degree in any university previously.

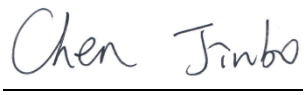

Chen Jinbo

Jul 04th, 2013

ACKNOWLEDGEMENTS

The research life during the past three years I have enjoyed here at the National University of Singapore (NUS) is wonderful undoubtedly. I have tremendously benefited from the guidance and discussions with the university professors and staff. First and foremost, I would like to express my sincere gratitude to my supervisors, Professor Choo Yoo Sang and Professor Chow Yean Khow, for their erudite and invaluable guidance throughout my study at NUS. Professor Choo's systematical way of thinking brought me into the offshore research life and his comprehensive research experience and engineering intuition inspired me to do the research on the cyclic constitutive modeling of clays. Professor Chow's solid research knowledge and the methodical way of working greatly enhanced my ability to explore into the fundamentals. Whether the fundamental comparison of the different element types or the practically adopted p-y curves, Professor Chow has always been ready to instruct and help me. I also want to express my appreciation to Professor Choo and Professor Chow for their great supports and guidance during the preparation of this thesis.

A very special thanks goes to Assistant Professor Goh Siang Huat, for his willingness and patient discussion on the typical soil behavior under monotonic and cyclic loading, without whom I cannot tackle the problem directly. Many thanks should be given to the Visiting Professor Peter William Marshall, Assistant Professor Qian Xudong and Associate Professor Tan Siew Ann for their invaluable discussion during my study.

As part of the Geotechnical Student Community, the benefits and satisfaction that I derived from the discussions with my friends are incomparable. I would like to take this opportunity to thank Dr. Wu Jun, Dr. Shen Wei, Dr. Chen Zhuo, Dr. Sun Liang,

Mr. Zhang Yang, Dr. Simon, Dr. Liu Xuemei, Dr. Wang Shasha, Dr. Ye Feijian, Dr. Subhadeep and Mr. Zhang Dongming, for their valuable information and encouragements. Greatful thanks are extended to the NUS staff Mr. Tan Lye Heng and Ms. Norela Bte Buang who helped me quite a lot during my study.

Last but not least, I am very grateful to the Lloyd's Register Foundation (LRF) for their strong support through the LRF Professorship and R&D Programme in Centre for Offshore Research and Engineering (CORE) at NUS. Sincere thankness should be given to Professor Chen Yiyi and Professor Wu Dingjun at Tongji University for recommending me to join NUS in 2010. No words can express my gratitude to my parents for loving me, supporting me and encouraging me in everything I have done in life. Very very special thanks should be given to my wife, who is always trusting me and standing by to help me.

TABLE OF CONTENTS

SUMMARY

Realistic modeling of the mechanical behavior of soil with reasonable material input is essential for the practical use of numerical methods for the solution of geotechnical problems. Due to the unsatisfactory prediction of the basic critical state models for heavily overconsolidated (*OC*) clays, the research conducted in this thesis dealt with the formulation of a new critical state model for heavily *OC* clays and clays under cyclic loading.

In place of the conventional Hvorslev surface, a failure envelope which is modified from the experimental findings explicitly enters into the model formulation. The peak strength of heavily *OC* clay can thus be predicted quite satisfactorily under drained loading. Meanwhile, the original critical state line (*CSL*) of the Modified Cam clay (MCC) model is repositioned in $v-\ln p'$ space to better predict the undrained shear strength of heavily *OC* clays. A load-path-dependent plastic modulus is proposed to introduce plastic strains within the bounding surface. Thus the cyclic behavior of normally consolidated (*NC*) to lightly *OC* clay can be reasonably simulated. Comprehensive comparisons of model predictions (single element) with laboratory test data are conducted on various clays (kaolin clay, Fujinomori clay and Boston Blue Clay (BBC)) under various loading conditions to fully evaluate the capability of the proposed model.

A well conductor in soft clay subjected to lateral loading is then simulated by using the proposed AZ-Cam clay model in the commercial software ABAQUS through the user-defined model subroutine (UMAT). For monotonic loading, the predicted head load-displacement response shows quite large difference among the various soil

constitutitve models. Thus the predicted response of the well conductor is rather sensititve to the soil model used. The predicted p-y curves from the AZ-Cam clay model agree reasonably well with the centrifuge tests. For cyclic loading, the AZ-Cam clay model is able to predict the softening and the hysteretic behavior of the conductor in cyclic displacement control loading. The predicted head response agrees reasonably well with the centrifuge test result.

Keywords:

Bounding surface; Clays; Constitutive model; Cyclic loading; Failure surface; Monotonic loading; P-y curve

LIST OF TABLES

LIST OF FIGURES

LIST OF SYMBOLS

a	Vertical intercept of failure envelope plotted in terms of $q/Mp' - \xi_d$
a_1	Parameter governing the decreasing rate of shear modulus
a_2	Parameter governing the decreasing rate of shear modulus
b	Parameter governing the failure surface
b_f	Intermediate principal stress parameter
C_p	Parameter governing $G_{\max}$
CICP	Triaxial isotropic consolidated constant p'
CID	Triaxial isotropic consolidated drained
CIDC	Triaxial isotropic consolidated drained compression
CIU	Triaxial isotropic consolidated undrained
CIUC	Triaxial isotropic consolidated undrained compression
CIUE	Triaxial isotropic consolidated undrained extension
CK_0UC	K_0 consolidated undrained compression
CK_0UE	K_0 consolidated undrained extension
CK_0UDSS	K_0 consolidated undrained direct simple shear
CSL	The critical state line
d	Vertical distance of new CSL and original CSL in $v - \ln p'$ space
DSS	Direct simple shear
e	Void ratio
$\mathbf{e}_s$	Deviatoric strain tensor
$\mathbf{e}_{s\text{-}rev}$	Deviatoric component of strain tensor at last loading reversal point

E_d	Deviatoric strain
F	Bounding surface (or yield surface)
g_b	3D bounding surface parameter
g_p	3D plastic potential parameter
G	Elastic tangent shear modulus
$G_{\max}$	Elastic shear modulus at very small strain range
$G_{\sec}$	Elastic secant shear modulus
h	Intercept of Hvorslev line
H	Plastic modulus
$\bar{H}$	Plastic modulus at the image point on the bounding surface
H_1	Plastic modulus at the first image point on the bounding surface
H_2	Plastic modulus at the second image point on the bounding surface
$\mathbf{I}$	Global internal force vector
$\mathbf{I}_\mathbf{E}$	Unit tensor
J	Deviatoric stress
k	Hardening paramter
k_s	Shakedown paramter
K	Elastic bulk modulus
K_{nc}	Effective horizontal stress coefficient of NC clay
K_{oc}	Effective horizontal stress coefficient of OC clay
m_h	Slope of Hvorslev line
m_r	Parameter governing $G_{\max}$
m	Parameter governing $G_{\max}$

M	Slope of CSL in $p'-q$ space
M_p	Peak stress ratio
M_{pp}	Parameter governing the plastic potential in deviatoric plane
n	Parameter governing $G_{\max}$
N	Vertical intercept of NCL in $v-\ln p'$ space
NC	Normally consolidated
NCL	Normal compression line
OC	Overconsolidated
OCR	Overconsolidation ratio
p	Mean stress
P	Plastic potential
P	Global applied load vector
p_{atm}	Atmospheric pressure
p_r	Reference pressure
p'	Effective mean stress
$\overline{p}'$	Effective mean stress at the projection of current stress on *BS*
$\overline{p}'_1$	Effective mean stress at first image point
$\overline{p}'_2$	Effective mean stress at second image point
p'_0	Initial effective mean stress
p'_c	Pre-consolidation pressure
p'_{c0}	Initial pre-consolidation pressure
p'_{cr}	Effective mean stress at the critical state
p'_e	Equivalent pressure

p'_{rel}	Effective mean stress at the reloading point
p'_{Tcr}	Effective mean stress at the intersection point of failure surface and the CSL in $p'-q$ space
q	Deviatoric stress
q_f	Failure deviatoric stress
$\overline{q}$	Deviatoric stress at the projection of current stress on *BS*
$\overline{q}_1$	Deviatoric stress at first image point
$\overline{q}_2$	Deviatoric stress at second image point
Q^e_{len}	Length of shear strain path
R_d	Bounding surface parameter on the dry side
R_w	Bounding surface parameter on the wet side
r	Decreasing rate of the elastic shear modulus
s	Deviatoric stress tensor
S_u	Undrained shear strength
S_{u-meas}	Measured undrained shear strength
$S_{uoc-meas}$	Measured undrained shear strength of heavily OC clay
$S_{uoc-MCC}$	The MCC model predicted undrained shear strength of heavily OC clay
SL	Swelling line
T	Undrained shear strength parameter
u	Pore water pressure
u	Global nodal displacements vector
v	Specific volume
v_0	Initial specific volume

v_c	Specific volume at p'_c on the NCL
v_k	Specific volume at $p' = 1kPa$ on the SL
w	Water content
X_b	Parameter determining g_b
X_p	Parameter ensuring the plastic potential passing the first image point
X_T	Parameter determining T in the deviatoric plane
X_β	Parameter determining β in the deviatoric plane
Y_b	Parameter determining g_b
Y_p	Parameter determining g_p
Y_T	Parameter determining T in the deviatoric plane
Y_β	Parameter determining β in the deviatoric plane
Z_b	Parameter determining g_b
Z_p	Parameter determining g_p
Z_T	Parameter determining T in the deviatoric plane
Z_β	Parameter determining β in the deviatoric plane
β	Peak strength parameter
χ	Parameter governing the failure surface
γ	Plastic modulus parameter
γ^s	Engineering shear strain
Γ	Vertical intercept of original CSL in $v - \ln p'$ space
δ	Distance from the origin of stress space to current stress point
δ_B	Distance from the origin of stress space to first image point

$\boldsymbol{\varepsilon}$	Strain tensor
ε_a	Axial strain
ε_r	Radial strain
ε_s	Deviatoric strain
ε_v	Volumetric strain
ε_v^e	Elastic volumetric strain
ε_v^p	Plastic volumetric strain
ζ_1	Measure of the deviation of p' from the initial state or reloading point
ζ_2	Measure of the deviation of q from the initial state or reloading point
η	Current stress ratio
η_0	Initial stress ratio
$\bar{\eta}_1$	Stress ratio at first image point
$\bar{\eta}_2$	Stress ratio at second image point
$\bar{\eta}_B$	Stress ratio at the projection of current stress on *BS*
η_{rel}	Stress ratio at the reloading point
η_{rev}	Stress ratio at the loading reversal point
θ	Lode's angle
θ_f	Lode's angle at failure
κ	Slope of SL in $v-\ln p'$ space
λ	Slope of NCL in $v-\ln p'$ space
Λ_p	Plastic volumetric strain ratio
ν	Poisson's ratio

ν'	Effective Poisson's ratio
ξ	State variable ensuring consistency condition
ξ_d	State parameter
$\boldsymbol{\sigma}$	Stress tensor
$\boldsymbol{\sigma}'$	Effective stress tensor
σ_i	Normal stress component of $\boldsymbol{\sigma}$
σ_i'	Effective normal stress component of $\boldsymbol{\sigma}'$
σ_{if}'	Failure effective normal stress
σ_h'	Effective horizontal stress
σ_v'	Current effective vertical stress
σ_{v0}'	Initial effective vertical stress
σ_{vc}'	Vertical effective stress at the beginning of shearing
σ_{vm}'	Maximum effective vertical stress in history
ς_2	Parameter measuring the deviation of q from the initial or loading reversal point
τ	Shear stress
τ_{ij}	Shear stress component of $\boldsymbol{\sigma}'$
χ	Material constant governing the nonlinearity of failure envelope
ω	State variable solving pre-negative problem
ω_r	Elastic modulus decreasing rate parameter
Ω	State variable ensuring the plastic modulus be path-dependent
$\{m\}$	Immaterial vector ensuring the plastic potential passing the current stress point

$\{\varepsilon\}$	Strain vector
$\{\sigma'\}$	Effective stress vector
$\left[D^e\right]$	Elastic stiffness matrix
$\left[D^{ep}\right]$	Elasto-plastic stiffness matrix

Chapter 1 **Introduction**

1.1 Introduction

With the development of powerful computers in the last two decades, numerical methods (for example, the finite element (FE) method) are more frequently used in the routine design. When solving practical boundary value problems, however, the accuracy of the numerical methods depends the characterization of the mechanical behavior of the material. Generally all the numerical results would be affected by the material constitutive model used. Thus realistic description of soil constitutive behavior plays an essential role in the accuracy of numerical prediction in geotechnical engineering. Thus tremendous research efforts have been and will continue to be directed towards this area.

1.2 General description of soil

Generally, soil is a highly complex porous material consisting of a soil skeleton and pore fluids. For fully saturated soil, the voids in the soil are filled with water forming a two-phase system. Some of the key features of soil in a multiphase state are summarized (Whittle, 1987).

(i) In general, there is no well defined region of linear soil behavior, even at small stress level or immediately after a load reversal (Hardin & Drnevich, 2002).

(ii) Soils are frictional materials, which depend on the mean effective stress as well as deviatoric stress.

(iii) There is a coupling effect between volumetric behavior and deviatoric shear behavior. For example, normally consolidated (NC) to lightly overconsolidated (OC) clays tend to contract during drained shearing and positive excess pore water

pressures are induced during undrained shearing. Heavily OC clays, however, tend to dilate during drained shearing and negative excess pore water pressure builds up in undrained shearing.

(iv) Though isotropic assumption is often made for the reconstituted soils, natural soils tend to be anisotropic due to their structure, depositional environment and subsequent loading history (Ladd *et al.*, 1977).

(v) In some modes of deformation, unstable strain softening behavior is observed.

(vi) Some soils exhibit significant time dependent behavior, like creep. Thus a real time scale must be used in their constitutive description (Prevost, 1976).

1.3 Dilemma in soil modeling

Since soils exhibit in such a complicated way, great attention has been focused on the theoretical modeling during the past six decades. Drucker *et al.* (1957) are the pioneers who first attempted to model soil behaviors within the framework of classical plasticity theory. Subsequent research work done on laboratory reconstituted clay by Roscoe and his researchers in the 1960s led to the development of Critical State Soil Mechanics (CSSM) (Schofield & Wroth, 1968), which consists of the original Cam clay (CC) model and later the modified Cam clay (MCC) model (Roscoe & Burland, 1968). Although the critical state concept of soil, when subjected to continued shear loading, the soil will ultimately reach a state where no volumetric strain occurs with further deviatoric strain, serves as a milestone in the theoretical modeling of soil behavior and inspires many more advanced and sophisticated models, up to now, there is no universal constitutive model that can describe the whole features of soil behavior while requiring a reasonable number of input model parameters.

Whittle (1987) attributed this limitation to the fact that the current ability to construct models outstripped the characterization of the soil behavior. Wroth & Houlsby (1985) suggested that the goal of developing comprehensive constitutive models for soil was overly ambitious and that a better approach was to tailor the complexity of the model to the accuracy of solution required for a given problem. Thus the modeling of soil really presents a trade-off between sophistication and the simplicity for application. The view held by Wood (1991) would thus be inspiring that the models should be hierarchic, to both consider the power and usefulness of model as well as the degree of difficulty and complexity involved.

1.4 Principle of effective stress

Terzaghi (1936) first postulated the fundamental principle of effective stress, which is stated as: "All measurable effects of a change in stress such as compression, distortion or a change of shearing resistance are exclusively due to the changes in effective stress." The effective stress principle can be expressed as follows:

$$\boldsymbol{\sigma}' = \boldsymbol{\sigma} - u\mathbf{I}_{\mathbf{E}} \tag{1.1}$$

where $\boldsymbol{\sigma}, \boldsymbol{\sigma}'$ are total and effective stress tensor respectively, the prime denotes 'effective'. The effective stress and effective stress invariants will all be labeled by prime in this thesis. The parameter u is the pore water pressure and $\mathbf{I}_{\mathbf{E}}$ is the unit tensor.

Following the effective stress principle, the mechanical behavior of soil is governed by the effective stresses in the soil which are carried by the soil skeleton. It is thus natural to formulate the constitutive model in terms of effective stress in order to truly represent the soil behavior. Throughout this thesis, the description of constitutive

models is based the continuum assumption. Thus the microstructure and particulate nature of soil are not of concern in the current study.

1.5 Aims of present study

The main aim of the present study is to construct a simple constitutive model for heavily OC clay under monotonic loading. The major effort will thus be focused on simulating the peak strength and ultimate strength of heavily OC clay in drained shearing and undrained shearing, respectively. The cyclic degradation and hysteretic behavior of NC to lightly OC clay will also be simulated. The proposed model will be verified through the comparison of model predictions and measured data in laboratory tests under various shearing modes.

Centrifuge tests on a well conductor in clay subjected to lateral loading (monotonic and cyclic loading) will be simulated in order to further verify the capability of the proposed model. The derived p-y curves will be compared to the ones used for the design of well conductors of offshore floating structures. The results from the simulation are expected to provide the basis of the fatigue life assessment of well conductors.

1.6 Layout of the thesis

The thesis consists seven chapters. Chapter 1 provides a general introduction of the current study. Chapter 2 presents a literature review on soil plasticity modeling.

Chapter 3 formulates the proposed model in the triaxial space. A failure surface modified from the published literature is introduced to better simulate the peak strength and ultimate strength of heavily OC clay in drained and undrained shearing,

respectively. Key attention will be paid on the formulation and the underlying philosophy of the plastic modulus.

Chapter 4 extends the model to the general stress space with detailed mathematical derivations. The implementation of the three-dimensional model in ABAQUS through the user-defined model subroutine (UMAT) will be described together with the associated stress updating scheme. The implementation is verified through the comparison of the prediction from the UMAT and ABAQUS built-in model.

Chapter 5 illustrates the physical meanings and laboratory determination methods of the model parameters. The model predictions for various shearing modes (triaxial shearing and direct simple shearing) under different loading conditions (monotonic and cyclic, drained and undrained) are compared to the test results. The capability and the shortcomings of the model are thus revealed.

Chapter 6 presents the results of the model prediction on the response of a well conductor in clay subjected to lateral loading.

Chapter 7 summarizes the general conclusions from the current study as well as recommendations for future study.

Chapter 2 **Literature Review**

2.1 Introduction

Most soil constitutive models have been developed within the framework of plasticity theory. The literature review will be confined to critical state models which are the building blocks for constructing a new constitutive model. After the description of the critical state models, the limitations of the critical state models, namely the poor prediction of peak strength of heavily OC clays on the dry side and the inability to simulate cyclic behavior, are addressed. It is useful to note here that the review and subsequent new constitutive model developed are restricted to clays. As great differences exist between clays and sands in the compressibility and permeability, many constitutive models are specifically developed for one type of soil (clay or sand), although more unified models are also available (Pastor *et al.*, 1990; Yu, 1998; Pestana & Whittle, 1999; McDowell & Hau, 2004; Yu *et al.*, 2007; Manzanal *et al.*, 2011).

2.2 Soil constitutive models

2.2.1 Critical state framework

The critical state framework was formulated in the 1960s at the University of Cambridge, although the critical concept was firstly proposed by Casagrande (1936). The framework is based on laboratory reconstituted clays and the soil is assumed to be isotropic.

In one-dimensional isotropic loading test, if a soil sample consolidated isotropically and then subjected to isotropic loading and unloading, the relationship between the specific volume v ($v=1+e$, e is the void ratio of soil) of soil sample and

the stress state typically follows the trend shown in Figure 2.1. As the problem is one-dimensional, the mean effective stress p' is enough to describe the stress state (a complete definition of all the stress and strain variables used in this thesis is provided in Appendix A and will not be repeated in the main thesis text). The line which the NC soil sample follows when subjected to compression is the isotropic normal compression line (NCL) and the line when the soil sample swells from the NCL is the swelling line (SL). It is assumed that in the $v-\ln p'$ space, NCL and SL are straight lines which can be expressed by following equations in CSSM:

NCL: $v = N - \lambda \ln p'$ 2.1

SL: $v = v_\kappa - \kappa \ln p'$ 2.2

where N, λ, κ are material constants. N is the intercept of NCL with v axis in $v-\ln p'$ space, λ, κ are the slopes of NCL and SL in $v-\ln p'$ space, respectively. v_κ is the intercept of SL with v axis in $v-\ln p'$ space, depending on the location from which point of NCL the soil swells. It is noted that the SL also serves as the reloading line before reaching the NCL.

Following the critical state concept, when the soil is subjected to continued shear loading, a critical state where no further change in the volume will be ultimately reached, although large shear distortion continues. It is assumed that this ultimate stress state will lie on a line called the critical state line (CSL) independent of the modes of shearing. The CSL is defined in $v-p'-q$ space as follows (Figure 2.2):

$q = Mp'$ 2.3

$v = \Gamma - \lambda \ln p'$ 2.4

where M, Γ are materials constants, M is the slope of CSL in $p' - q$ space, which can be related to the soil friction angle. Γ is the intercept of CSL with v axis in $v - \ln p'$ space. It is noted that N and Γ are inter-related based on the specific model formulation as will be shown in the later part of this thesis. Thus for model input, only one of them is sufficient.

Following the classical elasto-plastic theory (a berief description of the elasto-plastic theory is given in Appendix A), a yield surface which separates the purely elastic behavior from the elasto-plastic behavior has to be specified when constructing an elasto-plastic constitutive model. The following yield surface was proposed for the original Cam clay (CC) model by Schofield & Wroth (1968) as shown in Figure 2.3(a):

$$\frac{q}{Mp'} + \ln\left(\frac{p'}{p'_c}\right) = 0 \qquad 2.5$$

where p'_c is the intercept of the yield surface with p' axis, serving as the hardening parameter and is also called the pre-consolidated pressure.

As can be seen from Figure 2.3 (a), the logarithmic yield surface of the CC model has a sharp corner on the p' axis, which causes the incremental plastic strain remaining unknown if an associated flow rule is used. Due to this reason, Roscoe & Burland (1968) proposed a modified Cam clay (MCC) model by modifing the work dissipation equation used by Schofield & Wroth (1968) and proposed an elliptic curve, which smoothens the sharp corner of the CC yield surface (Figure 2.3 (b)):

$$\frac{q^2}{M^2} + p'\left(p' - p'_c\right) = 0 \qquad 2.6$$

Associated flow rule is assumed both in the CC model and the MCC model, so the plastic potential is the same as the yield surface. As stated before, the pre-consolidated pressure p_c' serves as the only hardening parameter. The evolution of p_c' is assumed to be related to the plastic volumetric strain ε_v^p. Thus the shear induced plastic deviatoric strain does not enter into the hardening parameter. Form Figure 2.1, it is easy to deduce the evolution of p_c' in an incremental form as follows:

$$\frac{dp_c'}{p_c'} = \frac{v}{\lambda - \kappa} d\varepsilon_v^p \tag{2.7}$$

Purely elastic behavior is assumed within the yield surface. The elastic bulk modulus K and elastic shear modulus G are used to represent the elastic behavior. As the SL serves as the unloading line and the reloading line before the stress state reaches the NCL, the bulk modulus can be easily obtained from Figure 2.1 as follows:

$$K = \frac{vp'}{\kappa} \tag{2.8}$$

In the work of Schofield & Wroth (1968), the soil is assumed to be rigid plastic. Thus there is no elastic deformation and the elastic shear modulus is infinite large. Thus the model cannot be used in the numerical simulation of a boundary value problem. Typically, there are two ways to determine the shear modulus: the first is to assume a finite constant shear modulus; and the second is to assume a constant Possion's ratio ν, and thus the shear modulus will be related to the bulk modulus K through following expression:

$$G = \frac{3(1-2\nu)}{2(1+\nu)} K \tag{2.9}$$

More discussions on the shear modulus will be presented in Chapter 3 when determining the shear modulus used in the new model in this thesis.

To implement the basic critical state models into a FE software, it is necessary to extend the models to general stress space. The extension to the general stress space requires some assumption about the shape of the yield surface in the deviatoric plane. The commonly used von Mises criterion implies that the yield surface in the deviatoric plane is a circle. Thus the soil strength is independent of the Lode's angle. This behavior generally contradicts with experimental data (Grammatikopoulou, 2004). Gens (1982) reported that the critical state friction angle ϕ_{cs}' for clays is the same under conditions of triaxial compression, extension and plane strain. Thus the strength of clay under these shearing modes would be different depending on the Lode's angle, and thus the magnitude of the intermediate principal stress. A better approach is thus to follow the Mohr Coulomb criterion to consider different strengths at different Lode's angles. However, the Mohr Coulomb hexagon has sharp corners, and additional procedure is necessary to smoothen these corners in numerical implementation. Other continuous shapes have been proposed by Matsuoka & Nakai (1974) and Lade & Duncan (1978) as shown in Figure 2.4. Vaneekelen (1980) proposed a general continuous shape, with which the von Mises criterion, Morh Coulomb criterion and Lade criterion can all be approximated by choosing appropriate parameters,

2.2.2 Summary on basic critical state model

The key ingredients presented in section 2.2.1 are sufficient to construct the basic critical state models. The CC model and the MCC model are called the basic critical state models for short in the following. Table 2.1 summarizes the five input parameters as well as the physical meaning. The models have been used frequently to reproduce

the major deformation characteristics of soft clay when subjected to monotonic loading in laboratory tests (Wroth & Houlsby, 1980; Houlsby *et al.*, 1982). It has also been implemented in various finite element (FE) programs (Randolph *et al.*, 1979; ABAQUS, 2011; Plaxis, 2011).

The basic critical state models capture many aspects of behavior of isotropic consolidated clays and have been proven to be useful in the numerical analysis of boundary value problems for NC to lightly OC clays (on the wet side) (Dasari, 1996; Mita, 2002). However, these models suffer from three major limitations: (i) the models tend to over predict the strength of heavily OC clays (on the dry side); (ii) for stress state within the yield surface, the models predict a purely elastic behavior, and are incapable for predicting the irrecoverable plastic strain within the yield surface when subjected to cyclic loading; (iii) the stiffness of soil will change abruptly when going from the elastic region into the plastic region.

2.2.3 The strength of heavily OC clays

Experimental investigations of the behavior of OC clays in both undrained and drained shear tests have been reported by various authors (Henkel, 1959; Henkel, 1960; Parry, 1960; Gens, 1982). These tests give a consistent pattern of behavior and demonstrate discrepancies with the basic critical state models (Whittle, 1987). A typical result of triaxial isotropic undrained compression (*CIUC*) tests is shown in Figure 2.5 (a), after Atkinson & Richardson (1987). It can be seen that the undrained stress paths of heavily OC clays (sample S3 to S6) in the tests stop much earlier before reaching the initial yield surface (roughly indicated by the red dash curve). However, in the basic critical state models' prediction, the stress path will go vertically until reaching the yield surface and then it follows a slight strain softening. Thus the peak

strength from the tests is significantly lower than the value predicted by the basic critical state models. From Figure 2.6 (b), it can be seen the stress state of heavily OC clays (sample S3 to S6) will approach the CSL but stop finally to the left of the CSL due to the local drainage as explained by Atkinson & Richardson (1987). The deviation of the prediction of the basic critical state models from the test results appears to increase with overconsolidation ratio (*OCR*). The *OCR* in the present study is defined as the ratio of the maximum past effective vertical stress σ'_{vm} to the current value before shearing σ'_{v0}.

Hvorslev (1936) found experimentally that a straight line approximates the failure envelope for OC soils satisfactorily as shown in Figure 2.6. The equation of this line can be described as:

$$\frac{q}{p'_e} = m_h \frac{p'}{p'_e} + h \qquad 2.10$$

where m_h, h are the slope and intercept of Hvorslev line, respectively. p'_e denotes the effective equivalent pressure, which is the effective pressure on the NCL at the current specific volume.

Zienkiewicz & Naylor (1973) adopted this straight Hvorslev line as the yield surface (thus known now as the Hvorslev surface) on the dry side in their use of the MCC model. A non-associated flow rule with dilatancy increasing linearly from zero at the critical state to some fixed value at $p' = 0$ is used. Thus excessive dilatancy rates and the numerical discontinuity at the critical state could be avoided. Potts & Zdravkovic (1999) used a non-associated flow rule with Hvorslev surface as the yield surface on the dry side and the MCC model yield surface as plastic potential. The generalization

of this option has been done by Mita (2002). Similar approach using the Hvorslev surface as yield surface has been suggested by Atkinson & Bransby (1978) as shown in Figure 2.7. The yield surface consists of the Hvorslev surface with tension cutoff on the dry side and Roscoe surface on the wet side. Instead of using Hvorslev on the dry side, Lade (1977) proposed a 'double hardening' model with a conical yields surface on the dry side and a cap yield surface on the wet side as shown in Figure 2.8. The 'double hardening' model assumes that two yield surfaces obey different hardening rules and the plastic strains generated from one yield surface have no effect on the other yield surface. This model has been used extensively at Imperial College in embankment construction, although the implementation of this model in numerical software is not straight forward (Potts & Zdravkovic, 1999).

Rather than using the Hvorslev surface, more recently, Atkinson (2007) proposed curved lines in $p'-q$ space to represent the peak strength of heavily OC clays based on extensive experimental results under various loading conditions. In his mind, only the curved line can represent the peak strength of unbonded soil over the range of effective stress from zero to the critical state. Besides, the straight line is also intrinsically unsafe under certain conditions (Atkinson, 2007). The above proposed curved lines with necessary modifications will directly enter into the new model developed in this thesis. Further details of Atkinson's proposal will be discussed in Chapter 3.

2.2.4 Cyclic constitutive models for clay

Cyclic loading is especially important for offshore foundation systems. Typically, three main aspects of soil response under cyclic loading have to be correctly simulated: (i) the cyclic degradation of soil strength; (ii) the accumulation of displacement under

continued cyclic loading; and (iii) the change of soil stiffness due to cyclic loading. For the foundation of conventional offshore platforms (e.g. fixed offshore platofrms with piled foundation or gravity based foundation), the bearing capacity under cyclic loading may govern the whole design (Andersen, 2009), although the displacement of the foundation may also be critical. Thus the cyclic degradation of soil strength is particular of concern (API-RP2A, 2000). For the fast growing offshore wind turbine industry, the lateral response of foundation under cyclic loading receives much more attention, as the superstructure is sensitive to the foundation displacement (Achmus *et al.*, 2009). Moreover, the primary design issues are deformation and stiffness rather than ultimate capacity, which may be different from the conventional offshore platform design (Leblanc *et al.*, 2010).

Modeling the soil cyclic behavior faces a dilemma in that in order to be sophisticated, more parameters are required which leads to the model being rather complex and some of the parameters are hard to determine. Thus a tradeoff must be made, balancing sophistication and simplicity. A practical way as suggested by Wroth & Houlsby (1985) is to tailor the complexity of the model to the accuracy of solution required for a given problem.

Whittle (1987) classified cyclic soil constitutive models into two types: (i) explicit model and (ii) implicit model. The explicit model uses the experimental results of simple cyclic tests on soils to develop relationships, which can be used to estimate the effects of whole cyclic histories. A monotonic loading model is necessary and then additional assumptions are made on the state variables of the monotonic loading model to take account of the cyclic loading effect based on the experimental tests. A good example of an explicit model is provided by Vaneekelen & Potts (1978) who describe the monotonic behavior of Drammen clay and then by using a fatigue parameter (the

excess pore water pressure generated in cyclic undrained loading), the cumulative effect can be taken into account. The cyclic pore pressure is related to the number of loading cycles and the cyclic shear stress level based on a large number of tests. More recently, Andersen (2009) presented results of cyclic direct simple shear (DSS) tests and cyclic triaxial tests in the diagrams where the number of cycles to failure is plotted as a function of average and cyclic shear stresses. Some typical results are shown in Figure 2.9. These results can be incorporated into the monotonic model to simulate the cyclic loading effects and thus also forms as an explicit model.

The explicit mdoels are straight forward to understand but cannot be used as general purpose constitutive models in boundary value problems. Because these models are based on large number of cyclic tests results of specific soils, and hence restricts the application of these models. Another shortcoming of these models is that even though the ultimate cyclic loading effects can be considered, the response during the cyclic loading history cannot be simulated. For these reasons, the focus of this thesis will be on the more general purpose models referred as implicit models.

The implicit model describes the general constitutive laws of soils under monotonic loading as well as cyclic loading. The whole cyclic loading history is thus simulated by updating state variables, which record the cyclic loading history. The complexity of the model thus depends on the number of state variables in the model. As stated in section 2.2.1, the basic critical state models predict purely elastic behavior within the yield surface. This elastic behavior within the yield surface fully de-couples volumetric and deviatoric shear behavior. Thus the accumulation of irrecoverable plastic volumetric strain (in the drained condition) or the excess pore water pressure (in the undrained condition) induced by a number of load cycles within the yield surface cannot be simulated. A natural extension of these models is thus trying to introduce

plastic strain within the conventional yield surface. Three main types of these extensions exist: (i) two-surfaces and multi-surface plasticity with kinematic hardening (Mroz, 1967; Prevost, 1977; Mroz *et al.*, 1978; Prevost, 1978; Mroz *et al.*, 1979, 1981); (ii) bounding surface models originally developed for metal plasticity (Dafalias, 1975; Krieg, 1975; Dafalias & Herrmann, 1982); and (iii) sub-loading surface models (Hashiguchi & Ueno, 1977; Hashiguchi, 1980, 1989). In essence, the bounding surface concept and sub-loading concept are practically identical, so the following review will only refer to the two-surfaces, multi-surface plasticity and the bounding surface plasticity.

Mroz (1967) was the first to develop a multi-surface kinematic hardening model for metals. In order to simulate the smooth change of stiffness, Mroz (1967) introduced a set of kinematic nesting surfaces of constant hardening moduli. The behavior within the first kinematic surface is assumed to be purely elastic. As loading or unloading continues, the behavior will become elasto-plastic once the stress state falls on the first surface. As further loading or unloading, the first surface is dragged along the stress path and the hardening modulus associated with the first surface applies until the stress state reach the next surface. Once the next surface reached, the hardening modulus associated with this new surface is activated and applies immediately. Meanwhile, the new surface moves together with the previous surface in the subsequent loading. The introduction of these surfaces and the corresponding hardening moduli in the stress space consequently leads to a piecewise linear stress-strain behavior. As the number of surfaces increase, a smooth stress-strain curve can be obtained. A similar model was developed by Iwan (1967) independently. Figure 2.10 shows the schematic layout of spring-slider system of Iwan (1967) and Figure 2.11 shows the resulting piecewise and smooth stress-strain curves (Byrne, 2000).

Mroz *et al.* (1978) and Prevost (1978) applied this concept to deal with both drained and undrained soil conditions. A schematic representation of these surfaces is shown in Figure 2.12. It it noted that in Figure 2.12 (a), the variation of hardening moduli is different from Mroz (1967) that the hardening moduli will be evaluated from a conjugate point, which will depend on the current stress state through a specific interpolation rule. Mroz *et al.* (1979) simplified the above multi-surface model into a two-surface model by considering only one kinematic yield surface within an outer surface. This outer surface serves as a state bounding surface, which separates all the possible stress state from impossible stress state (Figure 2.13). The inner yield surface translates within the bounding surface. The hardening modulus is evaluated from a conjugate point. Further, Al-Tabbaa (1987) and Al-Tabbaa & Wood (1989) developed a bubble model with a single kinematic yield surface (bubble) and an outer bounding surface designated by the conventional MCC yield surface (Figure 2.14). Stallebrass & Taylor (1997) extended this model to incorporate additional history surface in order to take into account of the small strain stiffness as well as the effects of recent stress history of OC clay (Figure 2.15). Basically, both the two-surface and three-surface bubble models are similar with the kinematic hardening model family (Mroz, 1967; Mroz *et al.*, 1978, 1979, 1981)

In the bounding surface models, the conventional yield surface is re-named as the bounding surface, which bounds all the possible stress states. A loading surface, which is homothetic to the bounding surface and always passes the current stress state, is introduced in order to simulate the plastic behavior within the bounding surface. If the stress state lies on the bounding surface, then the bounding surface models degenerate to the conventional elasto-plastic models and the conventional elasto-plastic theory applies. On the other hand, if the stress state is inside the bounding surface, plastic

strains are allowed if loading continues. To evaluate these plastic strains, as stated in Appendix A, the outward directions of the yield surface and plastic potential are required. These two directions are now determined from an image point on the bounding surface through a mapping rule. A radial mapping rule is used in Figure 2.16, relating the current stress point σ_0' to the image point on the bounding surface $\bar{\sigma}'$. The image point is the intersection point of the bounding surface and a straight line, which connects the origin of the stress space and the current stress point. The plastic modulus is now evaluated from the image point rather than from the current stress state. Besides, the plastic modulus depends on the proximity of the current stress point to the image point in the stress space.

Various models have been proposed based on the bounding surface concept since the pioneering work on soil by Dafalias & Herrmann (1982) (Lade, 1977; Whittle, 1987; Dasari, 1996; Stallebrass & Taylor, 1997; Pestana & Whittle, 1999; Atkinson, 2007; Yu *et al.*, 2007). For example, Whittle (1987) presented a MIT-E3 model, which is based on the previous work at MIT for clay under both monotonic loading and cyclic loading (Kavvadas, 1982). MIT-E3 model is a very sophisticated model combining the bounding surface concept and the small strain nonlinear elastic behavior of soil. It also takes into account the anisotropic behavior of soil. Whittle (1993) demonstrated the ability of the model to accurately represent the behavior of three different clays subjected to a variety of loading paths. However, the MIT-E3 model needs fifteen input parameters, some of which are hard to determine from laboratory tests. Besides, the formulation is rather complex and a numerical stability problem may be encountered when implementing this model in common numerical software. This model thus remains as a research model.

It should be noted that a key difference in the above bounding surface models is the formulation of the plastic modulus, which not only governs the nonlinearity and the coupling effect of the volumetric and deviatroic shear behavior, but also introduces new model parameters adding complexity to the model. Among the above models, the plastic modulus suggested by Pastor *et al.* (1985) is relatively simple and works quite well for a number of lightly OC clays under triaxial tests. This model will thus be further exploited in Chapter 3 to serve as a building block of the new model developed in this thesis.

2.2.5 Nonlinearity at small strain range

In the 1970's, conventional laboratory measurements of stiffness of OC clays showed values much lower than those estimated from the back analysis of the field performance of geotechnical structures. Similar differences were also found when the laboratory stiffness data was compared with values of stiffness derived from in situ field tests (Marsland, 1971; St. John, 1975; Grammatikopoulou, 2004).

Local measurements of strains on soil samples revealed that the stress-strain behavior of OC clays is highly non-linear, with high values of stiffness at small strains, which were not measured correctly with the earlier conventional overall measurements of strain (Costa-Filho & Vaughan, 1980; Burland & Symes, 1982; Grammatikopoulou, 2004). Atkinson & Sallfors (1991) idealized the variation of elastic shear modulus with shear strain as an S-shape curve as shown in Figure 2.17. In the figure, three regions were identified: (i) very small strains region (strains generally less than 0.001%), where the stiffness is almost constant with strain; (ii) small strain region (strains up to 1%), where the stress-strain behavior is highly nonlinear; (iii) large strain region (strain larger than 1%), where the stiffness is low and the soil is approaching failure (Atkinson

& Sallfors, 1991). Similar proposal has been used by Dasari (1996) as shown in Figure 2.18.

The elastic shear modulus at very small strain is commonly termed as $G_{\max}$. It is postulated that this value reflects the true 'elastic' properties of the soil skeleton (Whitman *et al.,* 1969). Thus estimation of $G_{\max}$ can be made by using techniques to measure the speed of elastic wave propagation in soil (Whittle, 1987). Laboratory resonant column tests and field cross-hole or down-hole techniques can also be employed to determine $G_{\max}$ (Woods, 1978; Subhadeep, 2009). Hardin & Black (1968) postulated that $G_{\max}$ of clay primarily depends on the void ratio and the mean effective stress. Viggiani & Atkinson (1995) related $G_{\max}$ to the mean effective stress p' and the *OCR* as

$$\frac{G_{\max}}{p_r} = m_r \left(\frac{p'}{p_r} \right)^n OCR^m \qquad 2.11$$

where p_r is a reference pressure, m_r, n, m are material constants.

Clayton (2011) summarized the recent research on $G_{\max}$ in his Rankine lecture that the shear modulus of a granular material at very small strain levels is affected fundamentally by three factors: (i) the void ratio of the specimen; (ii) the inter-particle contact stiffness, which will depend upon particle mineralogy, angularity and roughness, and effective stress; (iii) the deformation and the flexibility within individual particles, which will depend on particle mineralogy and shape. A similar expression as Viggiani & Atkinson (1995) is then proposed for sands and clays,

relating $G_{\max}$ in the vertical plane of soil sample to the mean effective stress p' and void ratio e as

$$G_{\max} = C_p \left(1+e\right)^{-3} \left(\frac{p'}{p_{atm}} \right)^{0.5} (MPa) \qquad 2.12$$

where C_p is a material constant and p_{atm} is atmospheric pressure.

To determine the variation of shear modulus with shear strains, Ishibashi & Zhang (1993) proposed to employ a hyperbolic function to describe the decreasing rate of shear modulus with shear strains. Subhadeep (2009) used an alternative hyperbolic form to describe the stress-strain curve as follows

$$G = \frac{G_{\max}}{\left[1+3G_{\max}\left|\varepsilon_s\right|/q_f\right]^2} \qquad 2.13$$

where $\left|\varepsilon_s\right|$ is the absolute value of generalized shear strains and q_f is the deviatoric stress at failure.

However, in a general soil constitutive model, if the elastic shear modulus is related to the shear strain, the model calibration will be rather difficult, especially in the presence of the plastic strains. A simpler method is to relate the elastic shear modulus to the change of stress level. With the increasing of stress level, shear strain will be induced, so the elastic shear modulus will decrease. Pestana & Whittle (1999) thus expressed the tangent elastic shear modulus in terms of the stress ratio as

$$\frac{G}{G_{\max}} = \frac{1}{\left(1+a_1\varsigma_2\right)\left(1+a_2\varsigma_2\right)} \qquad 2.14$$

where a_1, a_2 are material constants and ς_2 measures the deviation of the deviatoric stress from the initial loading or stress reversal point.

When the stress state deviates significantly from the initial loading or stress reversal point, the shear strain is typically quite large. In this large strain region, the stiffness is quite low due to large plastic strain, thus the modeling of shear modulus is not critical, Dasari (1996) employed a constant Poisson's ratio following Equation 2.9.

2.2.6 Hysteretic effect

If a constant Poisson's ratio is used, following Equation 2.8 and Equation 2.9, both G and K are linearly related to the mean effective stress but are independent of the deviatoric stress. In this case, the elastic formulation is theoretically unacceptable because it is not possible to define an elastic potential (Love, 1963). Thus the principle of energy conservation is violated and the elastic prediction will be path-dependent as demonstrated by Zytynski *et al.* (1978) and Whittle (1987). Whittle (1987) summarized three alternatives to solve this problem as: (i) relate G to both the mean effective stress and deviatoric stress; (ii) relate the elastic parameters to plastic deformation, thus treat the elastic parameters as state variables; (iii) assume that all closed load cycles in effective stress space will lead to some plastic strains, so there is no true elastic region.

Hueckel & Nova (1979) introduced a modified elastic behavior within the conventional yield surface. They assumed that that a uni-dimensional cycle of loading could be accurately described by a closed symmetric hysteresis loop. For each loop, the non-linearity of soil is independent of the magnitude of the maximum past stress, but instead, is related to a reference stress state which is called a stress reversal point.

This method has been employed by Whittle (1987, 1993) in the MIT-E3 model to define the perfect hysteretic behavior of Boston Blue Clay (BBC). A simpler form to describe the hysteretic behavior of soil is the Masing's rule (Masing, 1926), which is commonly used for soil under cyclic loading (Dasari, 1996; Papadimitriou & Bouckovalas, 2002; Subhadeep, 2009). Masing (1926) (as the original paper is not in English, the following statement is followed from Byrne (2000)) stated that: (i) the shear modulus on each loading reversal is assumed a value equal to the initial tangent modulus for the initial loading curve, called backbone curve; (ii) the shape of the unloading or reloading curves is the same as that of the initial loading curve, except that the scale is enlarged by a factor of two. A schematic representation of Masing's rule is shown in Figure 2.19. Pyke (1979) extended Masing's concept by adding two additional rules that: (i) the unloading and reloading curves should follow the initial loading curve (backbone curve) if the previous maximum shear strain is exceeded; (ii) if the current loading or unloading curve intersects the curve described by a previous loading or unloading curve, the stress-strain relationship follows that curve. Pyke's extension is shown in Figure 2.20.

2.3 Summary

In this chapter, common soil constitutive models are reviewed based on comprehensive literature. The framework of the basic critical state models-the CC model and the MCC model, is reviewed and previous research efforts on heavily OC clays are summarized. Various multi-surface and bounding surface models, which aim at modeling the cyclic behavior of soils are discussed. The nonlinearity at small strain and hysteretic behavior of soil are also summarized.

Table 2.1 Model parameters for basic critical state models

Parameter	Physical meaning
N	Critical state parameter. The intercepts of NCL with v axis in $v-\ln p'$ space
λ	Critical state parameter. The slop of NCL in $v-\ln p'$ space
κ	Critical state parameter. The slop of SL in $v-\ln p'$ space
M	Critical state parameter. The slope of CSL in $p'-q$ space.
G	Elastic shear modulus.

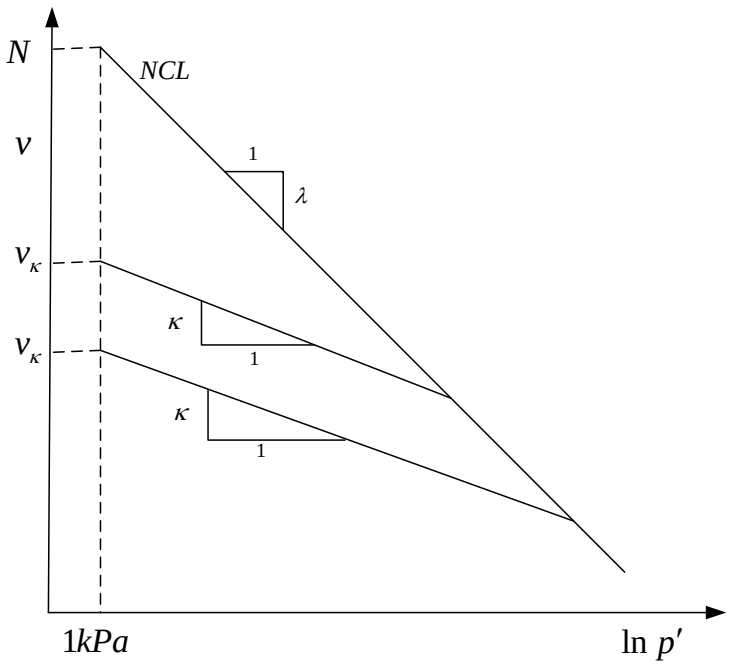

Figure 2.1 $v-\ln p'$ plot

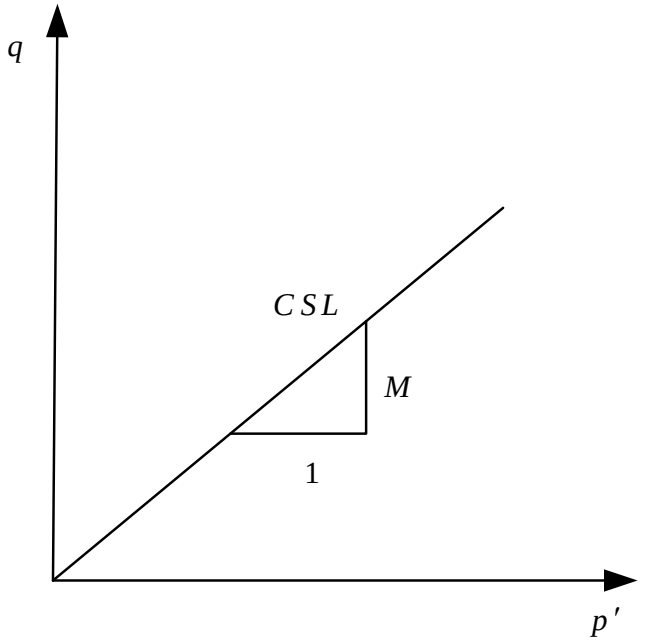

(a) $p'-q$ space

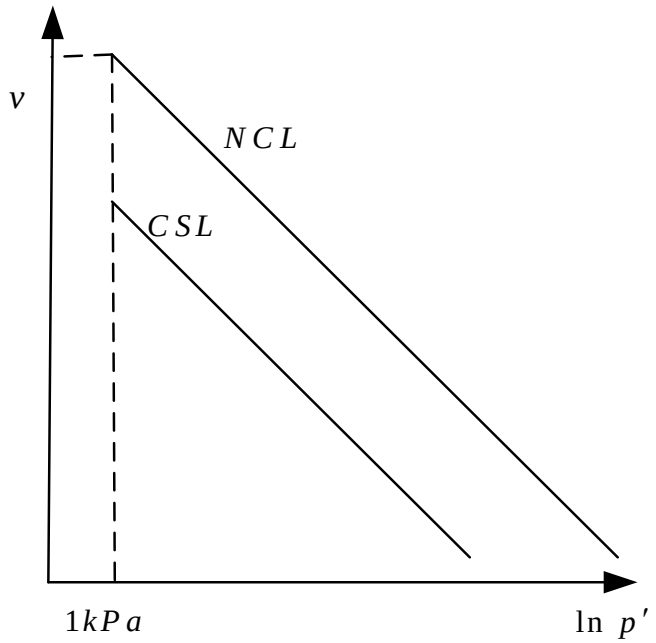

(b) $v-\ln p'$ space

Figure 2.2 Position of the *CSL*

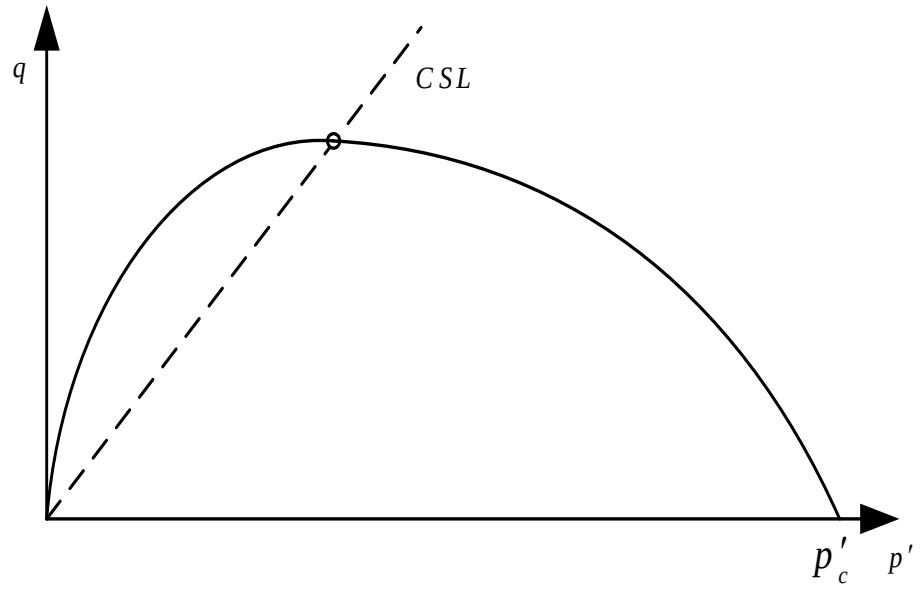

(a) The CC model

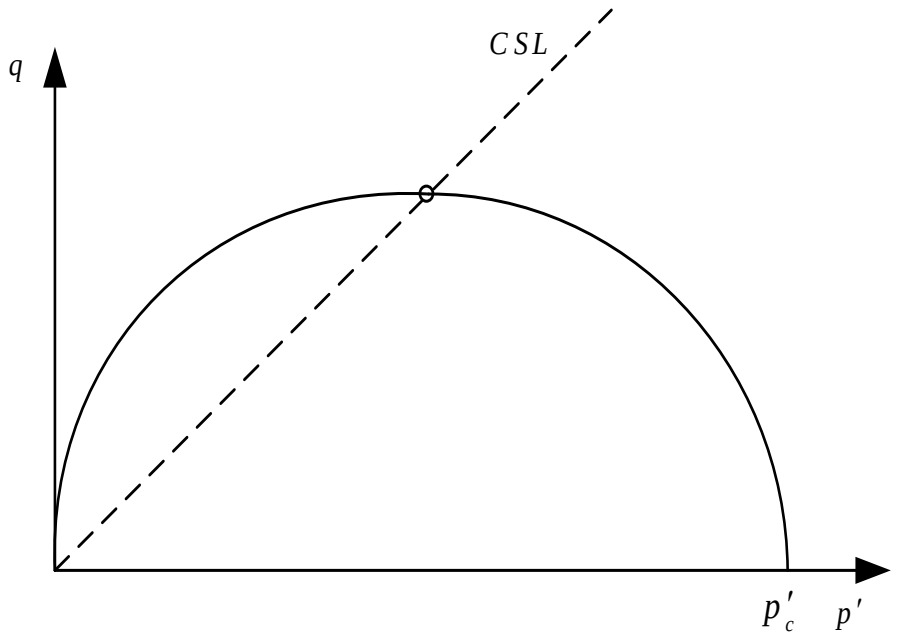

(b) The MCC model

Figure 2.3 Yield surface of the basic critical state models

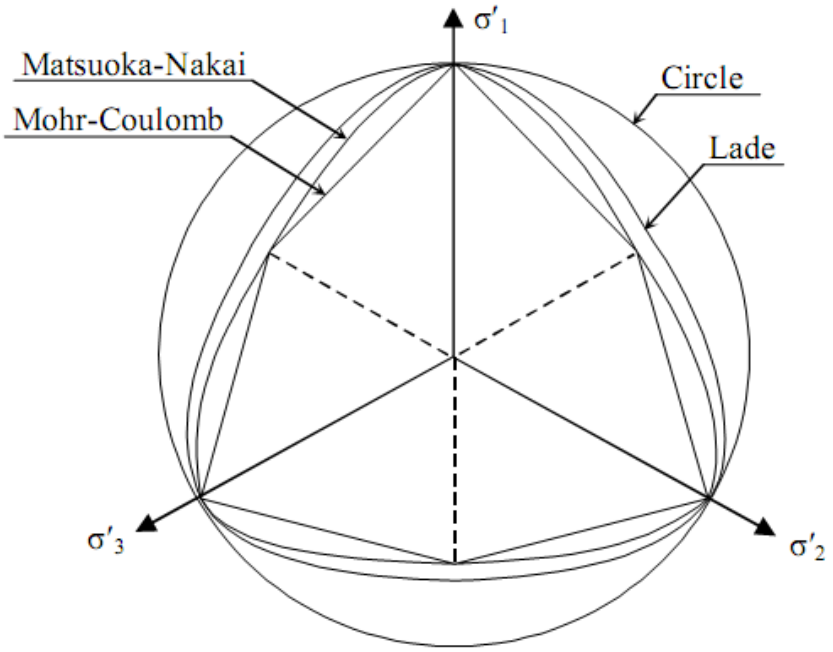

Figure 2.4 Bounding surface in deviatoric plane (Grammatikopoulou, 2004)

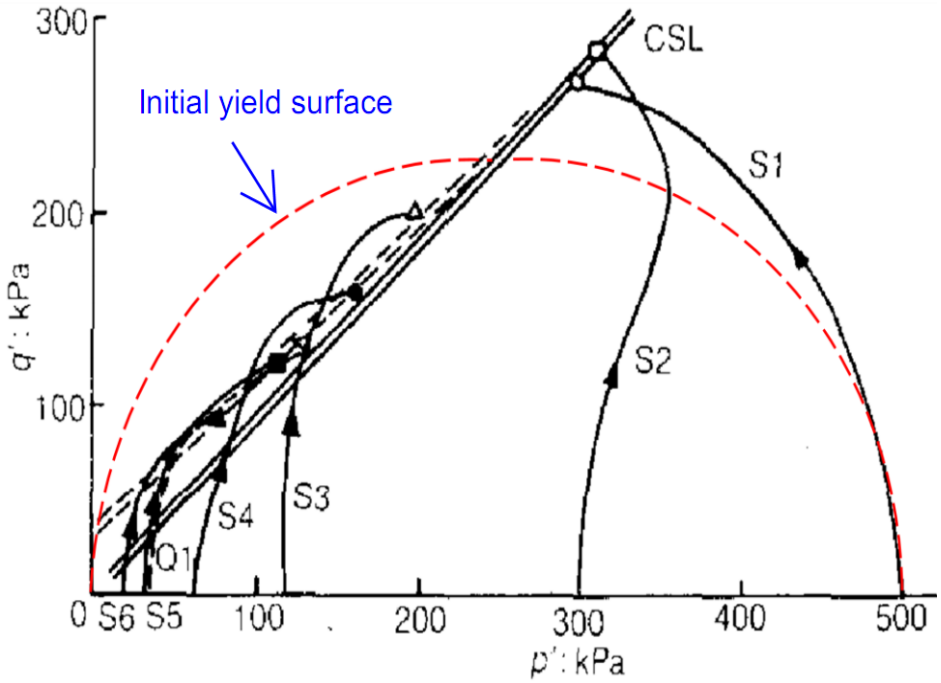

(a) $p'-q$ space

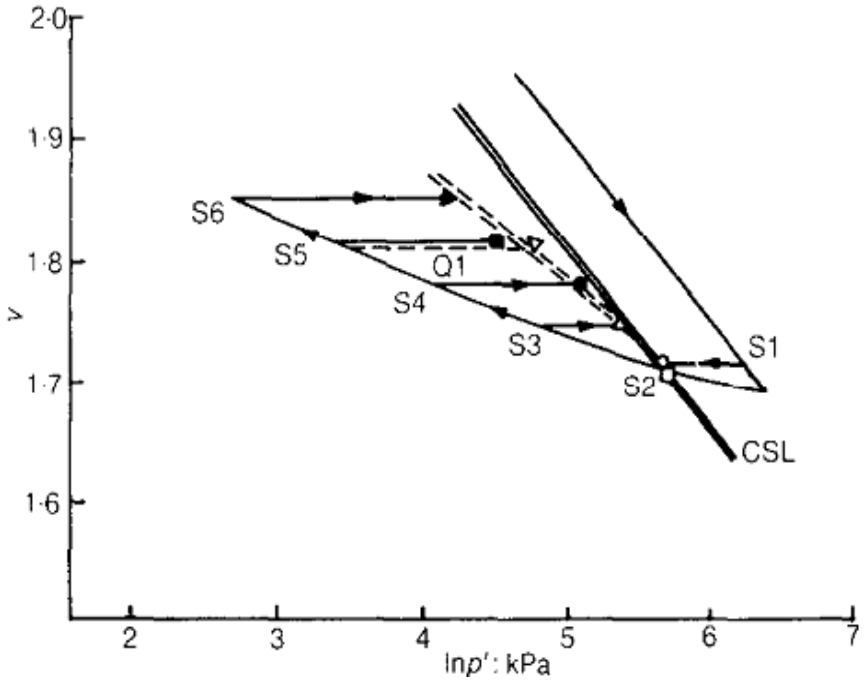

(b) $v - \ln p'$ space

Figure 2.5 Stress path (Atkinson & Richardson, 1987)

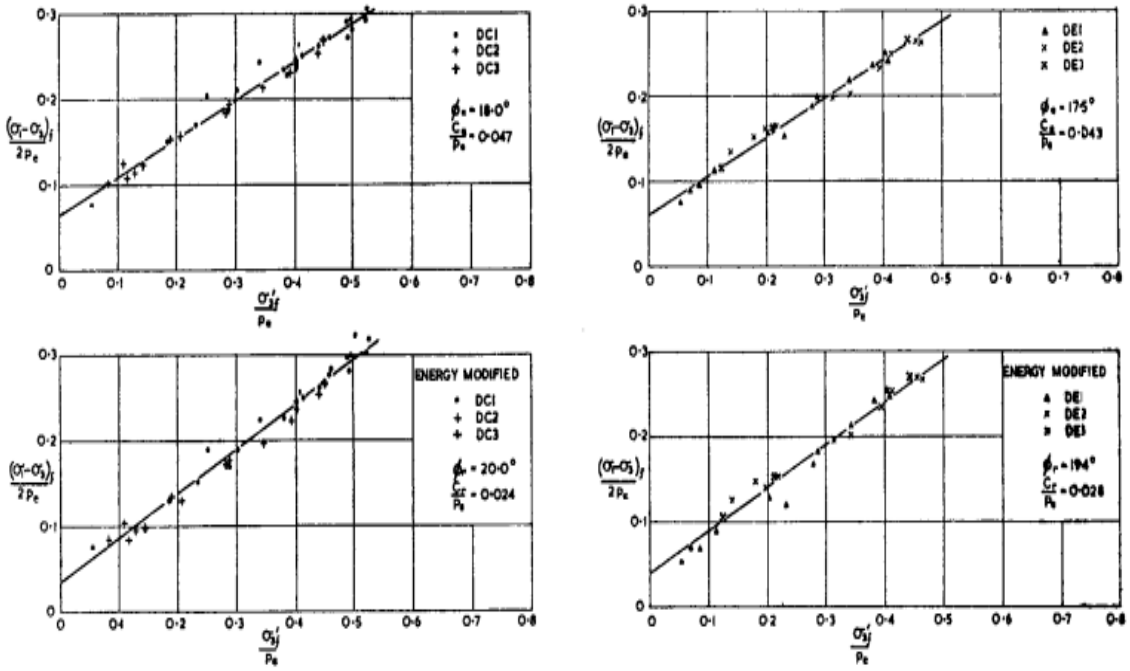

Figure 2.6 Hvorslev line for Weald clay (Schofield & Wroth, 1968)

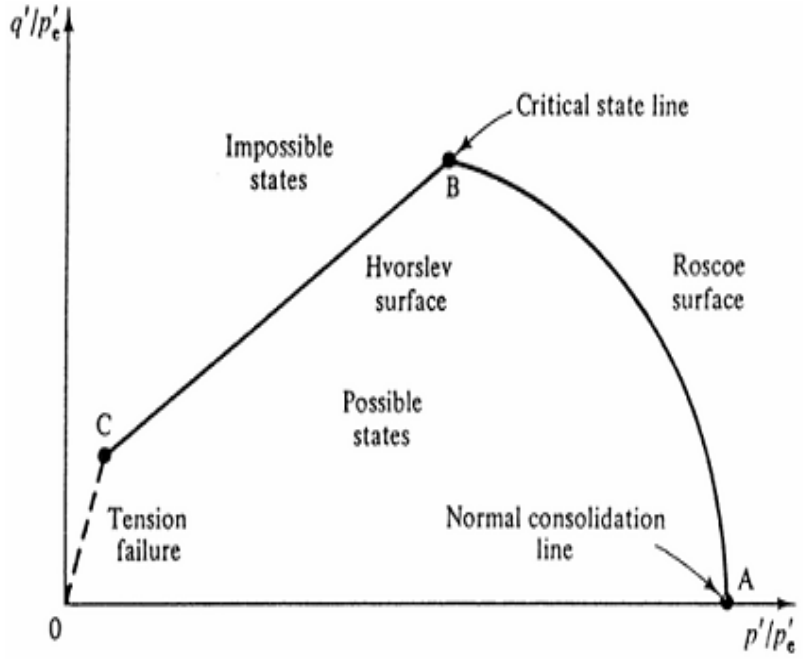

Figure 2.7 Hvorslev surface with tension cut-off (Atkinson & Bransby, 1978)

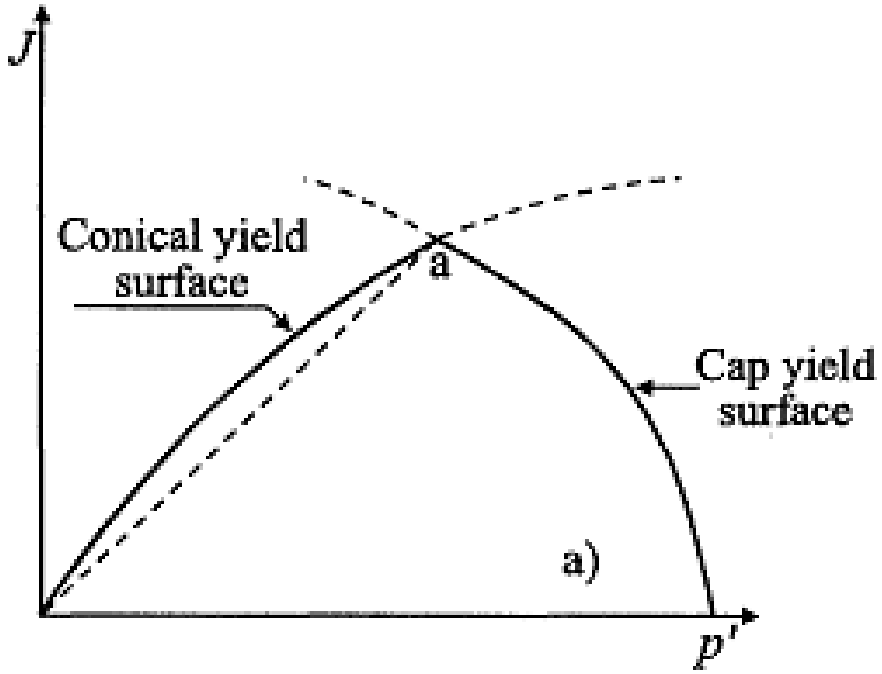

Figure 2.8 ‘Double hardening’ model yield surface (Potts & Zdravkovic, 1999)

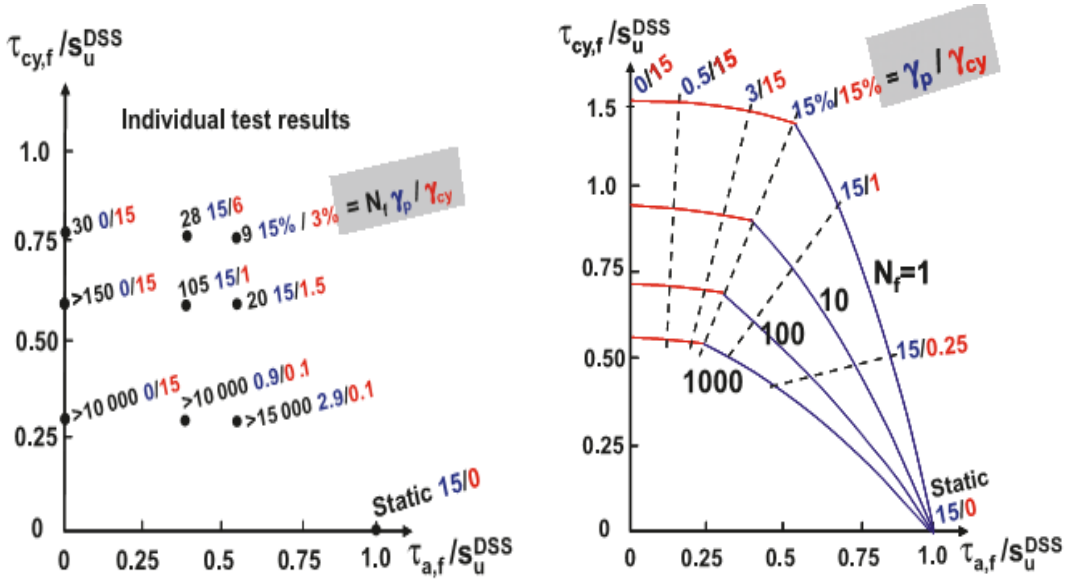

(a) DSS test

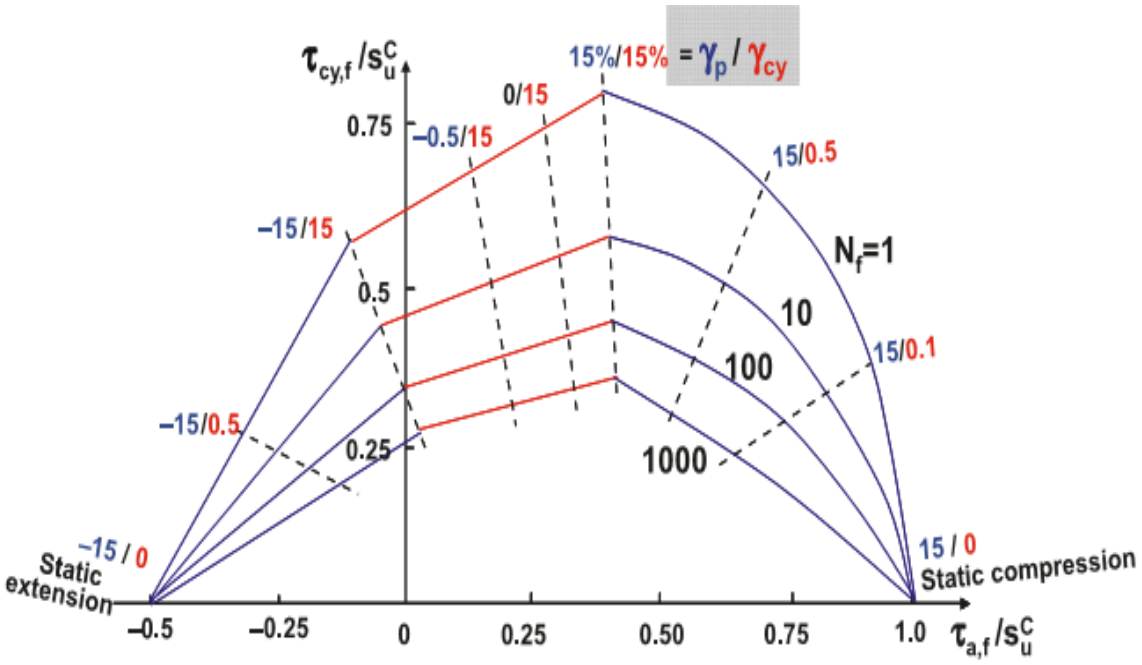

(b) Triaxial test

Figure 2.9 Number of cycles to failure (Andersen, 2009)

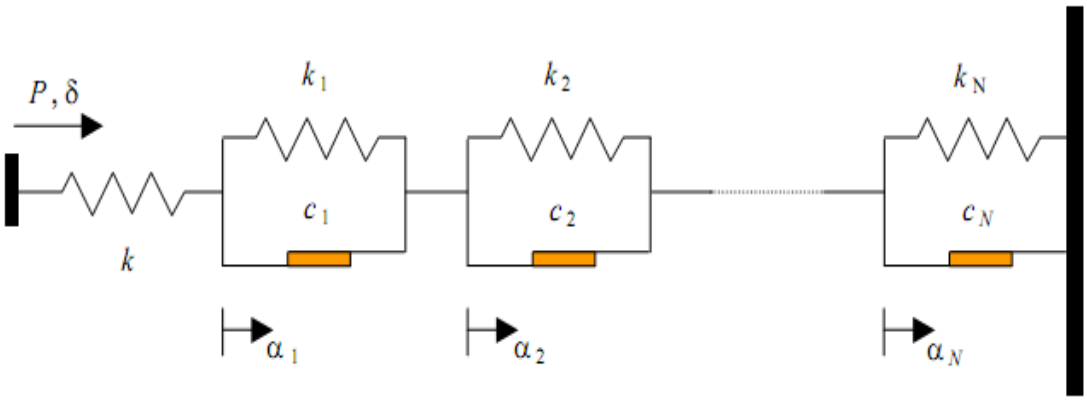

Figure 2.10 Schematic layout of spring-slider system (Byrne, 2000)

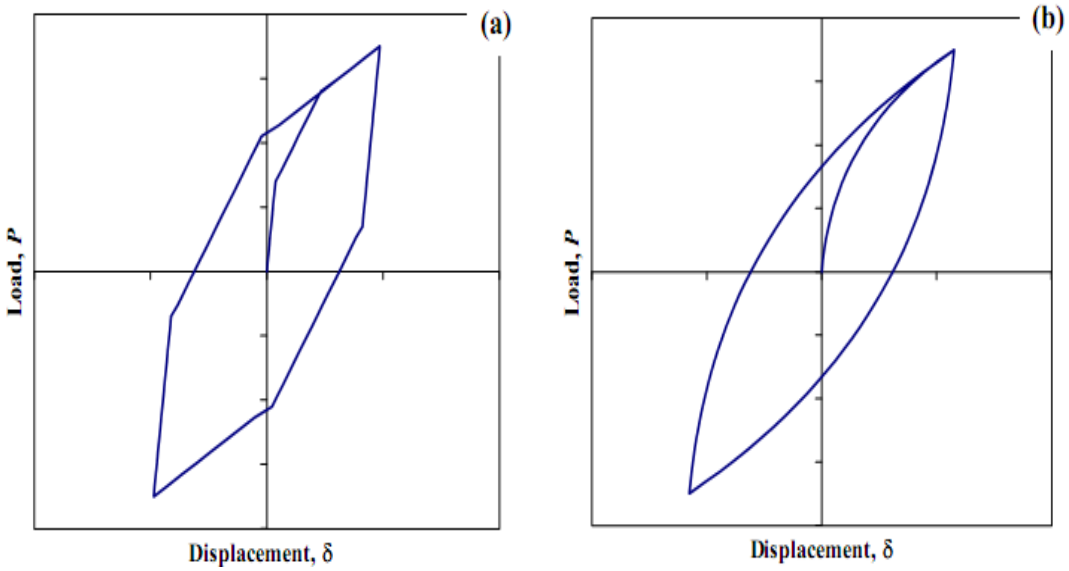

Figure 2.11 Piecewise and smooth stress strain curves (Byrne, 2000)

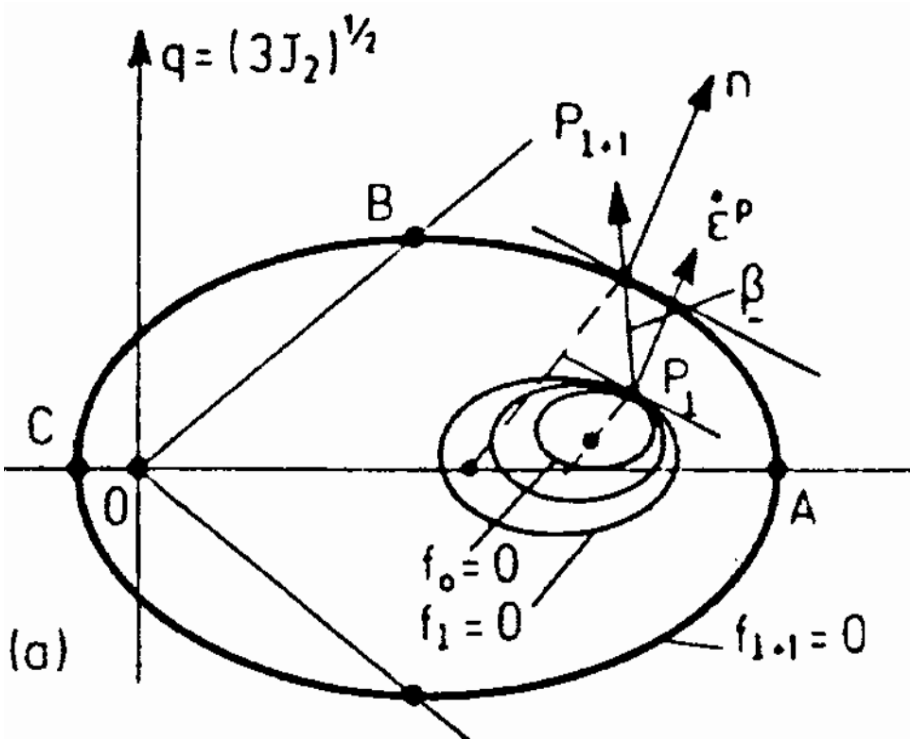

(a) Mroz *et al.* (1978)

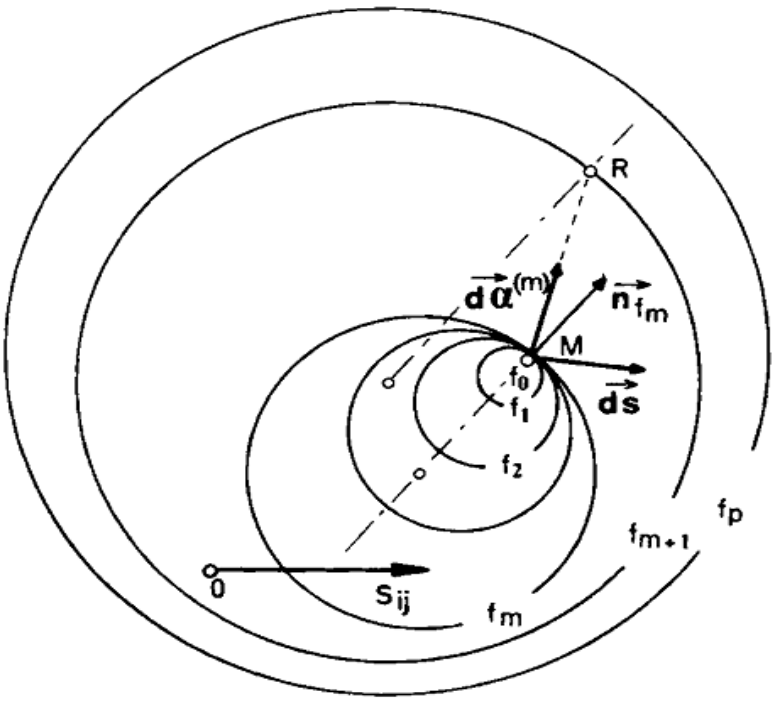

(b) Prevost (1978)

Figure 2.12 Multi-surface models

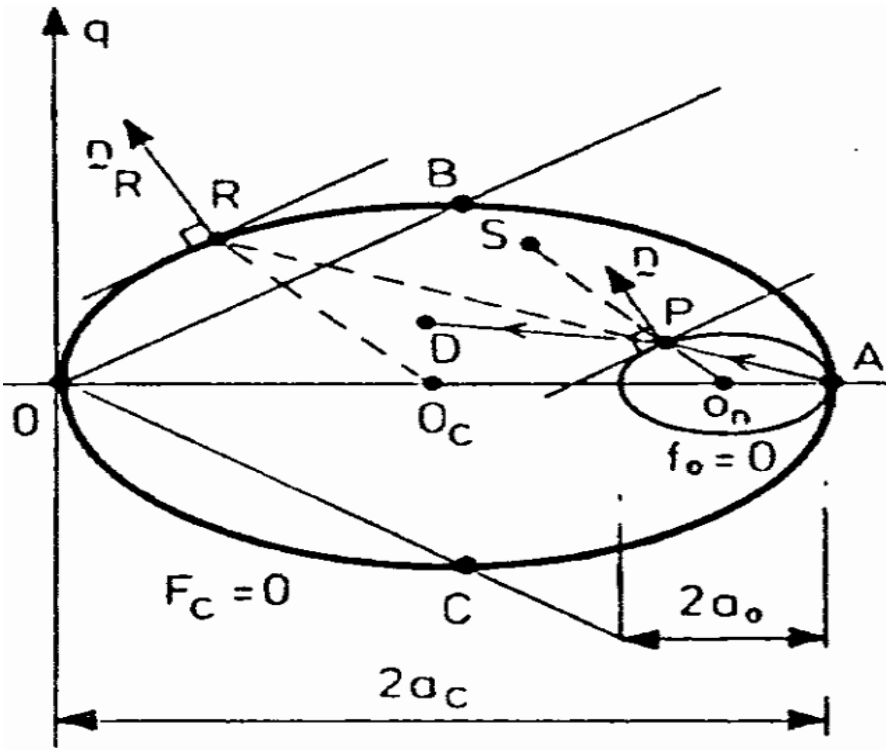

Figure 2.13 Two surface model (Mroz *et al.*, 1979)

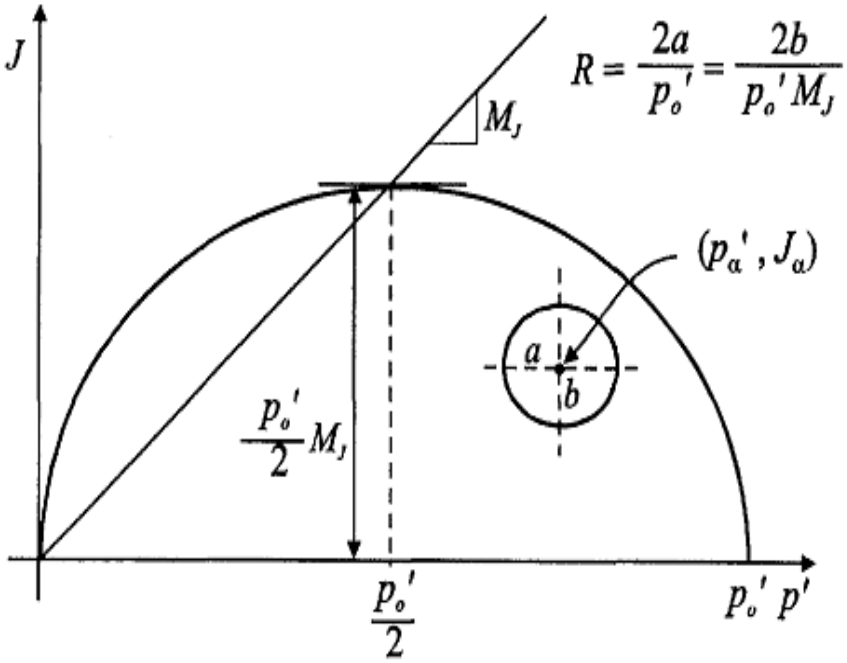

Figure 2.14 Bubble model (Al-Tabbaa, 1987)

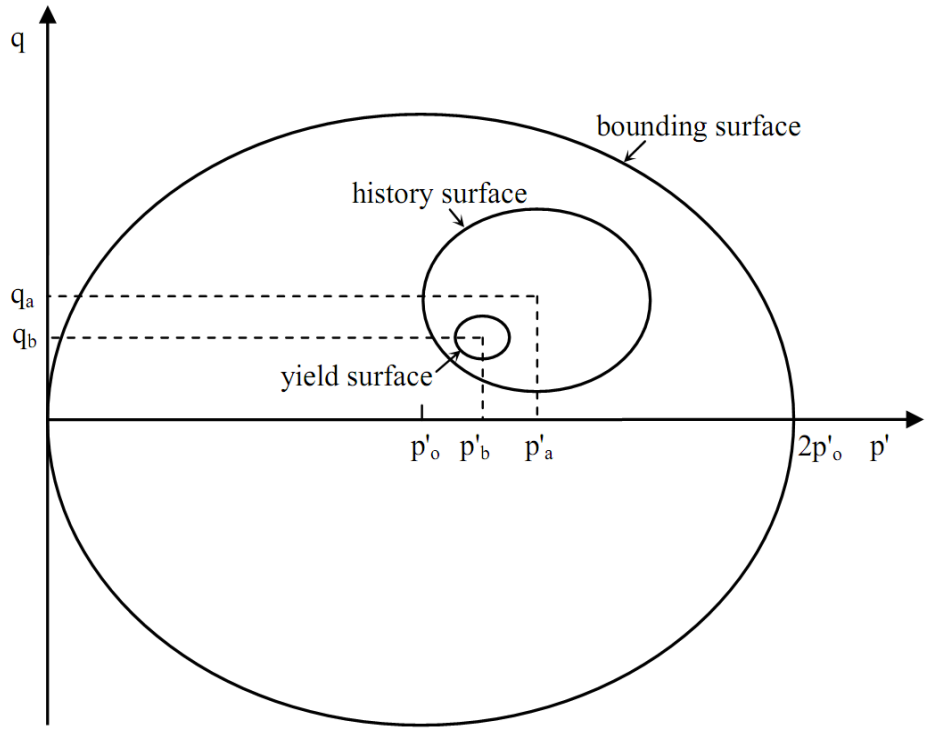

Figure 2.15 Three surface model (Stallebrass & Taylor, 1997)

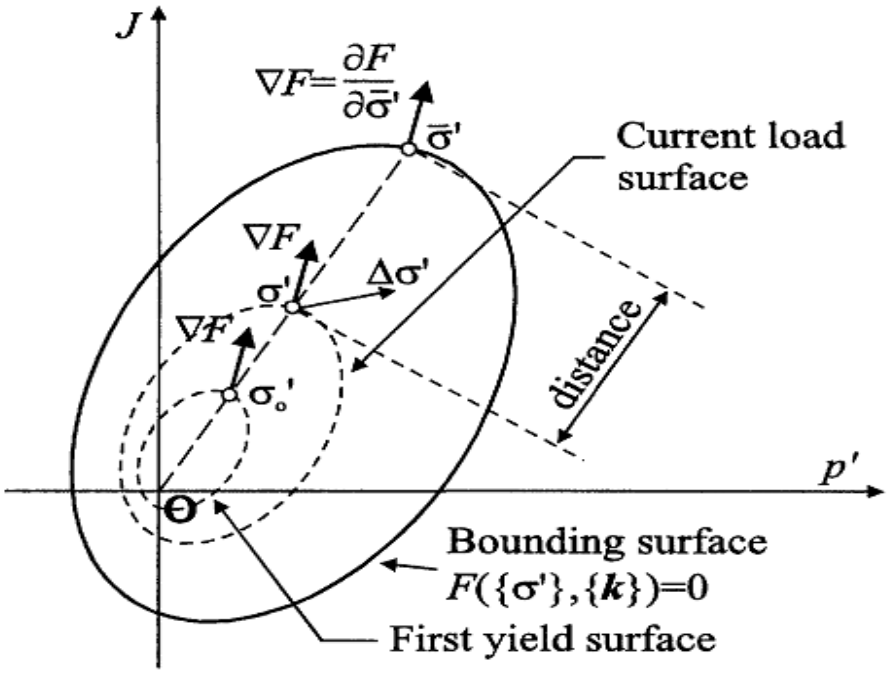

Figure 2.16 Bounding surface model (Potts & Zdravkovic, 1999)

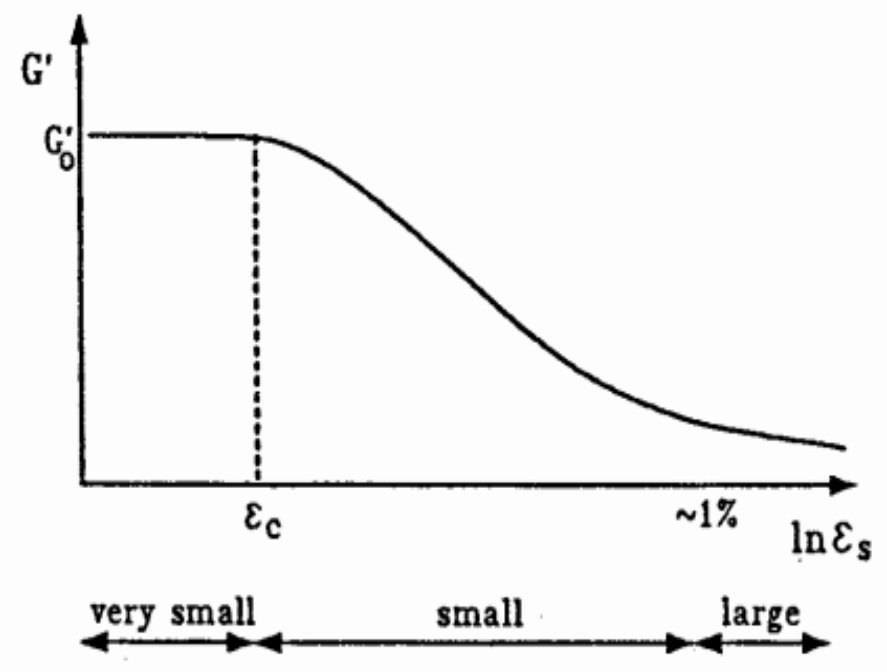

Figure 2.17 Variation of shear modulus with strain (Atkinson & Sallfors, 1991)

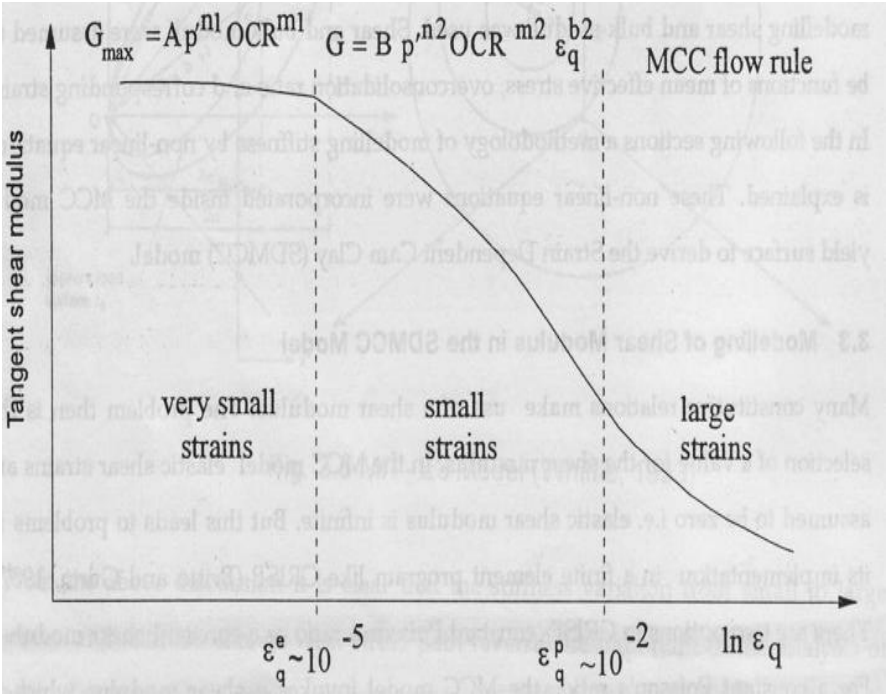

Figure 2.18 Variation of elastic shear modulus with strain (Dasari, 1996)

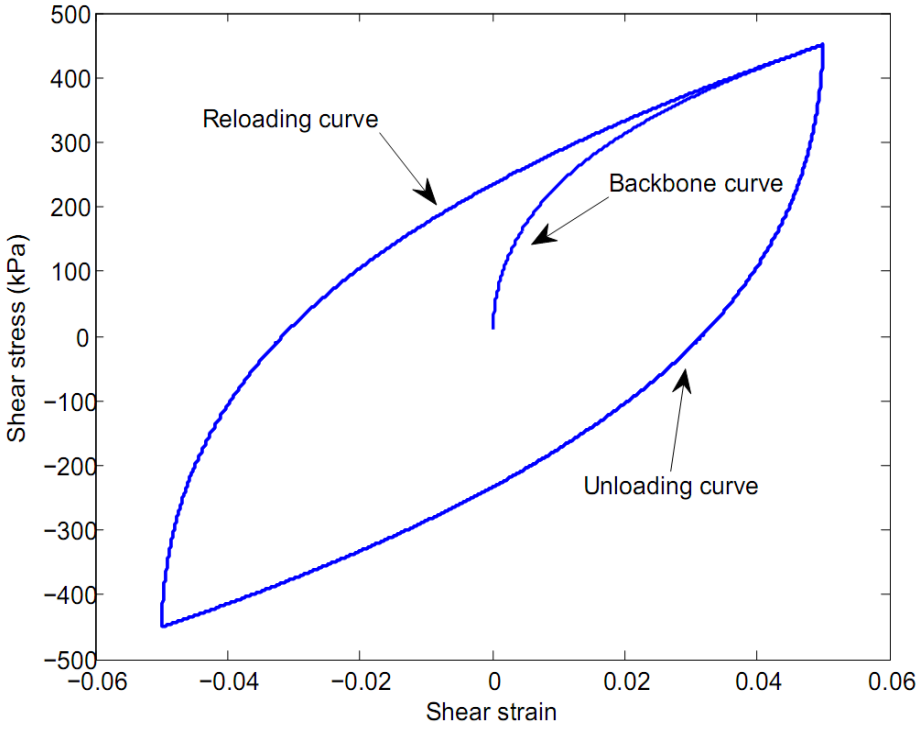

Figure 2.19 Depicts of Masing's rule

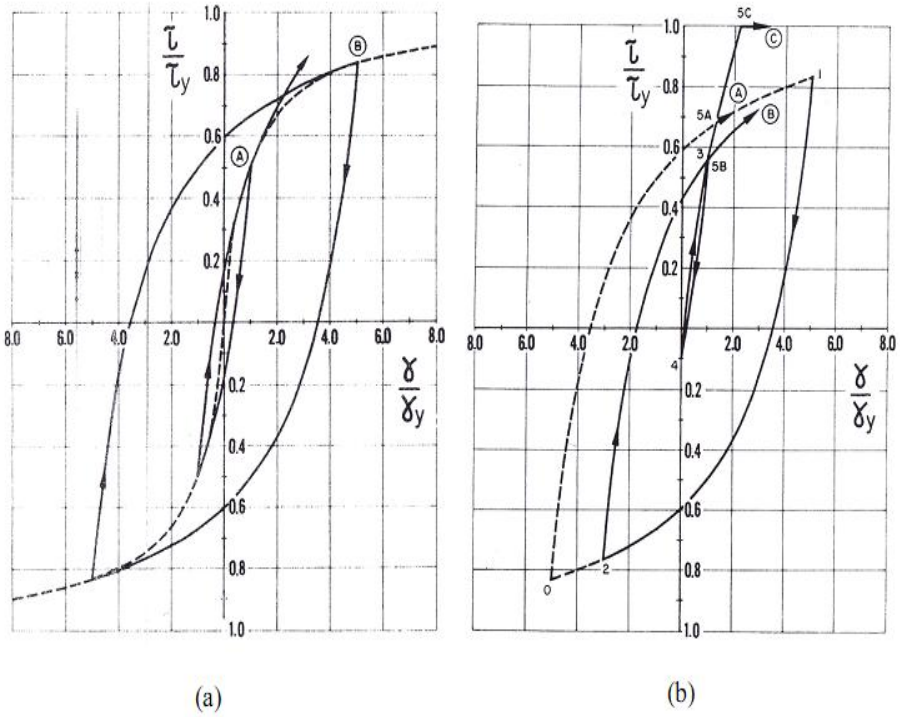

Figure 2.20 Pyke's extension of Masing's rule (Pyke, 1979)

Chapter 3 **Formulation of a new critical state model for clays**

3.1 Introduction

The basic critical state models predict much higher strength of clays on the dry side. The fully de-coupled volumetric and deviatoric behavior within the yield surface leads to the inability of these models to predict the plastic strains when the clay is subjected to cyclic loads. Both of these two limitations have been discussed in detail in Chapter 2. This chapter aims at overcoming these two shorting comings by constructing a new constitutive model for OC clays and soft clays under cyclic loads. The new model developed here is termed as 'AZ-Cam clay model' (as the main idea of the model was inspired by Atkinson (2007) and Zienkiewicz *et al.* (1985), which incorporates two main features: i) a failure envelope is introduced to better predict the peak strength and ultimate strength of heavily OC clays; and ii) the bounding surface concept is employed to simulate the plastic strains within the conventional yield surface.

To better present the philosophy of the AZ-Cam clay model, the experimental findings of Atkinson (2007), which is essential to the formulation of the dry side of the AZ-Cam clay model, will first be reviewed. The work of Zienkiewicz *et al.* (1985) will follow as the simple expression of plastic modulus used was reasonably successful in simulating various clays in the subcritical side as demonstrated in the paper. The detailed formulation of the AZ-Cam clay model and the interpretation of the input model parameters will be presented.

3.2 Atkinson's proposal for peak strength of clays on the dry side

Hvorslev (1936) found that a straight line can describe the failure envelope of OC soils satisfactorily in $p'-q$ space. However, Atkinson (2007) stated that only a curved line can represent the peak strength of unbonded soil over the range of effective stress from zero to the critical state. Meanwhile, a straight line is intrinsically unsafe under certain conditions. As shown in Figure 3.1, the dash line is a straight line which is supposed to be best fitted to the experimental peak strength P_1, P_2, P_3 as represented by the solid dots. The solid double line is the CSL and the solid curve best approximates the experimental data. From the figure, it is easy to conclude that there are certain ranges (e.g. to the left side of P_1 and to the right side of P_3), in which a straight line over predicts the peak strength.

Based on extensive experimental results on various clays subjected to a variety of loading paths, Atkinson (2007) suggested two proposals to represent the peak strength of OC clays as follows:

$$\frac{q}{Mp'_{cr}} = \left(\frac{p'}{p'_{cr}} \right)^b \tag{3.1}$$

and

$$\frac{q}{Mp'} = 1 + \chi \left(\Gamma - v_\kappa \right) \tag{3.2}$$

where p'_{cr} is known as the critical state pressure, which is the pressure on the CSL at the current specific volume. χ and b are material constants governing the nonlinearity of the curve when plotted in $p'-q$ space. The value of $\Gamma - v_\kappa$ indicates

the vertical distance of the current stress state to the CSL and is known as state parameter (Yu, 2006).

Mathematically, Equation 3.1 and Equation 3.2 are not exactly identical, although they could both fit the test data quite well as demonstrated in the paper (Atkinson, 2007). Equation 3.1 gives a power law which is similar to that proposed by Demello (1977) and used routinely in rock mechanics (Hoek & Brown, 1980). The peak strengths obtained from tests on six clays are shown in Figures 3.2 (a)-(f) as well as the failure envelope from Equation 3.1 (the straight line, plotted in logarithmic scale) following Atkinson (2007). Equation 3.2 is similar to the relationship between stress ratio and state parameter proposed by Been & Jefferies (1985). The same test data as in Figure 3.2 with the proposed line according to Equation 3.2 are shown in Figures 3.3 (a)-(f) following Atkinson (2007). Atkinson (2007) further pointed out that the present experimental data were not sufficiently precise to distinguish which of the two relationships fit the data best. Both of the two equations can thus be used to describe the peak strength of OC clays at the current stage. For the convenience of the model formulation, Equation 3.2 will be used in the current study.

3.3 Simple model for clays on the wet side

Mroz's series kinematic models as presented in Chapter 2 present a complex process of the evolution of the yield surfaces. However, it is not straight forward to completely determine the total 10 input parameters for the multi-surface model with cyclic degradation (Mroz *et al.*, 1981; Whittle, 1987). Dafalias & Herrmann (1982) presented a bounding surface model, which requires two input parameters to determine the plastic modulus. Zienkiewicz *et al.* (1985) further simplified the plastic modulus with only one input parameter through a power law as:

$$H = \bar{H}\left(\frac{\delta_B}{\delta}\right)^{\gamma} \qquad 3.3$$

where H and $\bar{H}$ are plastic moduli at the current stress point and the image stress point on the bounding surface respectively. δ and δ_B are the distance from the origin of the stress space to current stress point and image point respectively as shown in Figure 3.4. γ controls the non-linearity of the plastic modulus within the bounding surface.

As long as the plastic modulus has been determined, the elasto-plastic matrix can be determined from Equation A.42 in Appendix A. The outward direction of the yield surface and plastic potential are determined from the image stress point. The model requires only one additional parameter γ compared to those required for the basic critical state models. Figure 3.5 and 3.6 show the model prediction. Compared to the experimental data, a good agreement is achieved.

It is noted that the model presented by Zienkiewicz *et al.* (1985) ignores the behavior of clay on the dry side as the CSL is used as a part of the bounding surface. For this reason, the model always under predicts the peak strength of heavily OC clays. Combining with the proposal of Atkinson (2007) as stated in the previous section, it is now possible to formulate a constitutive model which can be used for clays over a wide range of *OCRs*.

3.4 Formulation of the AZ-Cam clay model in triaxial space

3.4.1 Introduction

As stated in section 3.1, the basic critical state models over predict the strength on the dry side and are unable to simulate the plastic strains within the yield surface The basic structure of the AZ-Cam clay model is within the framework of critical state models. Key attention will be paid on the modifications of the proposal of Atkinson (2007) on the dry side and the plastic modulus inspired by Zienkiewicz *et al.* (1985). Similar to most general soil constitutive models, the AZ-Cam clay model is constructed in terms of effective stresses, and compression is defined as positive. The behavior is also assumed to be time-independent. First the model will be formulated in triaxial space ($p'-q$ space). The generalized form in general stress space will be presented in Chapter 4.

3.4.2 Loading and unloading behavior

In the AZ-Cam clay model, when soil undergoes unloading, the behavior is always assumed to be elastic. However, when soil undergoes loading, the behavior is always elasto-plastic and thus there is no true elastic zone. The loading and unloading criterion follows Pastor *et al.* (1990) and Manzanal *et al.* (2011) as

Unloading: $dF = \left\{\frac{\partial F}{\partial \sigma}\right\}^T \left\{d\sigma^e\right\} < 0$ 3.4 (a)

Neutral loading: $dF = \left\{\frac{\partial F}{\partial \sigma}\right\}^T \left\{d\sigma^e\right\} = 0$ 3.4 (b)

Loading: $dF = \left\{\frac{\partial F}{\partial \sigma}\right\}^T \left\{d\sigma^e\right\} > 0$ 3.4 (c)

where F, $\{\sigma\}$ represent the yield surface and stress state, respectively. $\left\{d\sigma^e\right\}$ is the elastic stress increment vector as given in Appendix A.

3.4.3 Bounding surface

In the AZ-Cam clay model, the conventional yield surface is termed as the bounding surface. Thus the bounding surface separates all the possible stress state from the impossible stress state. Besides, it acts as the yield surface in conventional elasto-plastic theory. The bounding surfaces of the basic critical state models have been shown in Figure 2.3 in $p'-q$ space. In the basic critical state models, the critical state pressure p'_{cr}, which is the projection of the bounding surface apex on the p' axis, can be related to the pre-consolidation pressure p'_c as

$$p'_{cr} = \frac{p'_c}{R} \tag{3.5}$$

For the original Cam clay model, R equals 2.72 while for the MCC model, R equals 2.0.

As the relationship between p'_{cr} and p'_c governs the strength of soil on the wet side, a more general relationship is adopted in the AZ-Cam clay model as follows:

$$p'_{cr} = \frac{2}{2+R_w}\, p'_c \tag{3.6}$$

where R_w is an input material constant.

A generalized form of the MCC model yield surface, which is essentially the same as Zienkiewicz *et al.* (1985) on the wet side, is adopted to describe the bounding

surface in the AZ Cam-clay model (Figure 3.7). Combining with Equation 3.6, the bounding surface on the wet side is proposed as follows:

$$F = \frac{q^2}{M^2} + \frac{4}{R_w^2}\left(p' - \frac{2}{2+R_w} p_c' \right)^2 - \left(\frac{2}{2+R_w} p_c' \right)^2 = 0 \qquad 3.7$$

Mathematically, the left intersection point of Equation 3.7 with p' axis will be greater than zero if $R_w < 2$. Thus certain stress points with small mean effective stress will lie outside the bounding surface, which is not desirable physically. A different expression for the bounding surface on the dry side is proposed as:

$$F = \frac{q^2}{M^2} + \frac{4}{R_d^2}\left(p' - \frac{2}{2+R_w} p_c' \right)^2 - \left(\frac{2}{2+R_w} p_c' \right)^2 = 0 \qquad 3.8$$

where R_d is an input material constant.

It should be noted that as long as the value of R_d in Equation 3.8 remains not less than 2, the bounding surface can encompass all the stress points when they are approaching the origin of the stress space. If $R_d > 2$, the left intersection point of Equation 3.8 with p' axis will be negative, in this case, the volumetric deformation in tension will be allowed. Without sufficient experimental data, the AZ-Cam clay model currently assumes that soil cannot sustain the tensile mean effective stress ($p' < 0$). Besides, by incorporating a failure surface, the exact shape of the bounding surface on the dry side is not essential to the model. For these two reasons, the value of R_d thus can then be fixed at 2.

3.4.4 Failure envelope for heavily OC clays

It is helpful to clarify the difference between heavily OC clay and lightly OC clay defined in the current study. The heavily OC clay quoted in the present study is when the stress state goes through the CSL and enters into the dry side of the bounding surface under continued shearing, causing dilation. However, for lightly OC clay and NC clay, the stress state will always remain on the wet side and the behaviour is always contracting. This definition of heavily OC clay and lightly OC clay is consistent with the critical state framework.

The experimental data in Figure 3.2 and 3.3 presented by Atkinson (2007) reveal that the intercept of the proposed straight line with the vertical axis $\frac{q}{Mp'}$ (in Equation 3.2) may not equal to 1 based on the best curve fitting. Actually, this value was fixed manually by Atkinson, reflecting an assumption in the basic critical state models. The assumption is that soil under continued shearing will fall on a unique straight line (original CLS) in $v-\ln p'$ space, regardless of the mode of shearing (the CSL in the present study is repositioned in $v-\ln p'$ space, thus the CSL in the basic critical state models will be pre-fixed 'original' as will be used through out the rest of this thesis). As shown in Figure 3.8, the state parameter $\Gamma - v_{\kappa}$ becomes zero when the current stress point reaches the original CSL (the state parameter indicates the vertical distance of the current stress point A to the original CSL in $v-\ln p'$ space). However, if the actual critical state of soil lies to the left of the original CSL as represented by curve $a-b$, the state parameter will be larger than zero when the critical state is reached. In this case, the vertical intercept will be less than 1.

Experimental data of Henkel (1959) and Atkinson & Richardson (1987) indicate the failure state of NC clay will fall on a unique straight line (original CSL) when plotted in $v - \ln p'$. Henkel (1959) plotted the data in the relationship between water content w and p', as w can be linearly related to v, it is identical to making above statement).

It is helpful to clarify the failure state of clay. The failure state quoted in this study is the state where maximum shear stress occurs. For clays on the wet side of the critical state (for example, NC and lightly OC clay), during drained shearing, the soils compress, stiffen and strengthen. Once a region of soil becomes stiffer and stronger, further shearing in the surrounding soil will make it stiffer and so on (Atkinson & Richardson, 1987). During undrained shearing, the soil neither compresses nor dilates as the total volume remains the same. Thus the clay on the wet side will not form shear zone and the shear stress will continue increasing before reaching the critical state during drained and undrained shearing. For clay on the dry side, during drained shearing, part of soil dilates and becomes softer. Further shearing will make this region even much weaker. Thus further shearing will be concentrated on this weaker zone and a shear zone forms before reaching the critical state (Atkinson & Richardson, 1987). As dilation, softening and weakening only occur on the dry side of critical state in the presence of some drainage. During perfect undrained shearing, the soil on the dry side again neither compresses nor dilates. Thus the formation of shear zone before the critical state is unlikely unless the geometric strains are imposed (Atkinson & Richardson, 1987). Thus generally, the shear stress of soil on the dry side under perfect undrained shearing is not likely to fall. However, during the undrained test on heavily OC clay, it is common to see the shear stress falls suddenly. This phenomenon results from the local drainage occuring within the soil sample. If local drainage occurs, the

sample becomes a boundary value problem. Since the constitutive relation reflects the mechanical behavior of an ideal single element, thus any test results after local drainage may be less useful to calibrate the constitutive relations.

Thus for NC to lightly OC clay, the failure state is identical with the critical state. For heavily OC clay under drained shearing, the failure state comes before the critical state. From the test data of Parry (1958), the failure state of Weald clay (various *OCRs*) in the *CIU* compression loading almost lie on the CSL as shown in Figure 3.9. More comprehensively, Burland *et al.* (1996) reported that the peak strengths of four stiff clays lie close to the original CSL in *CIU* shearing, especially for Todi clay and Vallericca clay as shown in Figure 3.10. Therefore, it is reasonable to state the failure state of heavily OC clay under perfect undrained shearing coincides with the critical state. This claim is consistent with Atkinson (2003) that under perfect undrained condition, there is no peak strength before the critical state.

Following the above discussion, the critical state of heavily OC Weald clay and London clay lie to the left of the original CSL in $v-\ln p'$ space as show in Figure 3.11 after (Henkel, 1959) (To be noted, in Henkel (1959), the mean effective strress was reprented by *J*/3. While *J* is this thesis denotes the deviatoric stress). Burland *et al.* (1996) did not show the test result in $v-\ln p'$ space, but from the calculation of the undrained peak strength, the critical state of heavily OC clay will also lie to the left of the original CSL in $v-\ln p'$ space if the MCC bounding surface is used. It is noted that due to the strong dilation of the heavily OC clay, the local drainage may occur within the undrained soil sample (Atkinson and Richardson, 1987). However, from Parry (1960), the stress-strain relation of heavily OC Weald clay (the same test data with Henkel (1959)) does not show a strain-softening behavior. Thus the above

deviation from the original CSL cannot be fully explained by the local drainage as local drainage of heavily OC clay will lead to a softening behavior (Atkinson & Richardson, 1987). In Burland *et al.* (1996), the heavily OC Todi clay and Vallericca clay failed in bulging with the formation of shear plane after bulging. Thus it is reasonable to assume that clays have already failed before the possible local drainage occurs.

Thus a basic assumption is made that the critical state of heavily OC clays will generally lie to the left of the original CSL in $v-\ln p'$ space but is still on the original CSL in $p'-q$ space. Similar assumption is made implicityly by Dafalias & Herrmann (1982), Zienkiewicz et al. (1985) for heavily OC clay and Crouch & Wolf (1994) for heavily OC sand. Atkinson's proposal of Equation 3.2 is modified consequently by introducing a variable intercept with vertical axis as follows:

$$\frac{q}{Mp'} = a + \chi\left(\Gamma - v_{\kappa}\right) \tag{3.9}$$

where a is the intercept of the proposed straight line with the vertical axis based on best curve fitting as suggested by Atkinson (2007).

Equation 3.9 indicates a new straight CSL for heavily OC clay (shown in Figure 3.12), which lies below the original CSL if $a<1$. The vertical distance between the new CSL and the original CSL can be easily deduced from Equation 3.9 and is termed as d as follows:

$$d = \frac{1-a}{\chi} \tag{3.10}$$

A misleading conclusion may be reached from Equation 3.10 that the new CSL proposed herein is a fixed straight line with respect to the original CSL. However, it is not true as Equation 3.9 and Equation 3.10 are only applicable for heavily OC clays as will be discussed below.

In order to incorporate Equation 3.9 into the general constitutive model, Equation 3.9 should be manipulated in terms of p', q and the pre-consolidation pressure p'_c. It should be noted that though the new CSL proposed herein generally does not coincide with the original CSL, the manipulation of Equation 3.9 can be still conducted with the help of the original CSL. The state parameter $\Gamma - v_\kappa$ is not a measured term in the tests, but is defined under the existence of the original CSL. Thus in the final form of Equation 3.9, any term defined through the original CSL should be eliminated. As shown in Figure 3.12, the current stress point is represented as $A(v, p')$, the state parameter $\Gamma - v_\kappa$ can be obtained from the following equation:

$$\Gamma - v_\kappa = \lambda \ln\left(\frac{p'_o}{p'}\right) \tag{3.11}$$

where p'_o is effective mean pressure on the original CSL at the current specific volume, and is defined through:

$$v = \Gamma - \lambda \ln p'_o \tag{3.12}$$

Substitute Equation 3.11 into Equation 3.9 yields

$$\frac{q}{Mp'} = a + \chi\lambda \ln\left(\frac{p'_o}{p'}\right) \tag{3.13}$$

The current specific volume can also be specified through NCL as follows:

$$v = N - \lambda \ln p'_e \tag{3.14}$$

where p'_e is the equivalent pressure, the effective pressure on the NCL at current specific volume.

As p'_o is defined through the original CSL, it should be eliminated in the final form. This can be done by combing Equation 3.12 and Equation 3.14 as follows:

$$\Gamma - \lambda \ln p'_o = N - \lambda \ln p'_e \tag{3.15}$$

After simple manipulation, Equation 3.15 can be expressed as:

$$\ln p'_o = \frac{\Gamma - N}{\lambda} + \ln p'_e \tag{3.16}$$

The equivalent pressure can be obtained in terms of p'_c and v_c. v_c is the specific volume when the stress state lies on the NCL at pre-consolidation pressure p'_c. As shown in Figure 3.12, following equations hold:

$$v - v_c = \kappa \ln\left(\frac{p'_c}{p'}\right) \tag{3.17}$$

$$v - v_c = \lambda \ln\left(\frac{p'_c}{p'_e}\right) \tag{3.18}$$

Combining Equation 3.17 and Equation 3.18 yields

$$\kappa \ln\left(\frac{p'_c}{p'}\right) = \lambda \ln\left(\frac{p'_c}{p'_e}\right) \tag{3.19}$$

Combining Equation 3.16 and Equation 3.19 yields

$$\ln p'_o = \frac{\Gamma - N}{\lambda} + \frac{\lambda - \kappa}{\lambda} \ln p'_c + \frac{\kappa}{\lambda} \ln p' \qquad 3.20$$

Substitute Equation 3.20 into Equation 3.13 yields

$$\frac{q}{Mp'} = a + \chi(\Gamma - N) + \chi(\lambda - \kappa) \ln\left(\frac{p'_c}{p'}\right) \qquad 3.21$$

$(\Gamma - N)$ determines the position of the original CSL. In the AZ-Cam clay model, this value can be easily obtained with the help of Figure 3.12 that

$$\Gamma - N = (\kappa - \lambda) \ln \frac{2 + R_w}{2} \qquad 3.22$$

Substitute Equation 3.22 into Equation 3.21 yields

$$\frac{q}{Mp'} = a - \chi(\lambda - \kappa) \ln \frac{2 + R_w}{2} + \chi(\lambda - \kappa) \ln\left(\frac{p'_c}{p'}\right) \qquad 3.23$$

Introducing another two parameters, peak strength parameter β and ultimate strength T

$$\beta = \chi(\lambda - \kappa) \qquad 3.24$$

$$T = \exp\left(\frac{a - 1}{\beta}\right) \qquad 3.25$$

Substitute Equation 3.24 and Equation 3.25 into Equation 3.23 yields

$$\frac{q}{Mp'} = 1 + \beta \ln\left(\frac{Tp'_{cr}}{p'}\right) \qquad 3.26$$

where $p'_{cr} = \frac{2p'_c}{2+R_w}$. Employing $p'_{Tcr} = Tp'_{cr}$, Equation 3.26 can be further manipulated to

$$\frac{q}{Mp'} = 1 + \beta \ln\left(\frac{p'_{Tcr}}{p'}\right) \tag{3.27}$$

It should be noted that the parameter β in Equation 3.24 has the same physical meaning as χ. Typically, a is less than 1. T in Equation 3.25 is thus less than 1. Further attention being paid on Equation 3.26 reveals that if $\beta = T = 1$, then the curve represented by Equation 3.26 (or Equation 3.27) is exactly the same as the yield curve of the original Cam clay model.

3.4.5 Flow rule

The flow rule is specified to determine the plastic strain increments. In conventional plasticity theory, the outward normal directions of the yield surface and plastic potential at the current stress state are required. In the AZ-Cam clay model, both associated flow rule and non-associated flow rule can be specified. If the stress state remains on the bounding surface, the model degrades to the conventional elasto-plastic model. In the triaxial space, the outward normal direction of the yield surface can be determined as follows (the determination of the outward normal direction of the plastic potential is similar, as long as substituting the plastic potential for yield surface):

$$\left\{\frac{\partial F}{\partial \sigma'}\right\} = \left\{\frac{\partial F}{\partial p'}, \frac{\partial F}{\partial q}\right\} \tag{3.28}$$

$$\frac{\partial F}{\partial q} = \frac{2q}{M^2} \tag{3.29}$$

On the wet side:

$$\frac{\partial F}{\partial p'} = \frac{8}{R_w^2}\left(p' - \frac{2}{2+R_w} p_c' \right) \qquad 3.30\ (a)$$

On the dry side:

$$\frac{\partial F}{\partial p'} = \frac{8}{R_d^2}\left(p' - \frac{2}{2+R_w} p_c' \right) \qquad 3.30\ (b)$$

However, when the stress state lies within the bounding surface, the conventional yield surface does not exist, but the outward normal directions are still required in order to formulate the elasto-plastic matrix. A radial mapping rule is thus employed to relate the current stress point $A(p', q)$ in $p' - q$ space to a unique image point $B_1(\bar{p}_1', \bar{q}_1)$ on the bounding surface (' – ' indicates the stress point lies on the bounding surface and will be used throughout this thesis.). The outward normal direction at B_1 is used as the outward normal direction at the current stress state to evaluate the elasto-plastic matrix. The image point B_1 is determined by the interception of a straight line, which passes through the origin of the stress space and current stress point, with the bounding surface. A schematic presentation is shown in Figure 3.13. The outward normal direction at the current stress state is thus provided by following expressions:

$$\left\{ \frac{\partial F}{\partial \sigma'} \right\} = \left\{ \frac{\partial F}{\partial \bar{p}_1'}, \frac{\partial F}{\partial \bar{q}_1} \right\} \qquad 3.31$$

$$\frac{\partial F}{\partial \bar{q}_1} = \frac{2\bar{q}_1}{M^2} \qquad 3.32$$

On the wet side:

$$\frac{\partial F}{\partial \overline{p}_1'} = \frac{8}{R_w^2}\left(\overline{p}_1' - \frac{2}{2+R_w} p_c' \right) \tag{3.33}$$

On the dry side:

$$\frac{\partial F}{\partial \overline{p}_1'} = \frac{8}{R_d^2}\left(\overline{p}_1' - \frac{2}{2+R_w} p_c' \right) \tag{3.34}$$

where the subscript '1' denotes the first image point, which is used to differentiate from the second image point.

It it noted that in the critical state concept, when soil reaches the critical state, there will be no changes in the stress states and no further plastic volumetric strain. Thus the outward direction of the plastic potential will be vertical in $p'-q$ space. Based on the above discussed mapping rule, the outward direction will be vertical as long as the current stress point falls on the CSL if associated flow rule is used. It may not be at the critical state once the stress point reaches the CSL as the plastic modulus may not be zero. However, the CSL does act as a phase transform line. Under the CSL, soil undergoes volume contraction and there will be positive plastic volumetric strain during loading. Above the CSL, soil undergoes volume expansion and there will be negative plastic volumetric strain during loading.

3.4.6 Hardening rule

The hardening rule of the AZ-Cam clay model is exactly the same as that used in the basic critical state models. The single hardening parameter p_c' governs the expansion and the contraction of the bounding surface and no translation is permitted. p_c' depends uniquely on the plastic volumetric strain, regardless of whenever the stress state lies on or within the bounding surface. Any deviatoric strain thus has no effect on

the evolution of the bounding surface. Detailed expression has been specified in Equation 2.7 to relate p_c' to ε_v^p.

3.4.7 Plastic modulus

The plastic modulus governs the magnitude of the plastic strains as well as the hardening or the softening behavior of the materials. The description of the evolution process of the plastic modulus is thus the most important part in the bounding surface elasto-plastic theory. For conventional elasto-plasticity, the behavior is purely elastic within the yield surface. The plastic modulus is thus infinitely large, resulting in the elasto-plastic matrix to be the same as elastic matrix. In order to introduce plastic strains within the conventional yield surface, it is thus necessary to set a finite value to the plastic modulus. As stated in Chapter 2, the bounding surface models relate the plastic modulus at the current stress state to an image point on the bounding surface through a specific mapping rule. The key difference between these models is thus the different descriptions for the evolution of the plastic modulus within the bounding surface.

Another function of the plastic modulus is that it indicates that the strength will further increase when it is positive, and the strength will fall (softening behavior occurs) when it is negative if associated flow rule is used (Pastor *et al.*, 1990). Thus soils fall to the post-peak zone after the peak strength (for example, heavily OC clays under drained shearing), the plastic modulus should be negative in the post-peak region.

Various expressions for the plastic modulus have been proposed since Dafalias (1975) and Krieg (1975) as reviewed in the bounding surface models in Chapter 2. Among these expressions, two basic fundamentals can be identified as: (i) the plastic

modulus should be degenerated to the value evaluated from the image point on the bounding surface when the current stress point coincides with the image point; and (ii) the plastic modulus should increase with the increasing of the distance from the current stress point to the image point. In addition, the Masing effect suggests that the elastic zone can be considered to move with the current stress (Masing, 1926). It is thus necessary to consider soil behavior immediately after a loading reversal. Referring to the loading reversal, it may be occurred under different angles as the initial load path. The behavior may be different for different angles (Dasari, 1996). Without detailed explanation, the loading reversal presented here always refers to a reversal angle larger than 90 degree.

Two-surface or multi-surface models suggest that immediately the loading reversal, the soil behaves purely elastic within a defined yield surface (Mroz *et al.*, 1978; Al-Tabbaa, 1987). The MIT models set the plastic modulus to an infinite large value, so that the elastic zone contracts to a point and the plastic modulus depends on the load history. The expression proposed by Zienkiewicz *et al.* (1985), though very simple, is not appropriate for soils loading from non-isotropic condition as the expression is path-independent. Thus if the cyclic mean load level is relatively large, even under small cyclic load amplitude, excessive plastic strain will occur. As shown in Figure 3.14, the maximum and minimum cyclic loads are 60% and 50% of the failure load, respectively. Even under this relatively small cyclic load amplitude, the mean effective stress rapidly reduces as the model cannot store any loading information during the previous loading (the cyclic mean load level is defined as the arithmetical average of the maximum load and the minimum load occurred in a load cycle; the cyclic load amplitude is defined as the half of the variation of the cyclic load level in a load cycle in the current study).

In the AZ-Cam clay model, a load-path-dependent plastic modulus is suggested in order to take account of the effect of loading reversal. Immediately after a loading reversal, the plastic modulus becomes infinitely large and the elastic zone becomes a point as the MIT models. Further, the plastic modulus is evaluated from two image points on the bounding surface, rather than one image point as almost all the bounding surface models do until now in order to explicitly incorporate the failure envelope modified in section 3.4.4.

As in Figure 3.13, the current stress state is represented by $A(p',q)$, the first image point on the bounding surface $B_1(\bar{p}_1',\bar{q}_1)$ is determined by a radial mapping rule as discussed previously. The second image point on the bounding surface $B_2(\bar{p}_2',\bar{q}_2)$ is determined by the interception of the bounding surface with a straight line, which connects the origin of the stress space and point A_f. Point A_f is the vertical projection of the current stress point $A(p',q)$ on the failure envelope in $p'-q$ space, and point $B(\bar{p}',\bar{q})$ is the vertical projection of the current stress point $A(p',q)$ on the bounding surface in $p'-q$ space. Thus these three stress points A, A_f, B have the same mean effective stresses. It should be noted that the failure envelope modified in section 3.4.4 is a curved line in $p'-q$ space represented by $O-A_f-C_T$, and only applicable to heavily OC clays. As NC to lightly OC clays will not exhibit peak strength before going to the critical state, thus the CSL serves as the failure line. It is thus reasonable to extend the failure envelope modified in section 3.4.4 to incorporate part of the CSL C_T-C_a. Thus the full failure envelope will be represented by the curve $O-A_f-C_T-C_a$. With this extension, the second image point $B_2(\bar{p}_2',\bar{q}_2)$ can be uniquely determined and will never lie on the bounding surface on the wet side. If the

current stress point $A(p',q)$ lies to the right of C_T, $B_2(\bar{p}_2',\bar{q}_2)$ will always coincide with the apex of the bounding surface C_a, which is also the critical state point. Then if $A(p',q)$ lies to the left of C_T, $B_2(\bar{p}_2',\bar{q}_2)$ will lie on the bounding surface on the dry side.

Following Equation A.39, if an associated flow rule is used, the plastic modulus at $B_1(\bar{p}_1',\bar{q}_1)$ can be evaluated as:

$$H_1 = -\left\{\frac{\partial F}{\partial p_c'}\right\}^T \left[\frac{\partial p_c'}{\partial \varepsilon_v^p}\right] \left\{\frac{\partial P}{\partial \bar{p}_1'}\right\} \tag{3.35}$$

$$\frac{\partial p_c'}{\partial \varepsilon_v^p} = \frac{v p_c'}{\lambda - \kappa} \tag{3.36}$$

On the wet side:

$$\frac{\partial F}{\partial p_c'} = \frac{16}{R_w^2(2+R_w)}\left(\frac{2}{2+R_w}p_c' - \bar{p}_1'\right) - \frac{8}{(2+R_w)^2}p_c' \tag{3.37}$$

$$\frac{\partial P}{\partial \bar{p}_1'} = \frac{8}{R_w^2}\left(\bar{p}_1' - \frac{2}{2+R_w}p_c'\right) \tag{3.38}$$

On the dry side:

$$\frac{\partial F}{\partial p_c'} = \frac{16}{R_d^2(2+R_w)}\left(\frac{2}{2+R_w}p_c' - \bar{p}_1'\right) - \frac{8}{(2+R_w)^2}p_c' \tag{3.39}$$

$$\frac{\partial P}{\partial \bar{p}_1'} = \frac{8}{R_d^2}\left(\bar{p}_1' - \frac{2}{2+R_w}p_c'\right) \tag{3.40}$$

Substitute Equation 3.36 into Equation 3.35 yields

$$H_1 = -\frac{vp'_c}{\lambda-\kappa}\frac{\partial F}{\partial p'_c}\frac{\partial P}{\partial \overline{p}'_1} \qquad 3.41$$

where $\frac{\partial F}{\partial p'_c}$ and $\frac{\partial P}{\partial \overline{p}'_1}$ can be determined by Equation 3.37 to Equation 3.40.

The plastic modulus H_2 at $B_2\left(\overline{p}'_2, \overline{q}_2\right)$ can be obtained by substituting $\left(\overline{p}'_2, \overline{q}_2\right)$ with $\left(\overline{p}'_1, \overline{q}_1\right)$ in Equation 3.41. From the above deduction, it is easy to see that the plastic modulus of the image point will be positive on the wet side, negative on the dry side and zero at the critical state point (the plastic modulus will also be zero at the origin of the stress space when $p' = 0$).

From conventional plasticity theory, strain-softening begins when the plastic modulus becomes negative if an associated flow rule is employed. If a non-associated flow rule is used, strain-softening begins when the plastic modulus is positive (Buscarnera *et al.*, 2011). For bounding surface plasticity used in the current study, if the stress state lies within the bounding surface, the plastic modulus at the current stress is larger than the value at the first image point and the consistency condition is not required. Therefore, strain-softening begins when the plastic modulus becomes negative in the current study, regardless of the associated or non-associated flow rule.

Combining with the simple power law suggested by Zienkiewicz *et al.* (1985), the plastic modulus is proposed as follows:

$$H = \left(H_1 - H_2\right)\left(1 + \frac{\delta_B - \delta}{\delta_B}\right)^{\gamma} \qquad 3.42$$

where H is the plastic modulus at the current stress point $A(p',q)$. δ_B and δ are the distance from the origin of the stress space O to the first image point $B_1(\bar{p}_1',\bar{q}_1)$ and current stress point $A(p',q)$ respectively as shown in Figure 3.15. Parameter γ is an input material constant.

When the current stress point approaches the bounding surface on the wet side, the second image point will approach the critical state point on the bounding surface. Thus H_2 will be zero. Meanwhile, δ_B and δ will become the same, and H will approach H_1. Thus the smooth change of behavior is guaranteed when the stress state is approaching the bounding surface. Another feature of Equation 3.42 is the proposal of the plastic modulus reflects the physical meaning of the failure surface. As can be seen from Figure 3.15, when the current stress point $A(p',q)$ falls on the failure envelope, the first image point $B_1(\bar{p}_1',\bar{q}_1)$ coincides with the second image point $B_2(\bar{p}_2',\bar{q}_2)$. Thus H will become zero and the peak strength is reached. Since the failure envelope introduced here is based on extensive experimental data (Atkinson, 2007), using Equation 3.42 will obviously enhance the ability of the AZ-Cam clay model to predict the peak strength of OC clays.

However, Equation 3.42 suffers three main problems: (i) Equation 3.41 reveals that the plastic modulus on the bounding surface follows a parabolic law that decreases from zero at the critical state point to a certain negative value and then increases to zero at $p'=0$. Thus the value H_1-H_2 may become negative (and thus H becomes negative) before the current stress point reaches the failure envelope. This fact is not desirable since before reaching the failure envelope, the plastic modulus should be positive. This problem is termed as a pre-negative problem; (ii) If the current stress

point approaches the bounding surface from the dry side, the second image point may not coincide with the critical state point, thus H_2 may not be zero. This can lead to the inconsistency of the model as the current stress point approaches the first image point, but the plastic moduli of the current stress point and the first image point still remain different. This problem is termed as an inconsistency problem; (iii) The plastic modulus expressed in Equation 3.42 is still independent of the loading history. Thus excessive plastic strains can still occur even under small cyclic load level when the stress state near the bounding surface as discussed previously. From this point of view, no improvement is made regarding to the proposal of Zienkiewicz *et al.* (1985). This problem is termed as a path-independent problem. Three modifications are thus presented to overcome the above three shortcomings.

(i) Pre-negative problem

Rather than a simple difference of the plastic moduli at the two image points is used in Equation 3.42, a slightly different form is proposed to solve the pre-negative problem as follows:

$$H = \left(H_1 - \omega H_2\right)\left(1 + \frac{\delta_B - \delta}{\delta_B}\right)^{\gamma} \qquad 3.43$$

where ω is a positive scalar ensuring the value $H_1 - \omega H_2$ will be positive before the current stress point reaches the failure surface.

As stated previously, without sufficient experimental data on the tensile strength of clays, the clay is assumed to have no tensile strength. Thus the parameter R_d on the dry side of the bounding surface can be fixed at 2. When $B_1\left(\bar{p}_1', \bar{q}_1\right)$ lies on the wet side of the bounding surface, the plastic modulus can be specified as:

$$H_1 = \frac{4}{(2+R_w)} \frac{vp'_c}{\lambda-\kappa} \bar{p}'_1 \left(2\bar{p}'_1 - \frac{4}{(2+R_w)} p'_c \right) \tag{3.44}$$

The plastic modulus at the second image point can thus be obtained by substituting $\bar{p}'_1$ with $\bar{p}'_2$ in Equation 3.43 as follows:

$$H_2 = \frac{4}{(2+R_w)} \frac{vp'_c}{\lambda-\kappa} \bar{p}'_2 \left(2\bar{p}'_2 - \frac{4}{(2+R_w)} p'_c \right) \tag{3.45}$$

For simplicity, let $\rho = \frac{4}{(2+R_w)} \frac{vp'_c}{\lambda-\kappa}$, thus

$$H_1 - \omega H_2 = \rho \bar{p}'_1 \left(2\bar{p}'_1 - \frac{4}{(2+R_w)} p'_c \right) - \omega\rho \bar{p}'_2 \left(2\bar{p}'_2 - \frac{4}{(2+R_w)} p'_c \right) \tag{3.46}$$

The dry side of the bounding surface is described by

$$F = \frac{q^2}{M^2} + p'^2 - \frac{4}{2+R_w} p' p'_c = 0 \tag{3.47}$$

After a simple manipulation of Equation 3.47 yields

$$p' = \frac{4}{2+R_w} \frac{M^2 p'_c}{M^2+\eta^2} \tag{3.48}$$

where η is the stress ratio defined as $\eta = \frac{q}{p'}$.

Substituting Equation 3.48 into Equation 3.46 (noted that p' becomes $\bar{p}'_1$ and $\bar{p}'_2$ at first and second image point respectively) gives

$$H_1 - \omega H_2 = \rho p_c'^2 M^2 \left(\frac{4}{2+R_w} \right)^2 \left[\frac{2M^2}{\left(M^2 + \bar{\eta}_1^2 \right)^2} - \frac{1}{M^2 + \bar{\eta}_1^2} - \frac{2\omega M^2}{\left(M^2 + \bar{\eta}_2^2 \right)^2} + \frac{\omega}{M^2 + \bar{\eta}_2^2} \right]$$

3.49

where $\bar{\eta}_1, \bar{\eta}_2$ is the stress ratio at the first and second image point respectively. The subscript indicates the first and second image point.

Let $\omega = \frac{M^2 + \bar{\eta}_2^2}{M^2 + \bar{\eta}_1^2}$ and substitute it into Equation 3.49 gives

$$H_1 - \omega H_2 = 2\rho p_c'^2 M^4 \left(\frac{4}{2+R_w} \right)^2 \left[\frac{\bar{\eta}_2^2 - \bar{\eta}_1^2}{\left(M^2 + \bar{\eta}_1^2 \right)^2 \left(M^2 + \bar{\eta}_2^2 \right)^2} \right] \qquad 3.50$$

It is then obvious that $\omega = \frac{M^2 + \bar{\eta}_2^2}{M^2 + \bar{\eta}_1^2}$ can solve this pre-negative problem satisfactorily. Before the current stress point reaches the failure envelope (Figure 3.15), $\bar{\eta}_2 > \bar{\eta}_1$, thus $H_1 - \omega H_2 > 0$. When the two image points coincide, $\bar{\eta}_2 = \bar{\eta}_1$, thus $H_1 - \omega H_2 = 0$. If the current stress state is outside the failure envelope, $\bar{\eta}_2 < \bar{\eta}_1$, then the plastic modulus is negative.

Another choice of ω is to let $\omega = \left(\frac{M^2 + \bar{\eta}_2^2}{M^2 + \bar{\eta}_1^2} \right)^2$ and substituting it into Equation 3.49 gives

$$H_1 - \omega H_2 = \rho p_c'^2 M^2 \left(\frac{4}{2+R_w} \right)^2 \left[\frac{\bar{\eta}_2^2 - \bar{\eta}_1^2}{\left(M^2 + \bar{\eta}_1^2 \right)^2} \right] \qquad 3.51$$

Thus both $\omega = \frac{M^2 + \bar{\eta}_2^2}{M^2 + \bar{\eta}_1^2}$ and $\omega = \left(\frac{M^2 + \bar{\eta}_2^2}{M^2 + \bar{\eta}_1^2} \right)^2$ can solve the pre-negative problem satisfactorily. As H_2 is always non-positive, thus any value larger than $\omega = \frac{M^2 + \bar{\eta}_2^2}{M^2 + \bar{\eta}_1^2}$ can solve the pre-negative problem. Thus for simplicity, $\omega = \frac{M^2 + \bar{\eta}_2^2}{M^2 + \bar{\eta}_1^2}$ will be used in the AZ-Cam clay model.

(ii) Inconsistency problem

As stated before, any value larger than $\omega = \frac{M^2 + \bar{\eta}_2^2}{M^2 + \bar{\eta}_1^2}$ can solve the pre-negative problem. Thus a simple method to solve the inconsistency problem is to introduce a state variable ξ, multiplied with ω. The plastic modulus is thus expressed as

$$H = \left(H_1 - \xi \omega H_2 \right) \left(1 + \frac{\delta_B - \delta}{\delta_B} \right)^{\gamma} \tag{3.52}$$

There are two requirements of ξ: (i) ξ should be a positive value no less than 1 before the current stress point reaches the failure envelope, or else the pre-negative problem may remain unsolved; (ii) ξ should become zero when the current stress point approaches the first image point in order to solve the inconsistency problem. A simple expression satisfying the above requirements is provided as follows:

$$\xi = \left(\frac{\bar{\eta}_B - \bar{\eta}_1}{\bar{\eta}_B - \bar{\eta}_2} \right)^{0.2} \tag{3.53}$$

where $\bar{\eta}_B$ is the stress ratio at point B on the bounding surface.

From Figure 3.15, before $A(p',q)$ reaches the failure envelope, $\bar{\eta}_2 > \bar{\eta}_1$, thus $\xi > 1$. When $A(p',q)$ coincides with the first image point $B_1(\bar{p}_1', \bar{q}_1)$, $\bar{\eta}_B = \bar{\eta}_1$, then $\xi = 0$. Equation 3.53 can thus solve the inconsistency problem successfully. However, two further issues have to be noted: (i) When the current stress state is outside the failure envelope, then $\bar{\eta}_2 < \bar{\eta}_1$, thus $\xi < 1$. From Figure 3.15, if $A(p',q)$ is outside the failure envelope, then $B_1(\bar{p}_1', \bar{q}_1)$ and $B_2(\bar{p}_2', \bar{q}_2)$ will both lie on the dry side of the bounding surface, then both H_1 and H_2 will be negative. From Equation 3.50, if $\xi = 1$, H will be negative as $\bar{\eta}_2 < \bar{\eta}_1$, thus H will still be negative when ξ is introduced as H_2 is negative and $\xi < 1$. Thus the plastic modulus at the current stress state will be negative when the current stress point lies outside the failure envelope. The softening behavior can thus be simulated; (ii) There is a numerical singularity in Equation 3.53 when $\bar{\eta}_B = \bar{\eta}_2$, which occurs when point $B(\bar{p}', \bar{q})$ coincides with the critical state point. However, if point $B(\bar{p}', \bar{q})$ coincides with the critical state point, $B_2(\bar{p}_2', \bar{q}_2)$ will also coincide with the critical state point, thus H_2 will be zero, and thus H will be independent of H_2. This singularity can be easily avoided by manually setting ξ to a finite value when $B(\bar{p}', \bar{q})$ coincides with the critical state point and at the same time, the smooth change of H can also be guaranteed.

(iii) Path-independent problem

As stated before, the elastic zone can be considered to move with the current stress. It is thus natural to treat the soil as an elastic material immediately after a loading reversal. To incorporate the loading reversal effect, the exponential part in

Equation 3.52 is modified to be dependent on the load path. This modification can be achieved by introducing a parameter Ω. Thus the plastic modulus is expressed as

$$H = \left(H_1 - \xi\omega H_2\right)\left(1 + \Omega\frac{\delta_B - \delta}{\delta_B}\right)^{\gamma} \qquad 3.54$$

The parameter Ω depends on the load history, and becomes infinitely large immediately after a loading reversal. Thus the elastic zone degenerates to a point when a loading reversal occurs. Upon further loading, Ω decreases when the current stress point moves away from the reversal point. In one-dimensional isotropic loading condition, the distance from the current stress point to the reversal point can be measured by the mean effective stress p'. In the deviatoric plane, this distance can be measured by deviatoric stress ratio η. A simple expression of Ω is thus provided as follows:

$$\Omega = \frac{1}{\left(\zeta_1^2 + \zeta_2^2\right)^{0.5}} \qquad 3.55$$

where ζ_1 and ζ_2 measure the deviation to mean effective stress and deviatoric stress from the initial loading or reloading point, respectively.

A similar expression as that proposed by Pestana & Whittle (1999) is used for ζ_1 as follows:

If $p' > p'_{rel}$, then $\zeta_1 = 1 - \frac{p'_{rel}}{p'}$ 3.56 (a)

If $p' \le p'_{rel}$, then $\zeta_1 = 1 - \frac{p'}{p'_{rel}}$ 3.56 (b)

where p'_{rel} is the mean effective stress at the reloading point.

The conventional stress ratio difference is employed to determine ζ_2, which can be expressed as:

$$\zeta_2 = \left[(\eta - \eta_{rel}) : (\eta - \eta_{rel}) \right]^{\frac{1}{2}} \qquad 3.57$$

where η_{rel} is the stress ratio at the reloading point.

With the above expressions for ζ_1 and ζ_2, the plastic modulus H will depend on the loading history. Immediately after a loading reversal, Ω and H will become infinitely large as ζ_1 and ζ_2 will be zero. Thus the soil behavior immediately after a loading reversal is elastic. However, the elastic zone is merely a point as with further loading, ζ_1 and/or ζ_2 will increase, thus Ω and H will decrease to a finite value. Under one-dimensional isotropic loading, there will be no deviatoric stress. Thus ζ_2 remains at zero, and ζ_1 wholly governs the loading reversal effect. Larger plastic volumetric strains will occur if the distance from the current stress point to the reversal point increases since ζ_1 will increase, and thus Ω and H will decrease. When encountering the general loading condition, both ζ_1 and ζ_2 will increase (thus Ω and H will decrease) when the current stress point leaves away from the reversal point. Larger plastic strains will thus occur upon further loading since the current stress point will move further away from the reversal point in the stress space.

To sum up, a relatively simple expression is proposed to determine the plastic modulus at the current stress state as stated in Equation 3.53 and re-stated as follows:

$$H = \left(H_1 - \xi\omega H_2\right)\left(1 + \Omega\frac{\delta_B - \delta}{\delta_B}\right)^{\gamma} \qquad 3.58$$

Equation 3.58 only needs one input material constant γ, which is similar to that used by Zienkiewicz *et al.* (1985) if the failure envelope is pre-determined in $p' - q$ space. The plastic modulus expressed in Equation 3.58 is evaluated from two image points, rather than from a single image point as most bounding surface models do. For NC to lightly OC clays (the stress state lies to the right of C_T in Figure 3.15), H_2 will be zero. Thus the plastic modulus is exclusively evaluated from the first image point and independent of the second image point. This characteristic is consistent with the proposal of Schofield & Wroth (1968) and Atkinson (2007) where the failure envelope is only applicable for heavily OC clays. As the plastic modulus explicitly becomes zero at the failure envelope, which is a further extension of that proposed by Atkinson (2007) based on a serials laboratory experiments, it could enhance the capability of the AZ-Cam clay model to predict the peak strength of OC clays. Softening behavior can also be simulated when the stress state falls outside the failure envelope. The plastic modulus expressed in Equation 3.58 also considers the loading history and predicts a purely elastic behavior immediately after a loading reversal, although the elastic region is merely a point. This path-dependent characteristic avoids excessive plastic strains under small cyclic load level when the stress state near the bounding surface and is an improvement over the model proposed by Zienkiewicz *et al.* (1985) while retaining its simplicity. Table 3.1 summarized the expressions of the variables in Equation 3.58.

3.4.8 Shakedown behavior

When an elasto-plastic material is subjected to cyclic loading, generally three distinctive characteristics can be expected as summarized by Whittle (1987) and Yu

(2006): (i) Purely linear elastic behavior. If the cyclic load level is sufficient small, there will be no plastic deformation and any deformation is fully reversible. For isotropic materials, the volumetric and shear behavior are fully de-coupled. The stress-strain relationship can be seen from Figure 3.16 (a); (ii) Stabilized behavior. If the cyclic load level is moderate, it is possible that after a number of loading cycles, there will be no further accumulation of plastic strains. Generally two situations which are termed as elastic shakedown and purely hysteretic behavior can occur. In elastic shakedown, the behavior will be purely linear elastic after a number of loading cycles. However, the stress-strain relationship of the purely hysteretic behavior will be nonlinear hysteretic, although there will be no further accumulation of plastic strains. The stress-strain relationship of the stabilized behavior can be seen from Figure 3.16 (b) and Figure 3.16 (c); and (iii) Unstable behavior. In this case, the cyclic load level is relatively large. Thus the material will continue exhibiting plastic strains during subsequent loading cycles and will fail eventually owing to fatigue or excessive plastic deformation. The stress-strain relationship of this type of behavior can be seen from Figure 3.16 (d).

For cohesive soils, shakedown behavior has been observed for very small cyclic load levels where the plastic strains reach zero after a certain number of loading cycles and the behavior becomes purely elastic (Lesny & Hinz, 2007). As stated before, the plastic modulus plays a key role in determining the magnitude of plastic strain. A first step to consider the shakedown behavior of clays under cyclic loading qualitatively is to modify the formulation of the plastic modulus as expressed in Equation 3.58.

Since the shakedown behavior occurs after a certain number of loading cycles, which induce a certain amount of plastic strains, it is thus possible to relate the plastic modulus to the plastic strains. Yu *et al.* (2007) proposed to relate the plastic modulus

to the accumulated plastic deviatoric strain through a power law. This proposal is relatively straight forward as with the increased number of loading cycles, the accumulated plastic deviatoric strain will increase as well. By employing a power law, the plastic modulus may become sufficient large such that there will be little plastic strains. The shakedown behavior can thus be simulated eventually as long as the cyclic load level is sufficiently small. However, relating the plastic modulus to the accumulated plastic deviatoric strain through a power law suffers from a numerical difficulty. If after a number of loading cycles, the stress state is approaching the critical state, the volumetric strain will approach zero but the plastic deviatoric strain continues to increase and can be infinitely large. Thus relating the plastic modulus to the accumulated plastic deviatoric strain through a power law will cause numerical difficulty when the stress state is approaching the critical state.

A similar law as Yu *et al.* (2007) is employed in the AZ-Cam clay model such that the plastic modulus is related to the accumulated plastic volumetric strain rather than the accumulated plastic deviatoric strain as follows:

$$H = \left(H_1 - \xi\omega H_2\right)\left(1+\Omega\frac{\delta_B-\delta}{\delta_B}\right)^{\gamma\left(\varepsilon_v^p\right)} \tag{3.59}$$

where $\gamma\left(\varepsilon_v^p\right)$ can be expressed as

$$\gamma\left(\varepsilon_v^p\right) = \gamma\left(1+\int\left|d\varepsilon_v^p\right|\right)^{k_s} \tag{3.60}$$

where k_s is an input material constant, $\int\left|d\varepsilon_v^p\right|$ is the accumulated absolute plastic volumetric strain. This value can be calculated by summing up all the absolute value of the plastic volumetric strain occurred during the previous loading cycles.

By relating the plastic modulus to the accumulated absolute plastic volumetric strain, the above numerical difficulty can be eliminated as the plastic volumetric strain will be zero at the critical state. Since the elastic zone of the AZ-Cam clay model during loading is merely a point, plastic volumetric strain will always be generated during loading condition. Thus $\gamma\left(\varepsilon_v^p\right)$ will increase with the number of loading cycles. With increased $\gamma\left(\varepsilon_v^p\right)$, following Equation 3.59 , the plastic modulus will be larger than before if all the other factors remain the same, and thus less plastic strains will be generated. If the cyclic load level is not very large, there is a certain distance from the current stress state to the bounding surface. Thus the exponential part on the right hand side of Equation 3.59 can be sufficiently large so that there will be little plastic strains during loading. The shakedown behavior of clays under cyclic loading can thus be simulated qualitatively.

3.4.9 Elastic component

It is convenient to employ elastic bulk modulus K and elastic shear modulus G to represent the elastic behavior. K is defined exactly following basic critical state models as expressed in Equation 2.8. The determination of G is not quite straight forward. Typically, a finite constant G can be used or by assuming a constant *Poisson's ratio* ν as expressed in Equation 2.9.

3.4.10 Small strain nonlinearity and hysteretic behavior

3.4.10.1 Elastic bulk modulus

Elastic bulk modulus governs the volumetric response of soil. Thus it has a large effect on the volumetric strain during drained loading and excess pore water pressure generated during undrained loading. For purely elastic material under undrained

loading, as the volumetric response and shearing response are fully de-coupled, the elastic bulk modulus has almost no effect on the whole soil behavior if elastic shear modulus has been specified. Besides, there is relatively much less test data on the elastic bulk modulus of soil than on the elastic shear modulus in the small strain region. To retain the simplicity of the model, the bulk modulus of the basic critical state models (Equation 2.8) will be adopted even in the small strain region.

3.4.10.2 Elastic shear modulus

As stated in section 2.2.2, in order to determine the elastic shear component, a common choice is to adopt a constant Poisson's ratio ν or assuming a constant elastic shear modulus G. However, as discussed in section 2.2.6, a constant Poisson's ratio may lead to non-conservative behavior of soil. Houlsby (1985) suggested two options for the choice of G based on the conditions for conservative elastic behavior. (i) G is proportional to the mean effective stress p'. In order to preserve the conservation of the elastic behavior, the elastic bulk modulus K is slightly adjusted depending on the deviatoric stress (Potts & Zdravkovic, 1999). (ii) G is proportional to the pre-consolidation pressure p_c'. This case involves the coupling of the elastic behavior and plastic behavior, and the shape of the yield surface will be changed (Houlsby, 1982).

Generally, a constant Poisson's ratio will be used to evaluate G in the AZ-Cam clay model, although we are aware of the theoretical limitations as discussed previously. It is possible to incorporate $G_{\max}$ in the current study. The tangent elastic shear modulus G is thus related to $G_{\max}$ through Equation 3.61.

$$G = r\left(p', q\right) G_{\max} \qquad 3.61$$

where $r(p',q)$ is a decreasing function as specified in Equation 3.62 for monotonic loading.

$$r(p',q)=\frac{1+\exp(\varsigma_2)}{2\exp(\omega_r\varsigma_2)} \tag{3.62}$$

where ω_r is a input material constant governing decreasing rate of r. ς_2 measures the deviation of the deviatoric stress from the initial loading or loading reversal point, and is expressed as follows:

$$\varsigma_2=\left[(\eta-\eta_{rev}):(\eta-\eta_{rev})\right]^{\frac{1}{2}} \tag{3.63}$$

where η_{rev} is the stress ratio at the loading reversal point.

The reason to choose this specific expression for $r(p',q)$ is that it is relatively simple and only one parameter ω_r can model the variation of G. A second reason is that r in Equation 3.62 changes slowly when the deviatoric strain is small, and changes rapidly when deviatoric strain is large. This behavior is the same as (Ishibashi & Zhang, 1993) by using a hyperbolic function relating the shear modulus to shear strains. In this case, the elastic shear modulus determined from Equation 2.9 could serve as a lower bound of Equation 3.61 as Dasari (1996).

3.4.10.3 Discussion on Poisson's ratio

Since the elastic work cannot be negative under any stress changes, the theoretical limits for Poisson's ratio is $-1\le\nu\le0.5$. After a review of experimental data, Hardin (1978) concluded that Poisson's ratio for soils lies somewhere between 0 and 0.2 and that any value within this range is accurate enough for most purposes. Lade & Nelson

(1987) summarized that Poisson's ratio appears to be constant for a given void ratio, but may increase with increasing void ratio. With small strain stiffness (or a large constant value of G is used when the mean effective stress is low) incorporated in the AZ-Cam clay model, while the bulk modulus is still defined the same as the basic critical state models, the Poisson's ratio in the small strain range may be negative. A negative Poisson's ratio may be acceptable theoretically, but may not be reasonable physically for soil (Potts & Zdravkovic, 1999). However, as the shear modulus will decrease with increasing strains, this negative Poisson's ratio only occurs in the small strain range from the initial loading or after a loading reversal. For NC to lightly OC clays, the plastic strains are much larger than the elastic strains. Thus the shear modulus will degrade rapidly due to large plastic strains, and hence negative Poisson's ratio should not be a concern. For heavily OC clays, during initial loading, the clays will behave almost elastically (linear or non-linear due to the formulation of shear modulus). Thus Poisson's ratio has no effects during undrained loading as the effective stress path will be almost vertical in $p'-q$ space. During drained loading, negative *Poisson's ratio* will over predict the volumetric strain. As this occurs in the small strain range, it is believed that this effect is minor without further verification.

3.4.10.4 Hysteretic behavior

The hysteretic behavior of the AZ-Cam clay model is solely governed by the elastic shear modulus. From initial loading, Equation 3.61 and Equation 3.62 are combined to evaluate G. The Masing's rule is used to describe the stiffness after a loading reversal. Equation 3.62 is thus changed following Masing's suggestions as expressed in Equation 3.64

$$r(p',q)=\frac{1+\exp(\varsigma_2/2)}{2\exp(\omega_r\,\varsigma_2/2)} \qquad 3.64$$

To incorporate Pyke's first extension, Equation 3.62 is used to determine *G* in order to coincide with the backbone curve when the current stress ratio exceeds the maximum stress ratio the soil has ever encountered, rather than the maximum shear strain as proposed by Pyke (1979). For elastic material, the effect of using maximum stress ratio and maximum shear strain is the same. Thus the maximum stress ratio the soil has ever encountered serves as a 'remembering parameter' reflecting the soil stress history. If this value is exceeded, all the previously loading and unloading history will be removed. This is conceptually similar to the proposal of Hueckel & Nova (1979).To incorporate Pyke's second extension, Equation 3.64 will still be used but the reference stress state (the stress state when the loading reversal occurs) should be changed to the reference stress state used to define the previous loading curves. Thus the current loading path will follow the previous loading path with which the current loading path intercepts.

It is necessary to determine whether the loading reversal has occurred or not when using the Masing's rule. Stallebrass (1990) defined the reversal angle as the angle of rotation between the previous and current stress path direction. Dasari (1996) defined the reversal angle in the strain space. If the angle between the previous and current strain increment vectors is larger than 90 °, the stress path is deemed to have reversed. Whittle (1987) differentiated the reversal in volumetric behavior and shearing behavior. Thus the stress path reversal is defined through the shear behavior. A similar approach was used by Papadimitriou & Bouckovalas (2002). The loading reversal criterion for the current study directly follows Papadimitriou & Bouckovalas (2002) in that the shearing reversal is governed by the length of the shear strain path from the last reversal point, and is defined as

$$Q_{len}^{e} = \sqrt{(\mathbf{e}_{s} - \mathbf{e}_{s\text{-}rev}) : (\mathbf{e}_{s} - \mathbf{e}_{s\text{-}rev})} \qquad 3.65$$

where Q_{len}^{e} denotes the length of shear strain path, $\mathbf{e}_{s}$ is the deviatoric strain tensor defined in Equation A.14 in Appendix A and $\mathbf{e}_{s\text{-}rev}$ is the deviatoric strain tensor at the last loading reversal point. Loading reversal occurs where dQ_{len}^{e} (the incremental of scalar Q_{len}^{e}) changes signs.

3.5 Summary

This chapter describes the detailed mathematical formulation of the AZ-Cam clay model. A failure surface is introduced and extended based on the test data of various clays, and Zienkiewicz's simple proposal of plastic modulus is incorporated. The bounding surface, flow rule and hardening rule of AZ-Cam clay model are described and the underlying philosophy and mathematical formulation of the proposed plastic modulus are elaborated. The ability of the model to simulate qualitatively the shakedown behavior is guaranteed by relating the plastic modulus to the accumulated absolute volumetric strain. At the end of the chapter, the inclusion of small strain nonlinearity in the AZ-Cam clay model is presented and the limitations are discussed.

Table 3.1 Variables defining plastic modulus in AZ-Cam clay model

Parameter	Physical meaning
H	Plastic modulus at current stress point
H_1	Plastic modulus at first image point
H_2	Plastic modulus at second image point
ω	State variable solving pre-negative problem
ξ	State variable solving inconsistency problem
Ω	State variable making plastic modulus load-path-dependent
δ_B	Distance from origin of stress space to first image point on BS
δ	Distance from origin of stress space to current stress point
γ	Model constant governing the evolution of plastic modulus

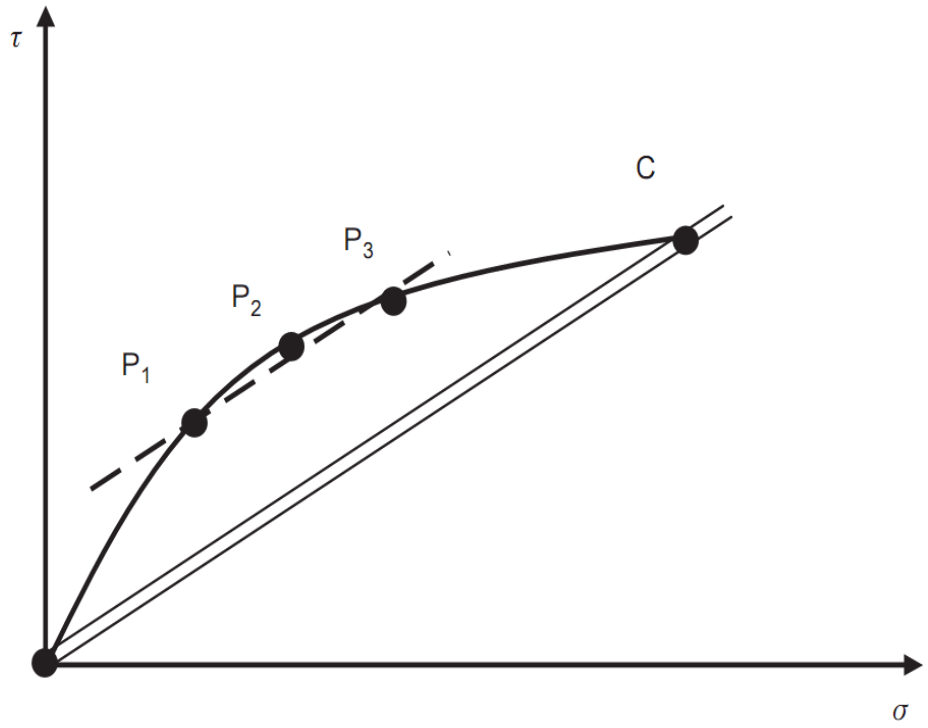

Figure 3.1 Peak strength representation after Atkinson (2007)

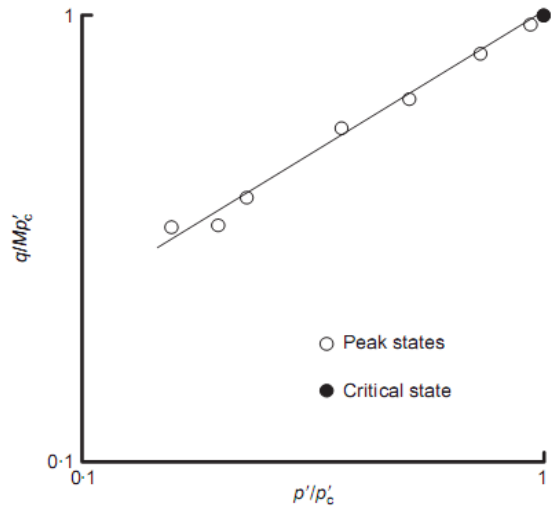

(a) Kaolin clay

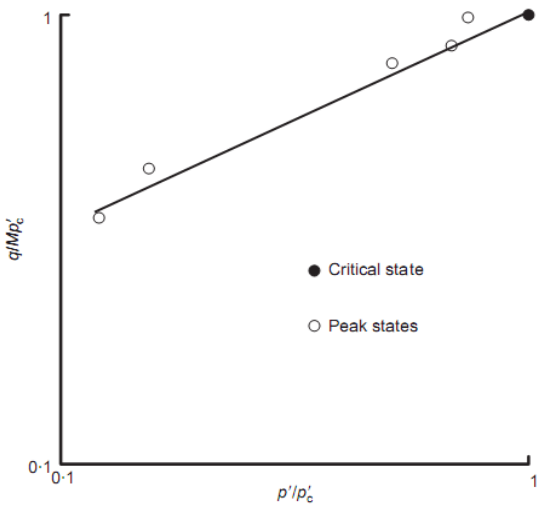

(b) Gault clay

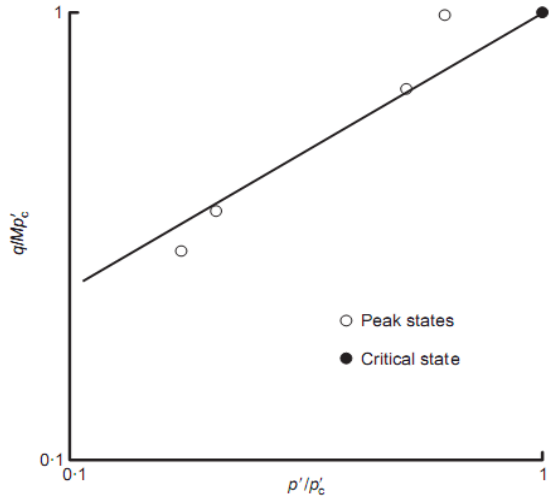

(c) Kimmeridge clay

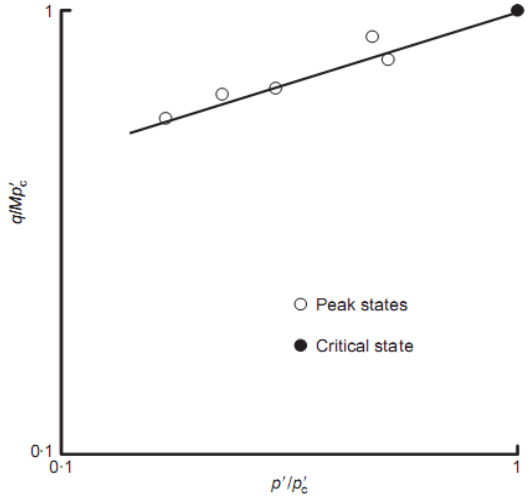

(d) London clay

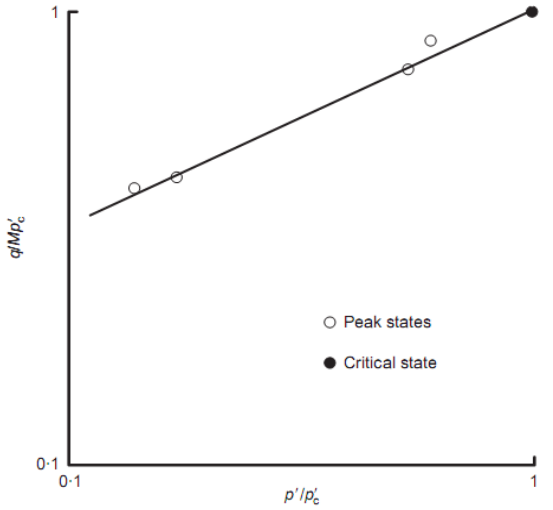

(e) Oxford clay

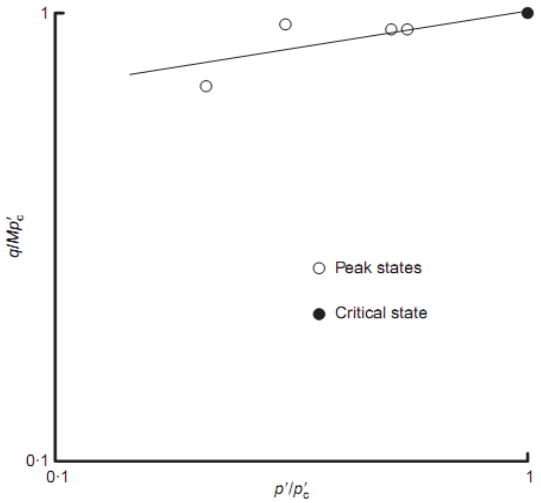

(f) Reading clay

Figure 3.2 Test data after Atkinson (2007)

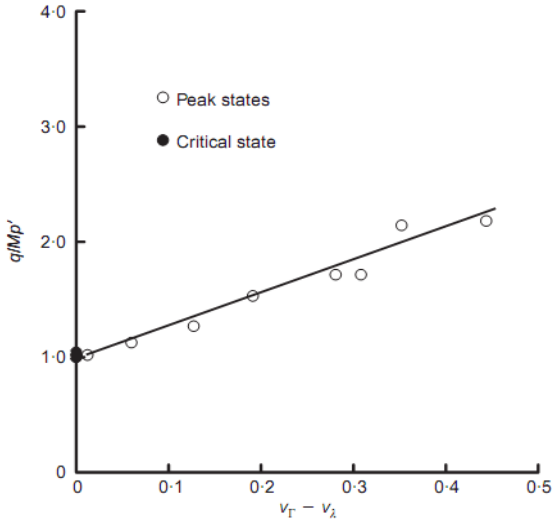

(a) Kaolin clay

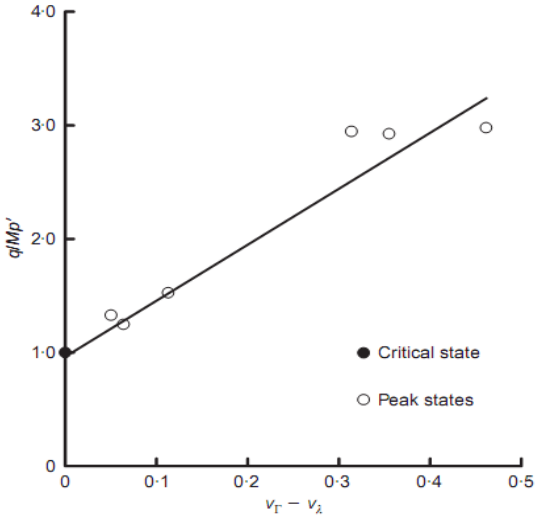

(b) Gault clay

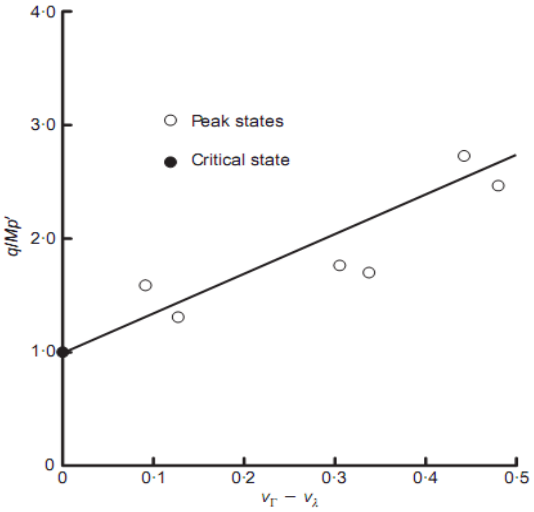

(c) Kimmeridge clay

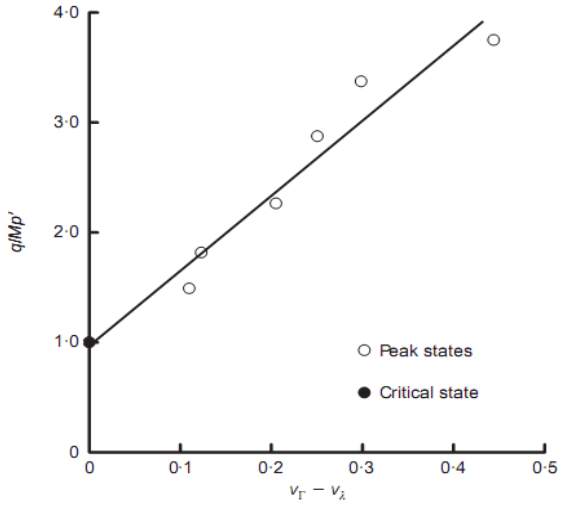

(d) London clay

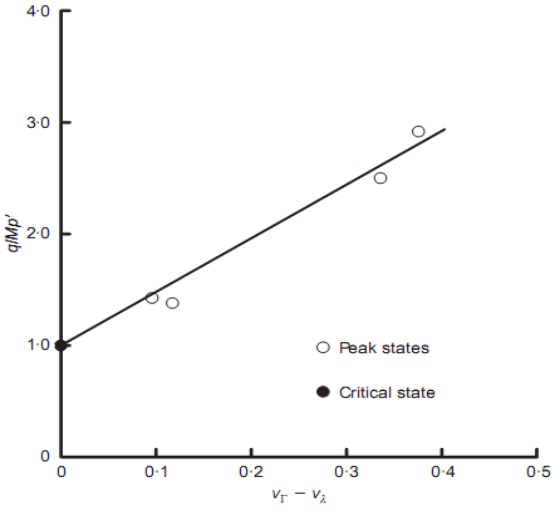

(e) Oxford clay

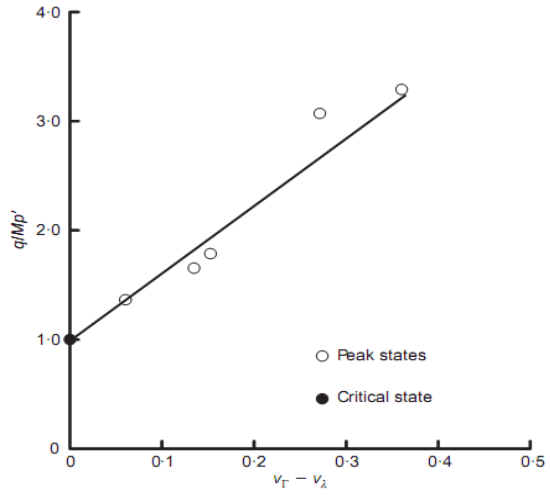

(f) Reading clay

Figure 3.3 Test data after Atkinson (2007)

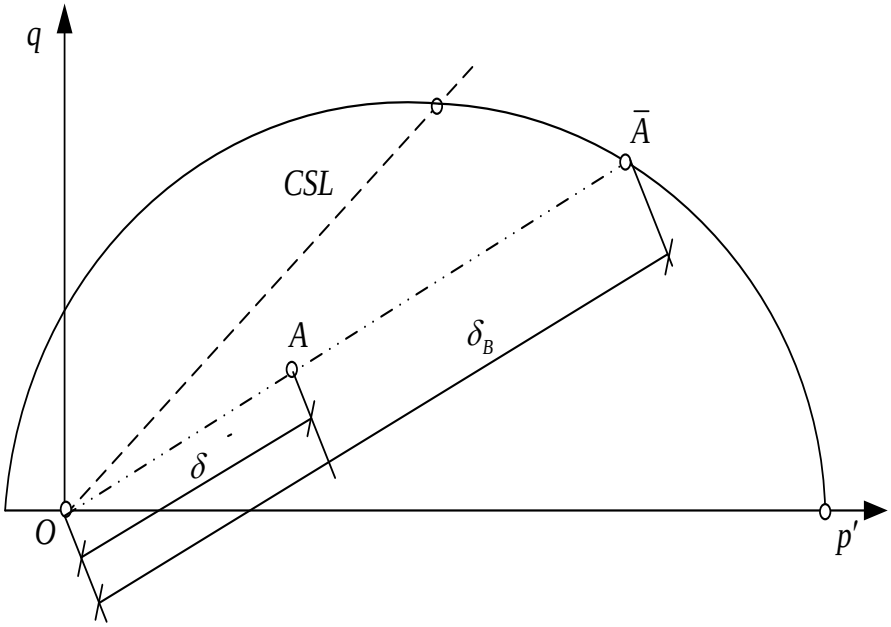

Figure 3.4 Determination of image stress point (Zienkiewicz *et al.*, 1985)

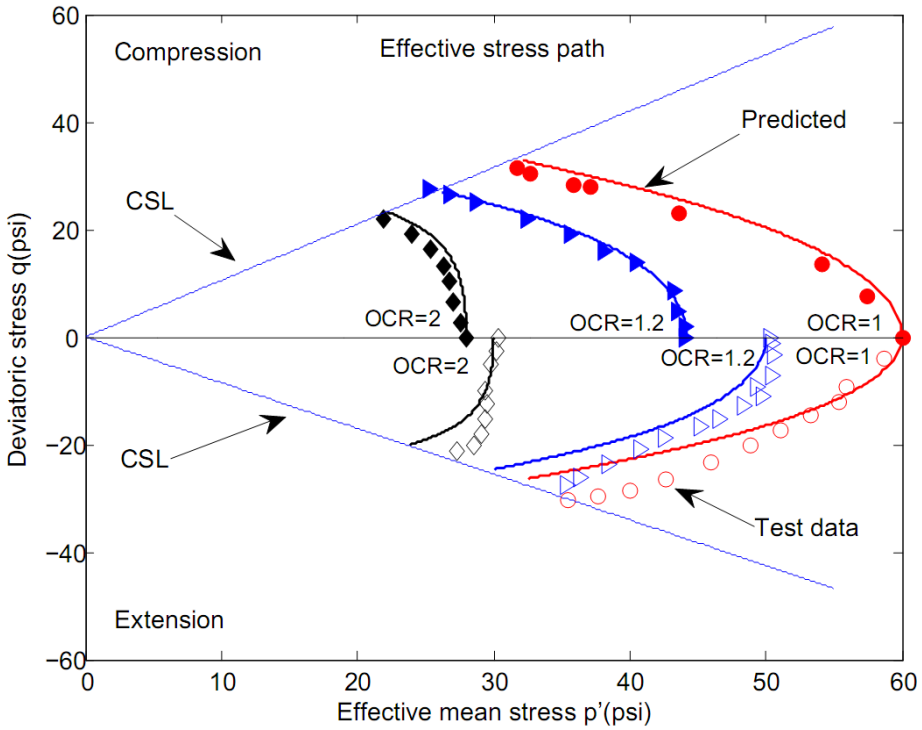

(a) Stress strain curves

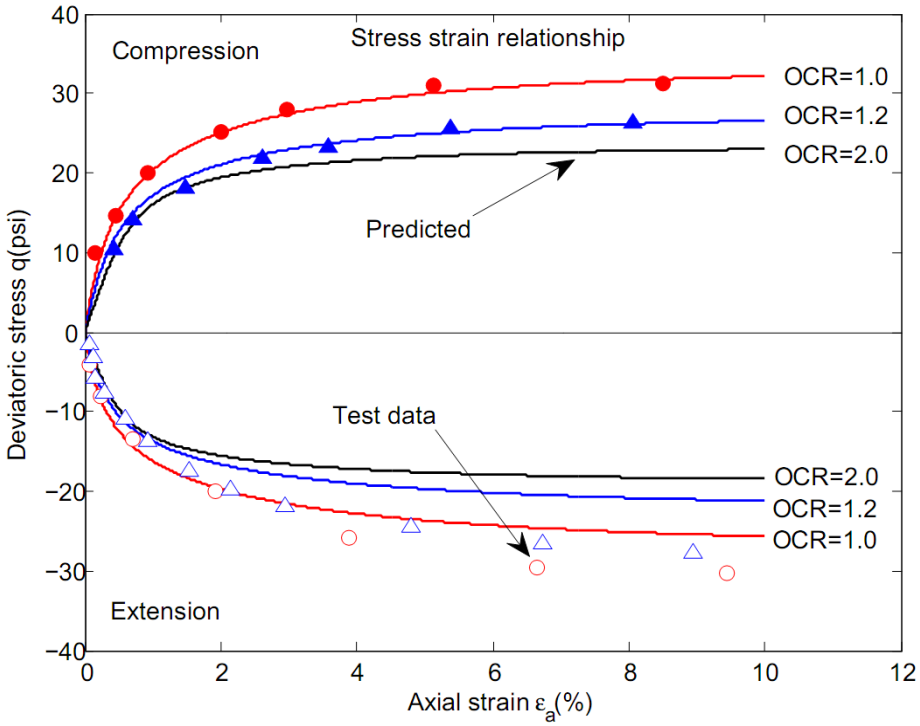

(b) Stress path

Figure 3.5 Prediction of the model (Zienkiewicz *et al.*, 1985)

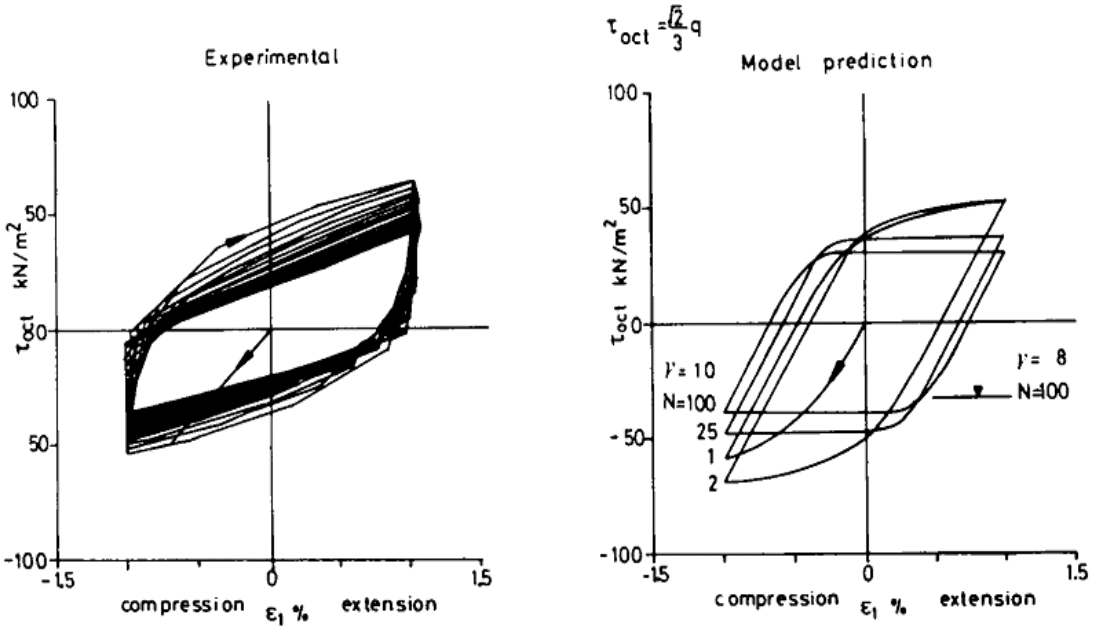

(a) Stress strain curves

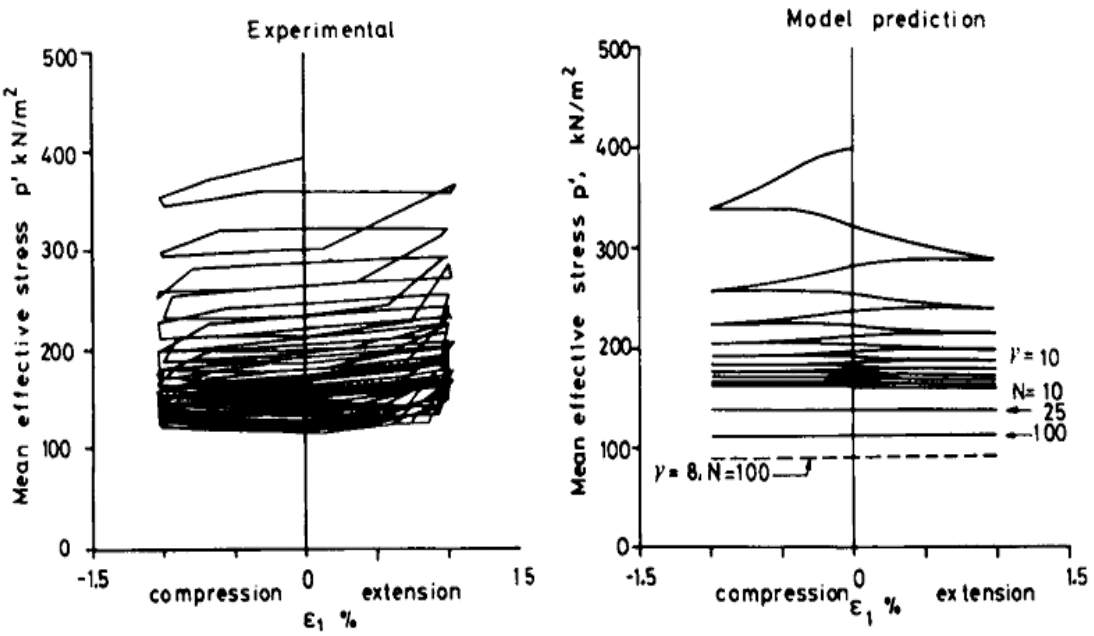

(b) Variation of mean effective stress

Figure 3.6 Prediction of the model (Zienkiewicz *et al.*, 1985)

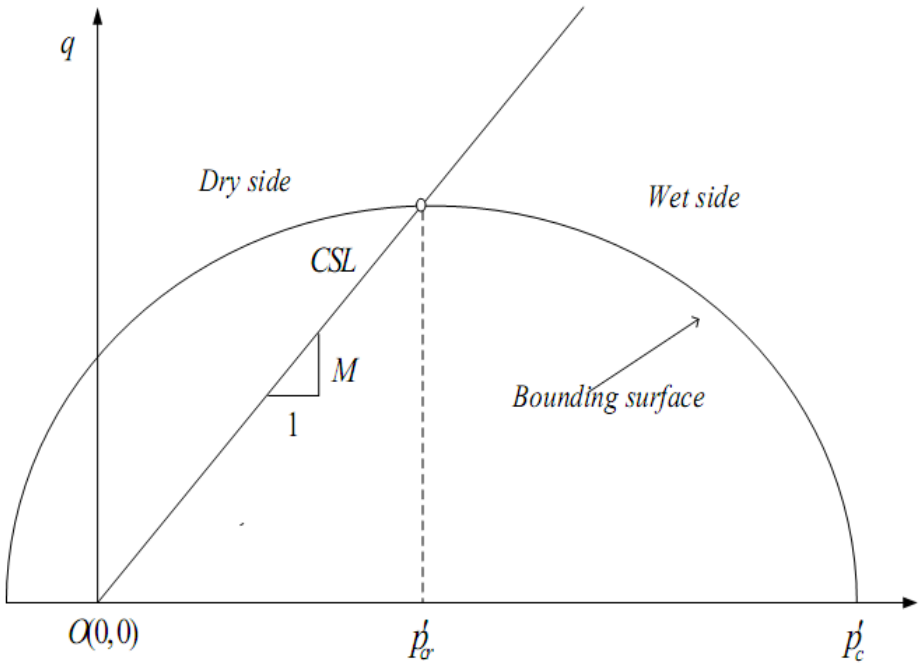

Figure 3.7 Bounding surface used in AZ-Cam clay model

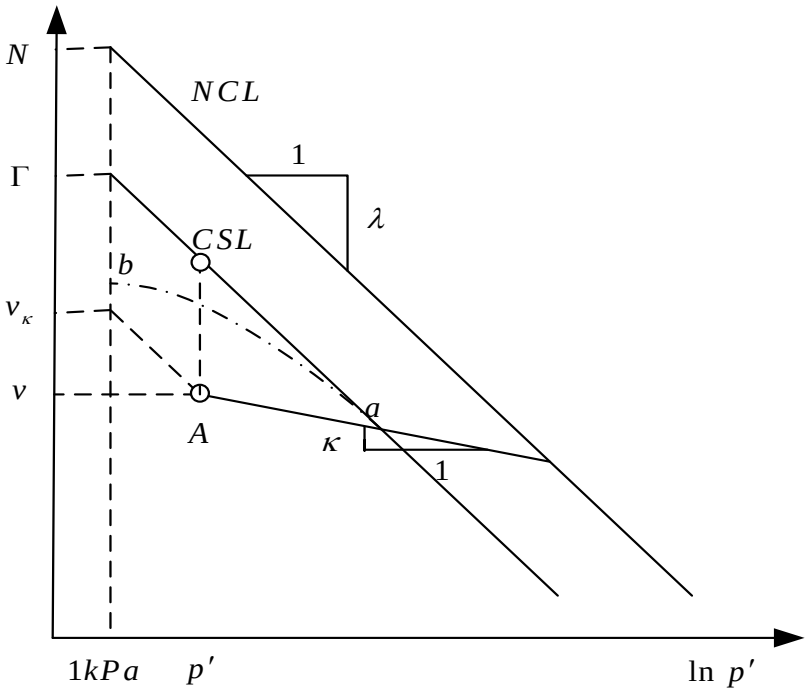

Figure 3.8 *CSL* in $v-\ln p'$ space

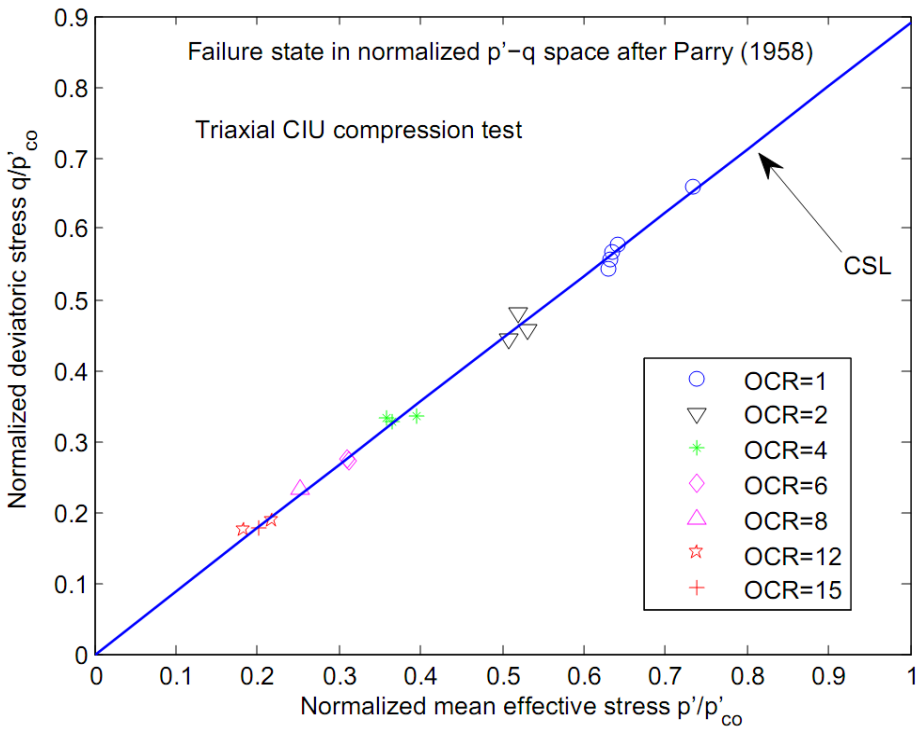

Figure 3.9 Failure state of Weald clay in *CIU* compression test (Parry, 1958)

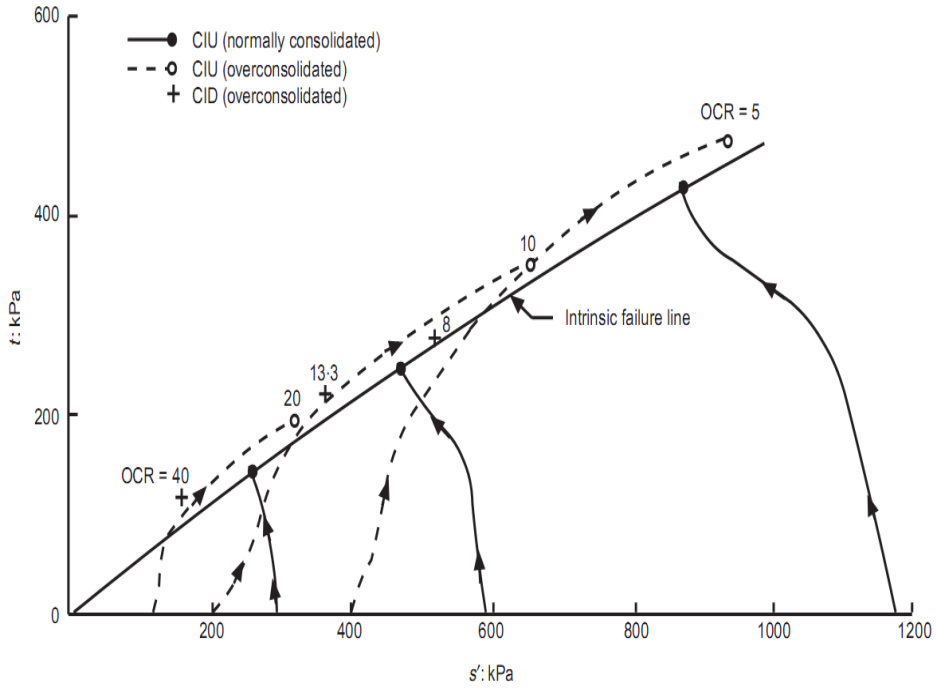

(a) Pietrafitta clay

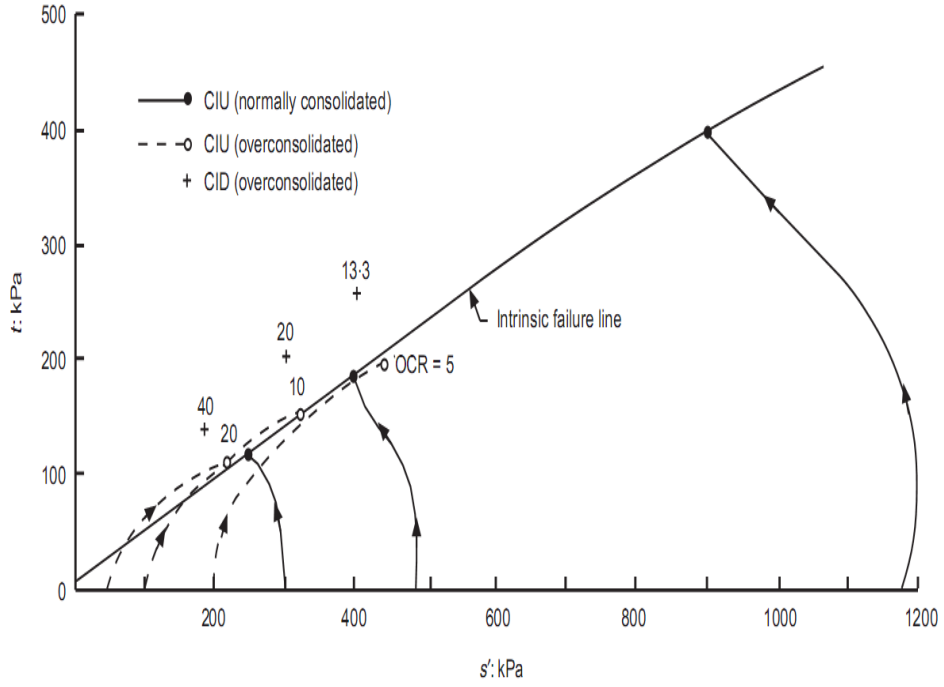

(b) Todi clay

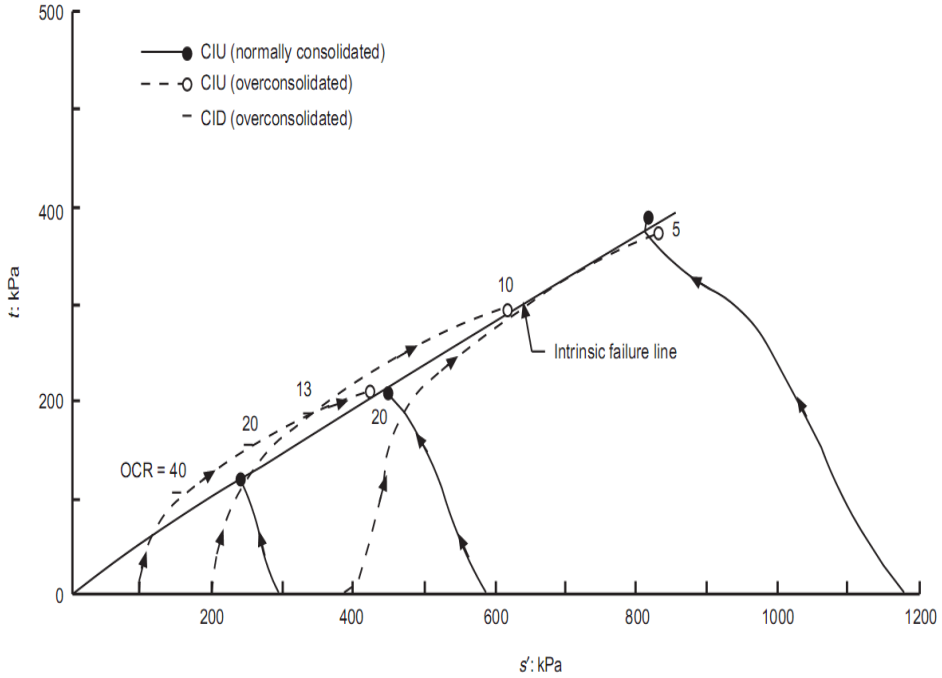

(c) Vallericca clay

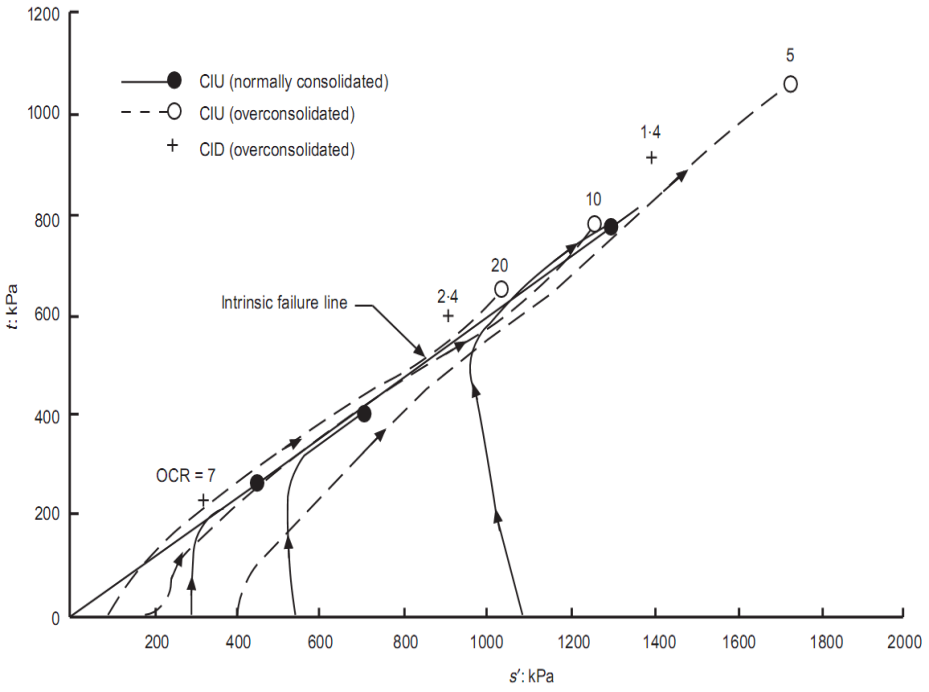

(d) Corinth marl

Figure 3.10 Stress path of various clays after Burland *et al.* (1996)

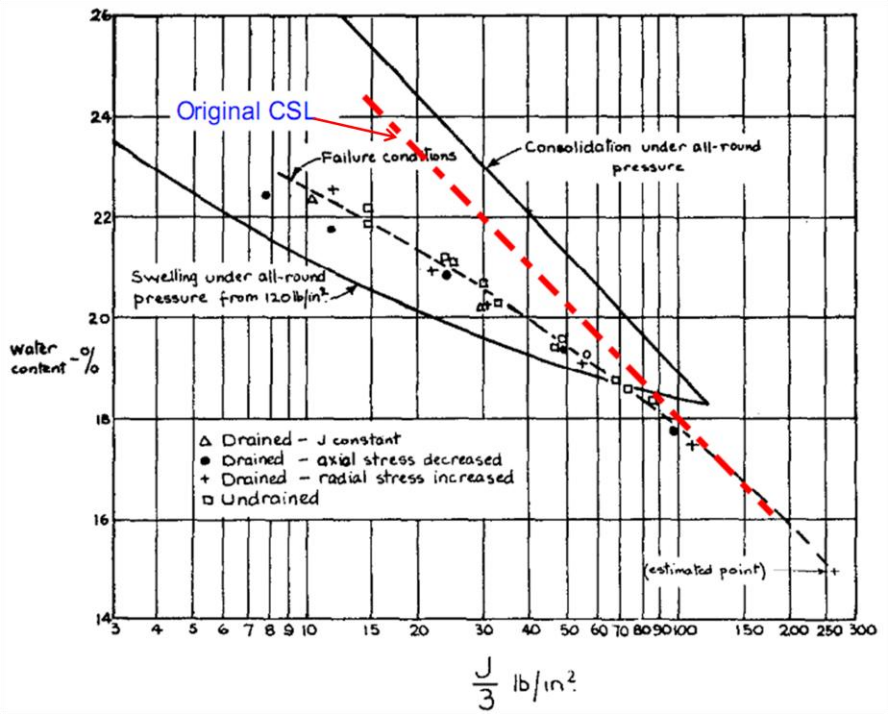

(a) Weald clay

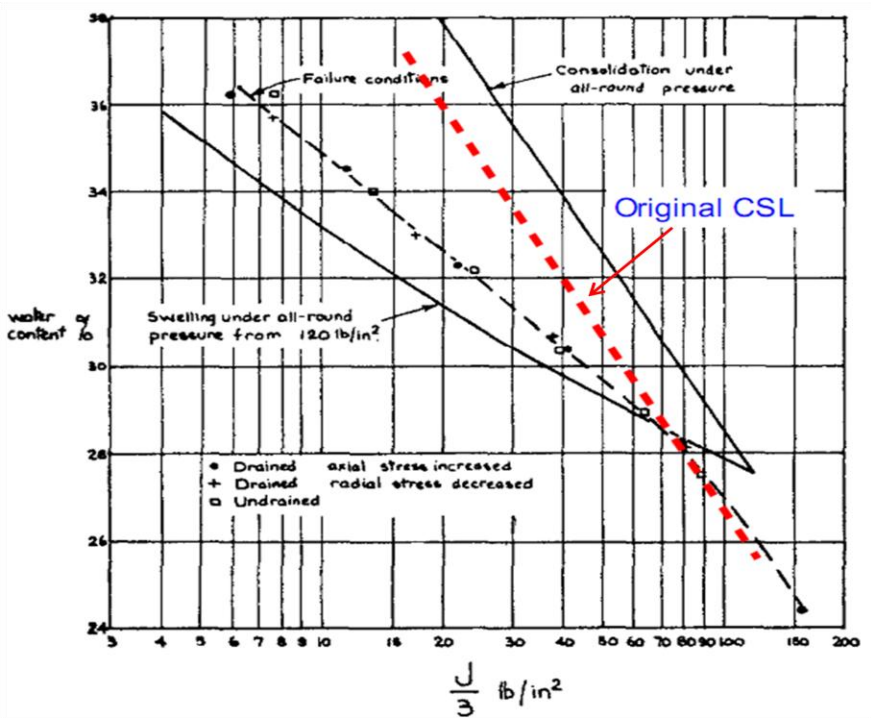

(b) London clay

Figure 3.11 Failure state in $v - \ln p'$ space (Henkel, 1959)

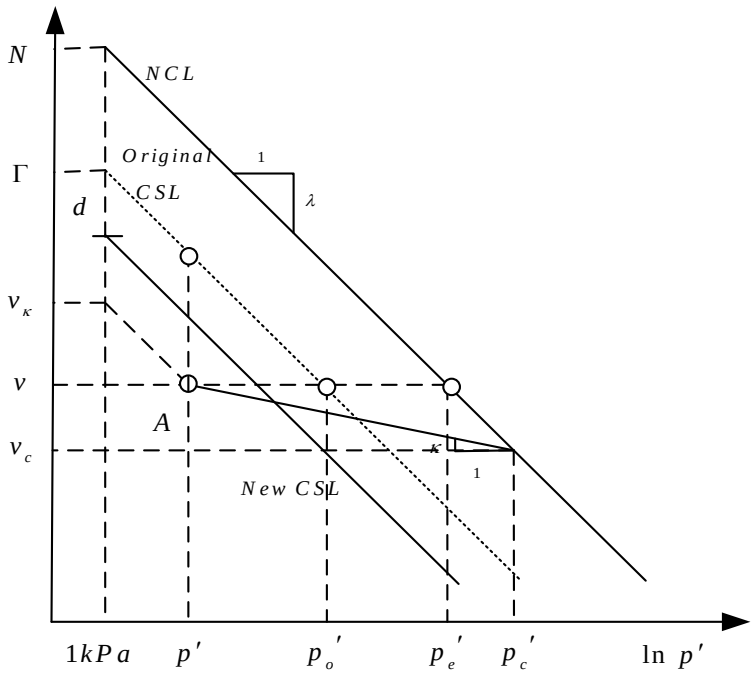

Figure 3.12 Position of new *CSL* in $v-\ln p'$ space

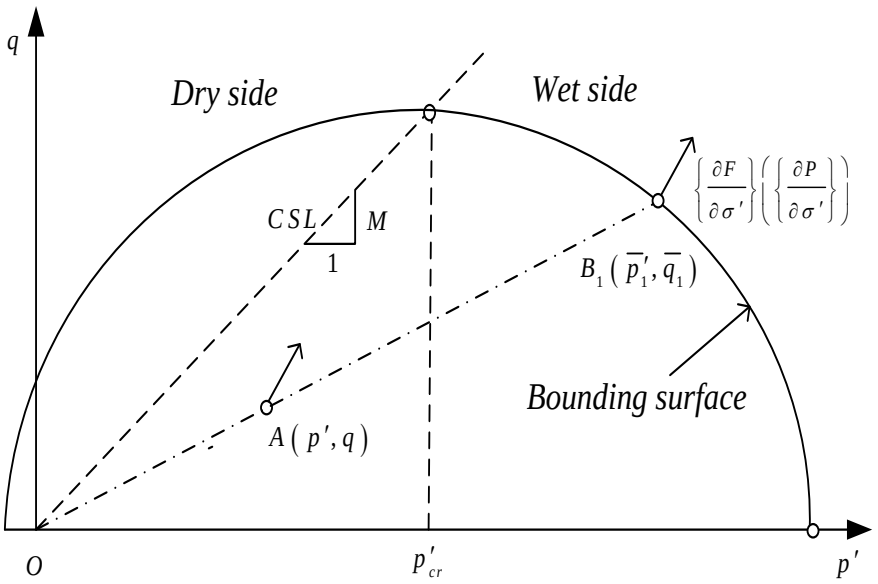

Figure 3.13 Determination of image point on bounding surface

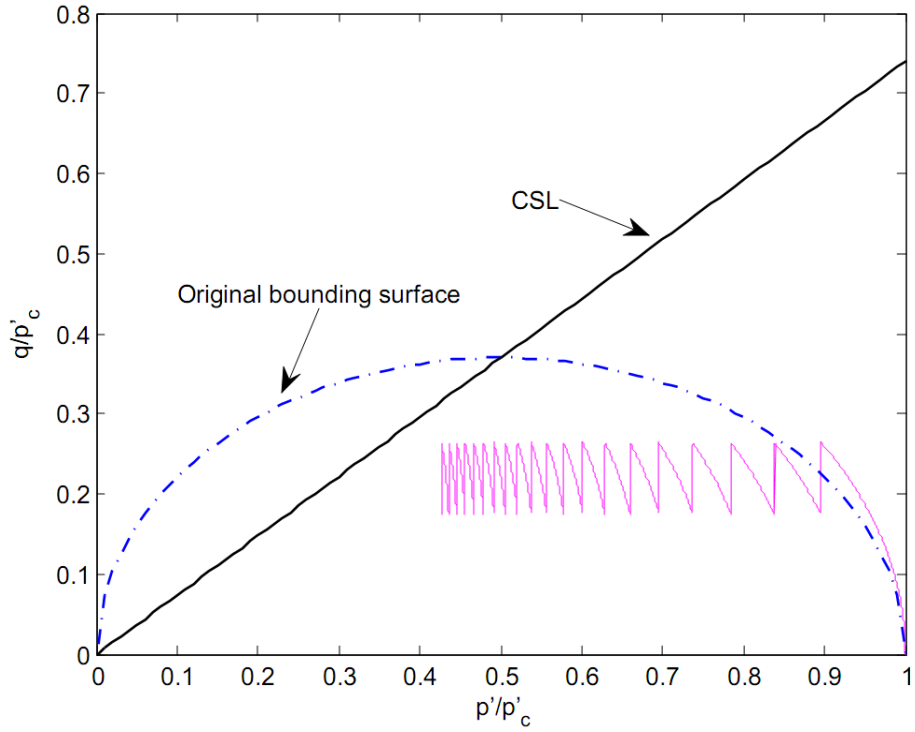

Figure 3.14 Effective stress path predicted by Zienkiewicz *et al.* (1985)

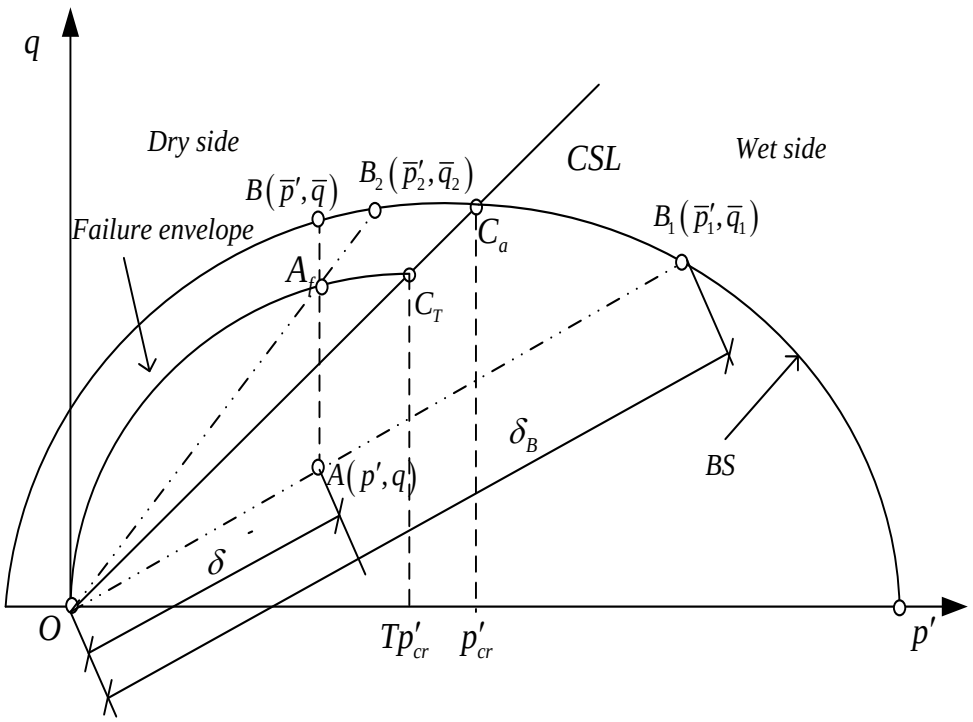

Figure 3.15 Determination of image points on bounding surface

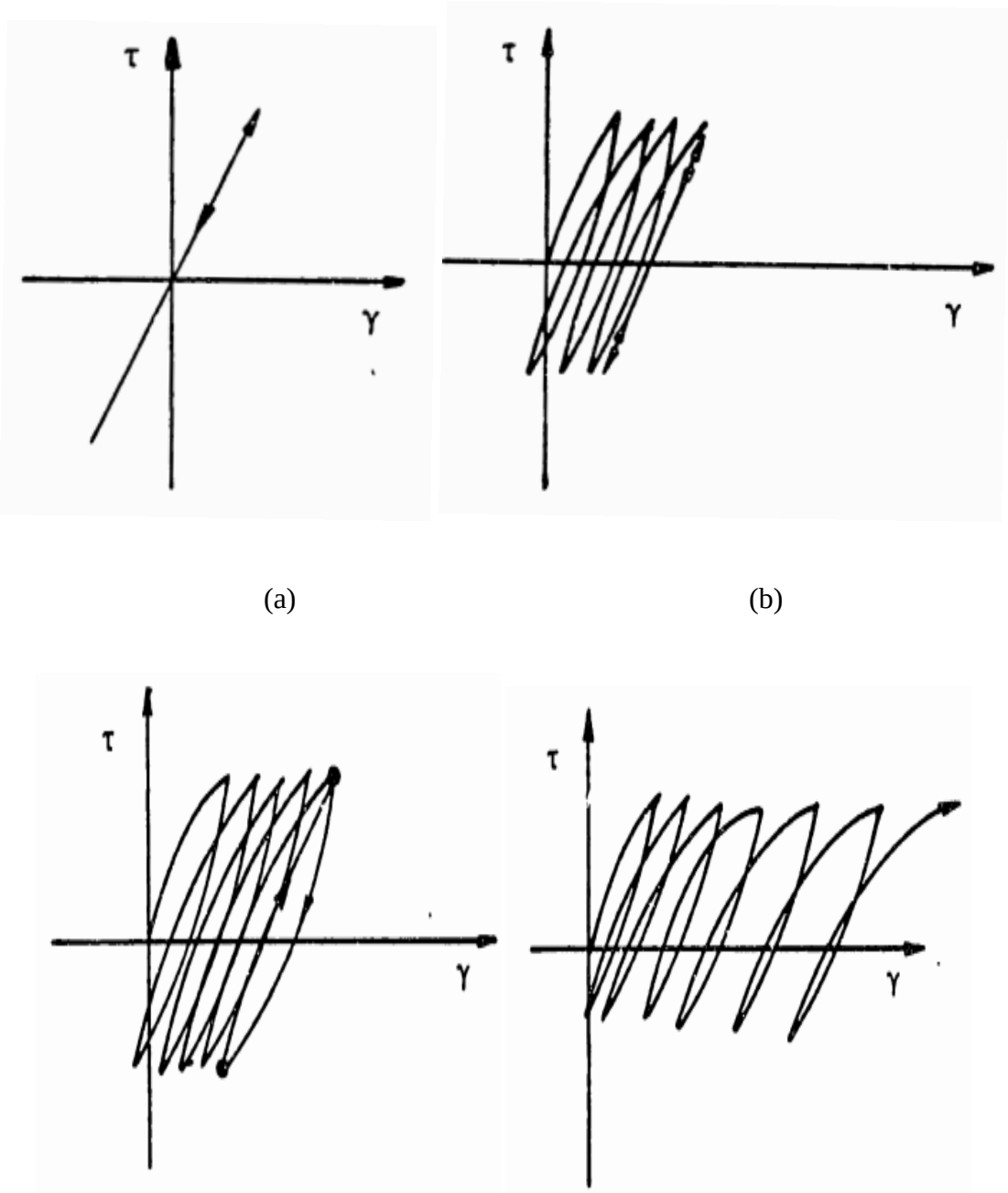

(a) (b)

(c) d)

Figure 3.16 Typical cyclic behavior after Whittle (1987)

Chapter 4 **Extension of the AZ-Cam clay model to general stress space and numerical implementation in ABAQUS**

4.1 Introduction

In this chapter, the extension of the AZ-Cam clay model in general stress space will be described. The generalization to 3-dimensional space is necessary for implementing this model into the commercial finite element software ABAQUS (2011) through UMAT, which is the user subroutine in ABAQUS as will be described in detail in this chapter. The shape of the bounding surface, plastic potential and failure envelope in the deviatoric plane will be presented. The numerical implementation with the associated stress schemes will be shown in the second part of this chapter, followed by the verification of the implementation.

4.2 Extend to general stress space

4.2.1 Stress and strain variables in general stress space

As the AZ-Cam clay model is formulated based on the isotropic assumption, thus three stress invariants can fully describe the whole model. A common choice for these three stress invariants are p', J, θ as defined in section A.1.3 of Appendix A.

4.2.2 Surfaces in the deviatoric plane

In order to avoid the numerical singularity, the bounding surface, plastic potential and failure surface in the deviatoric plane in the AZ-Cam clay model follows the proposal of Vaneekelen (1980) as

$$g(\theta) = \frac{X}{\left[1 + Y \sin(3\theta)\right]^{Z}} \qquad 4.1$$

where $g(\theta)$ measures the distance from current stress state to isotropic axis in deviatoric plane. Thus by choosing appropriate parameters, von Mises criterion, Morh Coulomb criterion and Lade criterion can all be approximated

4.2.3 Surfaces in general stress space

4.2.3.1 Bounding surface in general stress space

The mathematical form of bounding surface in general stress space is given as

Subcritical region: $F = \frac{1}{2}\frac{\mathbf{s:s}}{g_b(\theta)^2} + \frac{4}{R_w^2}(p' - \frac{2}{2+R_w}p_c')^2 - \left(\frac{2}{2+R_w}p_c'\right)^2 = 0$ 4.2 (a)

Supercritical region: $F = \frac{1}{2}\frac{\mathbf{s:s}}{g_b(\theta)^2} + \frac{4}{R_d^2}(p' - \frac{2}{2+R_w}p_c')^2 - \left(\frac{2}{2+R_w}p_c'\right)^2 = 0$ 4.2 (b)

$g_b(\theta)$ takes the form as Equation 4.1 as expressed in Equation 4.3

$$g_b(\theta) = \frac{X_b}{\left[1 + Y_b \sin(3\theta)\right]^{Z_b}} \qquad 4.3$$

where X_b, Y_b, Z_b are material constants.

Substitute Lode's angle of 30^0 and -30^0 into Equation 4.3 and take the ratio of these two values yields

$$\frac{g_b(-30^0)}{g_b(+30^0)} = \frac{(1 - Y_b)^{Z_b}}{(1 + Y_b)^{Z_b}} \qquad 4.4$$

where $g_b\left(-30^0\right)$ and $g_b\left(+30^0\right)$ correspond to triaxial compression and triaxial extension, respectively. Following the Mohr Coulomb criterion, Equation 4.4 can be manipulated as

$$\frac{\left(1-Y_b\right)^{Z_b}}{\left(1+Y_b\right)^{Z_b}}=\frac{6-3\sin\left(\phi'_{cs}\right)}{6+3\sin\left(\phi'_{cs}\right)} \tag{4.5}$$

With Equation 4.5, it is possible to choose certain pair of X_b, Y_b, Z_b to obtain a continuous shape.

4.2.3.2 Plastic potential in general stress space

The plastic potential takes the same form as the bounding surface in general stress space as expressed in Equation 4.2, except that the $g_b\left(\theta\right)$ is replaced by $g_p\left(\theta\right)$, which is given in Equation 4.6

$$g_p\left(\theta\right)=\frac{X_p}{\left[1+Y_p\sin\left(3\theta\right)\right]^{Z_p}} \tag{4.6}$$

where X_p is a model state variable ensuring the plastic potential always passes through the first image point on the bounding surface. Y_p, Z_p are material constants describing the shape of the plastic potential, and can be different from the value used for the bounding surface. Thus non-associated flow rule is possible. Besides, following Potts & Zdravkovic (1999), Y_p, Z_p determine the failure Lode's angle at plane strain condition as expressed by

$$\tan\theta=-\frac{3Y_pZ_p\cos\left(3\theta\right)}{1+Y_p\sin\left(3\theta\right)} \tag{4.7}$$

Generally, most soils fail with Lode's angle between $-10^0 \sim -25^0$ under plane strain condition (Mita, 2002). Thus by choosing certain pair of Y_p, Z_p, the Lode's angle at failure in plane strain condition can be taken into consideration.

4.2.3.3 Failure envelope in general stress space

The failure envelope in general stress space is expressed as

$$\frac{J}{g_b(\theta)\,p'} = 1 + \beta(\theta)\ln\left[\frac{T(\theta)\,p'_{cr}}{p'}\right] \tag{4.8}$$

where $\beta(\theta)$ and $T(\theta)$ are peak strength and ultimate strength parameters in the deviatoric plane, both of which now depend on the Lode's angle. To relate the failure surface to the Lode's angle is consistent with the recommendation of Mita (2002).

$\beta(\theta)$ and $T(\theta)$ control the shape of failure envelope and the relative distance to the bounding surface at a specific Lode's angle. It is generally difficult to truly define the variation of these two parameters with Lode's angle. However, it is easy to define $\beta(-30^0), T(-30^0)$ (triaxial compression) and $\beta(+30^0)$, $T(+30^0)$ (triaxial extension) as will be discussed in Chapter 5. Thus $\beta(\theta)$ and $T(\theta)$ take the general shape of Equation 4.1 as

$$\beta(\theta) = \frac{X_\beta}{\left[1 + Y_\beta \sin(3\theta)\right]^{Z_\beta}} \tag{4.9}$$

$$T(\theta) = \frac{X_T}{\left[1 + Y_T \sin(3\theta)\right]^{Z_T}} \tag{4.10}$$

where $X_\beta, Y_\beta, Z_\beta$ and X_T, Y_T, Z_T are material constants for $\beta(\theta)$ and $T(\theta)$, respectively.

With the known value of β and T in triaxial compression and triaxial extension, it is possible to determine the appropriate pairs for $X_\beta, Y_\beta, Z_\beta$ and X_T, Y_T, Z_T.

4.3 Elasto-plastic stiffness matrix in general stress space

The general equation of the elasto-plastic stiffness matrix is specified in Equation A.42 in Appendix A. The hardening rule in general stress space remains the same as that in the triaxial stress space since the hardening parameter p_c' depends solely on the plastic volumetric strain. The remaining parameters to fully define elasto-plastic stiffness matrix are the two outward directions $\left\{\frac{\partial F}{\partial \sigma'}\right\}$ and $\left\{\frac{\partial P}{\partial \sigma'}\right\}$. As the plastic potential takes a similar form as the bounding surface and only differs in the shape in the deviatoric plane, thus only $\left\{\frac{\partial F}{\partial \sigma'}\right\}$ will be determined since $\left\{\frac{\partial P}{\partial \sigma'}\right\}$ can be obtained by substituting the parameters Y_b, Z_b used for bounding surface in Equation 4.3 by Y_p, Z_p. The detailed derivation follows Grammatikopoulou (2004).

$\left\{\frac{\partial F}{\partial \sigma'}\right\}$ is expanded as expressed in Equation 4.11

$$\left\{\frac{\partial F}{\partial \sigma'}\right\} = \left(\frac{\partial F}{\partial \sigma_x'}, \frac{\partial F}{\partial \sigma_y'}, \frac{\partial F}{\partial \sigma_z'}, \frac{\partial F}{\partial \tau_{xy}}, \frac{\partial F}{\partial \tau_{yz}}, \frac{\partial F}{\partial \tau_{zx}}\right) \tag{4.11}$$

By employing $\{s\}^T = \left(\sigma_x' - p', \sigma_y' - p', \sigma_z' - p', \tau_{xy}, \tau_{yz}, \tau_{zx}\right)$, each term on the right hand of Equation 4.11 is given as

$$\frac{\partial F}{\partial \sigma'_x}=\frac{\partial F}{\partial p'}\frac{\partial p'}{\partial \sigma'_x}+\frac{\partial F}{\partial s}\frac{\partial s}{\partial \sigma'_x}=\frac{1}{3}\frac{\partial F}{\partial p'}+\frac{1}{3}\left(2\frac{\partial F}{\partial\left(\sigma'_x-p'\right)}-\frac{\partial F}{\partial\left(\sigma'_y-p'\right)}-\frac{\partial F}{\partial\left(\sigma'_z-p'\right)}\right) \quad 4.12 \text{ (a)}$$

$$\frac{\partial F}{\partial \sigma'_y}=\frac{\partial F}{\partial p'}\frac{\partial p'}{\partial \sigma'_y}+\frac{\partial F}{\partial s}\frac{\partial s}{\partial \sigma'_y}=\frac{1}{3}\frac{\partial F}{\partial p'}+\frac{1}{3}\left(2\frac{\partial F}{\partial\left(\sigma'_y-p'\right)}-\frac{\partial F}{\partial\left(\sigma'_x-p'\right)}-\frac{\partial F}{\partial\left(\sigma'_z-p'\right)}\right) \quad 4.12 \text{ (b)}$$

$$\frac{\partial F}{\partial \sigma'_z}=\frac{\partial F}{\partial p'}\frac{\partial p'}{\partial \sigma'_z}+\frac{\partial F}{\partial s}\frac{\partial s}{\partial \sigma'_z}=\frac{1}{3}\frac{\partial F}{\partial p'}+\frac{1}{3}\left(2\frac{\partial F}{\partial\left(\sigma'_z-p'\right)}-\frac{\partial F}{\partial\left(\sigma'_x-p'\right)}-\frac{\partial F}{\partial\left(\sigma'_y-p'\right)}\right) \quad 4.12 \text{ (c)}$$

$$\frac{\partial F}{\partial \tau_{yx}}=\frac{\partial F}{\partial s}\frac{\partial s}{\partial \tau_{yx}} \quad 4.12 \text{ (d)}$$

$$\frac{\partial F}{\partial \tau_{yz}}=\frac{\partial F}{\partial s}\frac{\partial s}{\partial \tau_{yz}} \quad 4.12 \text{ (e)}$$

$$\frac{\partial F}{\partial \tau_{zx}}=\frac{\partial F}{\partial s}\frac{\partial s}{\partial \tau_{zx}} \quad 4.12 \text{ (f)}$$

The value of $\frac{\partial F}{\partial p'}$ is determined as

On the wet side: $\frac{\partial F}{\partial p'}=\frac{8}{R_w^2}\left(p'-\frac{2}{2+R_w}p'_c\right)$ 4.13 (a)

On the dry side: $\frac{\partial F}{\partial p'}=\frac{8}{R_d^2}\left(p'-\frac{2}{2+R_w}p'_c\right)$ 4.13 (b)

The key is to evaluate $\left\{\frac{\partial F}{\partial s}\right\}$, which is given as follows:

$$\left\{\frac{\partial F}{\partial s}\right\}=\frac{\partial F}{\partial Q}\left\{\frac{\partial Q}{\partial s}\right\}+\frac{\partial F}{\partial \theta}\left\{\frac{\partial \theta}{\partial s}\right\} \quad 4.14$$

where $Q = \mathbf{s} : \mathbf{s}$. Thus

$$\frac{\partial F}{\partial Q} = \frac{1}{2g^2(\theta)} \tag{4.15 (a)}$$

$$\frac{\partial F}{\partial \theta} = \frac{3QZ_bY_b\cos(3\theta)}{g_b{}^2(\theta)\left[1+Y_b\sin(3\theta)\right]} \tag{4.15 (b)}$$

From the definition of Lode's angle of Equation A.9, the value of $\left\{\frac{\partial \theta}{\partial s}\right\}$ is obtained as

$$\left\{\frac{\partial \theta}{\partial s}\right\} = \frac{\sqrt{3}}{2\cos(3\theta)\left(\frac{1}{2}Q\right)^{1.5}}\left[\frac{3\det(\mathbf{s})}{2Q}\left\{\frac{\partial Q}{\partial s}\right\} - \left\{\frac{\partial \det(\mathbf{s})}{\partial s}\right\}\right] \tag{4.16}$$

Substituting Equation 4.16 into Equation 4.14 yields

$$\left\{\frac{\partial F}{\partial s}\right\} = \left[\frac{\partial F}{\partial Q} + \frac{\partial F}{\partial \theta}\frac{3\sqrt{3}\det(\mathbf{s})}{8\cos(3\theta)\left(\frac{1}{2}Q\right)^{2.5}}\right]\left\{\frac{\partial Q}{\partial s}\right\} - \frac{\sqrt{3}\det(\mathbf{s})}{2\cos(3\theta)\left(\frac{1}{2}Q\right)^{1.5}}\frac{\partial F}{\partial \theta}\left\{\frac{\partial \det(\mathbf{s})}{\partial s}\right\} \tag{4.17}$$

Then substituting Equation 4.15 into Equation 4.17 gives

$$\left\{\frac{\partial F}{\partial s}\right\} = \alpha_1\left\{\frac{\partial Q}{\partial s}\right\} + \alpha_2\left\{\frac{\partial \det(\mathbf{s})}{\partial s}\right\} \tag{4.18}$$

where α_1 and α_2 is defined as

$$\alpha_1 = \frac{1}{2g_b^2(\theta)} + \frac{9\sqrt{3}QZ_bY_b\cos(3\theta)\det(\mathbf{s})}{8g_b^2(\theta)\left[1+Y_b\sin(3\theta)\right]\cos(3\theta)\left(\frac{1}{2}Q\right)^{2.5}} \tag{4.19 (a)}$$

$$\alpha_2 = -\frac{3\sqrt{3}QZ_bY_b\cos(3\theta)\det(\mathbf{s})}{2g_b^2(\theta)\left[1+Y_b\sin(3\theta)\right]\cos(3\theta)\left(\frac{1}{2}Q\right)^{1.5}} \quad \text{4.19 (b)}$$

The value of Q is calculated as

$$Q = \left(\sigma_x' - p'\right)^2 + \left(\sigma_y' - p'\right)^2 + \left(\sigma_z' - p'\right)^2 + 2\tau_{xy}^2 + 2\tau_{yz}^2 + 2\tau_{zx}^2 \quad \text{4.20}$$

Thus $\left\{\frac{\partial Q}{\partial s}\right\}$ is evaluated as

$$\left\{\frac{\partial Q}{\partial s}\right\} = \left(\frac{\partial Q}{\partial\left(\sigma_x' - p'\right)}, \frac{\partial Q}{\partial\left(\sigma_y' - p'\right)}, \frac{\partial Q}{\partial\left(\sigma_z' - p'\right)}, \frac{\partial Q}{\partial\tau_{xy}}, \frac{\partial Q}{\partial\tau_{yz}}, \frac{\partial Q}{\partial\tau_{zx}}\right) \quad \text{4.21}$$

The term on the right hand side of Equation 4.21 are provided as

$$\frac{\partial Q}{\partial\left(\sigma_x' - p'\right)} = 2\left(\sigma_x' - p'\right) \quad \text{4.22 (a)}$$

$$\frac{\partial Q}{\partial\left(\sigma_y' - p'\right)} = 2\left(\sigma_y' - p'\right) \quad \text{4.22 (b)}$$

$$\frac{\partial Q}{\partial\left(\sigma_z' - p'\right)} = 2\left(\sigma_z' - p'\right) \quad \text{4.22 (c)}$$

$$\frac{\partial Q}{\partial\tau_{xy}} = 4\tau_{xy} \quad \text{4.22 (d)}$$

$$\frac{\partial Q}{\partial\tau_{yz}} = 4\tau_{yz} \quad \text{4.22 (e)}$$

$$\frac{\partial Q}{\partial\tau_{zx}} = 4\tau_{zx} \quad \text{4.22 (f)}$$

The value of $\det(\mathbf{s})$ is calculated as

$$\det(\mathbf{s}) = \left(\sigma'_x - p'\right)\left(\sigma'_y - p'\right)\left(\sigma'_z - p'\right) - \left(\sigma'_x - p'\right)\tau_{yz}^2 - \left(\sigma'_y - p'\right)\tau_{zx}^2 - \left(\sigma'_z - p'\right)\tau_{xy}^2 + 2\tau_{xy}\tau_{yz}\tau_{zx}$$

4.23

Thus $\left\{\frac{\partial \det(\mathbf{s})}{\partial s}\right\}$ is calculated as

$$\left\{\frac{\partial \det(\mathbf{s})}{\partial s}\right\} = \left(\frac{\partial \det(\mathbf{s})}{\partial\left(\sigma'_x - p'\right)}, \frac{\partial \det(\mathbf{s})}{\partial\left(\sigma'_y - p'\right)}, \frac{\partial \det(\mathbf{s})}{\partial\left(\sigma'_z - p'\right)}, \frac{\partial \det(\mathbf{s})}{\partial \tau_{xy}}, \frac{\partial \det(\mathbf{s})}{\partial \tau_{yz}}, \frac{\partial \det(\mathbf{s})}{\partial \tau_{zx}}\right) \qquad 4.24$$

The term on the right hand side of Equation 4.24 are provided as

$$\frac{\partial \det(\mathbf{s})}{\partial\left(\sigma'_x - p'\right)} = \left(\sigma'_y - p'\right)\left(\sigma'_z - p'\right) - \tau_{yz}^2 \qquad 4.25\ (a)$$

$$\frac{\partial \det(\mathbf{s})}{\partial\left(\sigma'_y - p'\right)} = \left(\sigma'_z - p'\right)\left(\sigma'_x - p'\right) - \tau_{zx}^2 \qquad 4.25\ (b)$$

$$\frac{\partial \det(\mathbf{s})}{\partial\left(\sigma'_z - p'\right)} = \left(\sigma'_x - p'\right)\left(\sigma'_y - p'\right) - \tau_{xy}^2 \qquad 4.25\ (c)$$

$$\frac{\partial \det(\mathbf{s})}{\partial \tau_{xy}} = -2\left(\sigma'_z - p'\right)\tau_{xy} + 2\tau_{yz}\tau_{zx} \qquad 4.25\ (d)$$

$$\frac{\partial \det(\mathbf{s})}{\partial \tau_{yz}} = -2\left(\sigma'_x - p'\right)\tau_{yz} + 2\tau_{xy}\tau_{zx} \qquad 4.25\ (e)$$

$$\frac{\partial \det(\mathbf{s})}{\partial \tau_{zx}} = -2\left(\sigma'_y - p'\right)\tau_{zx} + 2\tau_{xy}\tau_{yz} \qquad 4.25\ (f)$$

Substituting Equation 4.22 and Equation 4.25 into Equation 4.18 gives the value of $\left\{\frac{\partial F}{\partial s}\right\}$. Combining the value of $\left\{\frac{\partial F}{\partial s}\right\}$ and $\frac{\partial F}{\partial p'}$, the outward normal direction of the bounding surface $\left\{\frac{\partial F}{\partial \sigma}\right\}$ can be fully defined.

4.4 Numerical implementation in ABAQUS

4.4.1 UMAT in ABAQUS/Standard

The implementation of the AZ-Cam clay model in ABAQUS/Standard is through UMAT. UMAT is the user subroutine for defining a material's mechanical behavior in ABAQUS. Thus various constitutive models can be implemented as alternatives to the built-in models. This function greatly increases the freedom of users dealing with various materials. The two main functions of UMAT are: (i) Updating the stresses in the FE model due to the changes of strains which are provided by ABAQUS at the start of each interation; (ii) Providing a Jacobian matrix for formulating the global stiffness matrix in the FE model. It should be noted that the Jacobian matrix provided by UMAT does not necessarily exactly reflect the true behavior of material constitutive relations. This is because the global stiffness matrix employed only affects the number of iterations rather than the accuracy (Appendix B presents the numerical algorithm in ABAQUS to solve the nonlinear global equations). However, the updated stresses provided by UMAT should truly reflect the constitutive relations of the material. The detailed description of UMAT can be found in the ABAQUS manual (ABAQUS, 2011).

4.4.2 Stress point algorithm

4.4.2.1 Explicit sub-stepping algorithm

The key part of implementing a constitutive model is the stress point algorithm, which updates the stresses given by the strain increments. The stress point algorithm used in the current study is the explicit sub-stepping algorithm, which is based on the work of Sloan (1987), Abbo & Sloan (1996) and Potts & Zdravkovic (1999). However, the stress point algorithm of all the built-in models in ABAQUS is the implicit return algorithm. A brief comparison of the explicit sub-stepping algorithm and the implicit return algorithm is given in Appendix C.

At each integration point, the stress increment due to the strain increment of an elasto-plastic material is obtained as

$$\{d\sigma\} = \left[D^{ep}\right]\{d\varepsilon\} \tag{4.26}$$

For the AZ-Cam clay model, the behavior on loading will always be elasto-plastic and elastic behavior only occurs during unloading. Thus before employing the sub-stepping algorithm, loading/unloading criterion specified in section A.5 should be used to check whether the strain increments correspond to loading or unloading. If unloading occurs, the material is firstly assumed to be elastic before the current strain increments $\{d\varepsilon\}$. Thus the stress increments can be obtained as

$$\left\{d\sigma^{e}\right\} = \left[D^{e}\right]\{d\varepsilon\} \tag{4.27}$$

The stress increments are thus added to the stress state $\{\sigma_0\}$, which is just before the current strain increments. Thus the updated stress state can be obtained as

$$\{\sigma\} = \{\sigma_0\} + \{d\sigma^e\} \quad 4.28$$

As the bounding surface embraces all the possible stress states, it is necessary to ensure that the updated stress state lies within or on the bounding surface. However, as shown in Figure 4.1, if the final stress state (represented by C in Figure 4.1) lies outside of the bounding surface, plastic strain occurs during the strain increments $\{d\varepsilon\}$, thus violates the initial assumption of purely elastic. It is thus necessary to split the strain increments $\{d\varepsilon\}$ into two parts and the elastic stress increments should also be changed as

$$\{d\varepsilon\} = \alpha\{d\varepsilon\} + (1-\alpha)\{d\varepsilon\} \quad 4.29\ (a)$$

$$\{d\sigma^e_{new}\} = \alpha\{d\sigma^e\} \quad 4.29\ (b)$$

where the first part of right hand side of Equation 4.29 (a) corresponds to the elastic behavior, which starts from the stress state A and terminates at B on the bounding surface as shown in Figure 4.1. The second part of right hand side of Equation 4.29 (a) corresponds to the elasto-plastic part $B-C$. $\{d\sigma^e_{new}\}$ denotes the elastic stress increments occur along the elastic strain path $A-B$. Specific techniques would be employed to find out the value of α as will be discussed in the next section. However, if the transition from unloading to loading occurs within the bounding surface, it is thus not possible to differentiate this phenomenon and purely elastic behavior would be predicted whenever loading occurs. Thus some errors are inevitably introduced which restrains the incremental size of strains.

As long as the behavior becomes elasto-plastic, the modified Euler scheme with automatically error control is used to evaluate the plastic strains and other

corresponding state variables as follows. To be consistent with the above discussed possible elastic behavior, the strain increments are specified as $(1-\alpha)\{d\varepsilon\}$. At the beginning of elasto-plastic behavior, the stress state is obtained by combining Equation 4.28 and Equation 4.29 (b). The strain increments are then sub-divided into a number sub-steps as

$$\left\{d\varepsilon_s^i\right\} = \Delta T^i (1-\alpha)\{d\varepsilon\} \qquad 4.30$$

where $\left\{d\varepsilon_s^i\right\}$ is the strain increments in one sub-step, the superscript indicates the number of sub-step. ΔT^i expresses the proportion of strain increments in one sub-step to the total strain increments corresponding to the elasto-plastic behavior. In each sub-step, a first estimation of stress changes will be based on the stress state at the beginning of that sub-step as

$$\left\{d\sigma_1^i\right\} = \left[D^{ep}\left(\left\{\sigma_0^i\right\},\left\{k_0^i\right\}\right)\right]\left\{d\varepsilon_s^i\right\} \qquad 4.31\ (a)$$

$$\left\{d\varepsilon_{s1}^{ip}\right\} = \left\{d\varepsilon_s^i\right\} - \left[D^e\left(\left\{\sigma_0^i\right\}\right)\right]^{-1}\left\{d\sigma_1^i\right\} \qquad 4.31\ (b)$$

$$\left\{dk_1^i\right\} = \left\{dk\left(\left\{d\varepsilon_{s1}^{ip}\right\}\right)\right\} \qquad 4.31\ (c)$$

where $\left\{\sigma_0^i\right\}$ and $\left\{k_0^i\right\}$ are the stress state and the hardening parameters at the beginning of each sub-step, respectively. $\left\{d\varepsilon_{s1}^{ip}\right\}$ are the plastic strains during the sub-step. $\left\{d\sigma_1^i\right\}$ and $\left\{dk_1^i\right\}$ are then used to update the stress state and hardening parameters, from which a second estimation of stress changes are obtained as

$$\left\{d\sigma_2^i\right\} = \left[D^{ep}\left(\left(\left\{\sigma_0^i\right\}+\left\{d\sigma_1^i\right\}\right),\left(\left\{k_0^i+dk_1^i\right\}\right)\right)\right]\left\{d\varepsilon_s^i\right\} \qquad 4.32\ (a)$$

$$\left\{d\varepsilon_{s2}^{ip}\right\}=\left\{d\varepsilon_{s}^{i}\right\}-\left[D^{e}\left(\left\{\sigma_{0}^{i}\right\}+\left\{d\sigma_{1}^{i}\right\}\right)\right]^{-1}\left\{d\sigma_{2}^{i}\right\} \qquad 4.32\ (b)$$

$$\left\{dk_{2}^{i}\right\}=\left\{dk\left(\left\{d\varepsilon_{s2}^{ip}\right\}\right)\right\} \qquad 4.32\ (c)$$

Thus the actual changes of stress and strain variables in one sub-step are taken as the average of the above two calculations as

$$\left\{d\sigma^{i}\right\}=\frac{1}{2}\left(\left\{d\sigma_{1}^{i}\right\}+\left\{d\sigma_{2}^{i}\right\}\right) \qquad 4.33\ (a)$$

$$\left\{d\varepsilon_{s}^{ip}\right\}=\frac{1}{2}\left(\left\{d\varepsilon_{s1}^{ip}\right\}+\left\{d\varepsilon_{s2}^{ip}\right\}\right) \qquad 4.33\ (b)$$

$$\left\{dk^{i}\right\}=\frac{1}{2}\left(\left\{dk_{1}^{i}\right\}+\left\{dk_{2}^{i}\right\}\right) \qquad 4.33\ (c)$$

The error introduced in one sub-step can be estimated as

$$R=\frac{\left\|\left\{E_{r}\right\}\right\|}{\left\|\left\{\sigma_{0}^{i}\right\}+\left\{d\sigma^{i}\right\}\right\|} \qquad 4.34$$

where '$\|\ \|$' indicates the norm of the vector and $\{E_r\}$ is defined as

$$\left\{E_{r}\right\}=\frac{1}{2}\left(\left\{d\sigma_{2}^{i}\right\}-\left\{d\sigma_{1}^{i}\right\}\right) \qquad 4.35$$

The value R is then compared with the error tolerance TOL (10^{-4} is used in the current study). If $R \le TOL$, then the solution is acceptable, and the next sub-step or next increment is carried out subsequently. However, if $R > TOL$, then the error introduced in the current sub-step is not acceptable and the incremental size of the current sub-

step should be further reduced. The new strain increments in the *ith* sub-step can be obtained by revising the ΔT^i following Abbo & Sloan (1996) as

$$\Delta T^i_{new} = 0.7\left(\frac{TOL}{R}\right)^{0.5} \qquad 4.36$$

where ΔT^i_{new} is the new ΔT^i used in the current sub-step. With this updated ΔT^i_{new}, the same calculation is repeated until the error associated with the predicted stresses is acceptable. Thus the above scheme ensures that the error introduced can be controlled automatically.

At the end of the *ith* sub-step, the updated stresses, hardening parameters and plastic strains can be obtained as

$$\left\{\sigma^i\right\} = \left\{\sigma^i_0\right\} + \left\{d\sigma^i\right\} \qquad 4.37\ (a)$$

$$\left\{\varepsilon^{ip}_s\right\} = \left\{\varepsilon^{ip}_{s0}\right\} + \left\{d\varepsilon^{ip}_s\right\} \qquad 4.37\ (b)$$

$$\left\{k^i\right\} = \left\{k^i_0\right\} + \left\{dk^i\right\} \qquad 4.37\ (c)$$

where $\left\{\varepsilon^{ip}_{s0}\right\}$ is the plastic strains at the beginning of the sub-step.

Current strain increments will be completed when the summation of ΔT^i in all the sub-steps equals to 1 and then the next strain increments begin. Thus the calculation can be carried out by assuming a single sub-step in each strain increments as the error can be controlled automatically and the program can reduce the value of ΔT^i automatically if necessary.

Though the error tolerance *TOL* specified in each sub-step is rather small, there is a possibility that the accumulated errors may be large if the size of the strain increments is relatively large. For stress state within the bounding surface, it is not possible to check or improve the magnitude of the accumulated errors, and the only way is to refine the size of the strain increments. For stress state lying on the bounding surface, the next location of stress state should also lie on the bounding surface if loading occurs (consistency condition). However, as errors are inevitably introduced during integration, the final stress state at the end of one strain increments may not lie exactly on the bounding surface, which is commonly termed as drifting from the bounding surface. The correction of drifting from the bounding surface will be discussed below.

4.4.2.2 'Pegasus' method for computing α

As pointed out previously, when the material goes into the elasto-plastic region from the purely elastic region in one strain increment, the portion of strain increments corresponding to the elastic behavior should be determined. The elastic portion is indicated by the value of α. The value of α can be obtained by solving the following equation

$$F\left(\left(\left\{\sigma_0^i\right\}+\alpha\left\{d\sigma^e\right\}\right),\left\{k_0^i\right\}\right)=0 \qquad 4.38$$

where $\left\{d\sigma^e\right\}$ is provided in Equation 4.27. Thus Equation 4.38 contains only one variable α, which serves as the root of Equation 4.38. The common techniques for solving the root of an equation are the Regula Falsi method and the Newton-Raphson method. The Regula Falsi method is a linear interpolation method with numerical efficiency of 1 (the convergence is linear). Thus relatively larger number of iterations

will be necessary to reach high accuracy. The Newton-Raphson method is very fast with numerical efficiency of 2 (the convergence is quadratic). However, the direction of bounding surface is necessary in order to find α which adds considerable complexity to that method. A modified Regula Falsi method, so-called Pegasus method is reported by Dowell & Jarratt (1972). As the method is relatively simple compared to the Newton-Raphson method, but with relatively high numerical efficiency of 1.642 (the convergence is super-linear), this method is used to calculate α.

From Equation 4.38, it is certain that $F(\alpha=1)>0$ and $F(\alpha=0)\le 0$. If the initial stress state lies on the bounding surface, theoretically $F(\alpha=0)=0$, but for Pegasus method, the root should be bracketed by two value α_{i-1},α_i such that $F(\alpha_{i-1})F(\alpha_i)<0$. Thus the starting value for α when the stress state lies on the bounding surface should not be zero. As $F(\alpha=1)>0$ and $F(\alpha=0)<0$, it is easy to find a starting value α_0 such that $F(\alpha_0)<0$. Thus the starting value for α is chosen as α_0 and 1.0. The procedure for calculating α is thus as follows, which directly follows Dowell & Jarratt (1972).

(1) $F(\alpha_{i-1})F(\alpha_i)<0$, α_{i+1} is calculated by linear interpolation so that

$$\alpha_{i+1}=\frac{\alpha_{i-1}F(\alpha_i)-\alpha_i F(\alpha_{i-1})}{F(\alpha_i)-F(\alpha_{i-1})};$$

(2) If $F(\alpha_{i+1})F(\alpha_i)<0$, then $(\alpha_{i-1},F(\alpha_{i-1}))$ is replaced by $(\alpha_i,F(\alpha_i))$, however if $F(\alpha_{i+1})F(\alpha_i)>0$, then $(\alpha_{i-1},F(\alpha_{i-1}))$ is replaced by $\left(\alpha_{i-1},\frac{F(\alpha_{i-1})F(\alpha_i)}{F(\alpha_i)+F(\alpha_{i+1})}\right)$;

(3) Replace $\left(\alpha_i, F\left(\alpha_i\right)\right)$ by $\left(\alpha_{i+1}, F\left(\alpha_{i+1}\right)\right)$ so that the function values used at each iteration will always have opposite signs.

The basic philosophy of this method is to scale down the value $F\left(\alpha_{i-1}\right)$ by the factor $F\left(\alpha_i\right)/F\left(\alpha_i\right)+F\left(\alpha_{i+1}\right)$ in order to prevent the retention of an end-point. This leads to an order of convergence which is superior to that of linear iteration while still retaining the advantage of bracketing the zero sought (Dowell & Jarratt, 1972). The criterion for terminating iterations should be specified such that the changing of α is less than 0.1% of the previous value which is used in the current study.

4.4.2.3 Correcting the drift from the bounding surface

As stated in section 4.4.2.1, if the strain increment size is relatively large, cumulative errors may be considerable, such that the stress state may lie outside the bounding surface at the end of the strain increment. This phenomenon is commonly termed as drift from the bounding surface. It is thus necessary to correct the final stress state at the end of the each strain increments if it lies outside the bounding surface. Potts and Gens (1985) discussed five methods to project the final stress state to the bounding surface and concluded that some of those can lead to substantial errors. Potts and Gens (1985) and Potts & Zdravkovic (1999) recommended using an alternative method which is adopted in the current study.

The variables at the beginning of the strain increments are represented as stress state $\left\{\sigma_0\right\}$, plastic strains $\left\{\varepsilon_0^p\right\}$ and hardening parameters $\left\{k_0\right\}$. The final states at the end of the strain increments are denoted as final stress state $\left\{\sigma_1\right\}$, final plastic strains $\left\{\varepsilon_1^p\right\}$ and final hardening parameters $\left\{k_1\right\}$. The states after correcting are denoted as

'correct' stresses state $\{\sigma_c\}$, 'correct' plastic strains $\{\varepsilon_c^p\}$ and 'correct' hardening parameters $\{k_c\}$. If the stresses are corrected from $\{\sigma_1\}$ to $\{\sigma_c\}$, elastic strains should be invoked as

$$\{d\varepsilon^e\} = \left[D^e\right]^{-1}\left(\{\sigma_c\} - \{\sigma_1\}\right) \tag{4.39}$$

Assuming the total strain increments remain the same, the above invoked elastic strains should be balanced by equal but opposite sign of plastic strains as

$$\{d\varepsilon^p\} = -\{d\varepsilon^e\} = -\left[D^e\right]^{-1}\left(\{\sigma_c\} - \{\sigma_1\}\right) \tag{4.40}$$

The plastic strains can be calculated following Equation A.19 and are re-expressed as

$$\{d\varepsilon^p\} = \Lambda\left\{\frac{\partial P\left(\{\sigma_0\},\{m\}\right)}{\partial \sigma_0}\right\} \tag{4.41}$$

Combining Equation 4.40 and Equation 4.41 gives

$$\{\sigma_c\} = \{\sigma_1\} - \Lambda\left[D^e\right]\left\{\frac{\partial P\left(\{\sigma_0\},\{m\}\right)}{\partial \sigma_0}\right\} \tag{4.42}$$

The change of plastic strains would inevitably cause changes in the hardening parameters as

$$\{dk\} = \left\{dk\left(\{d\varepsilon^p\}\right)\right\} = \left\{dk\left(\Lambda\left\{\frac{\partial P\left(\{\sigma_0\},\{m\}\right)}{\partial \sigma_0}\right\}\right)\right\} = \Lambda\left\{dk\left(\left\{\frac{\partial P\left(\{\sigma_0\},\{m\}\right)}{\partial \sigma_0}\right\}\right)\right\}$$

4.43 (a)

$$\{k_c\} = \{k_1\} + \{dk\} \tag{4.43 (b)}$$

The corrected stress state should necessary lie on the bounding surface and thus

$$F\left(\{\sigma_c\},\{k_c\}\right)=0 \tag{4.44}$$

Substituting Equation 4.42 and Equation 4.43 into Equation 4.44, and then expanding as a Taylor's series and neglecting terms in Λ^2 and above, yields

$$\Lambda=\frac{F\left(\{\sigma_1\},\{k_1\}\right)}{\left\{\frac{\partial F\left(\{\sigma_0\},\{k_0\}\right)}{\partial\sigma_0}\right\}^T\left[D^e\right]\left\{\frac{\partial P\left(\{\sigma_0\},\{m_0\}\right)}{\partial\sigma_0}\right\}-\left\{\frac{\partial F\left(\{\sigma_0\},\{k_0\}\right)}{\partial\sigma_0}\right\}^T\left\{dk\left(\frac{\partial P\left(\{\sigma_0\},\{m_0\}\right)}{\partial\sigma_0}\right)\right\}} \tag{4.45}$$

Substituting Equation 4.45 into Equation 4.42 and Equation 4.43, the 'correct' final state would be obtained.

Equation 4.45 is obtained by neglecting the terms Λ^2 and above in the Taylor's series expansion. Thus the corrected final stress will not lie exactly on the bounding surface, and thus a numerical tolerance should be specified and an iteration process would be necessary. The iteration process can be easily carried out by replacing $\left(\{\sigma_1\},\{k_1\}\right)$ by $\left(\{\sigma_c\},\{k_c\}\right)$ until the error is less than the tolerance.

4.5 Verification of implementation

This section presents comparisons of predicted responses in *CIU* test and *CID* test using the built-in MCC model in ABAQUS and the MCC model implemented through UMAT following the previously discussed numerical schemes. The verification of implemented MCC model is achieved by comparing the predictions from UMAT and the built-in MCC model in ABAQUS. In general, there is no method to check the implementation of the AZ-Cam clay model. However, the key part of UMAT is

updating the stresses using explicitly sub-stepping algorithm, and this part remains the same for the MCC model and the AZ-Cam clay model. For $OCR = 1$, by choosing appropriate parameters, the AZ-Cam clay model degenerates to the MCC model. Thus by verifying the implemented MCC model, the implementation of the AZ-Cam clay model can be verified indirectly. For heavily OC clay in *CIU* test, analytical solution of undrained shear strength from the AZ-Cam clay model can be determined. This analytical solution can be used to check the implementation of the model. In all the analyses, the soil sample is modeled as a single eight-node brick element (C3D8) in ABAQUS. Thus the true testing of the constitutive behavior of soil can be achieved. For undrained simulation, coupled fluid-soil analysis with zero flow at all the boundary conditions is conducted. The element type is pore-fluid element, which contains an additional degree of freedom of pore pressure as is available in ABAQUS. The full codes for the AZ-Cam clay model are given in Appendix D. The comparison of the UMAT MCC model and the ABAQUS built-in MCC model is based on the Bothkennar clay and the material constants are obtained from Potts & Zdravkovic (1999) with: $N = 2.67$, $\lambda = 0.181$, $\kappa = 0.025$, $M = 1.38$ and $G = 20000kPa$. The soil samples are all isotropically consolidated to $p' = 200kPa$ and then isotropically swell to get various OC clays.

4.5.1 Comparison of UMAT and built-in MCC model in *CIU* test

A NC clay sample subjected to monotonic *CIU* compression (*CIUC*) loading is simulated in this case. The total time increment in ABAQUS is 200s (for a static problem, the concept of 'time' in ABAQUS is not essential. It serves to record the increments in a step. More details are given in Appendix B). The initial incremental size is 0.01s and the maximum one is 2s. The incremental size is allowed to increase

based on the ABAQUS default error-control algorithm. The maximum change of pore water pressure during a single increment is $1kPa$. The above control is the same both for UMAT and the built-in MCC model. As can been from Figure 4.2 (a), the predictions from UMAT and the built-in MCC model agree quite well with the analytical solution after Potts & Zdravkovic (1999). Thus it is reasonable to conclude that the above incremental size is very fine and would result in the 'exact' result. From Figure 4.2, the results from UMAT and the built-in model are almost identical, which verifies the implementation.

4.5.2 Comparison of built-in and implemented MCC model in *CID* test

The incremental size is the same as in section 4.5.1. The results from UMAT and the built-in MCC model agree quite well as can be seen from Figure 4.3. To note that in Figure 4.3 (c), the soil is subjected to loading and unloading (strain control). The sample was initially loaded to an axial strain of 0.2 and then unloaded to 0.

4.5.3 Comparison of explicit and implicit stress scheme

The built-in MCC model in ABAQUS is implemented through an implicit method as discussed in section 4.4. However, an explicit method is used in implementing the AZ-Cam clay model and the MCC model in UMAT. The differences of these two methods are quite small if the load incremental size is sufficient small (Potts and Ganendra, 1994). However, there do exist some obvious differences when the incremental size is relatively large. As can be seen from Figure 4.4 (a) in *CIUC* test for NC clay, if the increment size is 0.1 (the incremental load is 10% of the total load), the explicit method is still able to accurately predict the stress behavior while the implicit method under predict the stress behavior, although the deviation from the exact value is rather small. This is expected as in *CIUC* test, the ratio of different components of

strain tensor remains the same and the loading is proportional, thus the explicit method is theoretically accurate as discussed in Appendix C. For *CID* test of NC clay (the soil is initially loaded to an axial strain of 0.2 and then unloaded to 0.0), the initial increment size is 0.001 and the maximum increment size is 0.05 with automatic increasing of increment size based on ABAQUS default algorithm. As can be seen from Figure 4.4 (b), the result from the explicit method agrees quite well with the 'exact value' while the deviation from the 'exact value' of the implicit method is quite significant. Although no further comprehensive comparisons are carried out, the explicit method seem to be more accurate based on the above comparison.

4.5.4 Comparison of built-in MCC and AZ-Cam clay model in *CIU* test

By choosing appropriate parameters, the AZ-Cam clay model will degenerate to the MCC model for NC clay. For the same soil parameters as in section 4.5.1, by choosing $\beta = 0.5$, $T = 0.9$, $\gamma = 6.0$ and $k = 0.0$, the comparison of the AZ-Cam clay model and the built-in MCC model for NC clay in *CIUC* test is shown in Figure 4.5. For heavily OC clay, the closed form undrained shear strength following isotropically consolidation can be deduced as will be presented in Chapter 5, which would be used to check the undrained shear strength of heavily OC clay from the implemented AZ-Cam clay model in ABAQUS. From Figure 4.5, the prediction of the implemented AZ-Cam clay model agrees well with the results from the built-in MCC model in ABAQUS for NC clay. The undrained shear strength of heavily OC clay (*OCR*=6) from the implemented AZ-Cam clay model agrees quite well with the theoretical value.

It is now reasonable to assert that the implementation of AZ-Cam clay model in ABAQUS through UMAT should be correct and further analysis could proceed.

4.6 Summary

In this chapter, the formulation of AZ-Cam clay model in the general stress space is presented. Key attention is paid on the outward direction of the bounding surface and plastic potential which are necessary to form the elasto-plastic matrix in three-dimensional space. The numerical implementation of the model in ABAQUS through UMAT is described subsequently and the stress point algorithms are addressed accordingly. The Pegasus method is used to find out the elastic portion of strain increment when the stress state goes from the elastic region into the elasto-plastic region. The Newton-Raphson method is employed to correct the drift problem. Finally, comparisons between the predictions of the ABAQUS built-in MCC model and the implemented UMAT MCC model are presented to verify the numerical scheme used in UMAT. The differences between the implicit method and the explicit method are compared. The verification of the implementation of the AZ-Cam clay model is achieved by the verification of the implemented UMAT MCC model and the comparisons of the predictions of the undrained shear strength of NC clay and heavily OC clay.

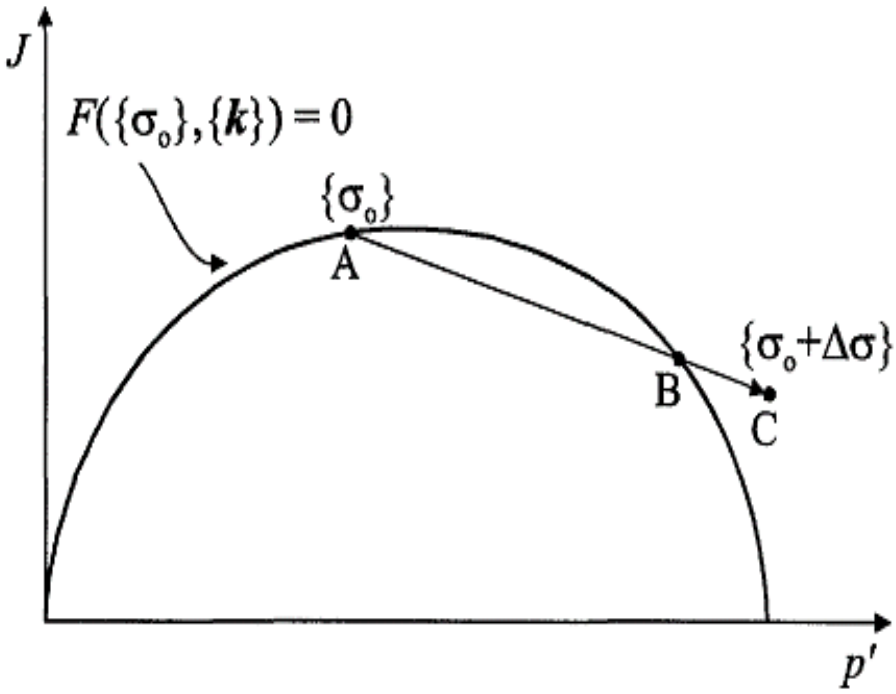

Figure 4.1 Unloading and loading transition (Potts and Zdravkovic 1999)

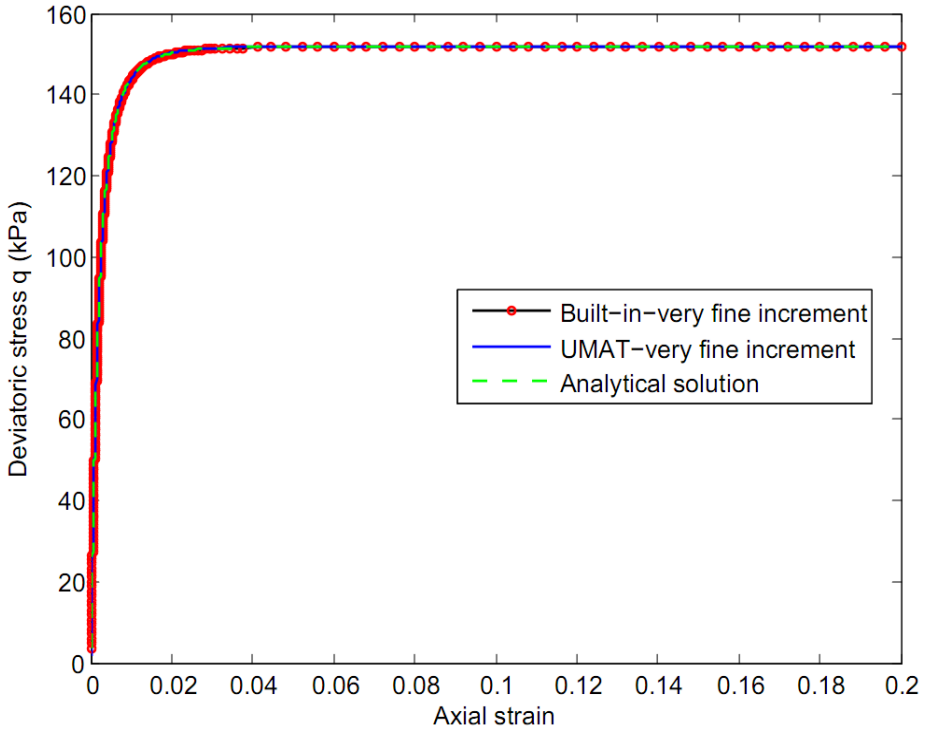

(a) Stress behavior-NC clay

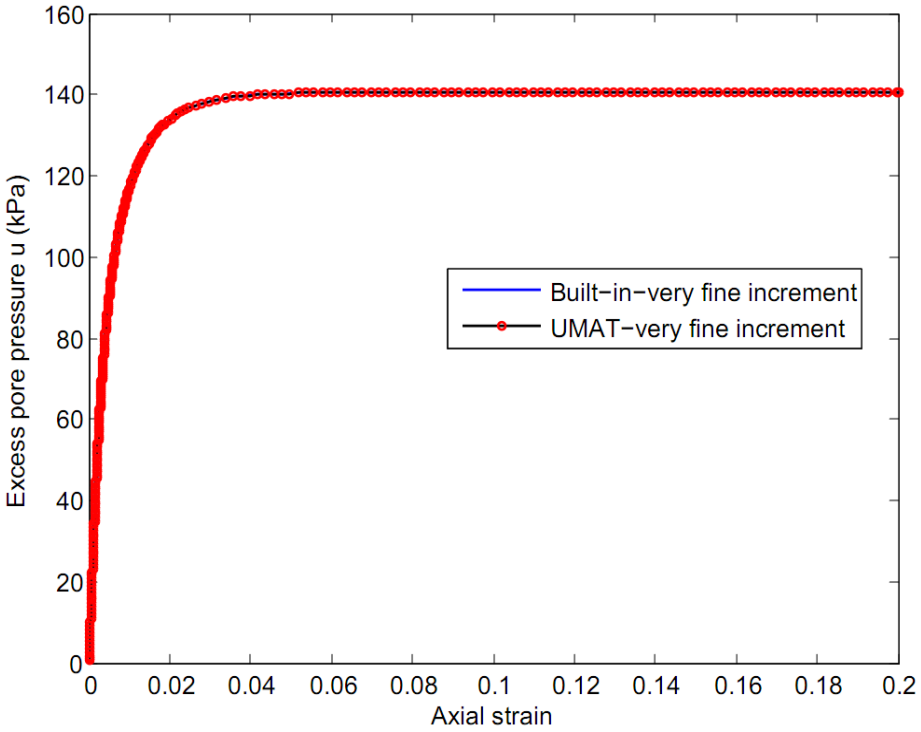

(b) Excess pore pressure behavior-NC clay

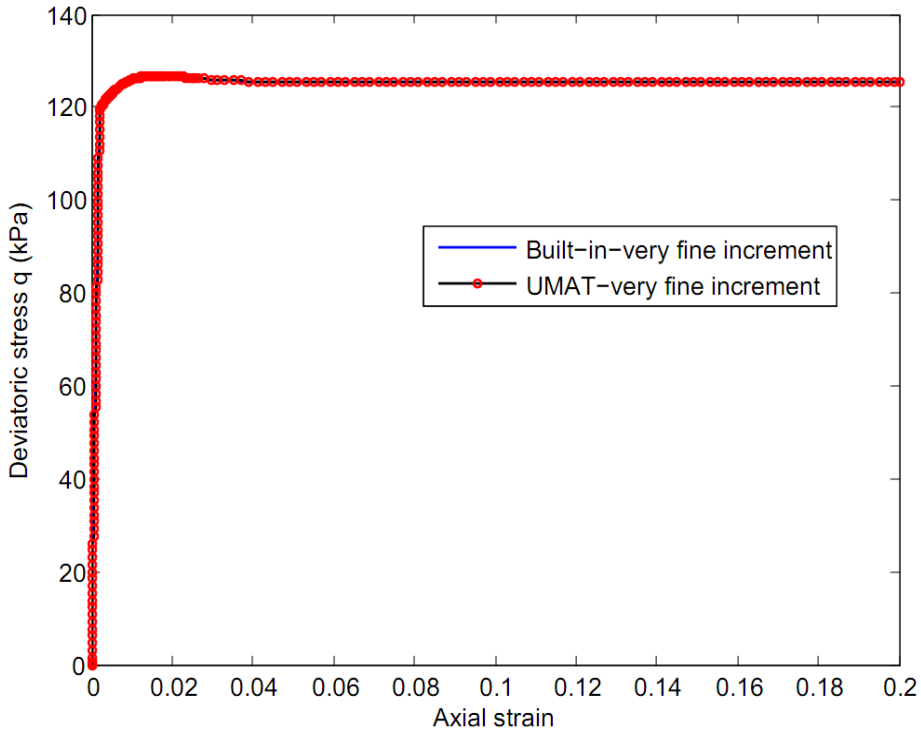

(c) Stress behavior-*OCR*=4

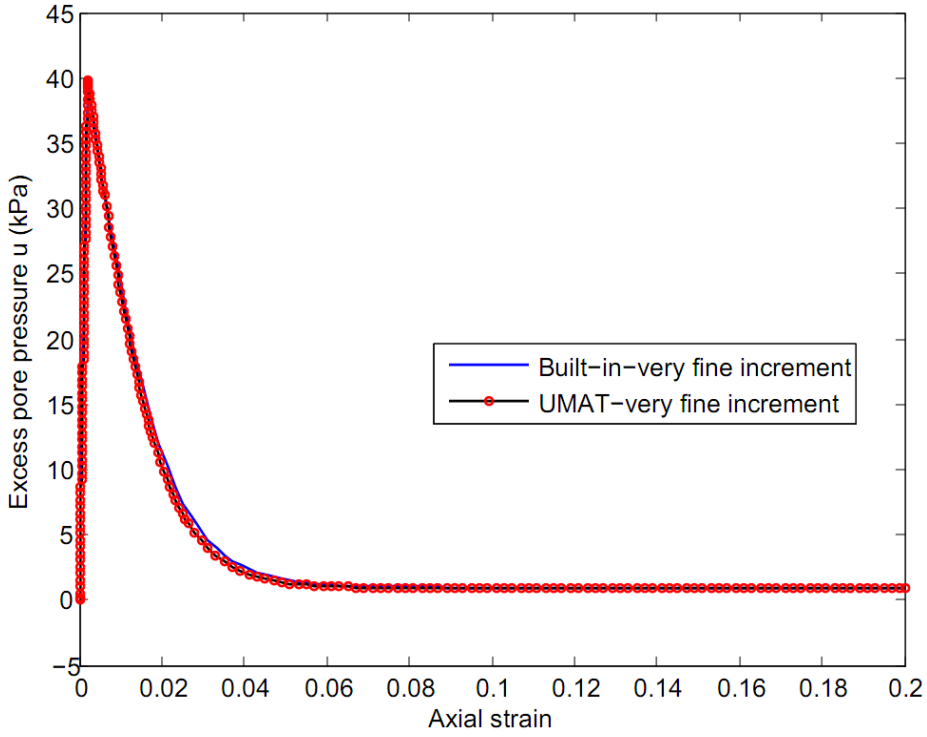

(d) Excess pore pressure behavior-*OCR*=4

Figure 4.2 Comparison of UMAT & built-in MCC model in ABAQUS-*CIU* test

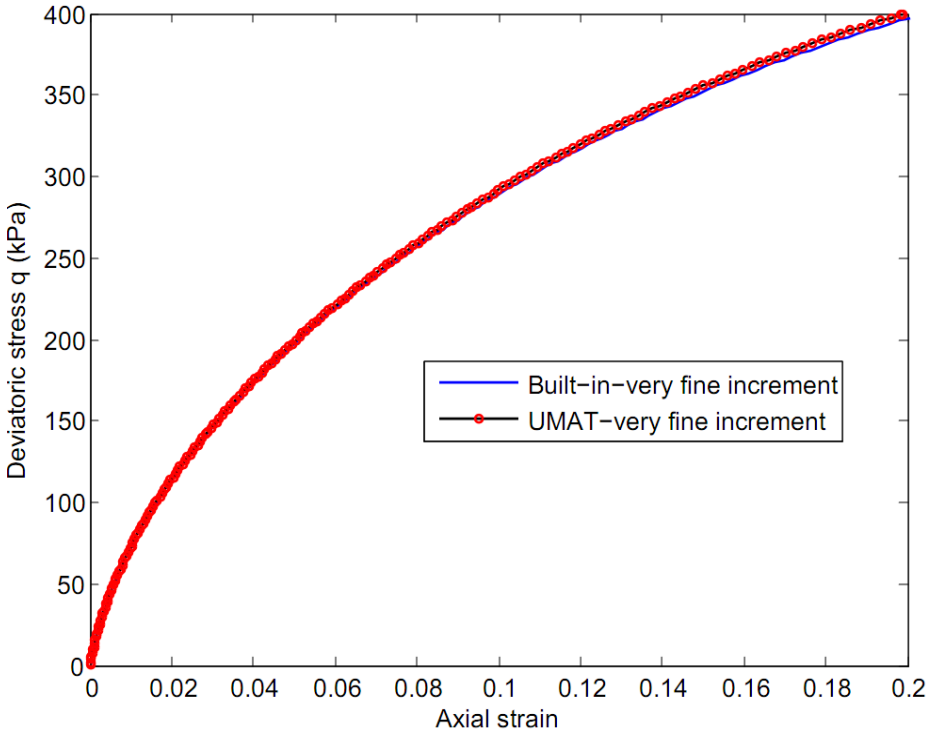

(a) Stress behavior-NC clay

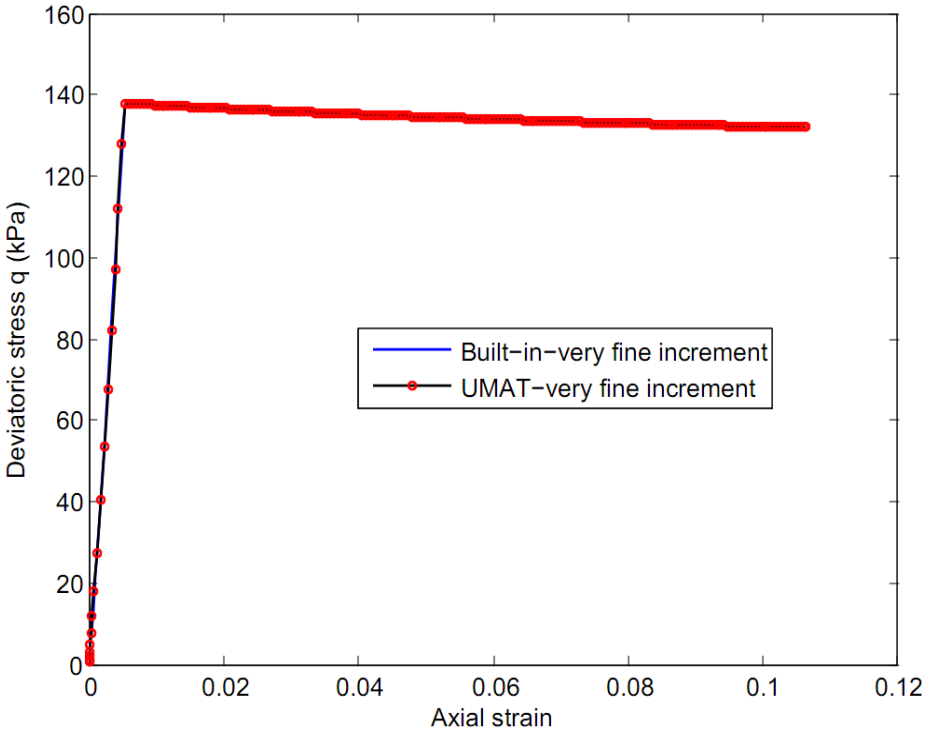

(b) Stress behavior-*OCR*=4

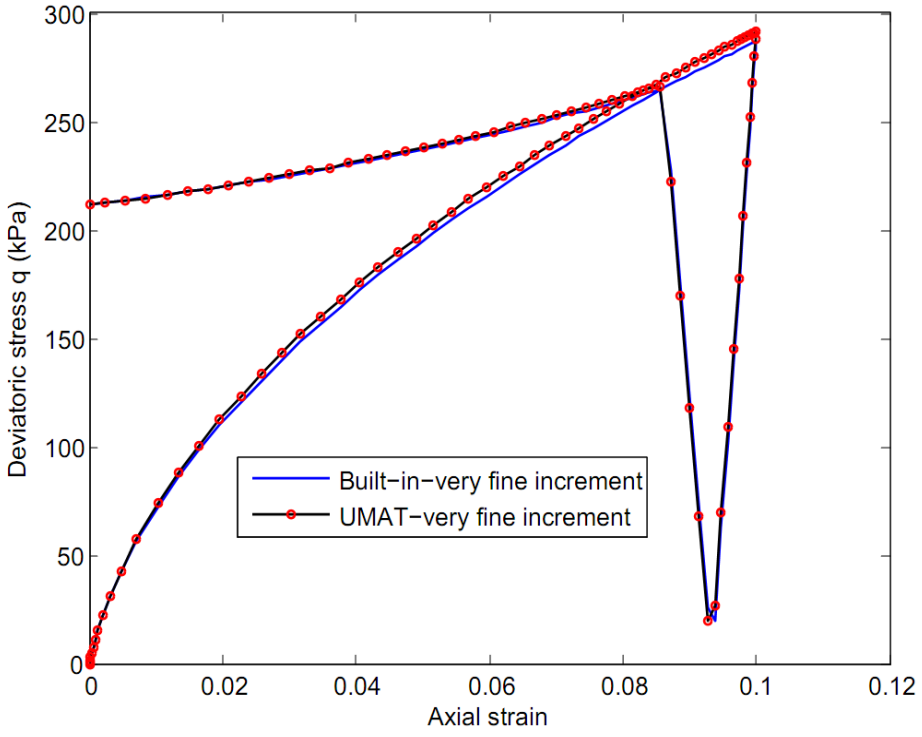

(c) Stress behavior with load cycles-NC clay

Figure 4.3 Comparison of UMAT & built-in MCC model in ABAQUS-*CID* test

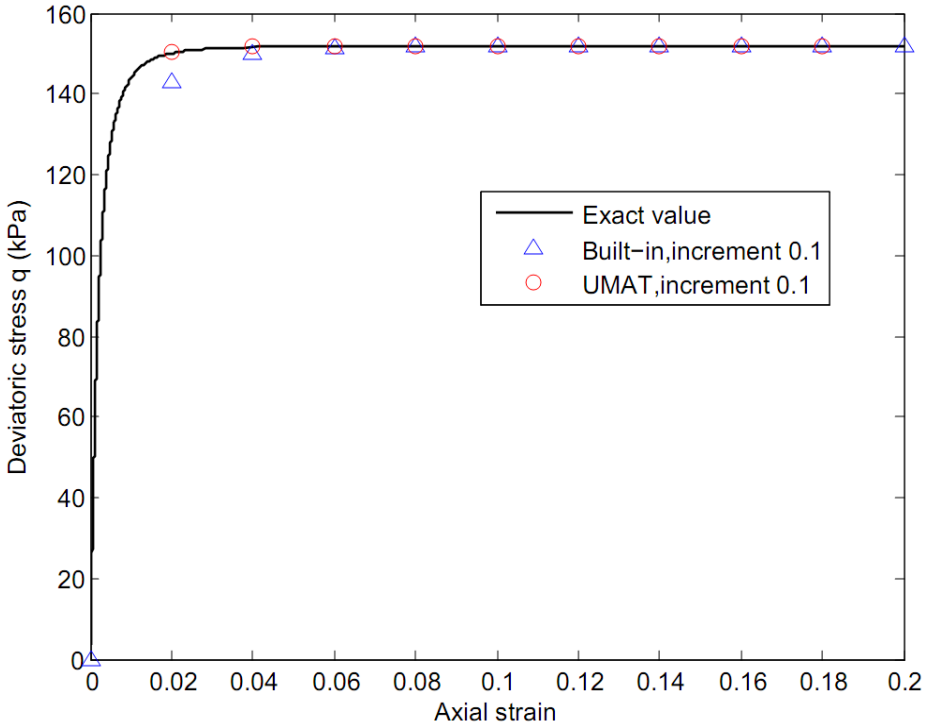

(a) Stress strain curve of NC clay-*CIU* test

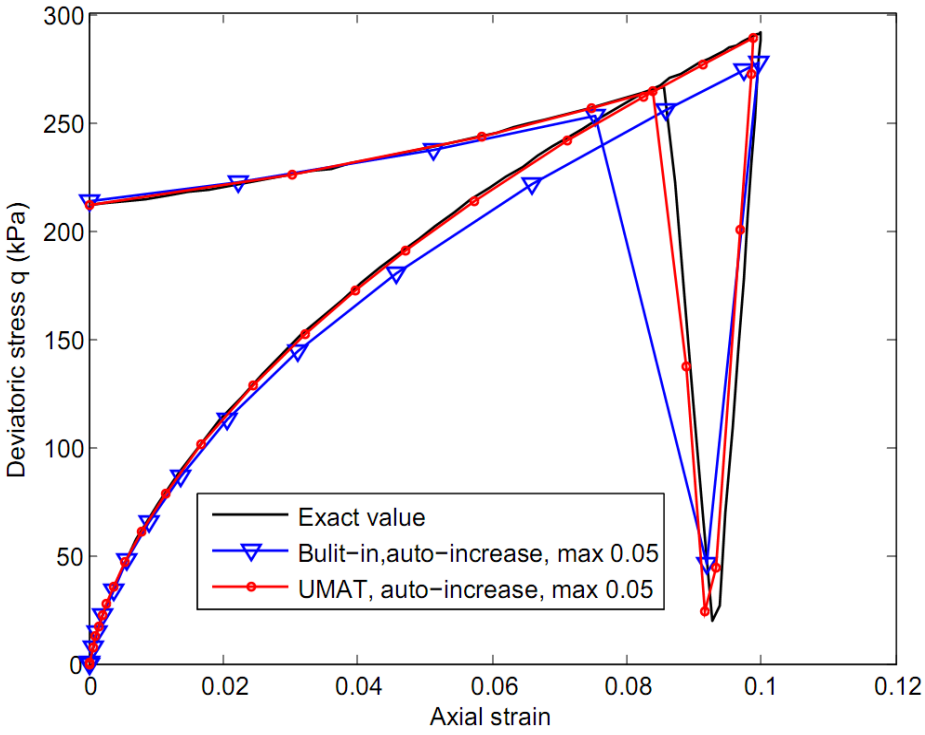

(b) Stress strain curve of NC clay-*CID* test

Figure 4.4 Comparison between explicit method and implicit method

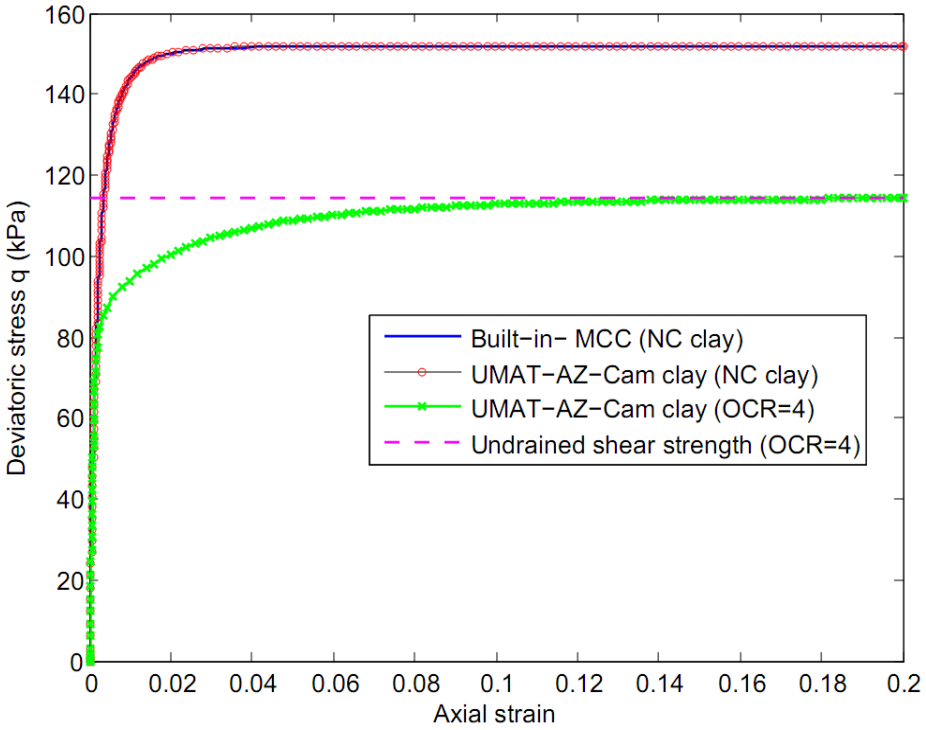

Figure 4.5 Verification of the implementation of AZ-Cam clay model

Chapter 5 **Material parameters determination and model evaluation**

5.1 Introduction

This chapter aims at providing the methods of determining the material parameters of the AZ-Cam clay model. The capability of the model in predicting the clay behavior in various laboratory tests both under monotonic loading and cyclic loading is also evaluated. The AZ-Cam clay model has ten material constants and additional specific information on the shear modulus of the soil (constant shear modulus, constant Poisson's ratio or the shear modulus at very small strain level). The effects of these material constants on the behavior of the model will firstly be discussed as well as the suggested methods to determine them. The model predictions in various laboratory tests under monotonic loading and cyclic loading will be presented subsequently. Measured data on the corresponding tests and other common model predictions will also be shown in order to demonstrate the ability and the limitations of the AZ-Cam clay model in predicting clay behavior under monotonic loading and cyclic loading. Table 5.1 gives the complete materials parameters of the model as well as a brief description of these parameters.

5.2 Material parameters determination

5.2.1 Critical state parameters

The critical state parameters N, λ, κ, M are the same as the basic critical state models, which can be determined from conventional laboratory tests (such as isotropic one-dimensional compression and extension tests, *CIU* test and *CID* tests).

5.2.2 Bounding surface parameters

R_w and R_d govern the size of the bounding surface on the wet side and on the dry side, respectively. Soil is conventionally assumed that it cannot sustain tensile mean effective stress. R_d is thus fixed at 2. R_w gives a general description of the bounding surface size. If R_w and R_d equal to 2, the bounding surface will be the same as the yield surface of the MCC model. The effect of R_w on the bounding surface in $p'-q$ space and on the CSL for NC clay in $v-\ln p'$ space is shown in Figure 5.1. The undrained shear strength of NC clays in *CIU* shearing can be deduced as follows. In undrained shearing, the total volumetric strain is zero and can be split into an elastic component and a plastic component as follows:

$$d\varepsilon_v^e + d\varepsilon_v^p = 0 \tag{5.1}$$

The elastic volumetric strain can be obtained with the help of bulk modulus as

$$d\varepsilon_v^e = \frac{\kappa}{v}\frac{dp'}{p'} \tag{5.2}$$

The plastic volumetric strain can be obtained from Equation 2.7 as

$$d\varepsilon_v^p = \frac{\lambda-\kappa}{v}\frac{dp_c'}{p_c'} \tag{5.3}$$

Combining Equation 5.1 with Equation 5.3 yields

$$\frac{\kappa}{v}\frac{dp'}{p'} = -\frac{\lambda-\kappa}{v}\frac{dp_c'}{p_c'} \tag{5.4}$$

Integrating the two sides of Equation 5.4 gives

$$\frac{\kappa}{v}\ln\left(\frac{p'}{p'_0}\right) = -\frac{\lambda-\kappa}{v}\ln\left(\frac{p'_c}{p'_{c0}}\right) \tag{5.5}$$

where p'_0 and p'_{c0} are initial mean effective stress and initial pre-consolidation pressure. For NC clay in *CIU* test, $p'_0 = p'_{c0}$.

Combining Equation 3.6 with Equation 5.5 gives the undrained shear strength as

$$S_u = \frac{M}{2}\left(\frac{2}{2+R_w}\right)^{1-\frac{\kappa}{\lambda}} p'_{c0} \tag{5.6}$$

Thus R_w can be evaluated from the *CIU* test as

$$R_w = 2^{\frac{\kappa}{\kappa-\lambda}}\left(\frac{S_{u-meas}}{Mp'_{c0}}\right)^{\frac{\lambda}{\kappa-\lambda}} - 2 \tag{5.7}$$

where S_{u-meas} is the measured undrained shear strength of NC clay in *CIU* test.

5.2.3 Ultimate strength parameter

The ultimate strength parameter T governs the critical state strength of clays subjected to continuous shearing. T is introduced following the assumption made previously that the ultimate position of heavily OC clay will generally lie to the left of the CSL in $v-\ln p'$ space but still on the CSL in $p'-q$ space. From Equation 3.26, it is obvious that the failure envelope is not fixed in stress space, but depends on p'_c (thus also on the plastic volumetric strain). The failure envelope will contract or expand with the bounding surface. For heavily OC clay, the critical state will be the interception of the curved failure envelope (C_T as shown in Figure 3.15) with the CSL, where plastic modulus is zero and no plastic volumetric strain will occur. Thus, the

relation between the critical state mean effective stress and the pre-consolidation pressure at the critical state of heavily OC clay can be obtained by combining Equation 3.6 and Equation 3.26 as

$$p'_{cr} = T\frac{2}{2+R_w}p'_c \qquad 5.8$$

In *CIU* test, Equation 5.1 to Equation 5.5 are still applicable. By combining Equation 5.8, the undrained shear strength of heavily OC clays under *CIU* tests is thus given by

$$S_u = \frac{M}{2}\left(\frac{2T}{2+R_w}\right)^{1-\frac{\kappa}{\lambda}} OCR^{-\frac{\kappa}{\lambda}} p'_{c0} \qquad 5.9$$

The undrained shear strength of heavily OC clays predicted by the MCC model under *CIU* tests is

$$S_u = M2^{\frac{\kappa-2\lambda}{\lambda}} OCR^{-\frac{\kappa}{\lambda}} p'_{c0} \qquad 5.10$$

T can thus be determined by combining the *CIU* test and the MCC model prediction as

$$T = \frac{2+R_w}{4}\left(\frac{S_{uoc-meas}}{S_{uoc-MCC}}\right)^{\frac{\lambda}{\lambda-\kappa}} \qquad 5.11$$

where $S_{uoc-meas}$ and $S_{uoc-MCC}$ are the measured and the MCC model predicted undrained shear strength of heavily OC clay in *CIU* test. The effect of *T* on the shape of failure envelope and typical effective stress path in undrained loading are shown Figures 5.2 and 5.3.

5.2.4 Peak strength parameter

Following the proposal of Atkinson (2007), the peak strength parameter β governs the shape of the failure envelope on the dry side and the relative distance of failure envelope to the bounding surface. Thus β has a great influence on the peak strength of heavily OC clays. This value can be determined through data regression following Atkinson (2007). As heavily OC clays will exhibit peak deviatoric stress before falling to the critical state under drained shearing, it is appropriate to evaluate β in drained loading tests. In *CID* test or in triaxial consolidated constant p' (*CICP*) tests, it is possible to determine β as follows:

$$\beta = \frac{M_p - M}{M \ln\left(\frac{2T\left(3-M_p\right)}{3\left(2+R_w\right)}\frac{p'_c}{p'_0}\right)}, \text{ in } CID \text{ tests} \qquad 5.12 \text{ (a)}$$

$$\beta = \frac{M_p - M}{M \ln\left(\frac{2T}{2+R_w}\frac{p'_c}{p'_0}\right)}, \text{ in } CICP \text{ tests} \qquad 5.12 \text{ (b)}$$

However, as p'_c is a state variable and depends on the plastic strains accumulated before the peak deviatoric stress is reached, it is thus not possible to determine this value from Equation 5.12. If the clay behavior before the peak deviatoric stress is purely elastic, p'_c will equal to p'_{c0}. Heavily OC clay will dilate during shearing. A first estimate of $p'_c = 0.9\,p'_{c0}$ could be used based on numerical parametric studies. A final value of β should be determined by matching the peak deviatoric stress from the stress-strain curves. The effect of β on the failure envelope and typical effective stress path in drained loading are shown in Figures 5.4 and 5.5.

5.2.5 Plastic modulus parameter

The plastic modulus parameter γ governs the evolution of the plastic modulus through a power law, which is similar to Zienkiewicz *et al.* (1985). It has significant effect on the plastic strain accumulated within the bounding surface and the change of stiffness within the bounding surface to the bounding surface. If γ becomes infinitely large, the behavior of clay within the bounding surface will be purely elastic. As long as γ remains a finite value, plastic strains may occur within the bounding surface during loading. For stress state lying on the bounding surface, the AZ-Cam clay model degenerates to the conventional elasto-plastic model. It is thus impossible to determine γ from NC clay. For heavily OC clays, as the stress state is in the deep interior of the bounding surface, the initial effective stress path in the undrained loading will almost be vertical in $p'-q$ space. The magnitude of γ has a relatively insignificant effect on the effective stress path. Besides, the undrained shearing strength of heavily OC clay is independent of γ as shown in Equation 5.9. It is thus appropriate to determine γ by matching the effect stress path or undrained shear strength S_u in *CIU* test on lightly OC clays. A typical effect of γ on undrained shear strength of lightly OC clay in the tests of Wroth & Loudon (1967) is shown in Figure 5.6. If γ is infinite large, the mean effective pressure at the critical state p'_{cr} can be normalized as

$$\frac{p'_{cr}}{p'_e} = \frac{\lambda-\kappa}{\lambda}\ln\left(\frac{2+R_w}{2}\right) \qquad 5.13$$

The undrained strength can thus be normalized as

$$\frac{S_u}{p'_e} = \frac{M}{2}\frac{\lambda-\kappa}{\lambda}\ln\left(\frac{2+R_w}{2}\right) \qquad 5.14$$

The normalized undrained shear strength from Equation 5.14 forms an upper bound of the undrained shear strength of lightly OC clay.

5.2.6 Shakedown parameter

For cohesive soils, shakedown status can be reached for very small cyclic load levels where the plastic strains reach zero after a certain number of loading cycles and the behavior becomes purely elastic as discussed in section 3.4.8. The proposed expression for plastic modulus (Equation 3.59) relates the shakedown behavior to the absolute value of plastic volumetric strains accumulated in the previous loading, thus qualitatively addressing the shakedown effect. Generally, the above method is applicable only for NC and lightly OC clays. For heavily OC clay, the stress state is in the deep interior of the bounding surface. Thus the predicted behavior by the AZ-Cam clay model would be nearly elastic (linear or non-linear) for small load levels. This may form a limitation of Equation 3.59 and further research may be necessary. The shakedown parameter k_s can be determined by parametric study simulating the stress-strain curve or plastic strain accumulation rate in stress-controlled cyclic tests. The effect of k_s on the accumulated plastic deviatoric strains (normalized with the plastic deviatoric strain occurred in the first cycle) is shown in Figure 5.7. The cyclic load level is indicated by $\frac{q}{q_f}$. Model inputs for this parametric study are based on the test by Li and Hum (2002) as will be presented below.

5.2.7 Elastic shear modulus

As the bulk modulus has been specified following the basic critical state models, generally, a constant Poisson's ratio can be designated to evaluate the elastic shear modulus. Typical value of effective Poisson's ratio for clay ranges between $0.2 \sim 0.3$.

An alternative is to use a constant value of secant shear modulus. As the secant shear modulus varies with strains, thus for a typical problem, the possible strains range should be predicted reasonably before specifying the value of secant shear modulus. Wroth (1971) advocated using a constant value of shear modulus which can be determined as

$$\left(\frac{G}{p'}\right)_{oc} = \left(\frac{G}{p'}\right)_{nc} \left(1 + C \ln OCR\right) \qquad 5.15$$

where the subscript oc and nc denote OC clay and NC clay. C is a model parameter.

To incorporate the small strain shear modulus, $G_{\max}$ can be measured in the laboratory using resonant column test or in the field by cross-hole or down-hole techniques (Wood, 1978; Whittle, 1987). However, it is rather difficult to determine the decreasing rate of the shear modulus, which is expressed in Equation 3.62. Furthermore, Equation 3.62 is proposed based on mathematical convenience and the physical S-shape trend of decreasing rate of the shear modulus. It is thus empirical in nature. The decreasing parameter ω_r can be determined only through parametric study. The degradation of secant shear modulus $G_{\sec}$ with shear strain calculated from Equation 3.62 in *CIU* tests (no plastic strains) is shown in Figure 5.8. Similar prediction by Pestana & Whittle (1999) is also shown for comparison.

5.3 Model evaluation

5.3.1 New position of the CSL

The deviation of the new CSL proposed in the present model from the original CSL is captured by the vertical distance d in $v-\ln p'$ space following Equation 3.10 as

$$d=(\kappa-\lambda)\ln T \tag{5.16}$$

For heavily OC clays, the critical state will always lie on this new CSL. This assumption simplifies the assumption made by Crouch & Wolf (1994) that the CSL beyond a certain void ratio would be different from the original CSL with a different slope in $v-\ln p'$ space. However, the failure envelope is only applicable to heavily OC clays. For NC clays, the CSL does not change. For lightly OC clays, the CSL would lie in between them, and depends on the initial pre-consolidation pressure and the value of γ. This idealized CSL is reasonable when comparing to the experimental findings of Henkel (1959). A schematic representation of the critical state is shown in Figure 5.9 and Figure 5.10.

5.3.2 Monotonic loading

For monotonic loading, the shakedown parameter should have no effect on the predicted behavior. Thus $k_s = 0.0$ is assumed for all the predictions on the monotonic behavior.

5.3.2.1 CIU tests by Wroth & Loudon (1967)

Wroth & Loudon (1967) presented the effective stress path in $p'-q$ space of kaolin clay with a wide range of *OCRs* in *CIU* tests. Figure 5.11 show the predicted

stress path of the MCC model, the model proposed by Zienkiewicz *et al.* (1985) and the AZ-Cam clay model. It is noted that there seem to be some inconsistencies with the test data and documented information on the three tests at *OCR* equal to 2.2, 4.0 and 8.1 in the original paper (Wroth and Loudon, 1967). Simple calculations from the starting intersection point of the effective stress path with p' axis leads to *OCRs* for these tests of 1.8, 3.0 and 6.5. So the calculated *OCRs* are used in the model prediction. For the material constants, R_w is determined from S_u of NC clay. γ is determined by matching the effective stress path at *OCR*=1.2. T is evaluated from S_u at *OCR*=6.5. Without information on drained shearing, β is evaluated by matching the effective stress path at *OCR*=6.5. Associated flow rule is used in the simulation. Without doubt, the MCC model predicts the vertical stress path within the bounding surface, resulting in larger strength predicted than the tests data for all *OCRs*. Zienkiewicz *et al.* (1985)'s model (using the MCC yield surface) predicts a curved stress path, which matches quite well with the tests data but slightly over predicts the undrained shear strength of lightly OC clays. For heavily OC clays, as the CSL was used as the failure envelope, the model under predicts the strength of heavily OC clays. The predictions of the AZ-Cam clay model agree quite well for NC to lightly OC clays. However, for heavily OC clays, although the ultimate strength agrees reasonably with the test data, there is some deviation on the dry side. The input parameters for the AZ-Cam clay model are summarized in Table 5.2.

5.3.2.2 CIU tests by Banerjee and Stipho (1978, 1979)

Banerjee & Stipho (1978, 1979) published extensive *CIU* tests results on NC to heavily OC kaolin clay. Commonly known model predictions of these tests as well as the predictions by the AZ-Cam clay model are shown in Figure 5.12 and Figure 5.13

for NC to lightly OC clays. Figure 5.14 and Figure 5.15 are shown for heavily OC clays. For the AZ-Cam clay model, the *CIUC* test on NC clay is used to determine R_w and γ is evaluated by matching the effective stress path of lightly OC clay at *OCR*=1.2. The *CIUC* test at *OCR*=12 is used to evaluate T and β. Associated flow rule is used in the simulation. Other parameters are directly obtained from the original paper as summarized in Table 5.3. It should be pointed out the parameter N is not provided in Banerjee and Stipho (1978, 1979). Instead, the initial specific volume v_0 was related to the water content w. Parameter N and initial specific volume v_0 can be inter-related.

Within expectation, the MCC model over predicts the undrained shear strength for all the cases. Both Zienkiewicz *et al.* (1985)'s model and the AZ-Cam clay model predict quite well for NC clays and lightly OC clays in the *CIUC* test but under predict the undrained shear strength in extension. For heavily OC clays, Banerjee and Stipho (1979) proposed to use the Hvorslev line as a yield surface combining with a non-associated flow rule and achieved relatively good prediction as shown in Figure 5.14 (b) and Figure 5.15 (b). However, as the method is still within the conventional elasto-plastic framework, the stiffness they predicted changes abruptly during the transition from the elastic to plastic region. The predictions of the AZ-Cam clay model for heavily OC clays are acceptable, although the prediction on excess pore water pressure in *CIU* extension (*CIUE*) is not quite satisfactory.

5.3.2.3 CIU tests by Kuntsche (1982)

A series of *CIU* tests were reported by Kuntsche (1982), which provided a basis for the assessment of soil constitutive models. This section presents the monotonic simulation of these tests using the proposed model. The value T is estimated from the undrained shear strength of *CIU* test at *OCR*=10, γ is estimated by best fitting the

undrained effective stress path of *CIU* test at *OCR*=2 and β is obtained by fitting the stress-strain curve of the sample at *OCR*=10. The rest of the material parameters for the AZ-Cam clay model are from the original paper (Kuntsche, 1982). Associated flow rule is used in the simulation. The input parameters are summarized in Table 5.4.

Figure 5.16 and Figure 5.17 show the predictions from the current model and the model after Zienkiewicz *et al.* (1985) together with the test data. Generally, the model prediction is satisfactory both in the effective stress path and stress-strain behavior. Although the model captures the undrained shear strength very well at all *OCRs*, there are some deviations in the predicted stress path with the test data. The predicted stress-strain behavior is satisfactory, but the stiffness at *OCR*=10 is over predicted. As expected, the model after Zienkiewicz *et al.* (1985) under predicts the undrained shear strength at *OCR*=10.

5.3.2.4 CIU tests by Li & Meissner (2002)

Figure 5.18 and Figure 5.19 show the predictions of the two-surface model developed by Li & Meissner (2002) and the AZ-Cam clay model on *CIU* tests of a commercially available clay after Li and Hun (2002). γ and β is determined by matching the effect stress path at *OCR*=1.6 and *OCR*=4, respectively. T is determined from the undrained shear strength at *OCR*=4. Associated flow rule is used in the simulation. The rest of the parameters are obtained from the original paper. The input parameters for AZ-Cam clay model is summarized in Table 5.5. Good agreements with the tests data have been achieved by the two-surface model and the AZ-Cam clay model. However, the AZ-Cam clay model over predicts the shear stiffness for NC and lightly OC clay.

5.3.2.5 CICP tests by Nakai & Hinokio (2004)

Nakai & Hinokio (2004) presented the comparisons of *CICP* tests results on Fujinomori clay and the prediction of t_{ij} model (Nakai & Matsuoka, 1986; Nakai, 1989) as shown in Figure 5.20 and Figure 5.21. The AZ-Cam clay model is employed to simulate these test results with associated flow rule. Test data at *OCR*=8 are used to evaluate T and β (T is chosen at a typical value of 0.7 due to the lack of undrained shearing data). The other parameters are obtained from the original paper as summarized in Table 5.6. It should be noted that N in Table 5.6 is the specific volume at the reference pressure ($98kPa$) in $v-\ln p'$ space, which is slightly different from the basic critical state model after Nakai (2004, 2011). The predictions of the MCC model are also shown in these figures for comparison. Within expectation, the MCC model's prediction agrees well with tests data for NC clays. However, for lightly to heavily OC clays, the MCC model over predicts the peak stress ratio, and this trend increases with increasing *OCRs*. The predictions of t_{ij} model agree satisfactorily for NC and lightly OC clays, but for heavily OC clays, some discrepancies occur, especially for the extension case. The predictions of the AZ-Cam clay model agrees quite well with the test data both for compression and extension case, although some departures exist in the prediction on the volumetric strains.

5.3.2.6 Tests on Boston blue clay (BBC)

The physical and engineering properties of BBC have been extensively studied at MIT in the past several decades (Bailey, 1961; Bensari, 1984; Fayad, 1986; Abdulhadi, 2009). The test data on BBC in this study are obtained from the literature (Fayad, 1986; Whittle, 1987; Whittle, 1993; Pestana *et al.*, 2002). R_w is estimated from *CIU* test at *OCR*=1 (these data are original from Braathen (1966), as this document is not

published, the data are obtained from Pestana *et al.* (2002). γ is determined by best fitting the effective stress path of lightly OC clay in *CIU* tests. The initial value of lateral stress coefficient for NC clay K_{0NC} is taken as 0.53. For OC clay, K_0 is given as $K_0 = 0.48OCR^{0.4}$ following Fayad (1986) and Whittle (1993). T can be determined from *CIU* test or K_0 consolidated undrained compression/extension (CK_0UC / CK_0UE) test. However, the values determined from different tests are largely different, which implicitly challenges the assumptions of the model. CK_0UC test at *OCR*=8 is thus used as the reference test resulting in $T = 0.763$ for triaxial compression. In order to simulate plane strain condition, the variation of T in the deviatoric stress plane should be defined. As relatively large scatter exists in the extension tests, which may due to the difficulties encountered in large strains (Pestana *et al.*, 2002), a lower bound S_u in CK_0UE test at *OCR*=4 is employed to determine *T*, resulting in $T = 0.4$ for triaxial extension. The variation of *T* in the deviatoric plane is taken as the form proposed by Vaneekelen (1980) for yield surface in the deviatoric plane as shown below

$$T = \frac{0.456}{\left[1 - 0.924\sin\left(3\theta\right)\right]^{0.2}} \qquad 5.17$$

$\beta = 0.8$ is used to fit the overall stress-strain behaviour for CK_0UC test at *OCR*=8 as no drained tests are available. Without further information, β is assumed to be constant in the deviatoric plane.

Mohr Coulomb criterion with smooth corner is used to specify the variation of M in the deviatoric plane as

$$\frac{M(\theta)}{\sqrt{3}} = \frac{0.608}{\left[1+0.629\sin(3\theta)\right]^{0.25}} \qquad 5.18$$

The magnitude of intermediate principle stress at critical state under plane strain condition is described by the value b_f (defined as $\frac{\sigma'_{2f}-\sigma'_{3f}}{\sigma'_{1f}-\sigma'_{3f}}$, where the subscript f indicates that the stress is at the failure status). Although large scatter exist in the measured b_f (Whittle, 1993), a value of 0.37 will be used as reported by Randolph & Wroth (1981) resulting in the Lode's angle $\theta = -8.5^0$ at the critical state. Following Equation 4.7, the plastic potential in the deviatoric plane is expressed as

$$\frac{M(\theta)}{\sqrt{3}} = \frac{X_p}{\left[1+0.248\sin(3\theta)\right]^{0.2}} \qquad 5.19$$

$G_{\max}$ is determined by matching the shear modulus at small strain in CK_0UC at $OCR = 8$ as follows:

$$\frac{G_{\max}}{p'_r} = 460\frac{p'}{p'_r}OCR^{0.3} \qquad 5.20$$

The decreasing rate parameter ω_r is determined from a parametric study, resulting in $\omega_r = 2$ as shown in Figure 5.22. The model input parameters for BBC are summarized in Table 5.7.

Figure 5.23 shows the comparison of the AZ-Cam clay model prediction and the *CIU* test results after Braathen (1966) (stress strain relation for *OCR*=2 is not available due to technical problem), where σ'_h is and horizontal effective stress respectively. For *OCR*=1, the test data shown slight softening behavior before reaching the critical state,

which cannot be predicted by the AZ-Cam clay model for NC clay. For *OCR*=4 and *OCR*=8, the predicted effective stress path agrees quite well with the test data at the initial stage of loading but slightly over predicts the peak stress ratio. Excellent agreement is obtained in stress-strain relation up to an axial strain of 2% at *OCR*=4 and 4% at *OCR*=8, after which the shear stress almost remains constant in the model prediction. Thus the model under predicts the undrained shear strength by around 15% both for *OCR*=4 and *OCR*=8. For comparison, Figure 5.24 shows the prediction on the same test by the MIT-S1 model after Pestana *et al.* (2002).

Figure 5.25 shows the comparison of the AZ-Cam clay model prediction and the CK_0UC test data. BBC exhibits obvious anisotropic behavior following K_0 consolidation. As the AZ-Cam clay model is constructed based on the isotropic behavior of clay, thus for CK_0UC at *OCR*=1 and *OCR*=2, the model is unable to predict the softening behavior and large deviation exists between the predicted effective stress and test data. At *OCR*=4, the predicted undrained shear strength agrees very well with the test data and the agreement in the stress-strain relation is satisfactory, both for CK_0UC and CK_0UE tests. As *OCR*=8 is a reference case used to evaluate the model parameters, excellent agreement is achieved at relatively large axial strain and the predicted undrained shear strength expectedly coincides with the test data. However, the model over predicts the peak stress ratio and over predicts the stiffness in axial strain range of $0.2 \sim 1\%$. Based on the parametric study, it is beyond the ability of the AZ-Cam clay model to match the stiffness in this range of strain. For comparison, Figure 5.26 shows the prediction on the same test by the MIT-S1 model after Pestana *et al.* (2002).

It is of great importance to conduct comparison of predictions with measured data for modes of shearing other than triaxial, which provides as an assessment of the predictive capabilities and limitations of the proposed model. The AZ-Cam clay model is thus employed to simulate the K_0 consolidated undrained direct simple shear (CK_0UDSS) tests on BBC. The test procedures have been extensively documented (Whittle, 1987). The key feature is that the sample is confined laterally by a wire-reinforced membrane to prevent lateral straining and undrained shearing is simulated by conducting constant volume (height) tests such that the total vertical stress is equal to the vertical effective stress. Figure 5.27 shows comparison of model predictions and measured effective stress paths (τ and σ_v' is the shear stress and vertical stress acting on horizontal planes in the sample) and the shear stress–strain behavior. Large discrepancies exist both in effective stress paths and initial stiffness in model predictions and test data at all *OCRs*. The model significantly overestimates the undrained shear strength by 40% at *OCR*=1 and 15% at *OCR*=2. However, the agreements at *OCR*=4 and *OCR*=8 are quite satisfactory. For *OCR* larger than 2, the measured data show negative pore pressure up to peak shear stress and softening occurs subsequently. However, as a small value (0.4) is assigned to T to reflect the undrained shear strength at the failure Lode's angle at 30^0 (e.g. triaxial extension), the dilation behavior only occurs at *OCR*=8 and no softening occurs at all *OCRs* in model predictions. The possible reasons for the relatively unsatisfactory model prediction may result from the isotropic assumption. Resedimented BBC shows highly anisotropic behavior (Fayad, 1986; Whittle, 1987). For comparison, Figure 5.28 and Figure 5.29 shows the prediction on the same test by MIT-E3 model after Whittle (1993) and MIT-S1 model after Pestana *et al.* (2002).

Figure 5.30 summarizes the AZ-Cam clay model predictions of normalized undrained shear strength S_u/σ'_{vc} (σ'_{vc} is the vertical effective stress at the beginning of shearing) in *CIUC*, CK_0UC, CK_0UE and CK_0UDSS tests with *OCR*. Generally, the model predictions agree quite well with the measured data. Due to the relatively larger uncertainties associated with the measured data in CK_0UE test, the model significantly underestimates the undrained shear strength at *OCR*=8. Besides, the model over predicts the undrained shear strength in CK_0UDSS for NC and lightly OC clay. This may due to the fact that anisotropy is most pronounced in NC and lightly OC BBC (Pestana *et al.*, 2002). For comparison, Figure 5.31 shows the prediction on the same test by MIT-E3 model after Whittle (1993) and MIT-S1 model after Pestana *et al.* (2002).

5.3.2.7 Shear strength of various types of heavily OC clays

In *CIUC/E* and triaxial isotropic consolidated plane strain (*CIUP*) shearing, S_u in the proposed model can be normalized as

$$\left[\frac{\left(S_u/p'_0\right)_{oc}}{\left(S_u/p'_0\right)_{nc}}\right]^{1/\Lambda_p} = T(\theta)\cdot OCR \qquad 5.21$$

where Λ_p is the plastic volumetric strain ratio and equals to $1-\frac{\kappa}{\lambda}$.

Equation 5.21 gives a general description of the S_u character of heavily OC clays. For the MCC model, $T(\theta)$ equals to 1, independent of shearing modes. As *T* is only applicable for heavily OC clays, the model prediction begins at *OCR*=3 both in Figure 5.32 and Figure 5.33, below which it is assumed to vary linearly between *OCR* of 1 and 3. In Figure 5.32, almost all the test data lie below the line predicted by the MCC

model. The introduction of the parameter T can generally capture the variation of $\left[\left(S_u/p_0'\right)_{oc}/\left(S_u/p_0'\right)_{nc}\right]^{1/\Lambda_p}$ with *OCRs*. Good agreement with the test data is achieved for kaolin clay and Todi clay using T=0.9 and T=0.5, respectively. For Vallericca clay and Corinth marl, good agreement is achieved using T=0.65, but under predicts for Corinth marl at small *OCRs* and over predicts at large *OCRs* of Vallericca clay.

Figure 5.33 shows the comparison of the predicted $\left(\tau_{\max}/\sigma_{v0}'\right)_{oc}/\left(\tau_{\max}/\sigma_{v0}'\right)_{nc}$ in CK_0UDSS test with the test data. The bounding surface is chosen the same as the yield surface of the MCC model with $M=1$ which has little effect on the prediction of the normalized value. $K_{nc}=0.5$ and $K_{oc}=K_{nc}OCR^{0.4}$, which are typical from the test data reported by Ladd *et al.* (1977) is adopted in the current study. $\Lambda_p=0.8$ is used following Wroth (1984). The predicted variation with T=0.8 falls close to the range of 7 types of clays after Ladd *et al.* (1977). However at large *OCRs*, the model tends to over predict the value. Thus T not only depends on the Lode's angle as has been proposed but also seems to be dependent on the stress history which is neglected in the present study.

The predicted variation of M_p/M in *CIDC* test is shown in Figure 5.34 based on the materials constants of Pietrafitta clay after Burland *et al.* (1996) and Mita *et al.* (2004) with T=0.65 based the regression in Figure 21. Good agreement is achieved for Pietrafitta clay with $\beta=0.35$ but slightly over predicts at relatively small *OCRs*. It is inappropriate to conduct a direct comparison of other types of clays as the material constants would be different, but the model does capture the variation trend that M_p/M increases with *OCRs*. At large *OCRs*, the variation becomes linear when *OCR* is plotted in logarithmic scale. Similar behavior can be found in the test data on Todi

clay and Corinth marl. However, it is difficult to reach the same conclusion for Weald clay as relatively large scatter exists.

Figure 5.35 shows the test data and the proposal of Atkinson (2007) following Equation 3.2, together with current proposal following Equation 3.9. There is no information about the value of S_u of the tested clays. T=0.8 is chosen to address the effect of T on the peak strength of OC clay. An average vertical intercept of -0.15 is used based on the χ value reported by Atkinson (2007). As can be seen, by introducing T, β may be changed to best fit the test data. Thus it is recommended to first determine T from S_u of heavily OC clays and then fit the data to get β rather than fixing the vertical intercept (0 in Figure 5.35) in advance based on the original assumption of the MCC model during data regression, although the proposal of Atkinson (2007) agrees quite satisfactorily with the test data.

5.3.2.8 Summary on monotonic loading

From the above comparison, the AZ-Cam clay model is able to simulate the isotropic behavior of clay in various modes of shearing. With the help of the failure surface incorporated in the model formulation, the model works well for evaluating the peak strength of heavily OC clay in drained shearing and the undrained shear strength in undrained shearing. However, the model does have limitations inherently on simulating the anisotropic behavior of clay as demonstrated by NC to lightly OC BBC. Further improvement of the model may be achieved by focusing on the anisotropic behavior of clay.

5.3.3 Cyclic loading

5.3.3.1 Cyclic loading excluding the small strain stiffness

5.3.3.1.1 Cyclic CIU test by Wroth & Loudon (1967)

Stress-control cyclic triaxial *CIU* tests with varied cyclic loading level on NC kaolin clay were presented by Wroth & Loudon (1967). The AZ-Cam clay model is employed to simulate this test using the same input parameters as those in Table 5.2. The shakedown parameter k_s is assumed to be zero as only five cycles will be simulated. Figure 5.36 plots the model simulation and the test result data of effective stress path in $p'-q$ space. As can be seen, quite satisfactory agreement is obtained within the first three cycles. However, relatively larger deviation exists in fourth and fifth cycles. As purely elastic behavior in the unloading process is assumed in the model formulation, the model is unable to predict the plastic behavior when unloading occurs. However, the plastic strain occurred in the unloading process in fifth cycle is obvious in the test.

5.3.3.1.2 Cyclic CIU test by Kuntsche (1982)

Two-way strain-control cyclic *CIU* tests with constant cyclic amplitude on NC kaolin clay were reported by Kuntsche (1982). This section presents the cyclic simulation of the AZ-Cam clay model using the same material parameters as those in section 5.3.2.3. $k_s = 0$ is used to match the decreasing rate of mean effective stress. However, the use of elastic shear modulus is crucial for the model prediction. The adoption of shear modulus has a significant effect on the shape of the stress-strain curves in the cyclic loading. Figure 5.37 and Figure 5.38 show the predicted and measured stress-strain curves (the shear stress τ_{oct} equals to $\frac{\sqrt{2}}{3}q$) and mean effective

stress by using: (a) a constant $G = 8000kPa$ (ν' varies); (b) a constant $\nu' = 0.15$ (G linearly depends on p'); and (c) a constant $\nu' = 0.10$ (G linearly depends on p').

As can be seen from Figure 5.37 (a), the measured stress-strain curves exhibit a larger stiffness when unloading occurs, then gradually decreases with further shearing. However, the predicted stiffness remains the same when unloading occurs, and the shape of the stress-strain curve in all three cases (Figures 5.37 (b) to (d)) differs significantly from the measured shape. Besides, the predicted shape is sensitive to the Poisson's ratio as can be seen from Figures 5.37 (c) and (d). This case demonstrates the complexity of shear modulus in the cyclic loading and the simple formula (a constant G or a constant ν') may not work satisfactorily. Although the model fails to capture the shape of the stress-strain curves, the degradation of shear stress is modeled quite well. Figure 5.38 further strengthen this conclusion through the predicted mean effective stress, which is insensitive to the shear modulus. The predicted value is quite close to the measured data.

5.3.3.1.3 Cyclic CIU test by Li & Meissner (2002)

Stress-control cyclic *CIU* tests with constant cyclic load level on NC clay were summarized by Li & Meissner (2002). Using the same material constants as those in section 5.3.2.4 and $k_s = 30$ is used by matching the stress-strain curves. Figures 5.39 to 5.41 show the model predicted stress-strain loop, excess pore water pressure, the corresponding measured data and the predicted value by Li and Hum (2002). As can be seen from these figures, the AZ-Cam clay model is able to capture the salient feature of stress-strain behavior in the cyclic loading. However, the excess pore water pressure is over predicted, although the variation trend is captured well.

5.3.3.1.4 Cyclic triaxial test by Nakai & Hinokio (2004)

Using the same material parameters as those in section 5.3.2.5 and $k_s = 0$ (as only 3 cycles are simulated), the predictions of the AZ-Cam clay model in cyclic triaxial tests on NC Fujinomori clay are shown in Figures 5.42 to 5.44. Figure 5.42 presents the model predictions of stress-control cyclic *CICP* test with constant cyclic load level as well as the predictions by Nakai & Hinokio (2004) using t_{ij} model and measured data. Simulation on stress-control cyclic *CICP* test with varied cyclic load level is shown in Figure 5.43 and stress-control cyclic *CID* test is shown in Figure 5.44. As can be seen from Figure 5.42 and 5.43, the AZ-Cam clay model under predicts the peak stress after a number of cycles. As the measure peak stress ratio is about 1.7 in constant cyclic load level test and 1.5 in varied cyclic load level test, these values exceed the critical state stress ratio value (1.36). Thus the model is inherently unable to predict these peak stress ratios. As the soil sample is normally consolidated before shearing, the soil is generally under compression and undergoes strain hardening, the accumulation rate of volumetric strain is decreasing with cyclic numbers. The predicted volumetric strains are smaller than the measured data as shown in Figures 5.42 to 5.44. For cyclic *CID* test, the model simulates the stress-strain loop and volumetric strain quite well, though the modeled hysteretic behavior is not very good.

5.3.3.2 Cyclic loading including the small strain stiffness

5.3.3.2.1 Cyclic CICP test by Dasari (1996)

A series of *CICP* tests on Gault Clay were conducted by Dasari (1996) with the measurement of the small strain stiffness. The accuracy of the measured axial strain was reported on the order of 2×10^{-5}. The material parameters for the AZ-Cam clay model to simulate these tests are directly following Dasari (1996). However, the

reported tests are insufficient to determine the values of T and β. $\beta = 0.65$ is estimated from the regression of Atkinson (2007) and $T = 0.9$ is assumed due to lack of further test data. Dasari (1996) expressed $G_{\max}$ as

$$G_{\max} = 886 p'^{0.79} OCR^{0.2} \qquad 5.22$$

Equation 5.22 was reported to be deduced from the measured data of heavily OC clays (the *OCRs* are 70, 35, 17.5, 8.7 as stated in Table 3.6 of Dasari (1996)). However, applying Equation 5.22 to predict $G_{\max}$ in the Test 1 to Test 5 in Table 2.3 in Dasari (1996) reveals Equation 5.22 significantly under estimate the value of $G_{\max}$. Meanwhile, close attention paid to the Table 2.3 and Table 3.6 in the original thesis of Dasari (1996), it is obvious that two soil samples with the same initial $p' = 100kPa$, but with different *OCR* of 2 and 35 respectively, $G_{\max}$ is even smaller for larger *OCR*. This behavior contradicts the direct result from Equation 5.22. One explanation may be $G_{\max}$ depends on the pre-consolidation pressure, and decreases with the increasing pre-consolidation pressure. To curtail the complexity, Equation 5.22 is still used but modified as

$$G_{\max} = 1650 p'^{0.79} OCR^{0.2} \qquad 5.23$$

The ratio of measured $G_{\max}$ (the value corresponding to the deviatoric strain less than 1×10^{-5}) to the value predicted by Equation 5.23 for various p' is shown in Figure 5.45 and the agreement is reasonable.

Theoretically, both γ and ω_r affect the decreasing rate of secant shear modulus with shear strain. However, the decreasing rate of tangent shear modulus is mainly

controlled by ω_r and is independent of γ as can be seen from Figure 5.46. ω_r is thus determined by matching the decreasing rate of tangent shear modulus and $\omega_r = 6.0$ gives a satisfactory agreement with measured data. γ is determined by matching the overall stress-strain curve. Figure 5.47 shows the variation of tangent shear modulus in *CICP* test with $p' = 50kPa$ and $OCR = 3.0$. With $\gamma = 14$, although the model over predicts the decreasing rate at initial stage of loading, good agreement is obtained at relatively large strain range ($\varepsilon_q \geq 1.0 \times 10^{-4}$). k_s is assumed to be zero (as only 1 cycle is simulated). Table 5.8 summarizes the material constants used in the AZ-Cam clay model for Gault Clay.

Figure 5.48 and Figure 5.49 show the comparison between model prediction and two identical cyclic *CICP* test results. It should be noted that minor difference exists in the measured data of Test 2 and Test 5. But for model predictions for these two tests are the same. The model prediction agrees well with the measured data at Test 5 before the first loading reversal occurs, but slightly over predicts the stiffness of Test 2. For cyclic loading, by using Masing's rule, the model captures the main feature of the measured data, but under predicts the decreasing rate of stiffness when loading reversal occurs. Thus large deviation exists in the unloading and reloading part of the stress-strain curve. Pyke's first extension to Masing's rule that current loading or unloading curve intersects the initial loading curve, the stress-strain relationship follows that curve during further shearing. This behavior is obvious from Figure 5.48, so there is an abrupt change of the stress-strain curve. This is due to the relatively small cyclic load level, and the soil remaining almost elastic as the behavior immediately after a loading reversal is pure elastic. However, smooth change of stiffness occurs in Test 5 as can be

seen from Figure 5.49. This is due to the relatively larger cyclic load level causing sufficient plastic strains, which degrades the strength of the soil.

5.3.3.2.2 Cyclic CIU test by Subhadeep (2009)

Kaolin clay has been used extensively at the National University of Singapore (NUS) and its physical properties are well documented (Goh, 2003). The cyclic *CIU* test on NC kaolin clay conducted by Subhadeep (2009) will be simulated by the AZ-Cam clay model. As the cyclic tests were carried out on NC clay, the values of T and β cannot be determined precisely, thus $T = 0.9$ and $\beta = 0.6$ is assumed. The expression of $G_{\max}$ is taken directly from Subhadeep (2009) as Equation 5.24

$$G_{\max} = 2060\, p'^{0.653} \qquad 5.24$$

R_w is preferred to be determined from the S_u of NC clay, however, there is no information on this. Therefore, R_w and ω_r are determined by fitting the stress-strain curves of the test CT3-1 and CT3-2 as reported by Subhadeep (2009). However, the agreement is not so good as the measurements at the small strain range of virgin NC clay sample on the first cycle are not quite satisfactory as shown in Figure 5.50.

As for NC clay subjected to initial loading, γ has no effect on the predicted behavior as the stress state always lie on the bounding surface and the model degenerates to the conventional elasto-plastic model. γ is thus appropriate to be determined from matching the stress-strain loop in the absence of the effective stress path of lightly OC clay in undrained shear. Although both γ and k_s affect the model prediction through plastic modulus, $k_s = 0$ is assumed in the absence of further information (The author is aware that a larger k_s will give a smaller γ). $\gamma = 10$ gives

a satisfactory simulation on Test CT3-1 as can been seen from Figure 5.51 and Figure 5.52. Table 5.9 summarizes the material parameters used in the AZ-Cam clay model for kaolin clay at NUS.

Figure 5.53 and Figure 5.54 show the model predictions with the measured test data on multi-stage cyclic *CIU* test on NC kaolin clay. The loading sequence for Figure 5.53 is 60 cycles with constant amplitude 0.137% (axial strain) immediately followed by 60 cycles with constant amplitude of 0.254%. The agreement between the test data and model prediction is satisfactory, in particular the model successfully predicts the degradation of the strength. However, in terms of damping (indicated by the area of closed stress strain loop), the model over predicts the damping by using Masing' rule. The loading sequence for Figure 5.54 is 60 cycles with constant amplitude of 0.137%, 0.254% and 0.548%, respectively, and finally 60 cycles with constant amplitude of 0.789%. The model under predicts the strength of the first loading cycle with amplitude of 0.789%, but agrees well with the final loading cycle. During 60 cycles with amplitude of 0.789%, the test data still show a significant reduction of strength, while the model predicts slight reduction due to the stress state migrating into the deeper interior of the bounding surface.

5.3.3.3 Summary on cyclic loading

From the above simulation in various cyclic loading tests, the AZ-Cam clay model is capable of predicting the cyclic behavior of NC to lightly OC clay. By employing a constant elastic shear modulus G or a constant Poisson's ratio, the model is able to predict the degradation of strength in cyclic undrained shearing. However, the predicted shape of the stress-strain loops is very sensitive to the value of G or Poisson's ratio. By incorporating the small strain stiffness and the Masing's rule, the

model can successfully simulate the degradation of strength and the hysteretic effect. However, the model tends to under predict the decreasing rate of shear modulus during the unloading and reloading process.

5.4 Summary

In this chapter, detailed description of the material constants of the AZ-Cam clay model is presented together with the laboratory determination methods. The model evaluation in laboratory tests is carried out subsequently and is divided into two aspects: simulation on monotonic loading and simulation on cyclic loading. For monotonic loading, by explicitly incorporating a failure surface, the model can successfully predict the peak strength of heavily OC clay in drained shearing and the undrained shear strength. For cyclic loading, the predicted stress-strain loops largely depend on the choice of elastic shear modulus. A constant elastic shear modulus or a constant Poisson's ratio can predict the degradation of strength quite well, but the shape of stress-strain loops is not satisfactory. By incorporating the small strain stiffness and the Masing's rule, the model is able to simulate the cyclic degradation and hysteretic effect of NC to lightly OC clay, although the model tends to under predict the decreasing rate of the stiffness during unloading. Further modification will need to be done for the model capability for predicting the cyclic behavior of heavily OC clay.

Table 5.1 Material constants of the AZ-Cam clay model

Parameter	Physical meaning	Evaluation method
N	Critical state parameter. The intercepts of NCL with v axis in $v-\ln p'$	Isotropic 1 D compression test
λ	Critical state parameter. The slop of NCL in $v-\ln p'$	Isotropic 1 D compression test
κ	Critical state parameter. The slop of SL in $v-\ln p'$	Isotropic 1 D loading and unloading tests
M	Critical state parameter. The slope of CSL in $p'-q$	Triaxial *CID*/*CIU* test
R_w	Bounding surface size parameter in the subcritical region.	Triaxial *CID*/*CIU* test
R_d	Bounding surface size parameter in the supercritical region.	Normally is fixed to 2
T	Ultimate strength parameter, governing the shape of the failure envelope in supercritical region.	Triaxial *CIU* test
β	Peak strength parameter, governing the shape of the failure envelope in supercritical region.	Triaxial *CID* or constant p' tests.
γ	Plastic modulus parameter, governing the accumulation of plastic strains within the bounding surface	Fitting the stress path within the bounding surface in triaxial *CIU* tests
k	Shakedown parameter, governing the plastic strain accumulation rate in cyclic loading	Cyclic triaxial *CID*/*CIU* test
G	Elastic shear modulus.	Constant *Possion's ratio* or G, or resonant column tests for $G_{\max}$.
ω_r	Decreasing rate of G ($G_{\max}$ is used)	Fitting the stress-strain curves

Table 5.2 Model constants for the tests of Wroth & Loudon (1967)

N	λ	κ	M	R_w
2.67	0.26	0.05	0.9	2.3
R_d	T	β	γ	ν
2	0.95	0.3	8	0.25

Table 5.3 Model constants for the tests of Banerjee & Stipho (1978, 1979)

v_0	λ	κ	M	R_w
$1+2.65w$	0.14	0.05	1.05 for compression, 0.85 for extension	3.44
R_d	T	β	γ	ν
2	0.9 for compression, 0.95 for extension	0.7	6	0.2

Table 5.4 Model constants for the tests of (Kuntsche, 1982)

v_0	λ	κ	M	R_w
1.667, 1.862, 1.728 for *OCR*=1,2,10 respectively	0.2	0.05	0.74 for compression; 0.6 for extension	2
R_d	T	β	γ	ν
2	0.5	0.4	8	0.1

Table 5.5 Model constants for the tests of Li & Meissner (2002)

N	λ	κ	M	R_w
2.06	0.173	0.034	0.772	1.7
R_d	T	β	γ	ν
2	0.65	0.4	4	0.35

Table 5.6 Model constants for the tests of Nakai & Hinokio (2004)

N	λ	κ	M	R_w
1.83	0.0508N	0.0112N	1.36 for compression, 1.0 for extension	2
R_d	T	β	γ	ν
2	0.7	0.2 for compression, 0.3 for extension	2	0.2

Table 5.7 Model constants for BBC

N	λ	κ	M	R_w
2.96	0.184	0.034	$\frac{M(\theta)}{\sqrt{3}} = \frac{0.608}{\left[1+0.629\sin(3\theta)\right]^{0.25}}$	3.6
R_d	γ	β	T	$G_{\max}$
2	6	0.8	$T = \frac{0.456}{\left[1+0.924\sin(3\theta)\right]^{0.2}}$	$\frac{G_{\max}}{p'_r} = 460\frac{p'}{p'_r}OCR^{0.3}\ \omega_r = 2$

Table 5.8 Model constants for Gault Clay

N	λ	κ	M	R_w	R_d
2.96	0.17	0.035	M=0.94 for compression M=0.71 for extension	2.0	2.0
γ	β	T	$G_{\max}$	ω_r	k
14	0.65	0.9	$G_{\max} = 1650\,p'^{0.79}OCR^{0.2}$	6.0	0

Table 5.9 Model constants for kaolin clay at NUS

N	λ	κ	M	R_w	R_d
3.8	0.244	0.053	M=0.98 for compression, M=0.74 for extension	1.6	2.0
γ	β	T	$G_{\max}$	ω_r	k
10	0.6	0.9	$G_{\max} = 2060\,p'^{0.653}$ and $\nu = 0.25$	5.0	0

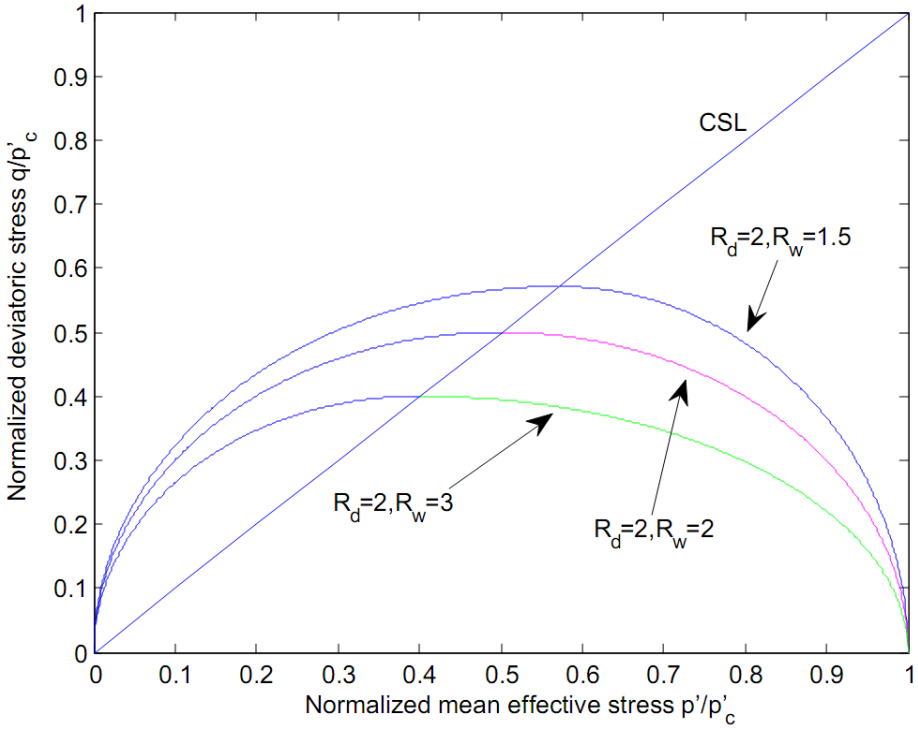

(a) Bounding surface

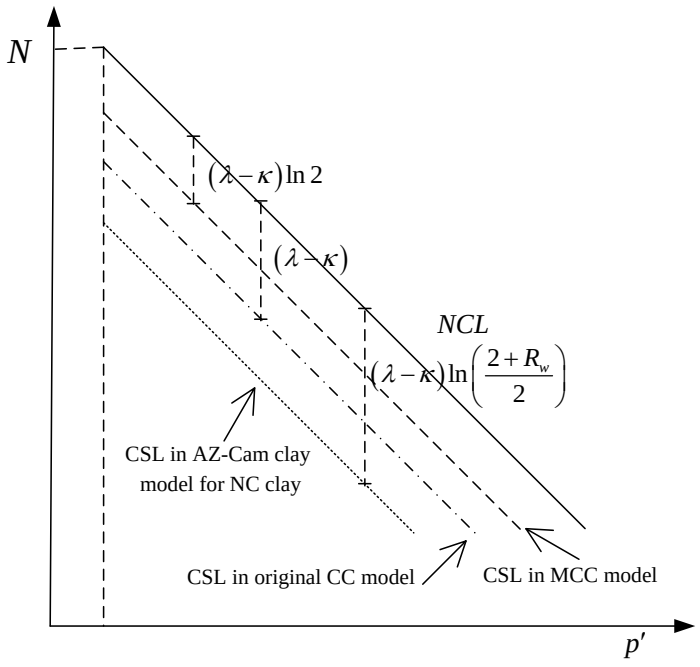

(b) CSL in $v-\ln p'$ space

Figure 5.1 Effects of R_w on bounding surface and *CSL*

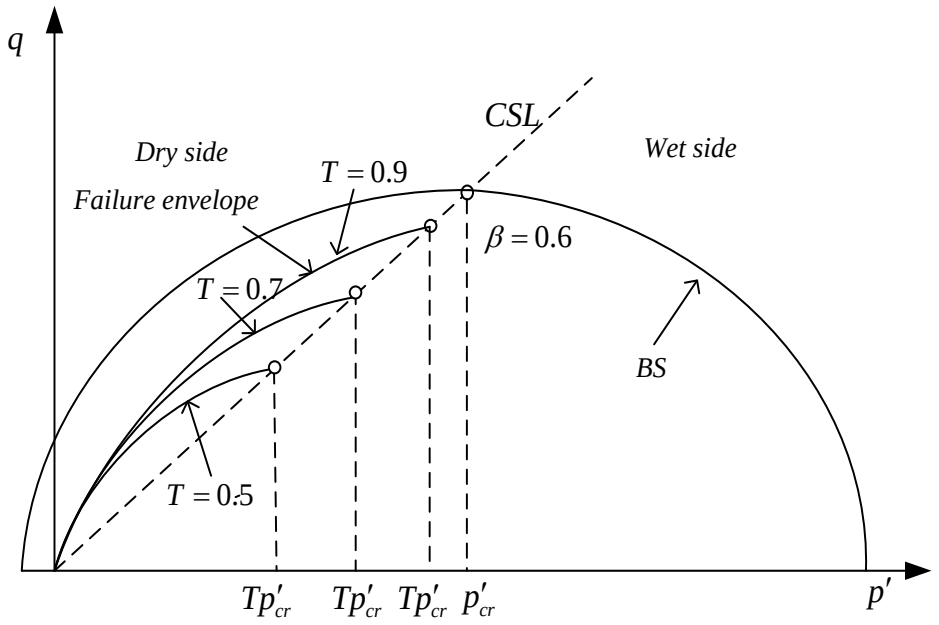

Figure 5.2 Effect of T on the shape of failure envelope

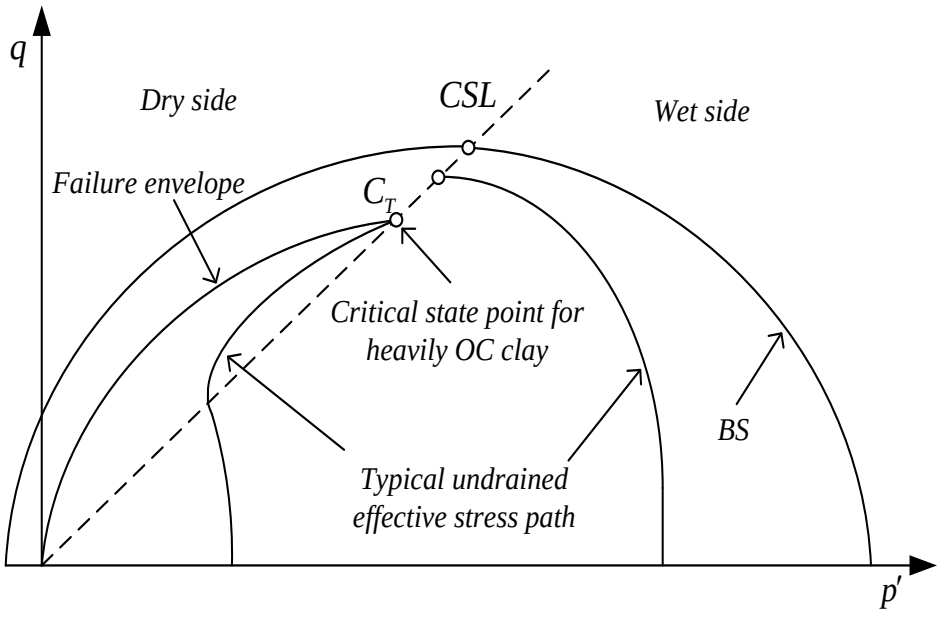

Figure 5.3 Typical effective stress path in undrained shearing

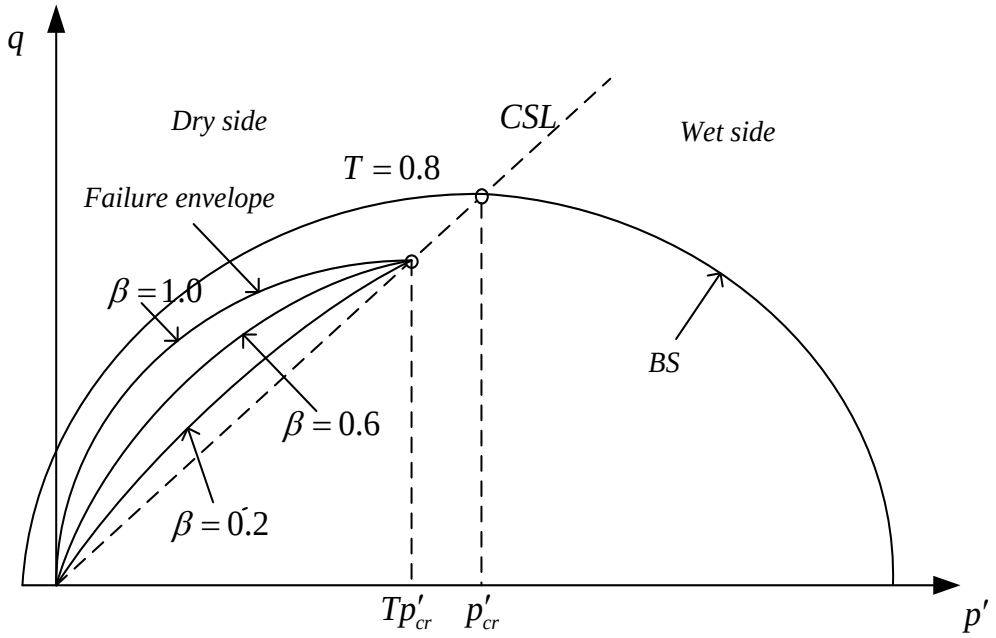

Figure 5.4 Effect of β on the shape of failure envelope

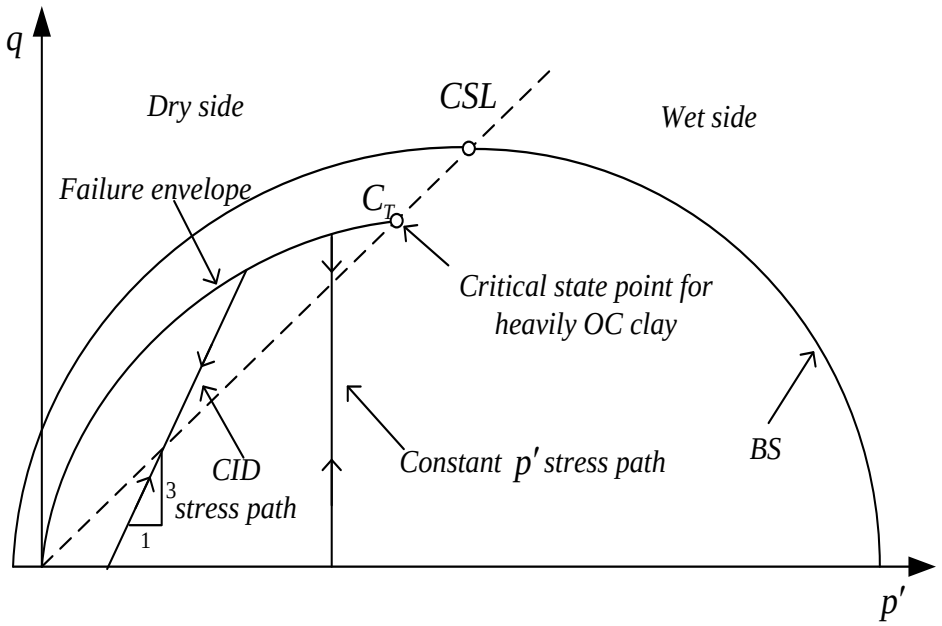

Figure 5.5 Typical effective stress path in drained shearing

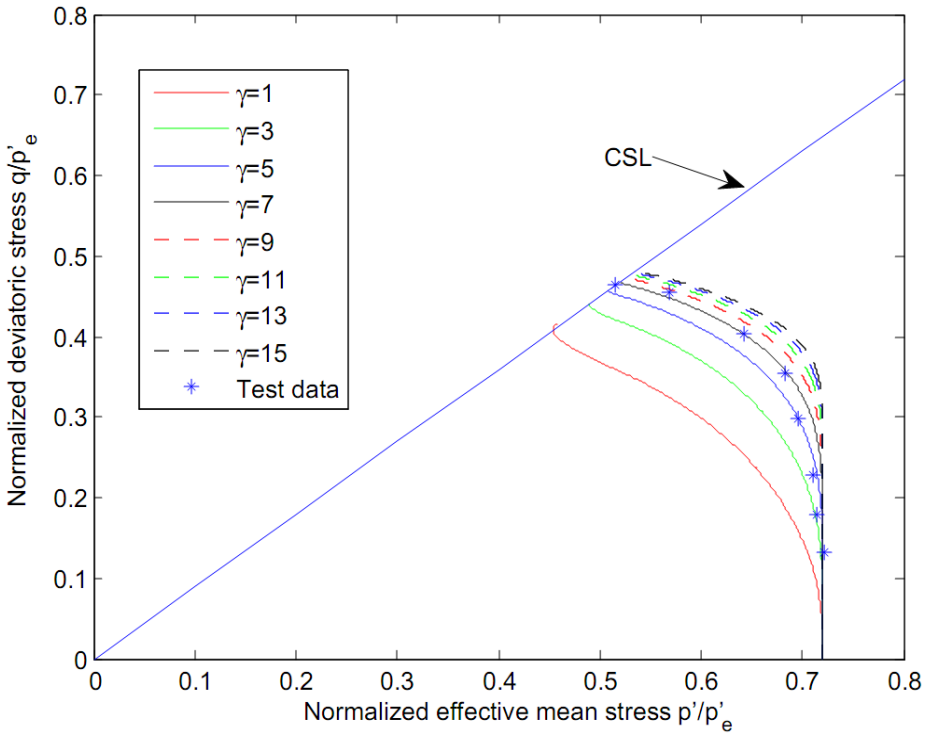

(a) Undrained stress path

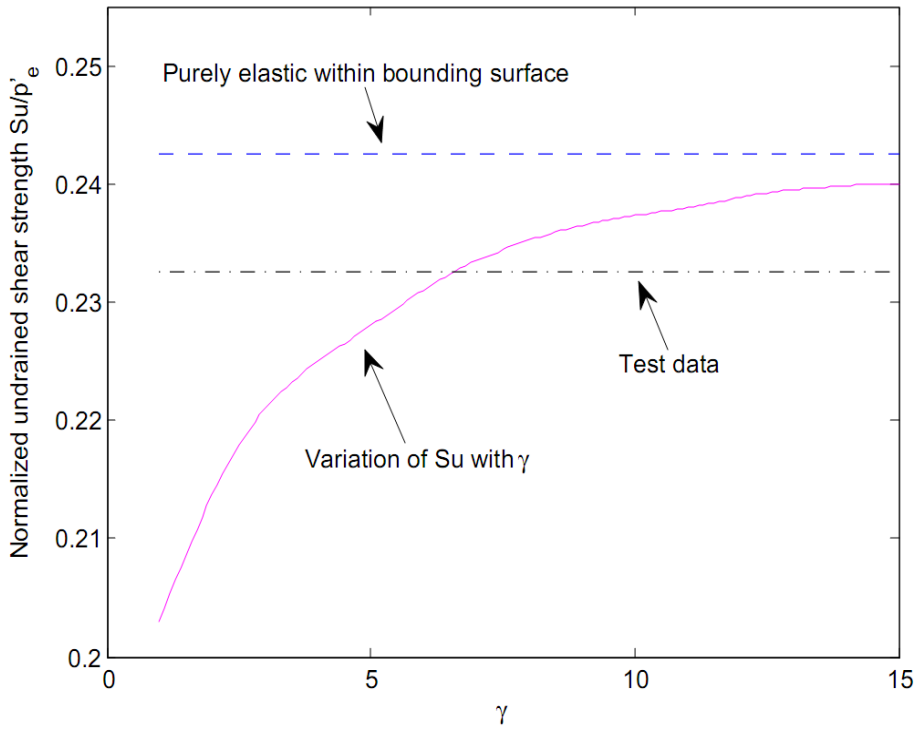

(b) Undrained shear strenght

Figure 5.6 Determination of γ

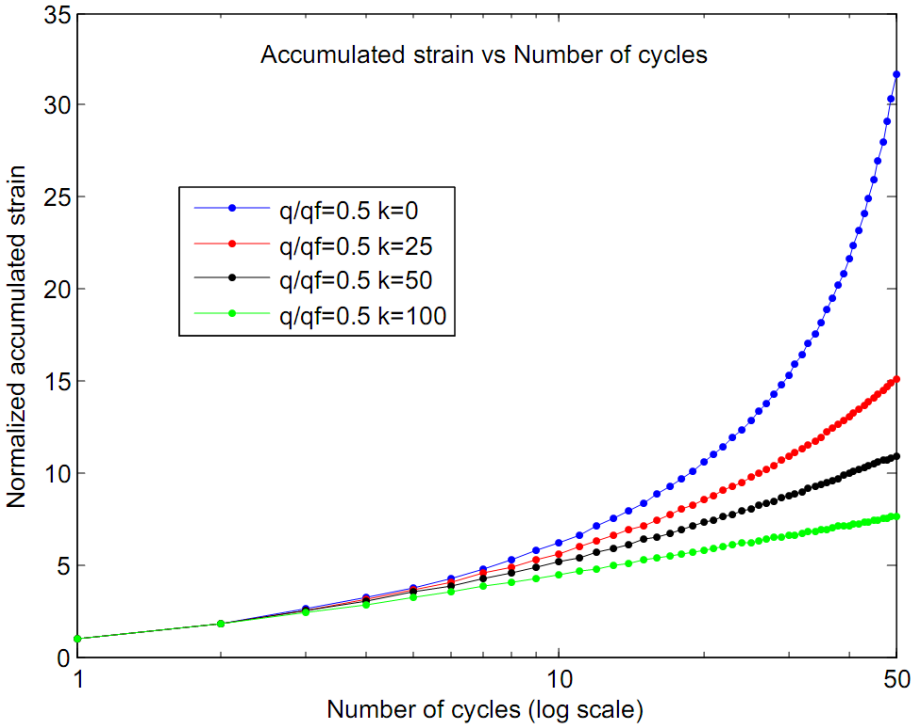

Figure 5.7 Determination of k

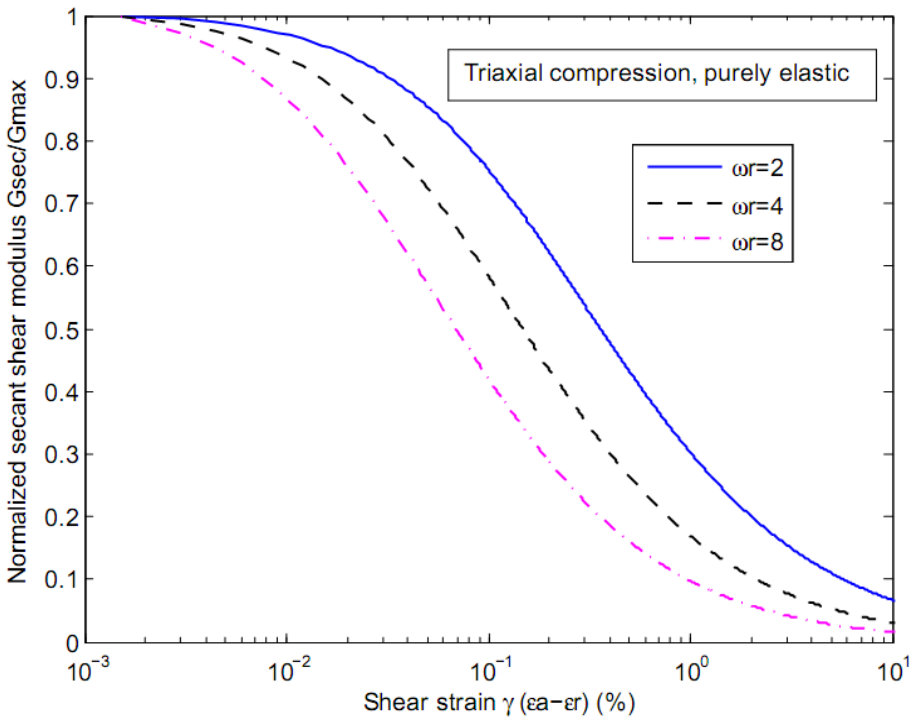

(a) AZ-Cam clay model

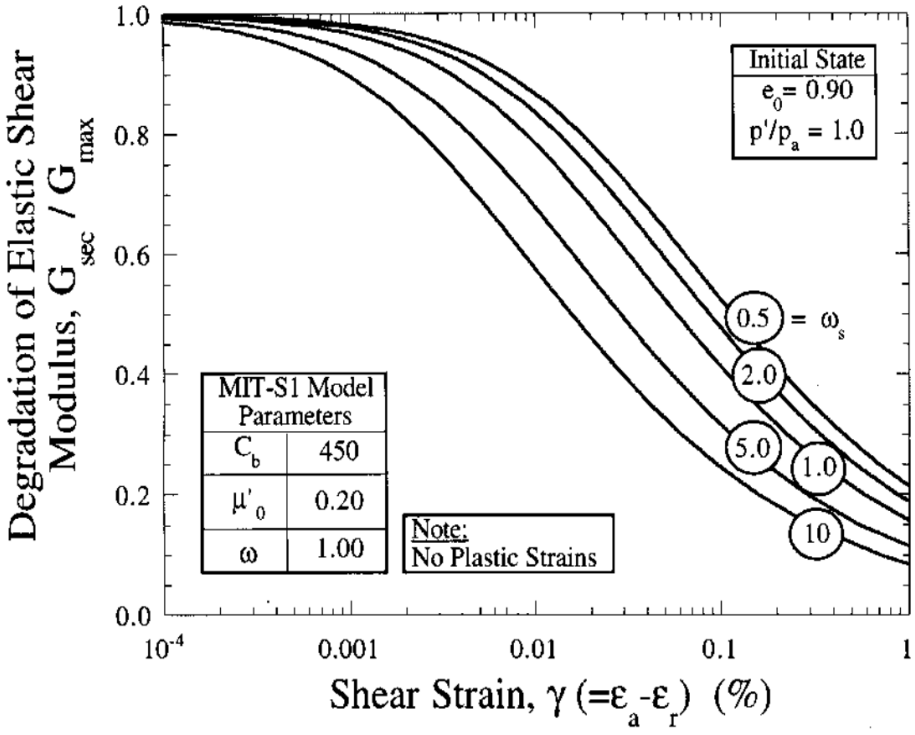

(b) Prediction after Pestana & Whittle (1999)

Figure 5.8 Comparison of decreasing rate of shear modulus

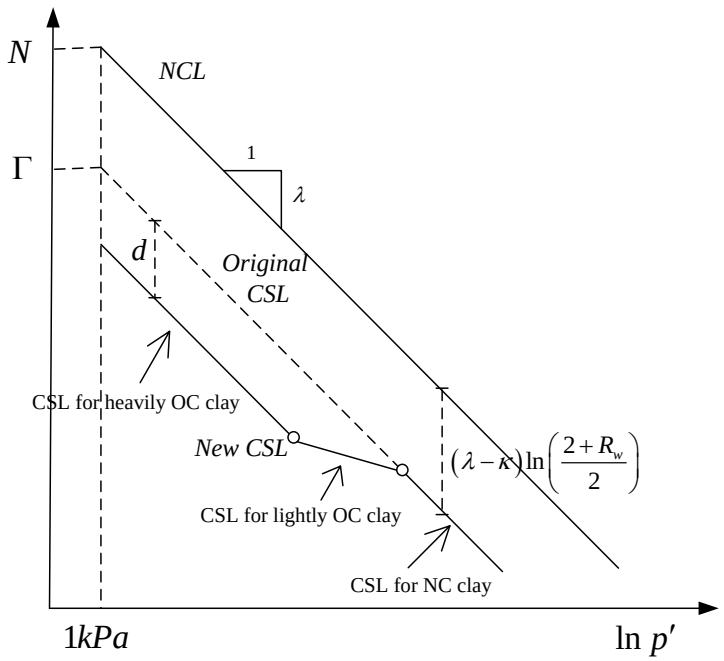

Figure 5.9 The position of new *CSL* in $v-\ln p'$ space

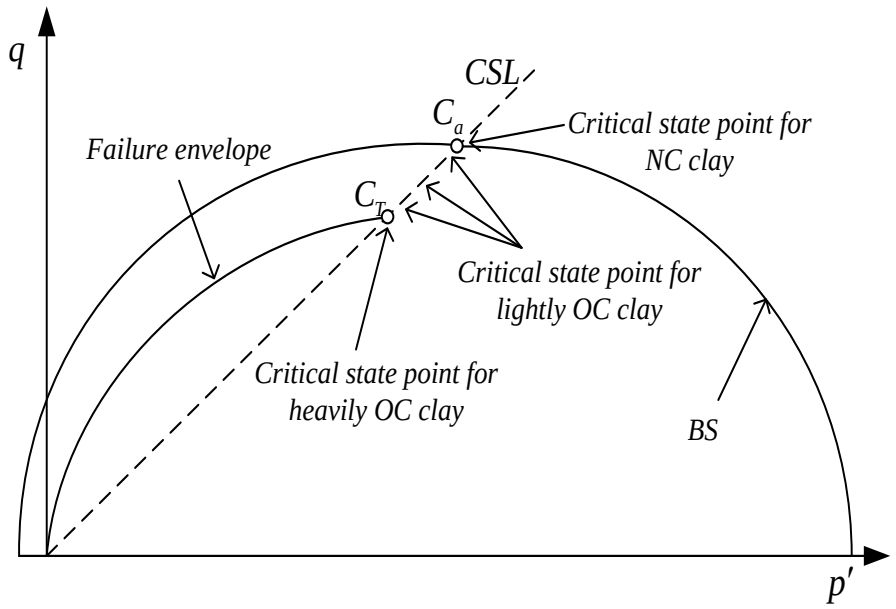

Figure 5.10 The position of critical state point in $p'-q$ space

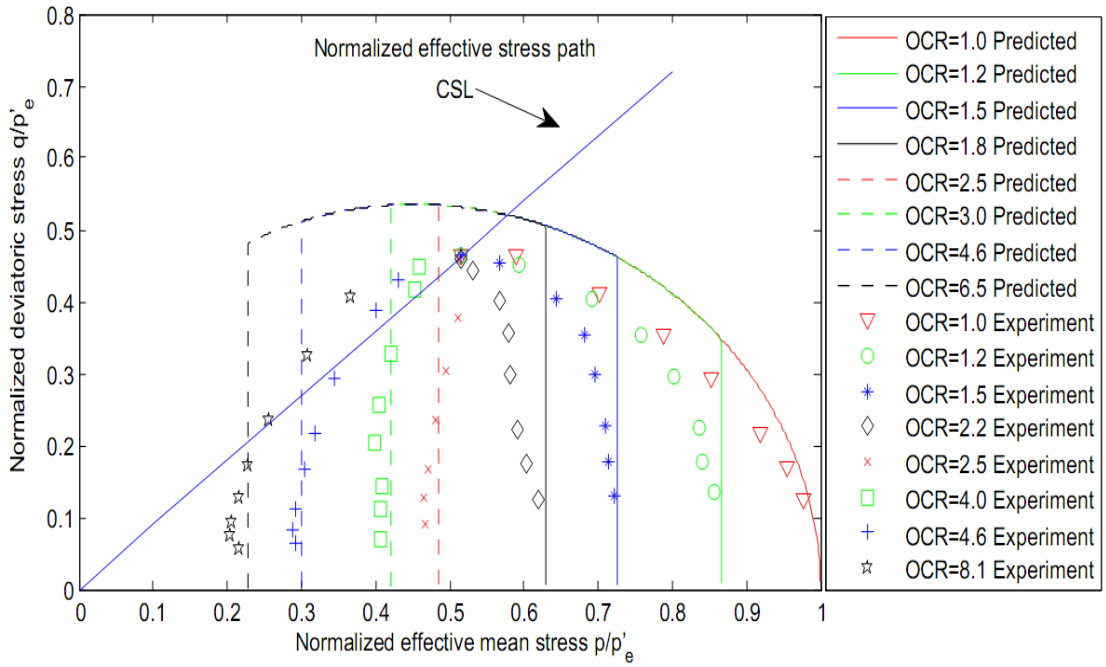

(a) MCC model prediction

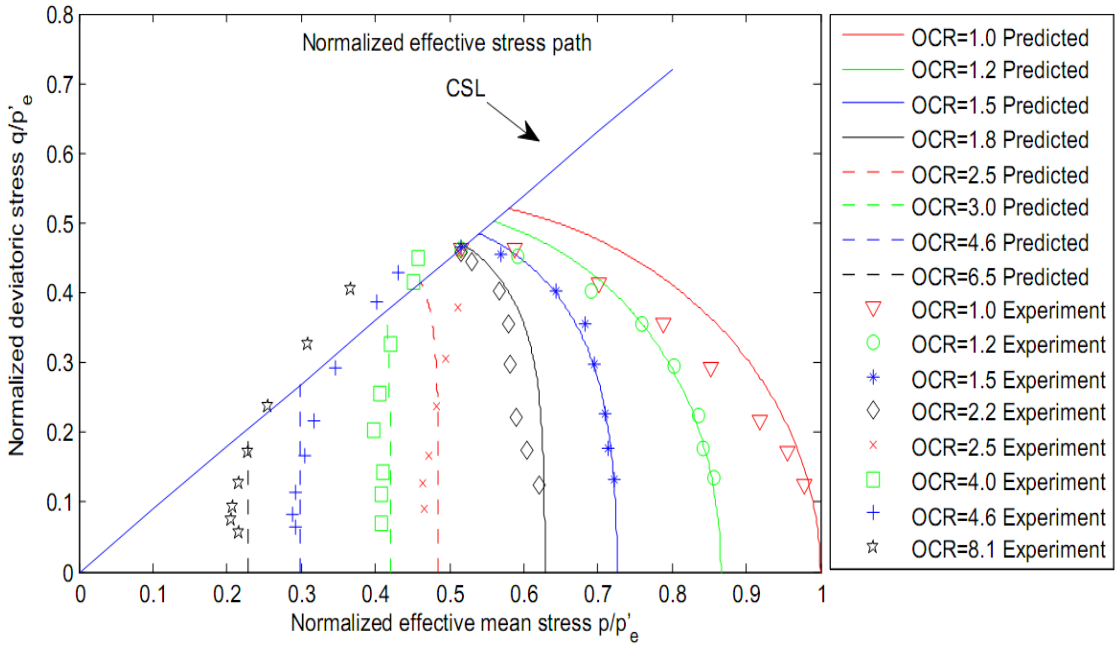

(b) Prediction using the model by Zienkiewicz *et al.* (1985)

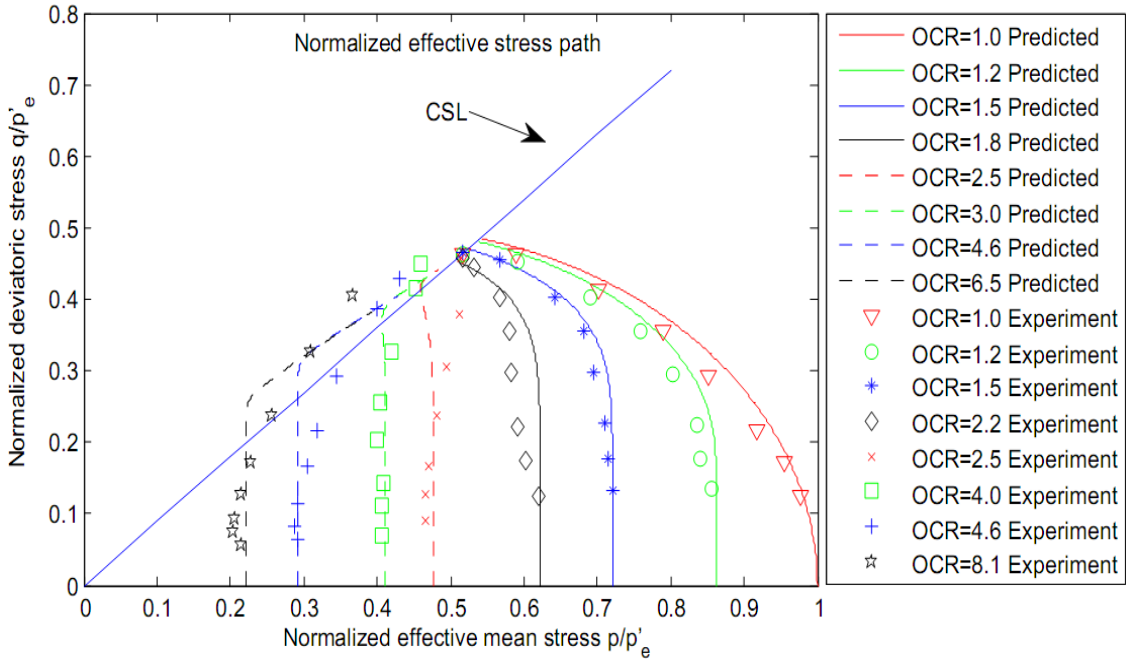

(c) AZ-Cam clay model prediction

Figure 5.11 Simulation on tests of Wroth & Loudon (1967)

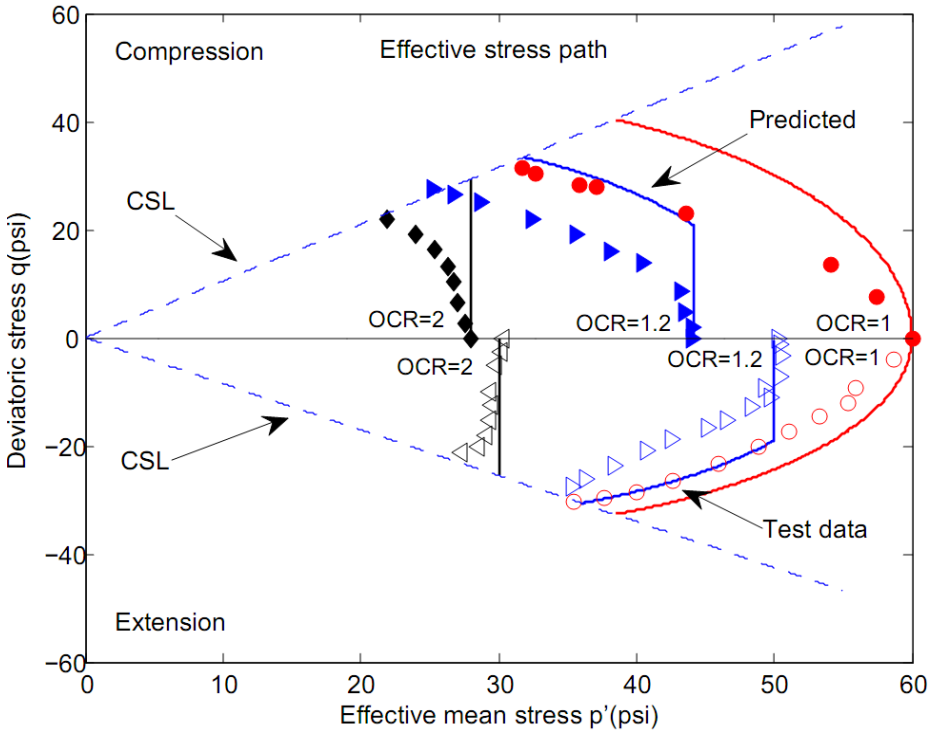

(a) MCC model prediction

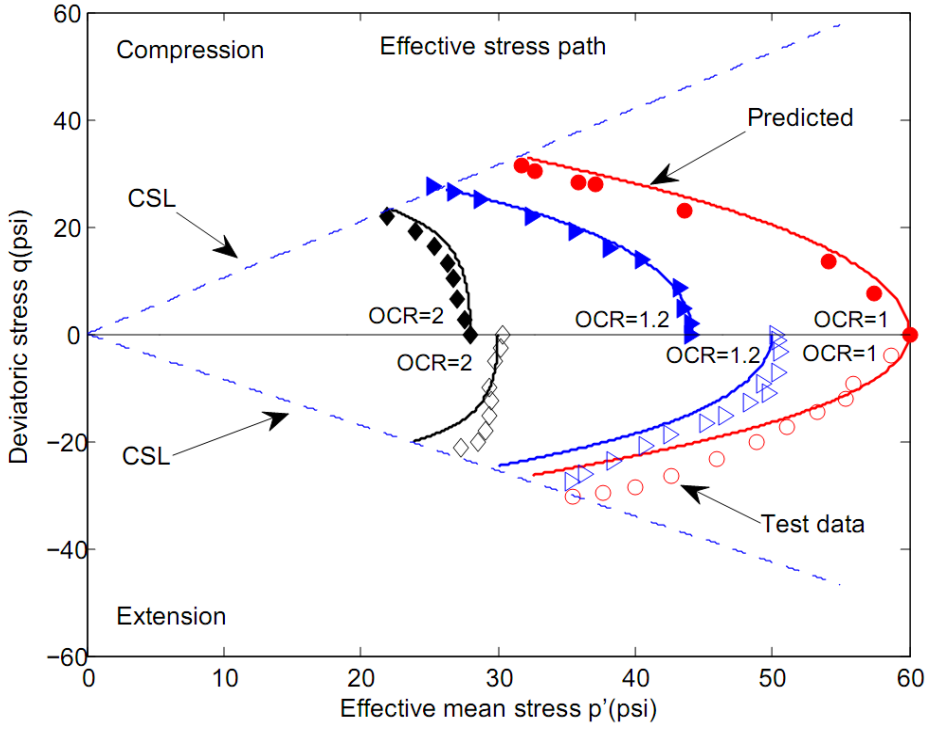

(b) Zienkiewicz *et al.* (1985) prediction

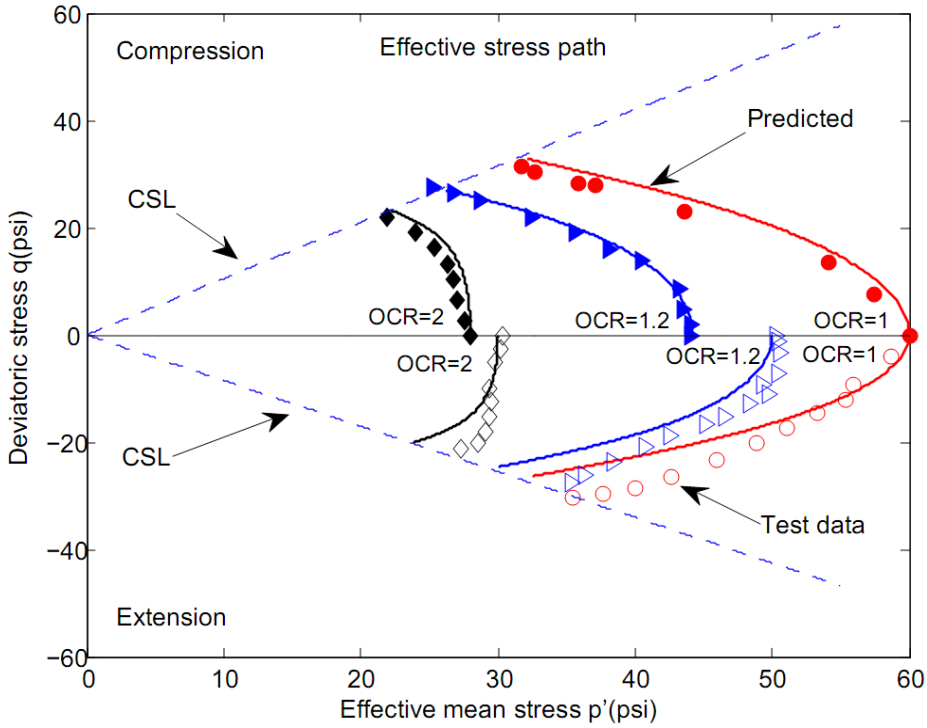

(c) AZ-Cam clay model prediction

Figure 5.12 Simulation on tests by Banerjee & Stipho (1978)-Effective stress path

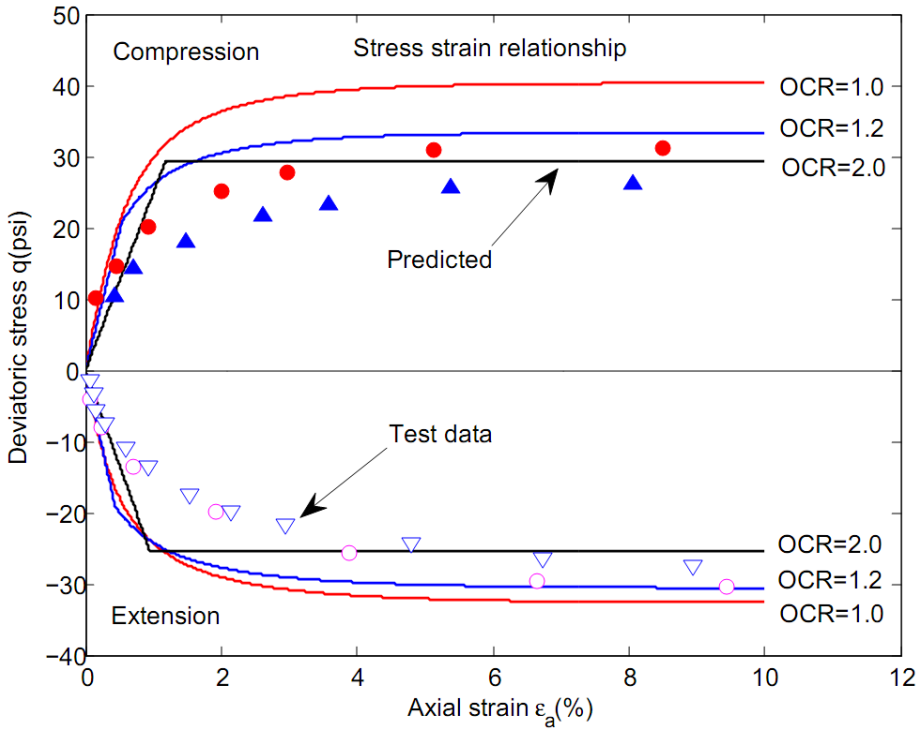

(a) MCC model prediction

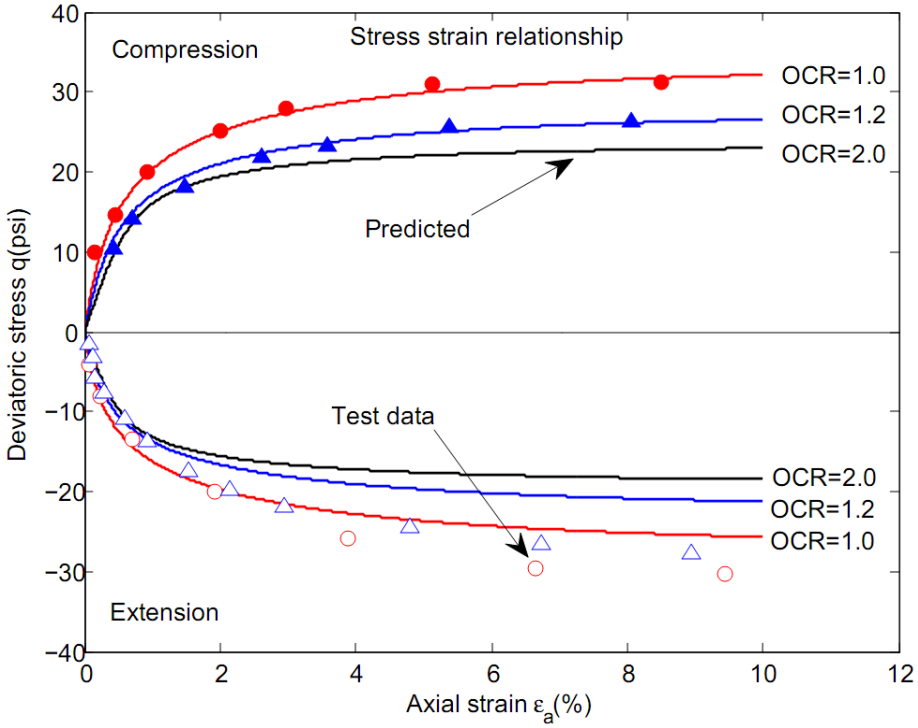

(b) Zienkiewicz *et al.* (1985) prediction

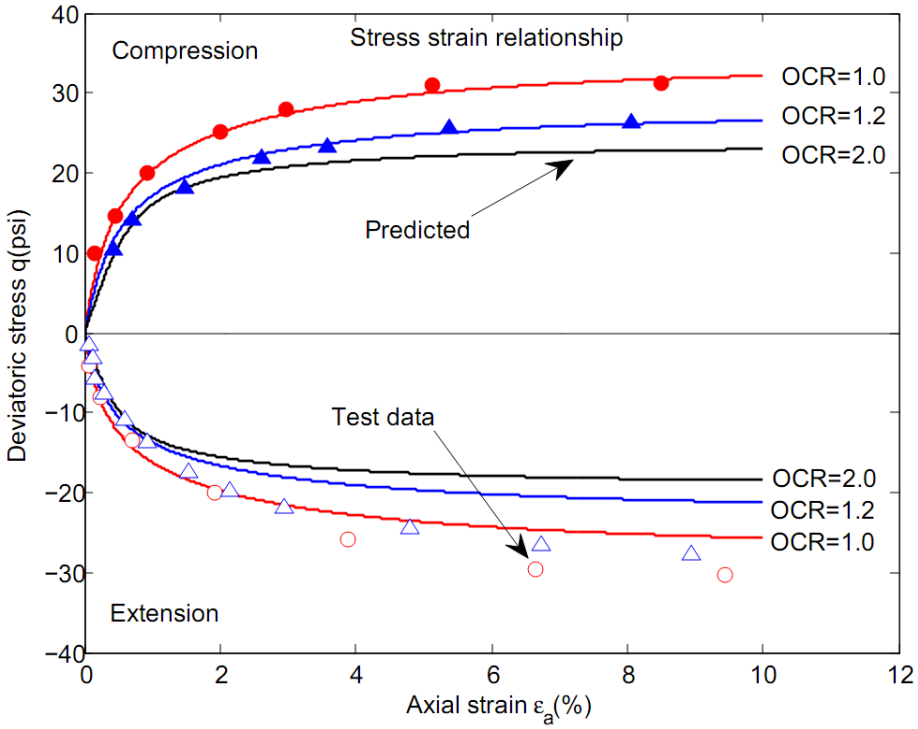

(c) AZ-Cam clay model prediction

Figure 5.13 Simulation on tests by Banerjee & Stipho (1978)-Stress strain curves

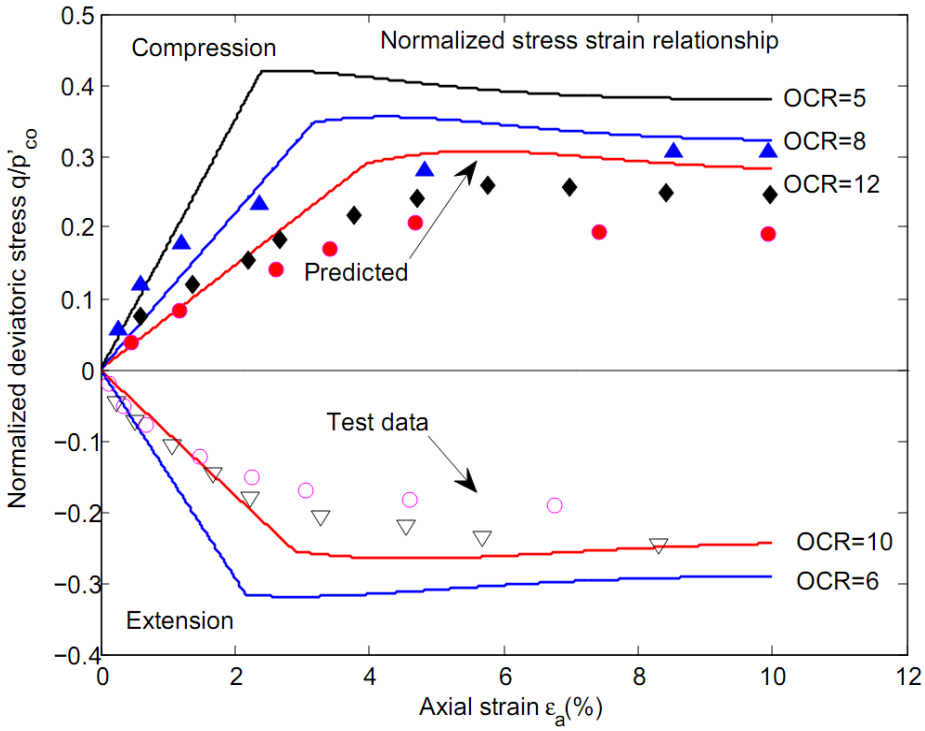

(a) MCC model prediction

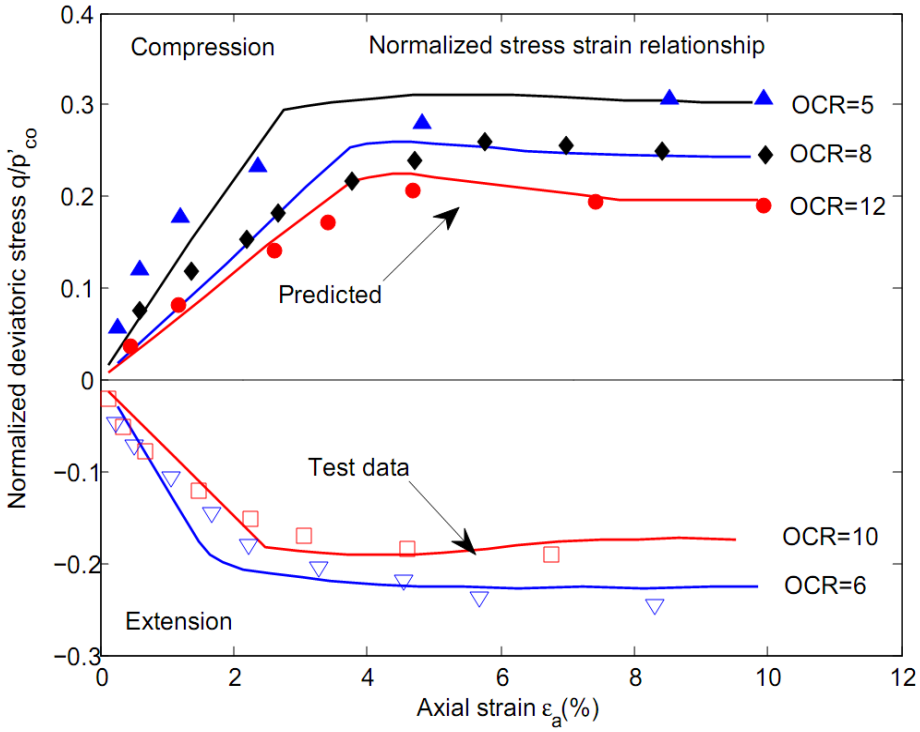

(b) Banerjee & Stipho (1979) prediction

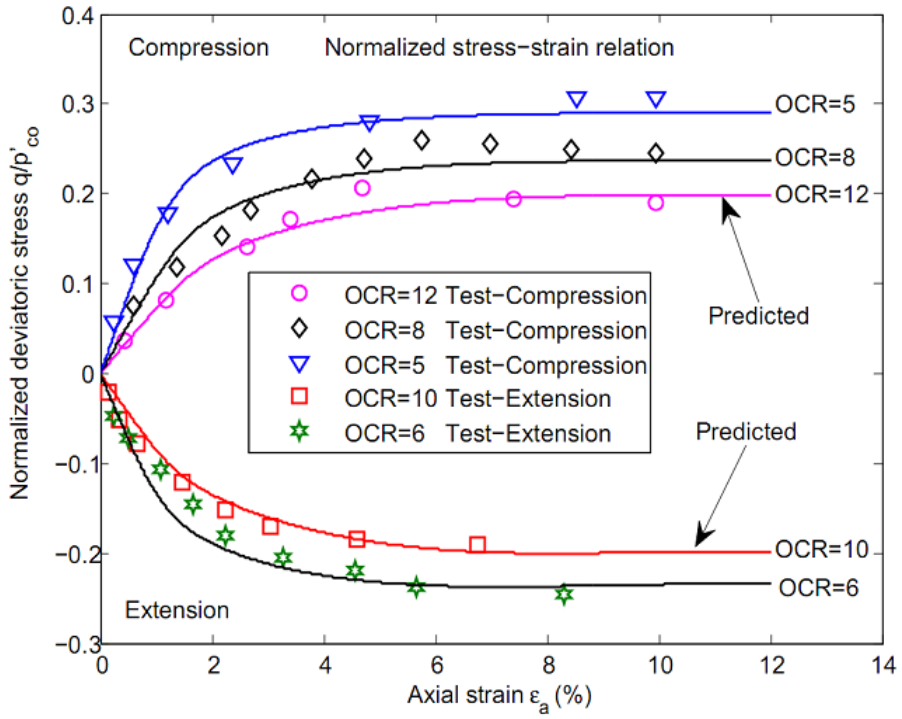

(c) AZ-Cam clay model prediction

Figure 5.14 Simulation on tests by Banerjee & Stipho (1979)-Stress strain curves

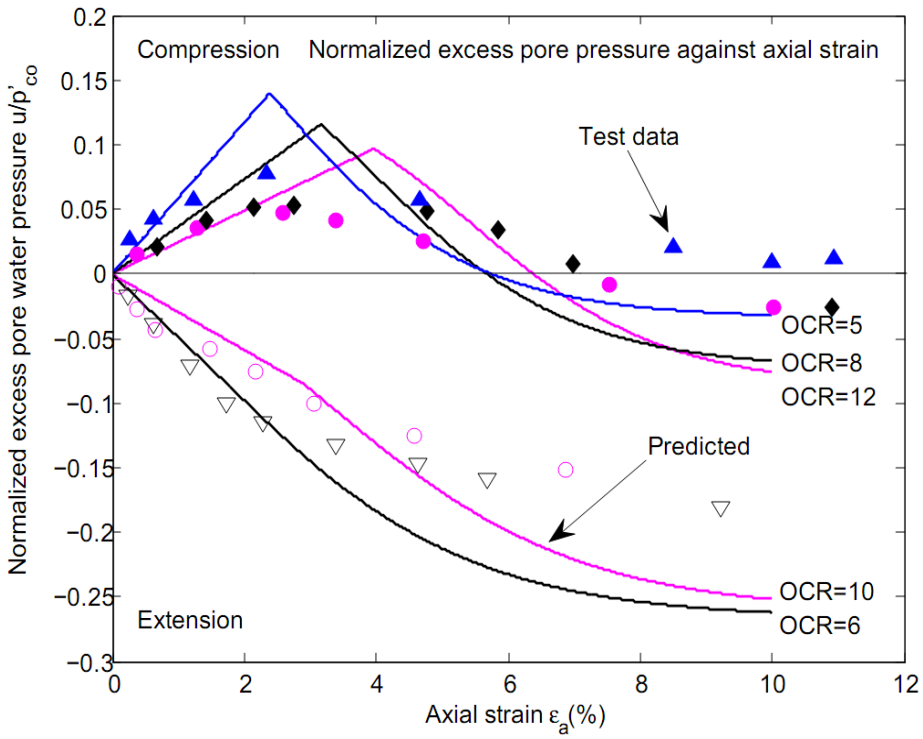

(a) MCC model prediction

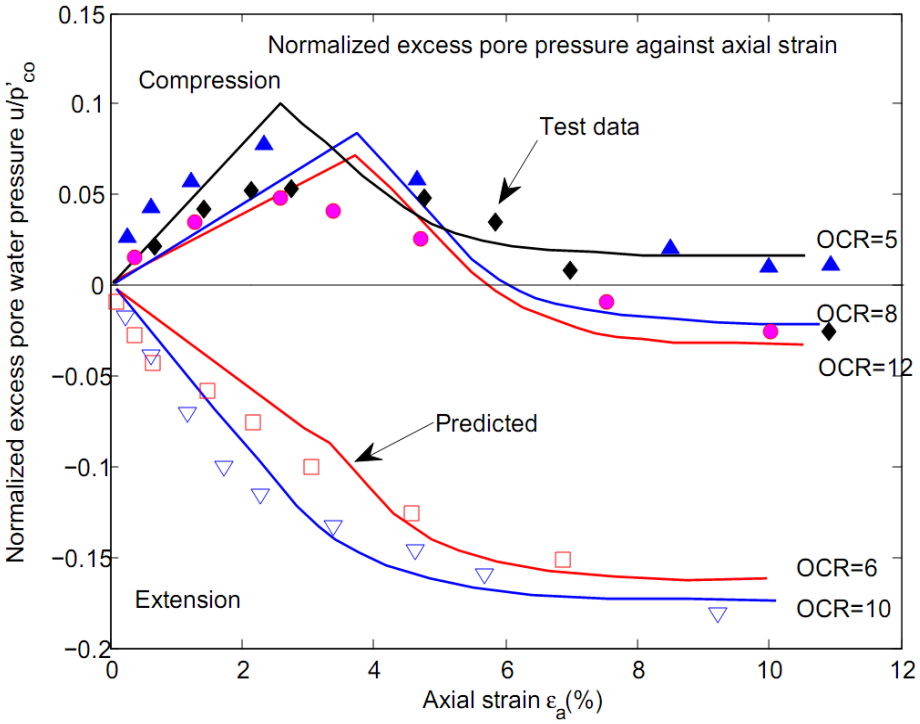

(b) Banerjee & Stipho (1979) prediction

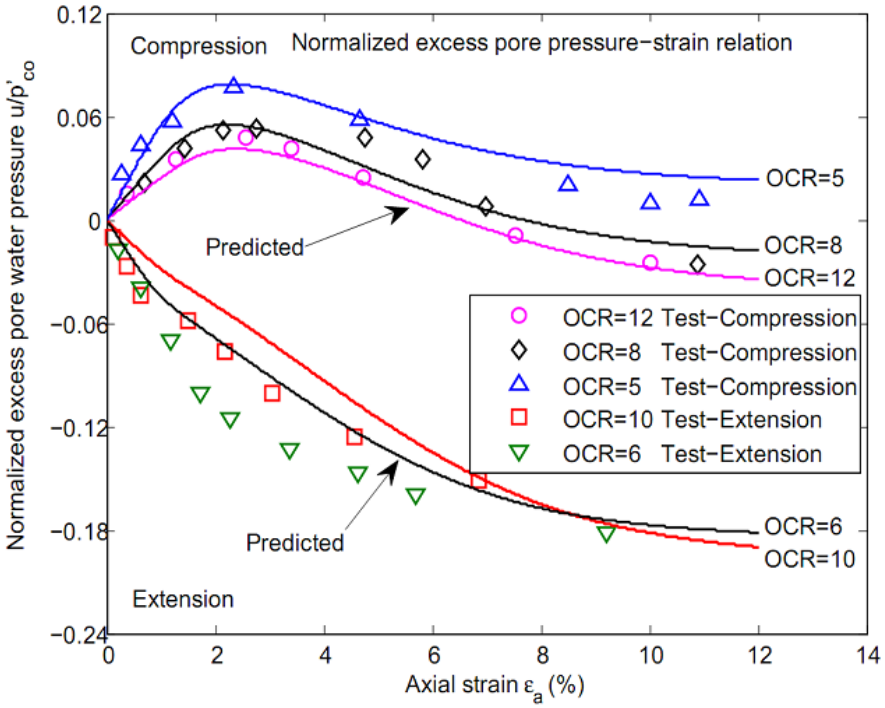

(c) AZ-Cam clay model prediction

Figure 5.15 Simulation on tests by Banerjee & Stipho (1979)-Excess pore pressure

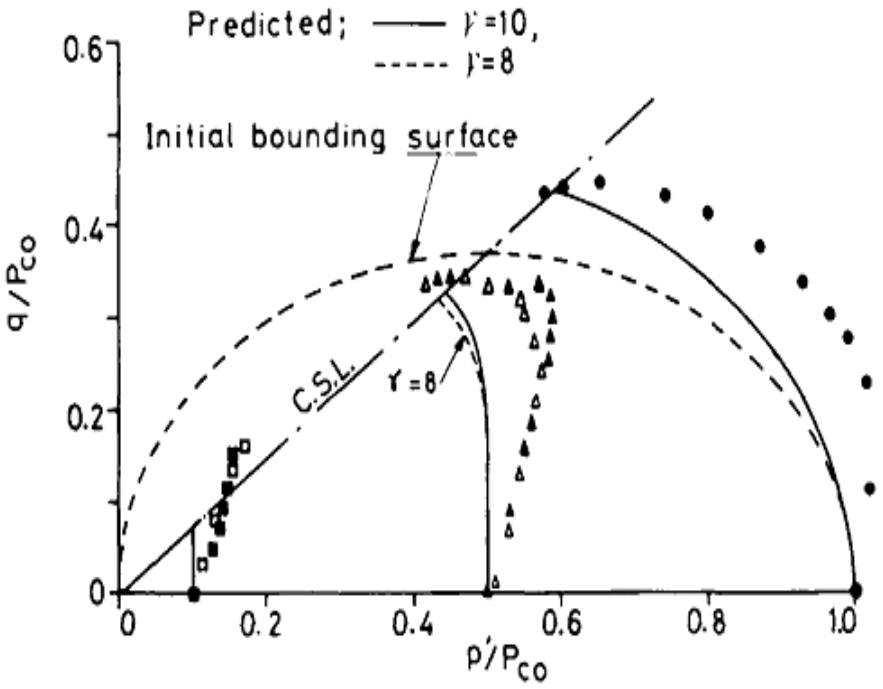

(a) Effective stress path after Zienkiewicz *et al.* (1985)

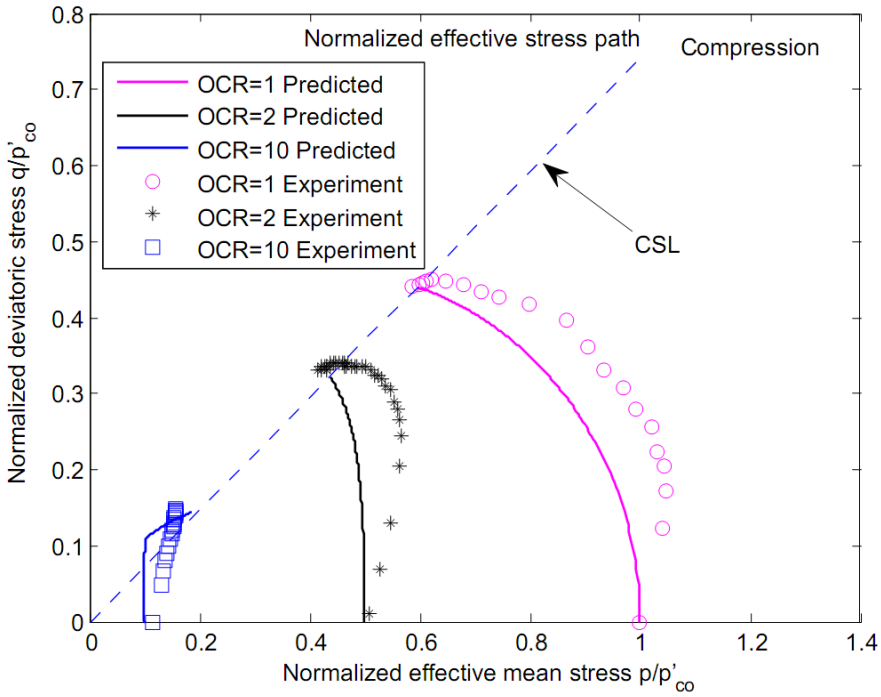

(b) Effect stress path from AZ-Cam clay model

Figure 5.16 Simulation on tests by Kuntsche (1982)

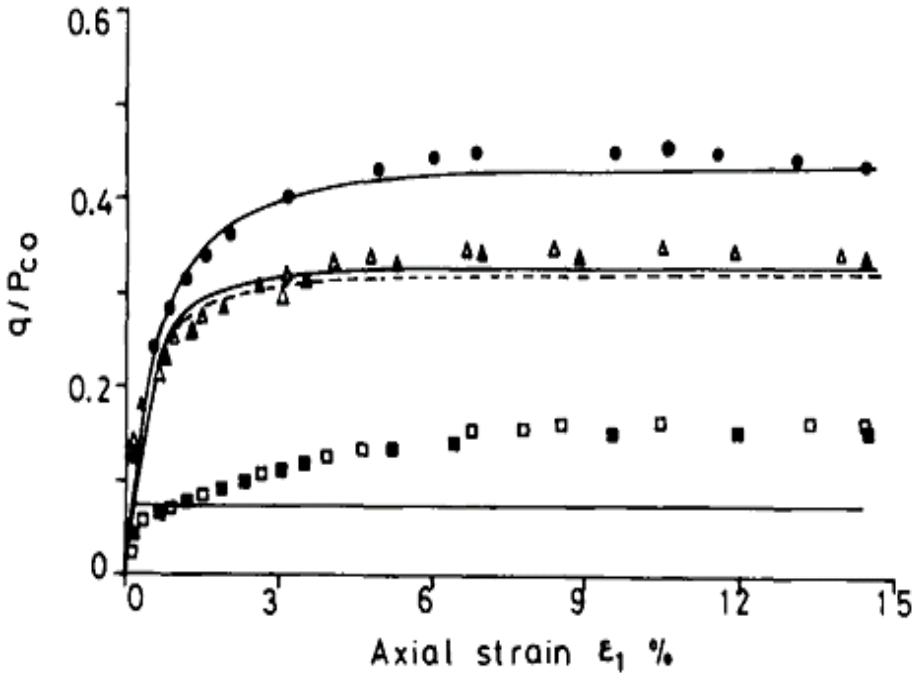

(a) Stress strain behavior after Zienkiewicz *et al.* (1985)

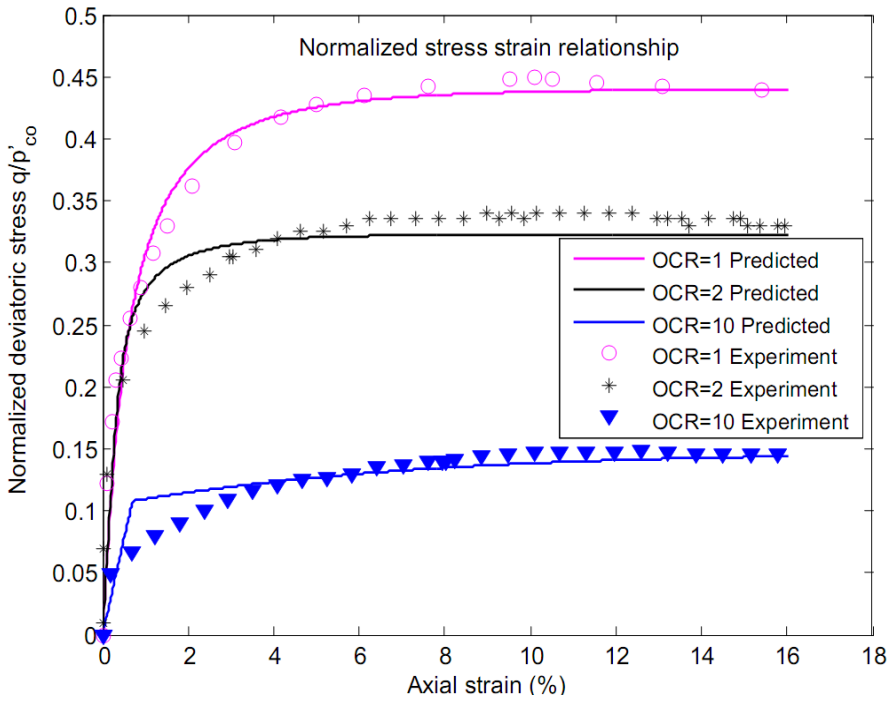

(b) Stress strain behavior from AZ-Cam clay model

Figure 5.17 Simulation on tests by Kuntsche (1982)

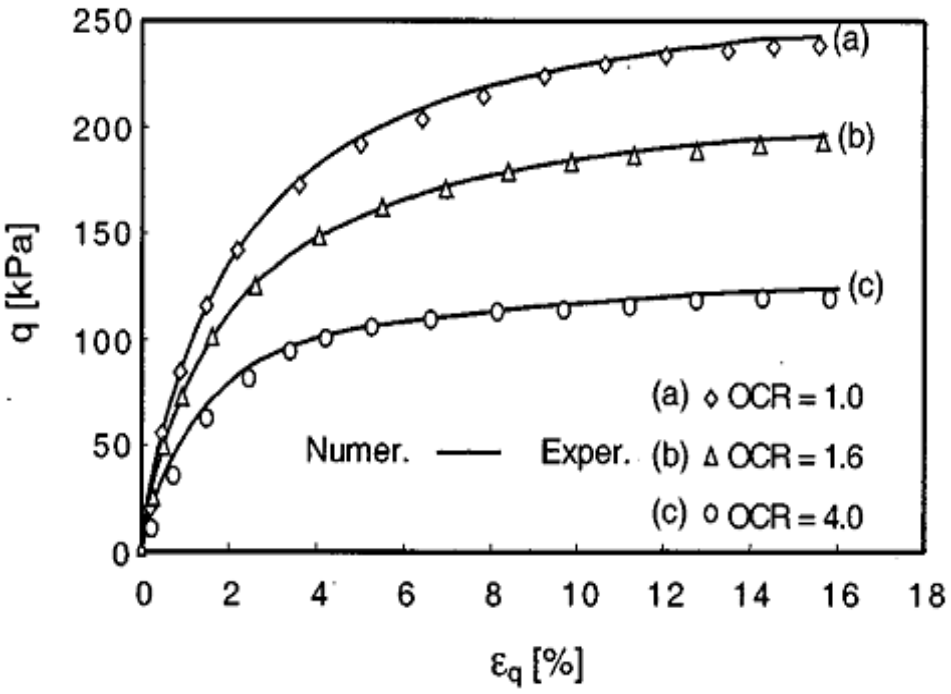

(a) Stress strain behavior after Li and Hun (2002)

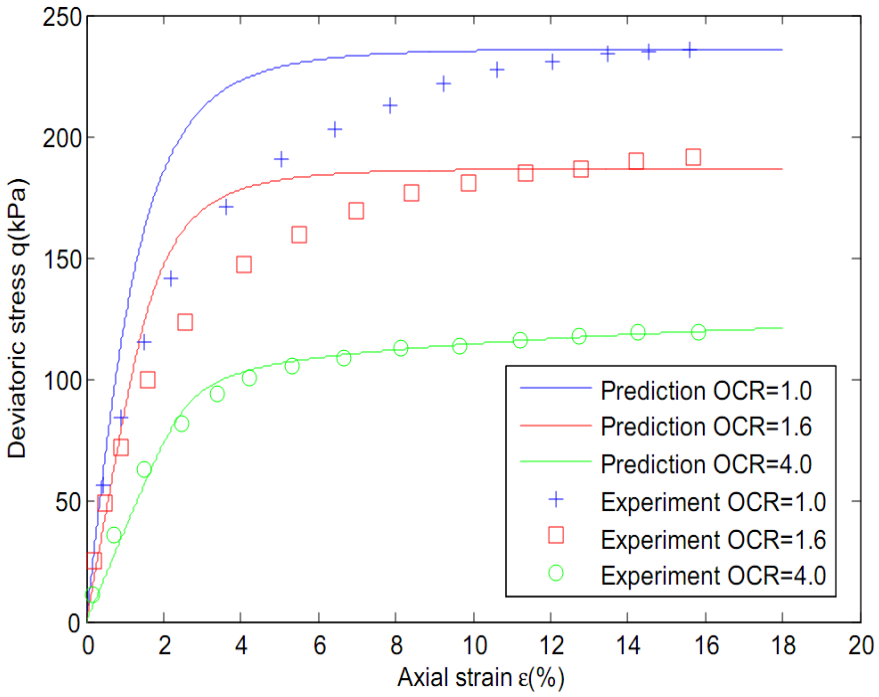

(b) Stress strain behavior predicted by AZ-Cam clay model

Figure 5.18 Simulation on tests by Li & Meissner (2002)

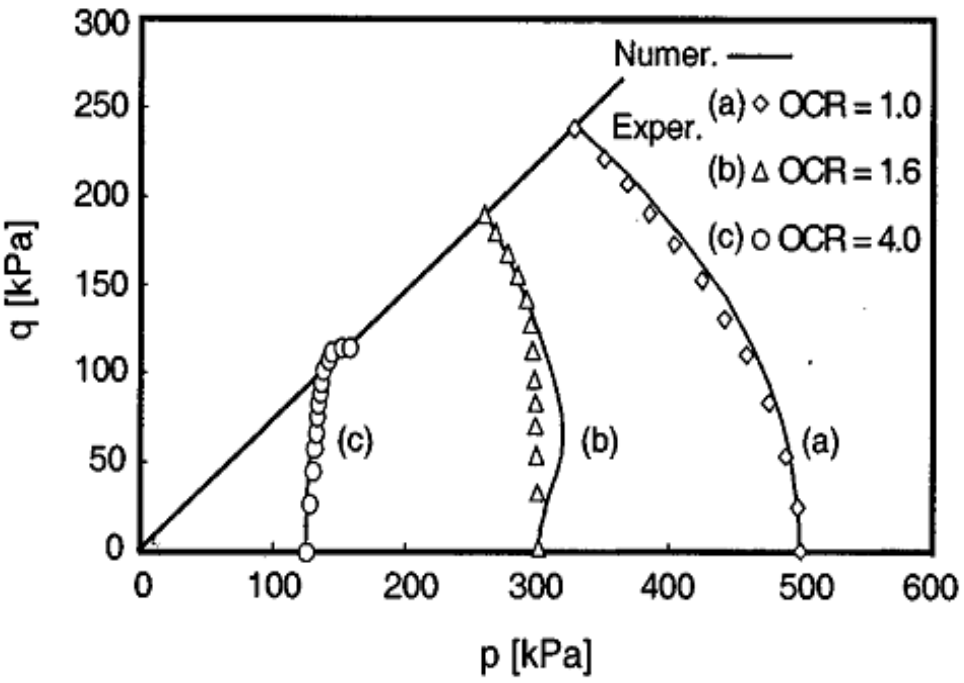

(a) Effective stress path after Li & Meissner (2002)

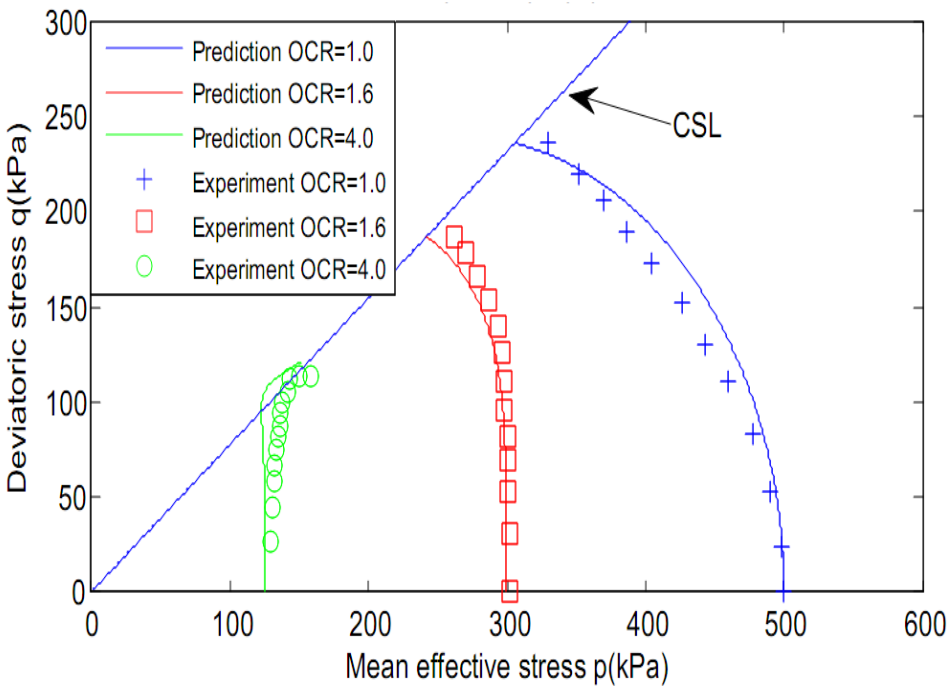

(b) Effective stress path after AZ-Cam clay model

Figure 5.19 Simulation on tests by Li & Meissner (2002)

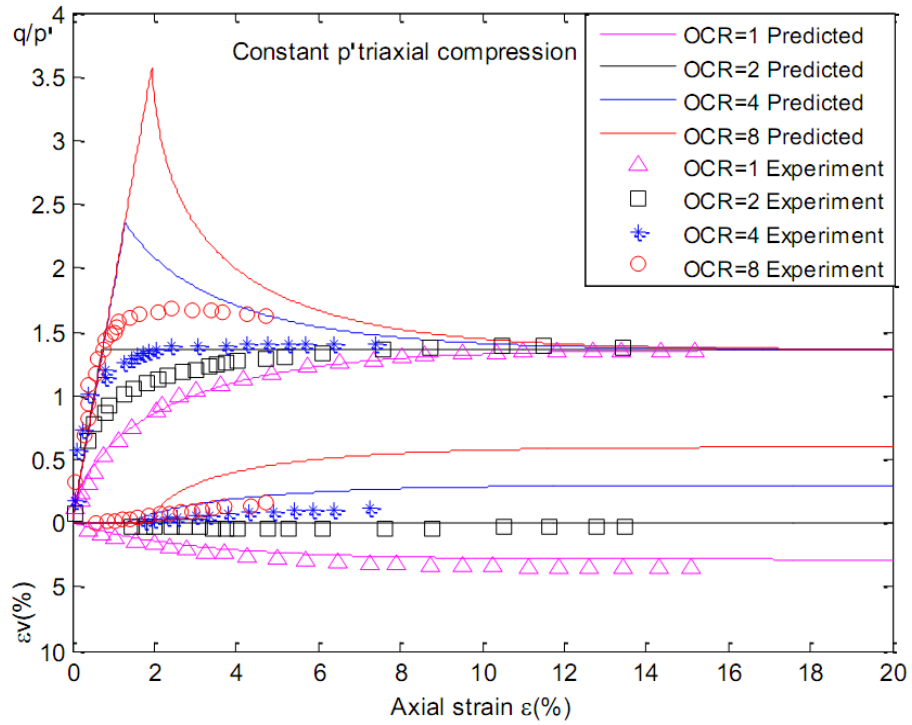

(a) MCC model prediction

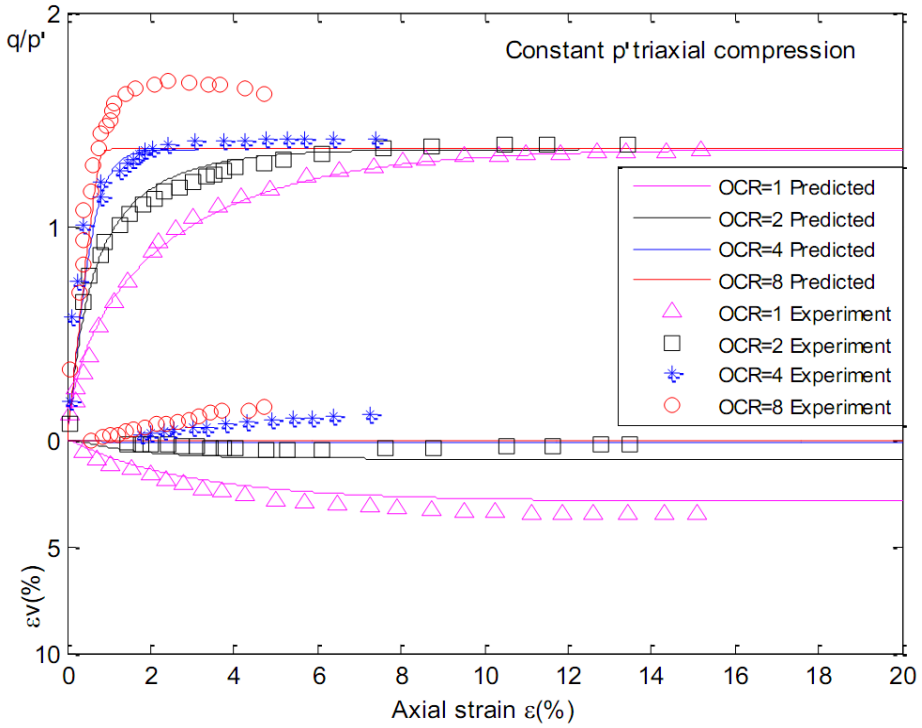

(b) Zienkiewicz *et al.* (1985) model prediction

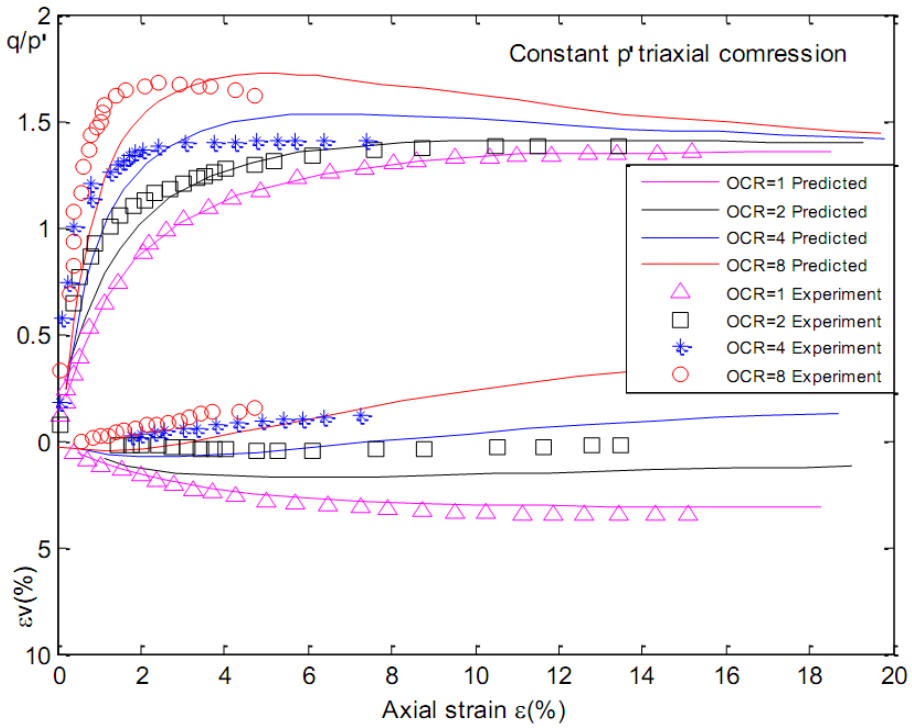

(c) Prediction after Nakai & Hinokio (2004)

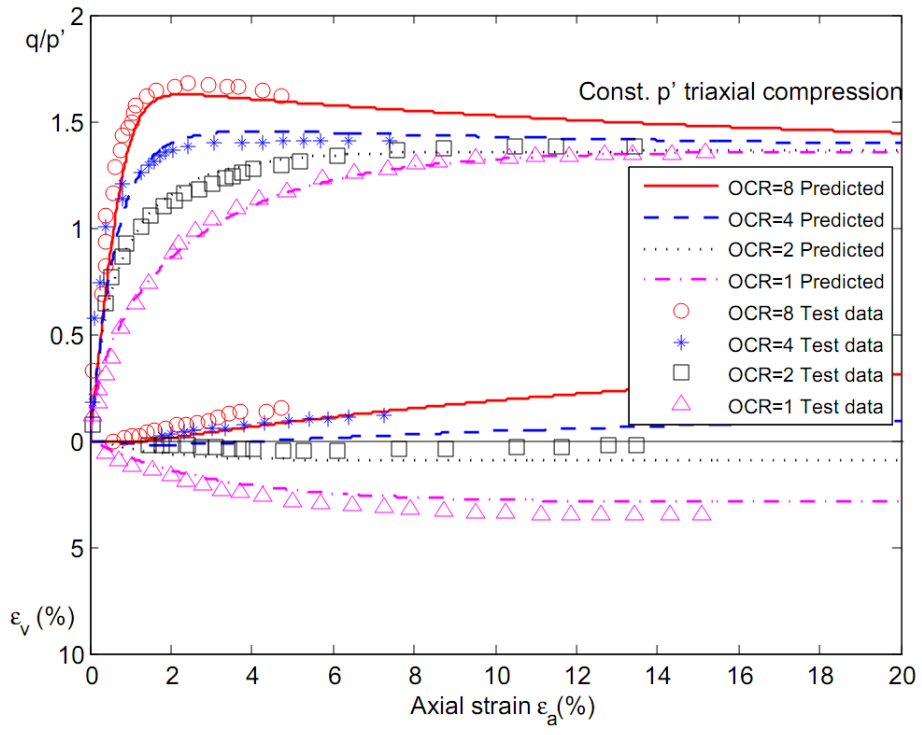

(d) AZ-Cam clay model prediction

Figure 5.20 Simulation on the test by Nakai & Hinokio (2004)-*CICP* compression

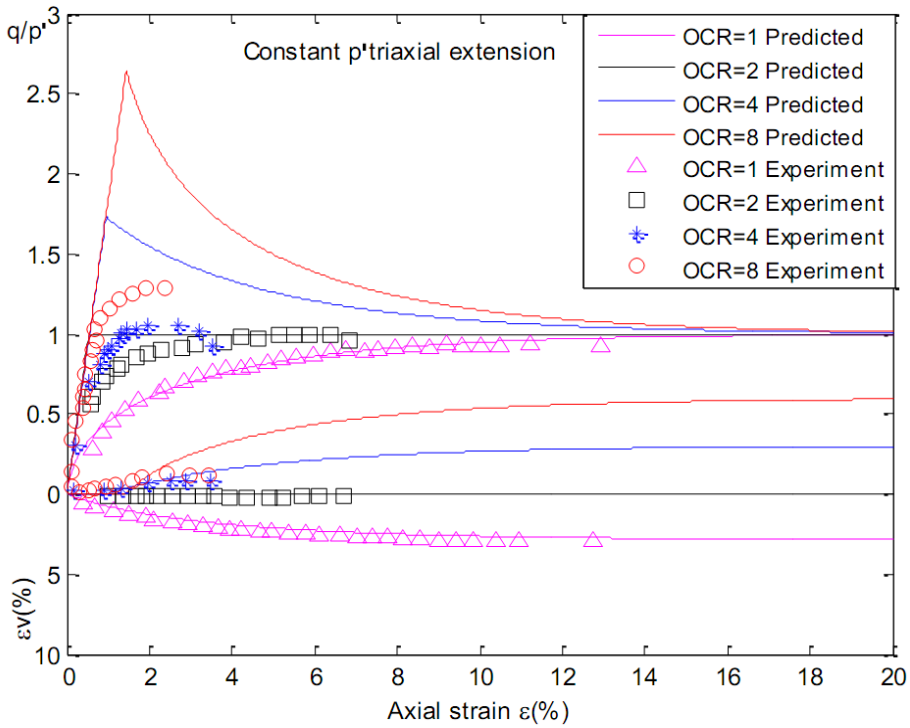

(a) MCC model prediction

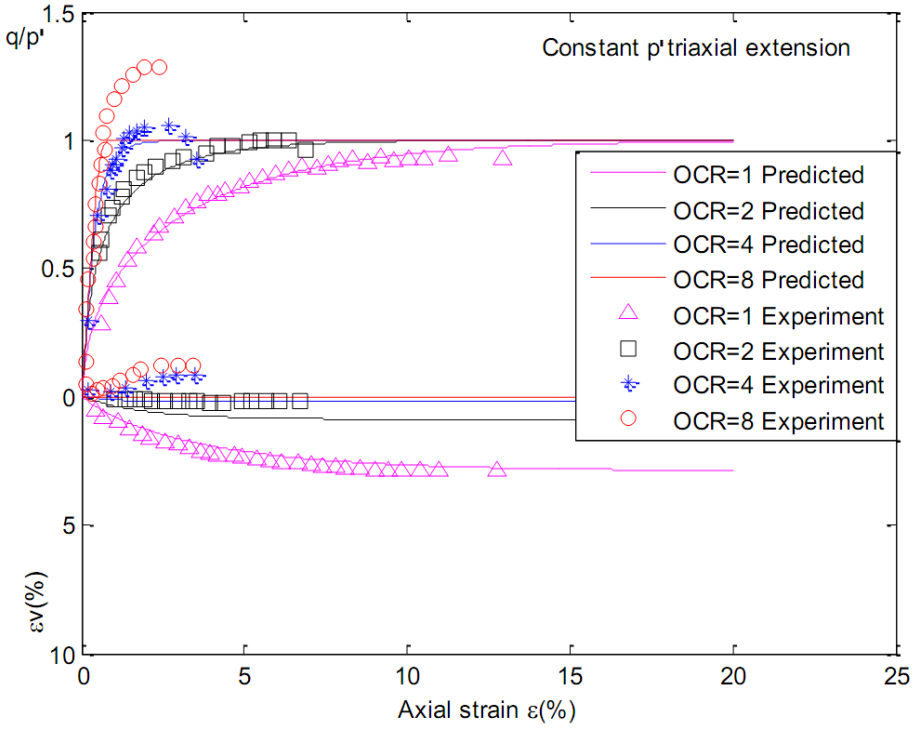

(b) Zienkiewicz *et al.* (1985) model prediction

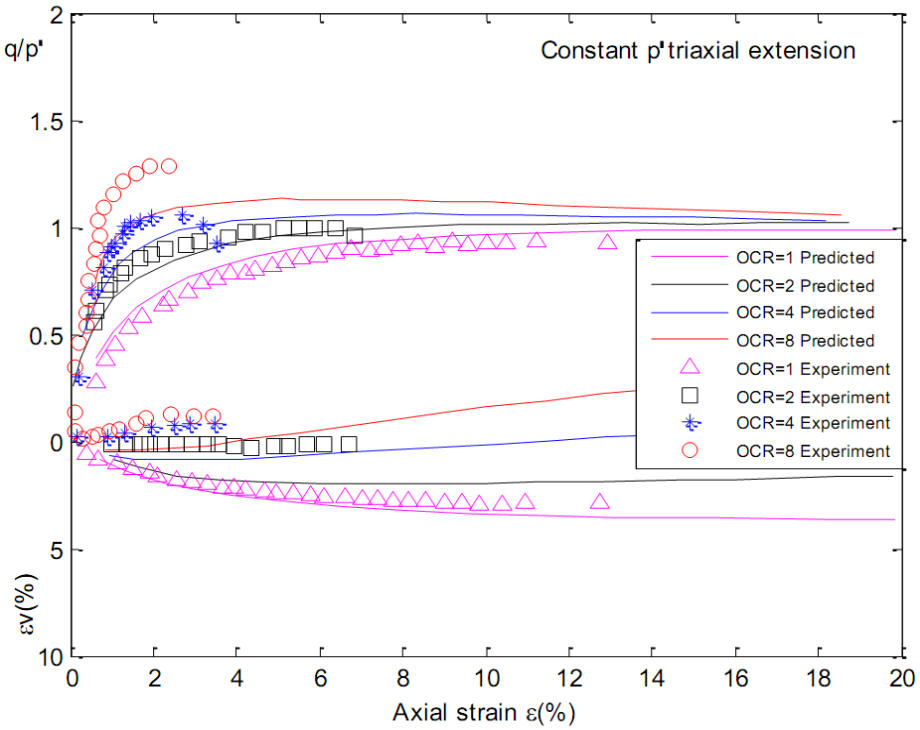

(c) Prediction after Nakai & Hinokio (2004)

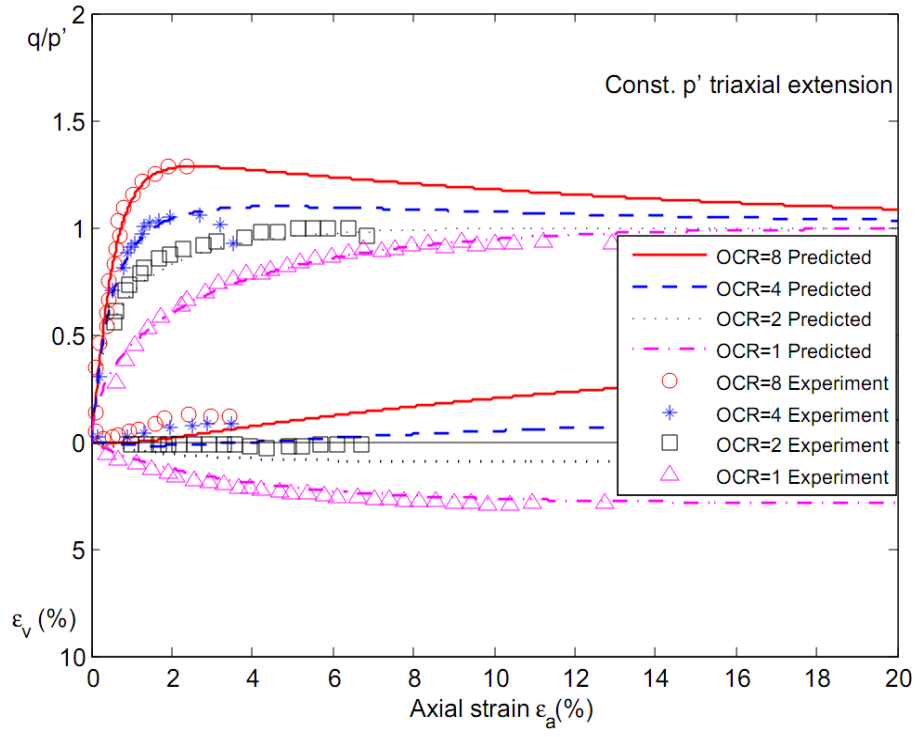

(d) AZ-Cam clay model prediction-*CICP* extension

Figure 5.21 Simulation on the test by Nakai & Hinokio (2004)-*CICP* extension

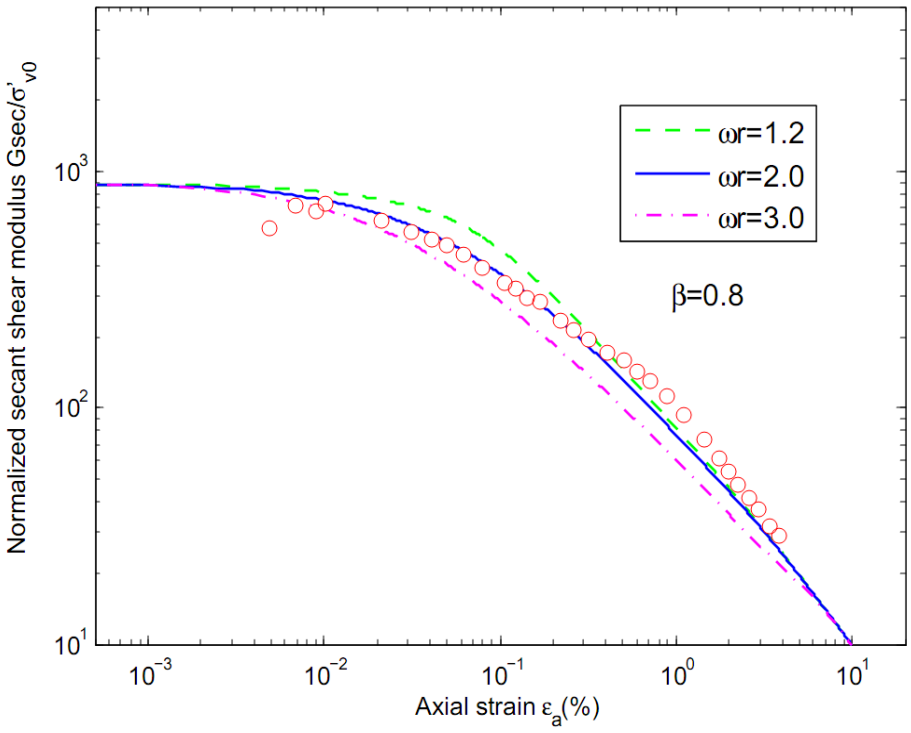

Figure 5.22 Estimation of ω_r for model input

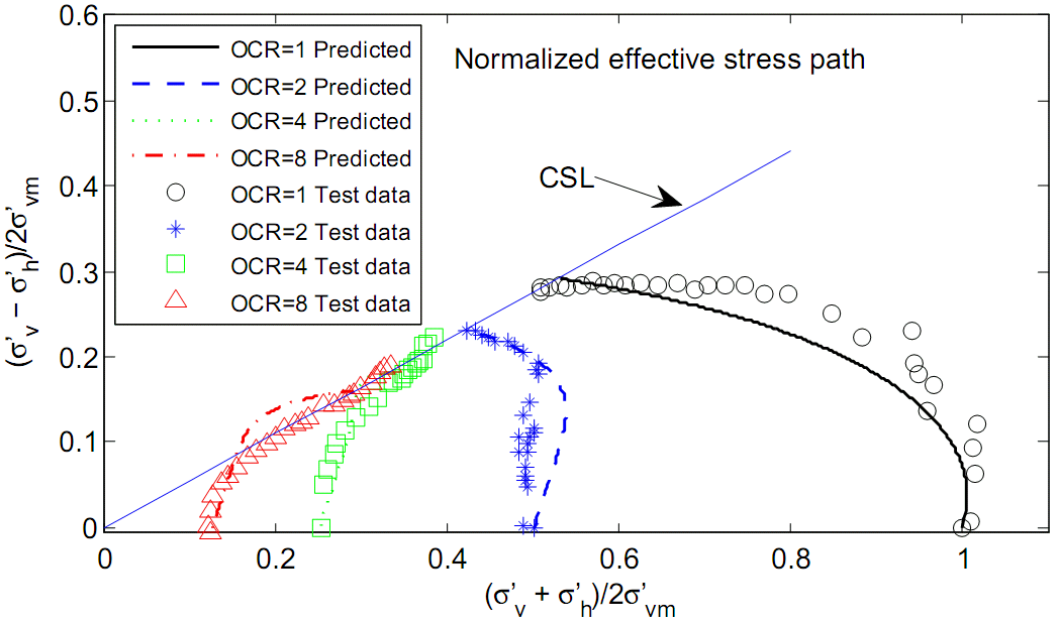

(a) Comparison of effective stress path

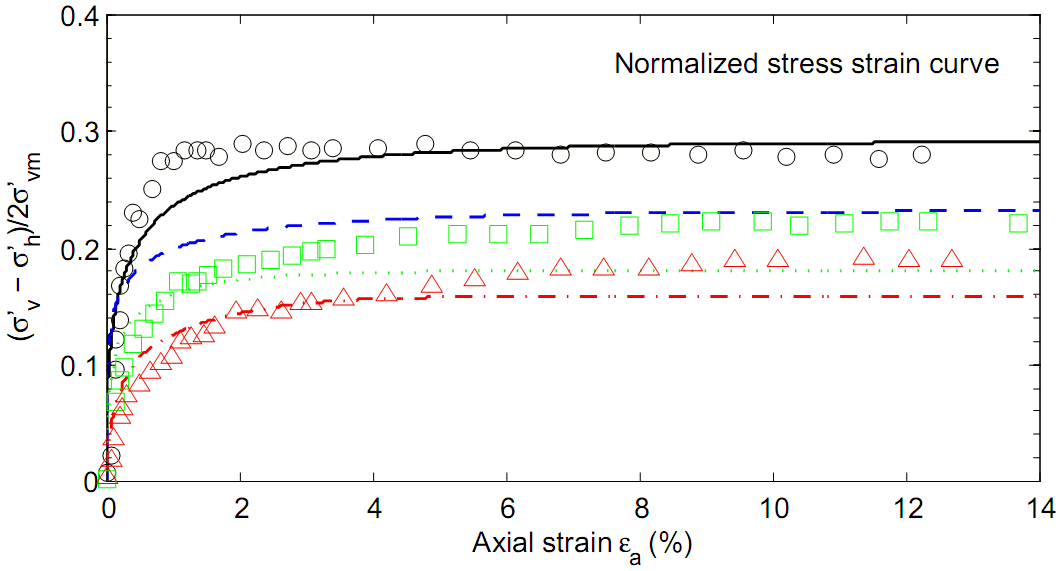

(b) Comparison of stress-strain behavior

Figure 5.23 Effect of *OCR* on the undrained behavior of BBC in *CIU* tests

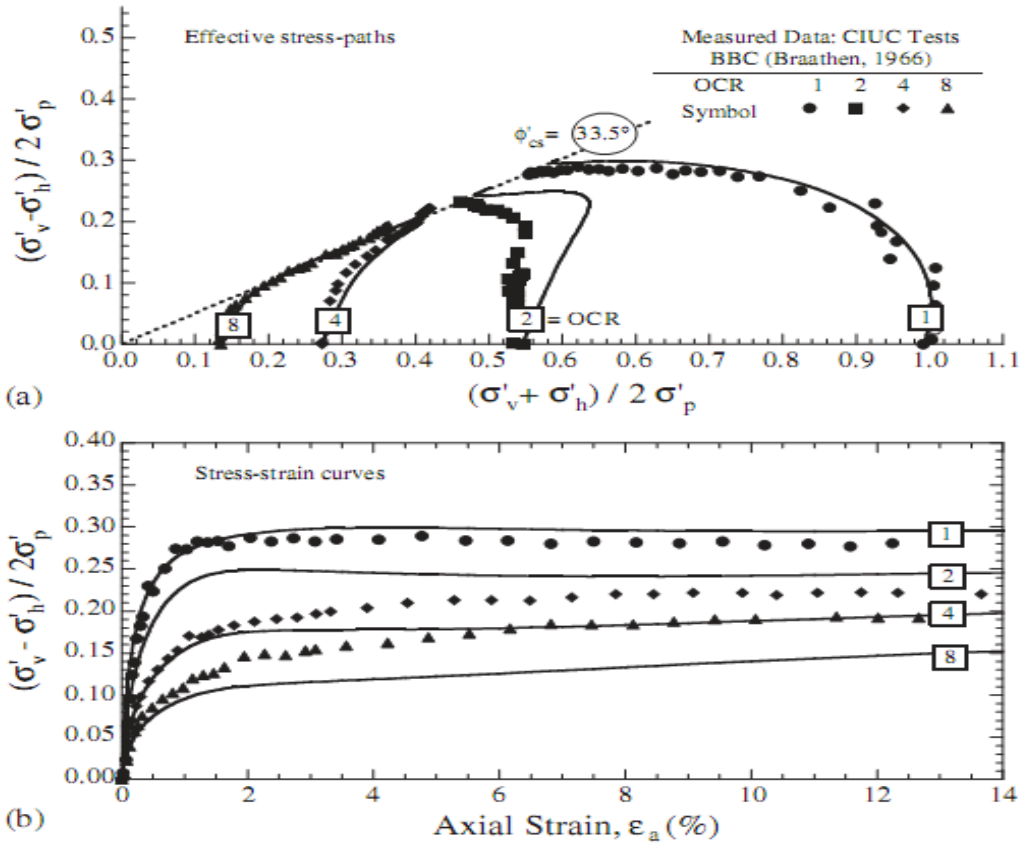

Figure 5.24 Predictions by MIT-S1 model after Pestana *et al.* (2002)

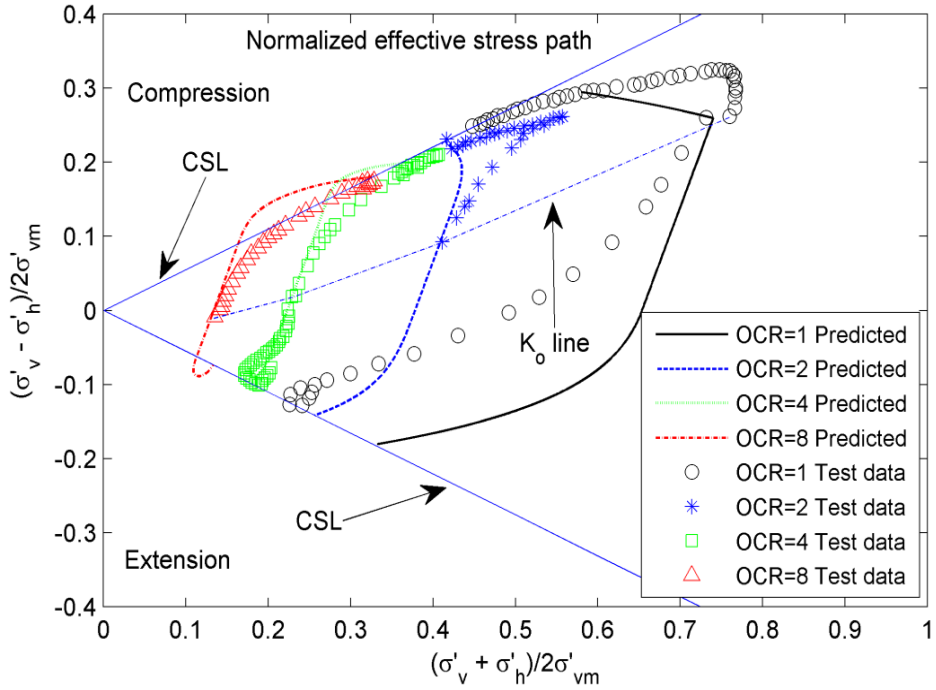

(a) Comparison of effective stress path

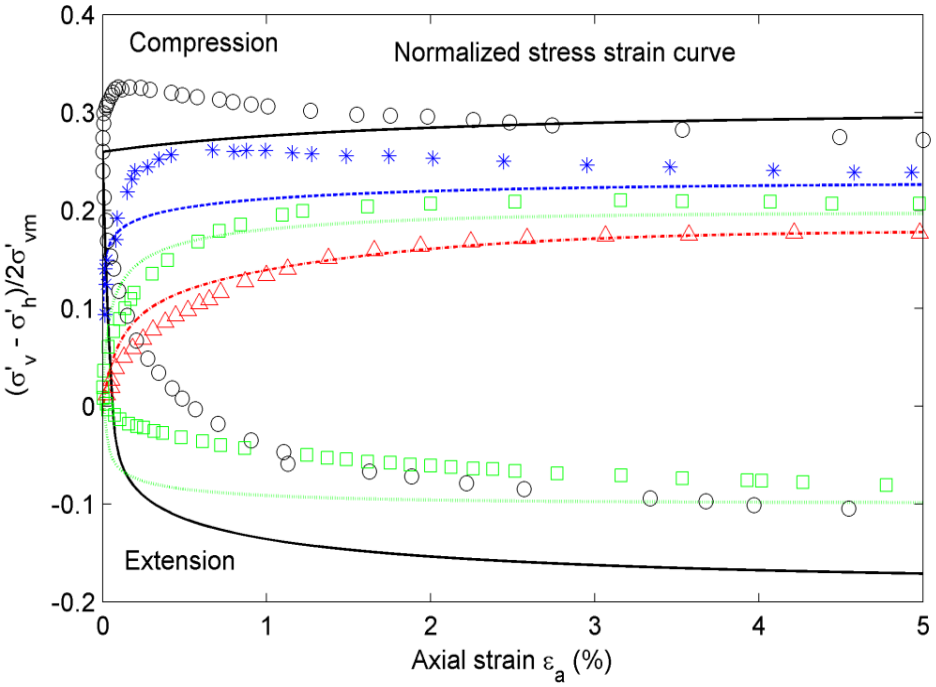

(b) Comparison of stress-strain behavior

Figure 5.25 Effect of *OCR* on the undrained behavior of BBC in CK_0UC tests

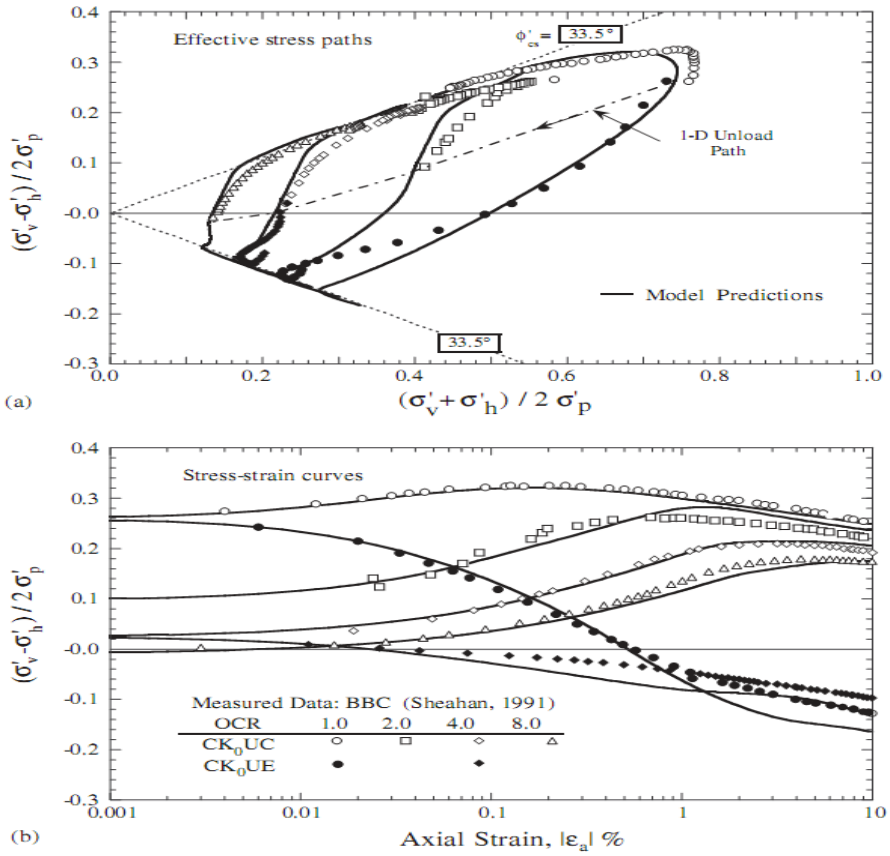

Figure 5.26 Predictions by MIT-S1 model after Pestana *et al.* (2002)

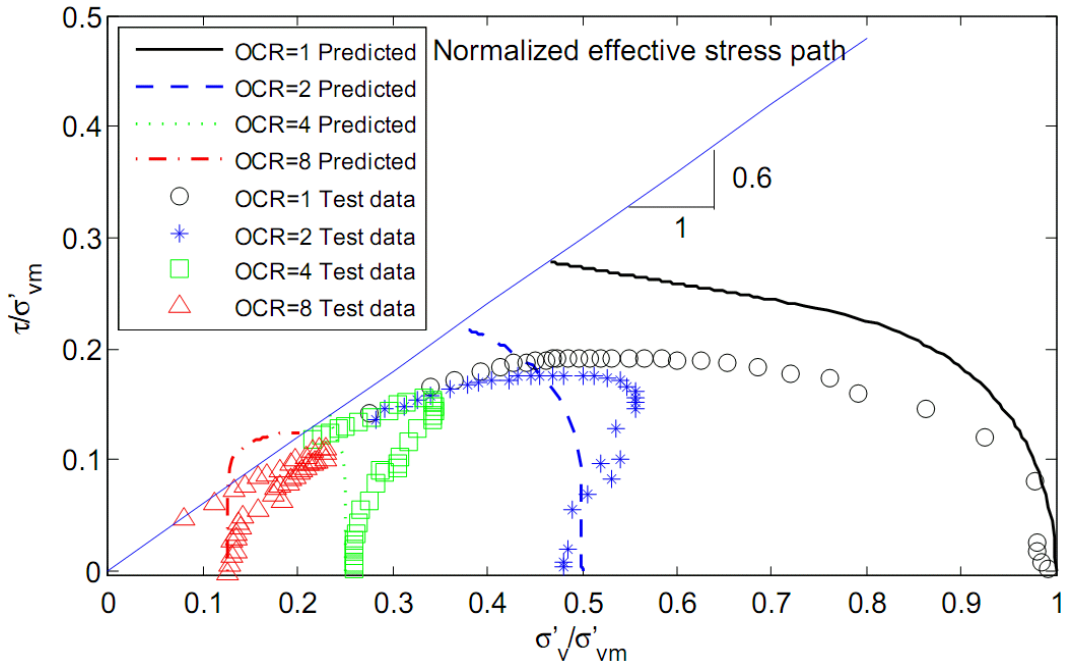

(a) Comparison of effective stress path

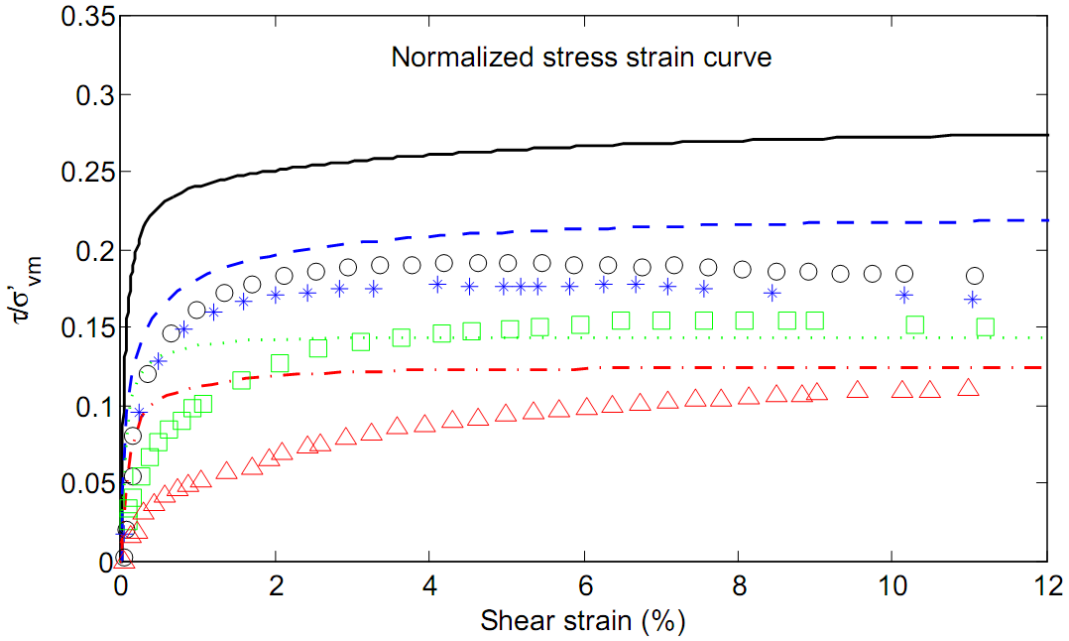

(b) Comparison of stress-strain behavior

Figure 5.27 Effect of *OCR* on the undrained behavior of BBC in CK_0UDSS tests

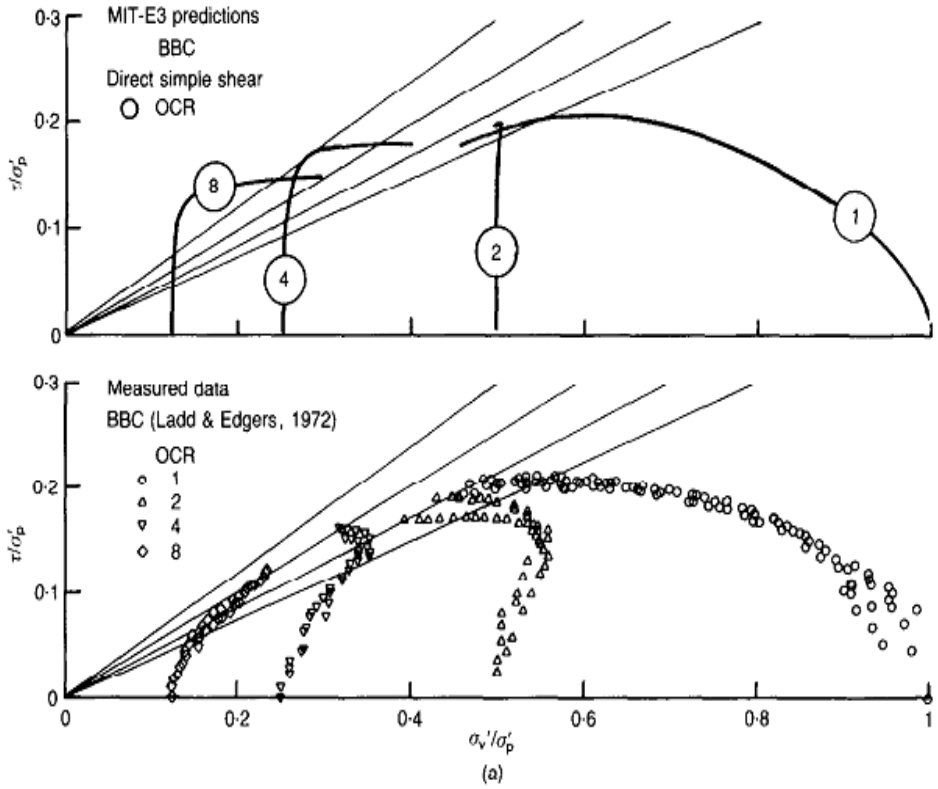

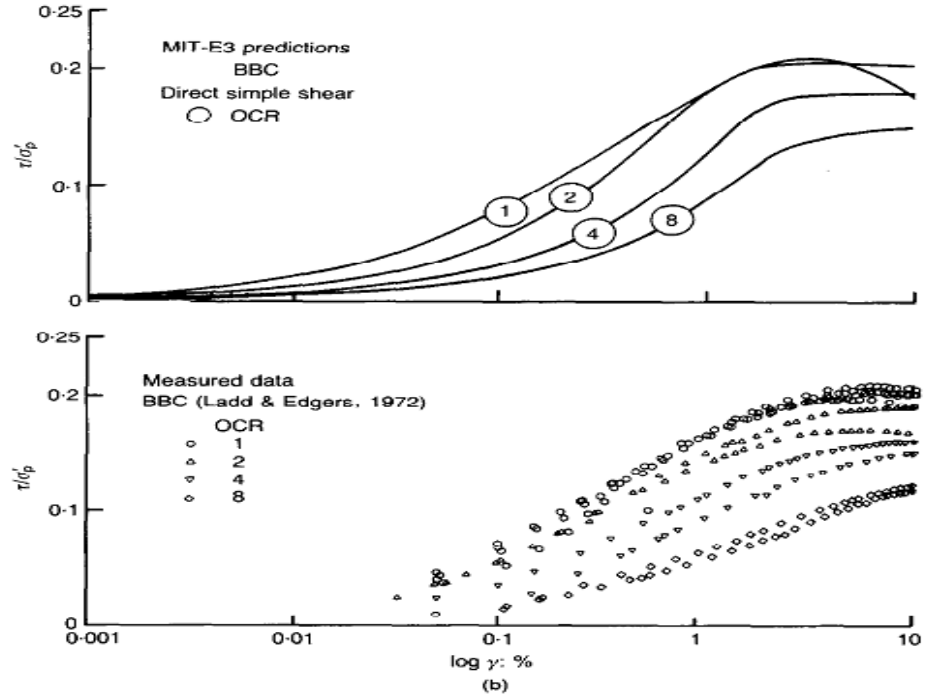

Figure 5.28 Predictions by MIT-E3 model after Whittle (1987)

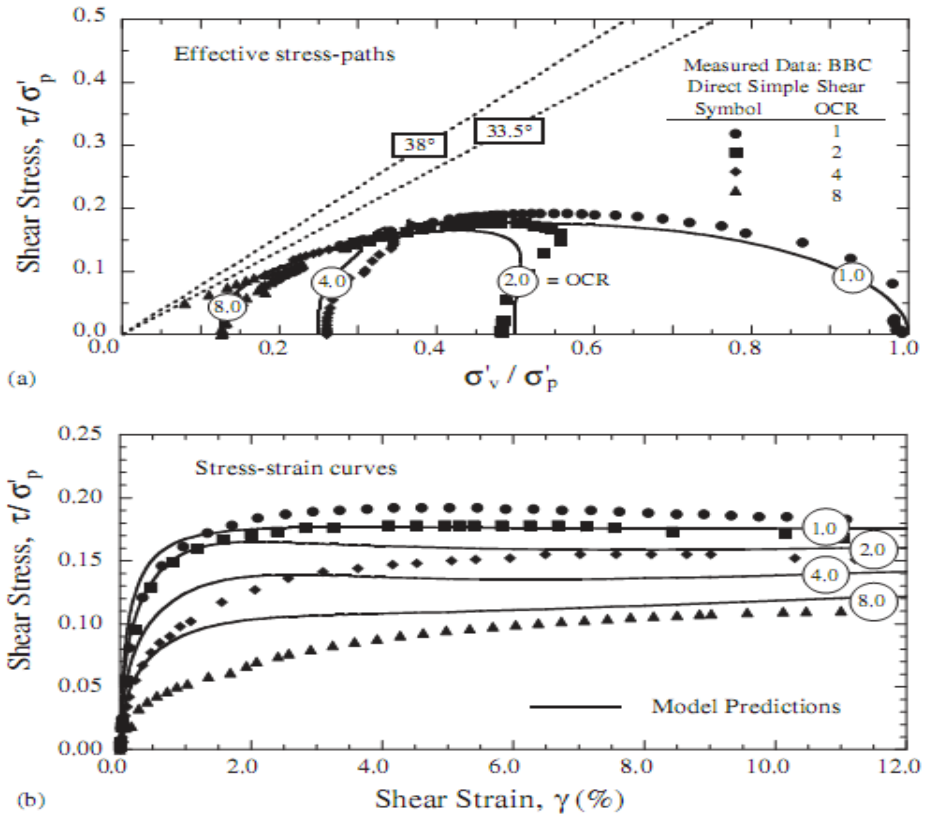

Figure 5.29 Predictions by MIT-S1 model after Pestana *et al.* (2002)

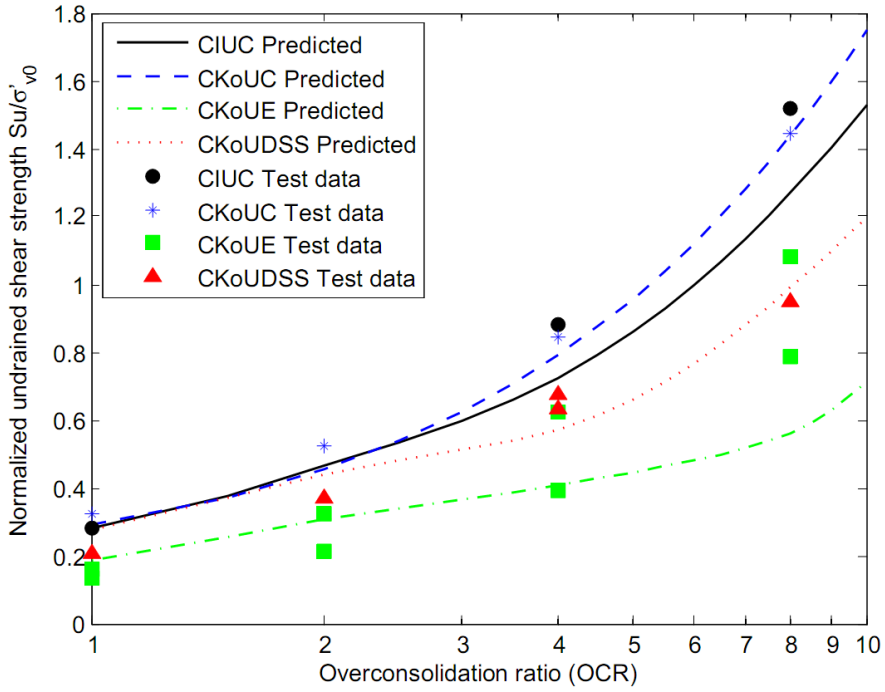

Figure 5.30 Model predictions of S_u of BBC for various modes of shearing

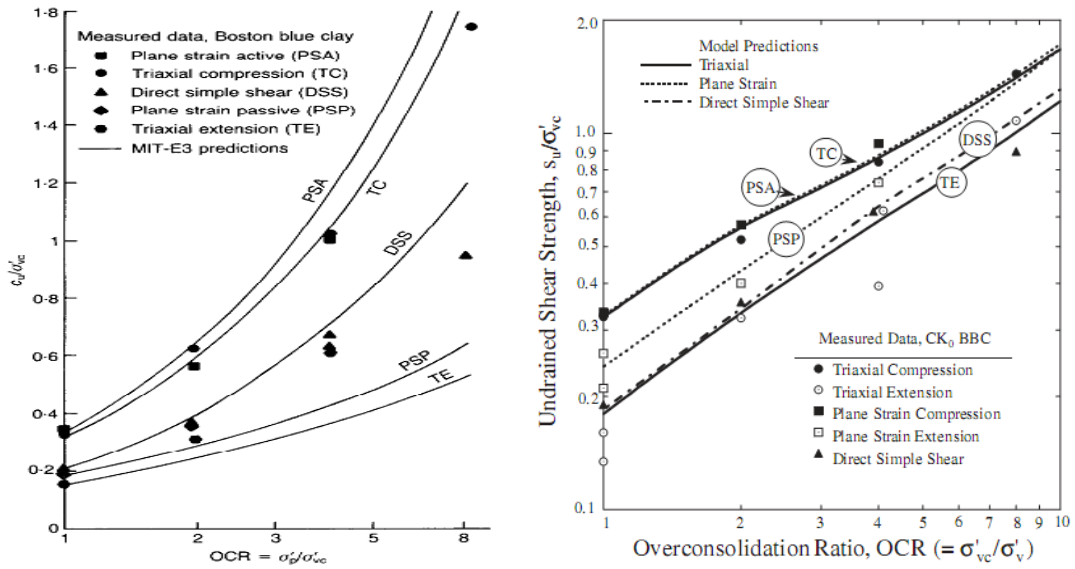

(a) MIT-E3 model (Whittle, 1987) (b) MIT-S1 model (Pestana *et al.*, 2002)

Figure 5.31 Other model predictions

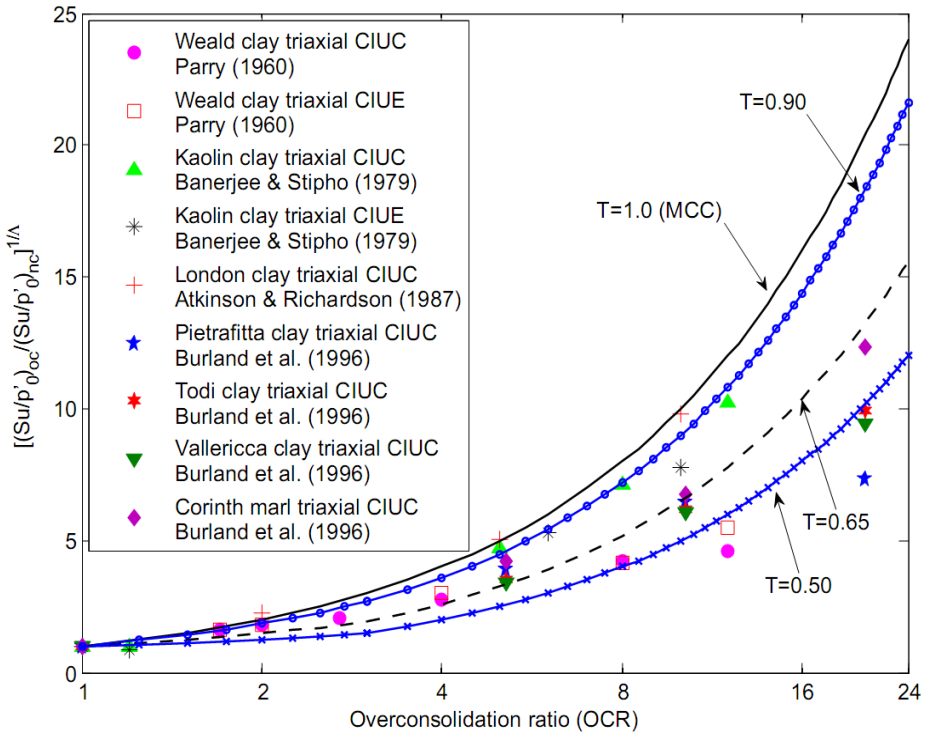

Figure 5.32 Variation of normalized undrained shear strength-*CIU* tests

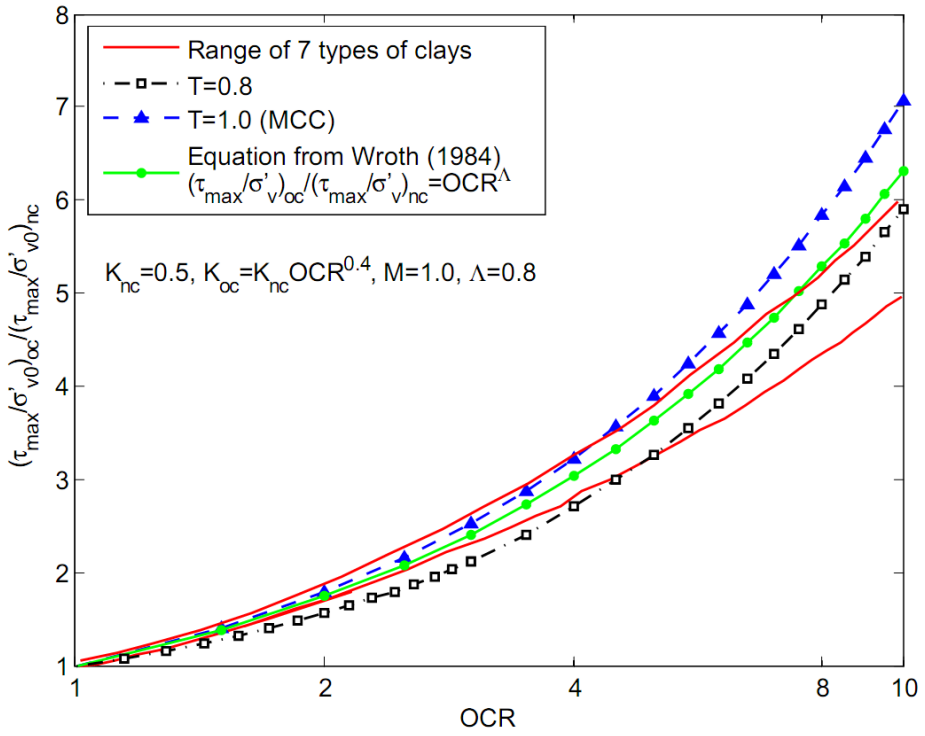

Figure 5.33 Variation of normalized undrained shear strength- CK_0UDSS tests

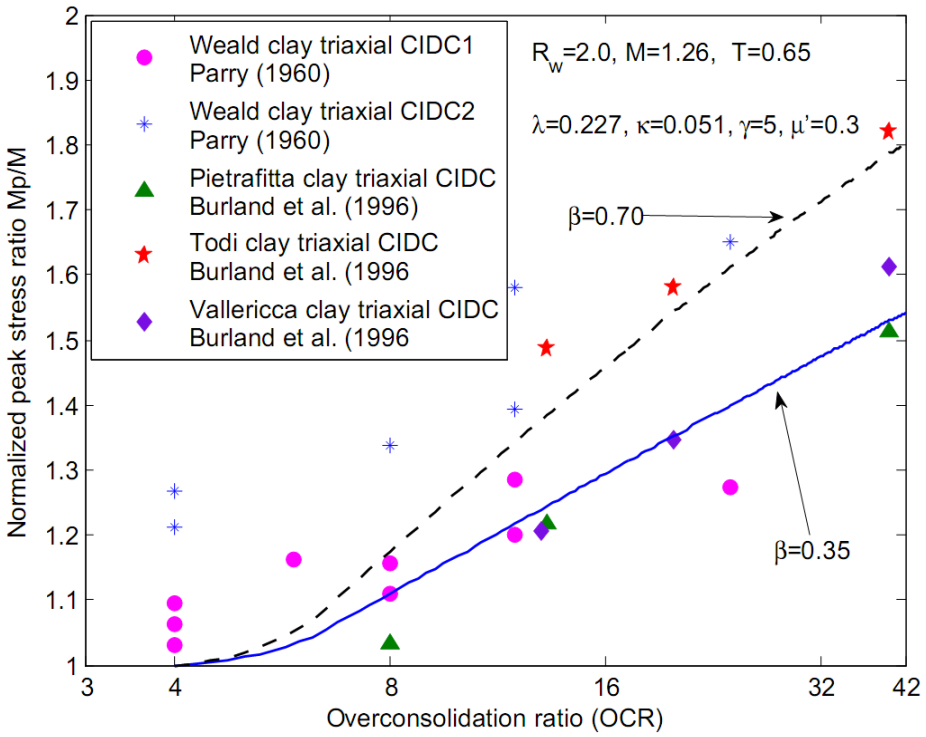

Figure 5.34 Variation of normalized peak stress ratio with *OCRs* in *CIDC* tests

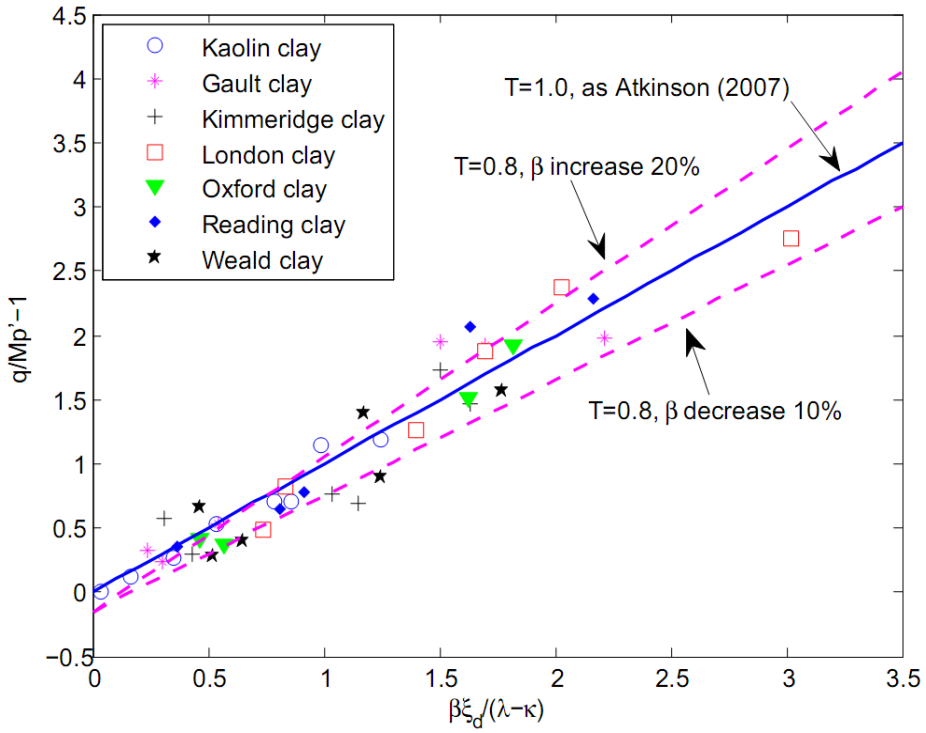

Figure 5.35 Peak state of OC clay normalized with state parameter

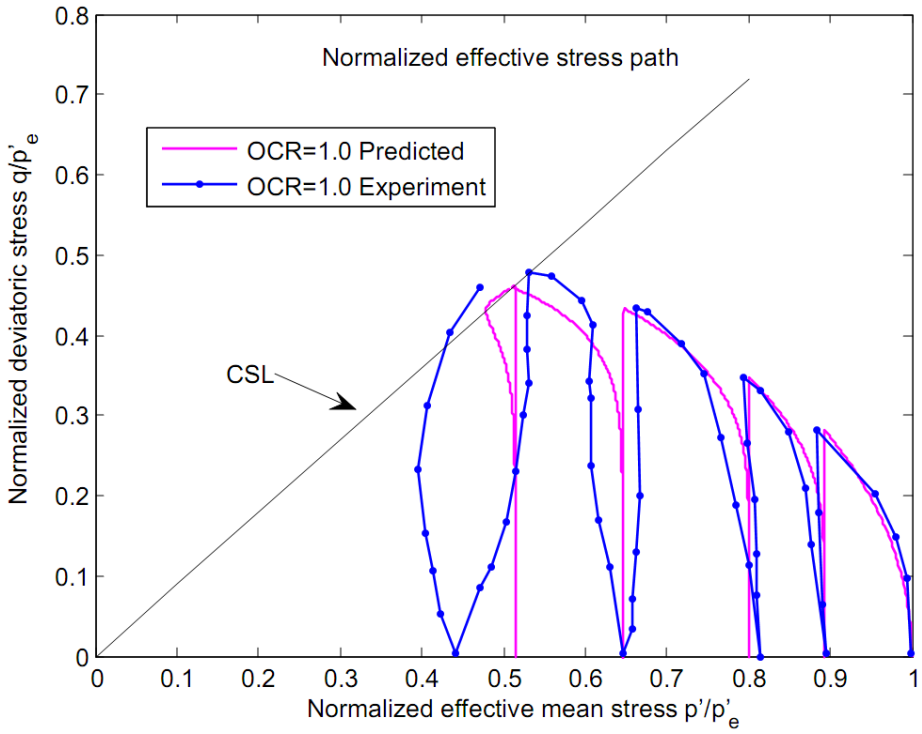

Figure 5.36 AZ-Cam clay model prediction of cyclic *CIU* test on NC kaolin clay

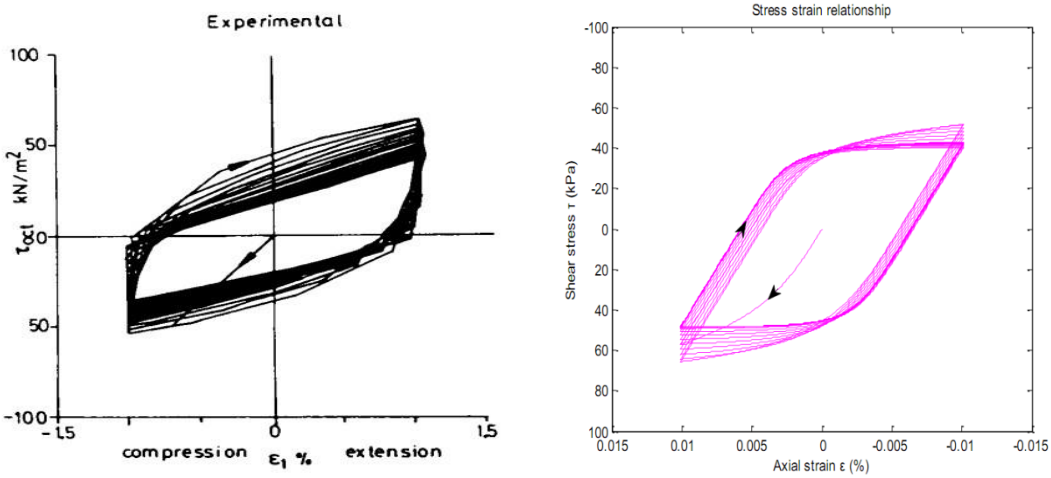

(a) Measured data (b) Predicted using $G = 8000kPa$

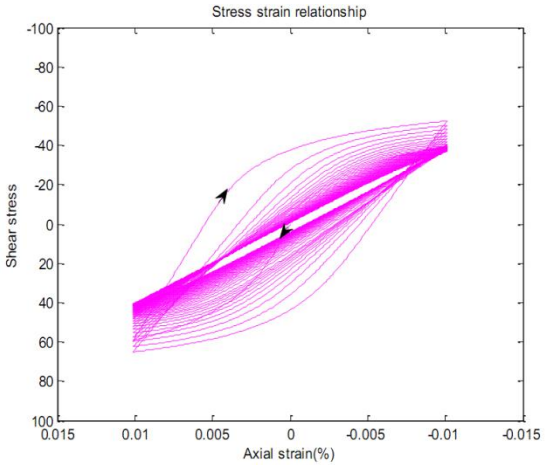

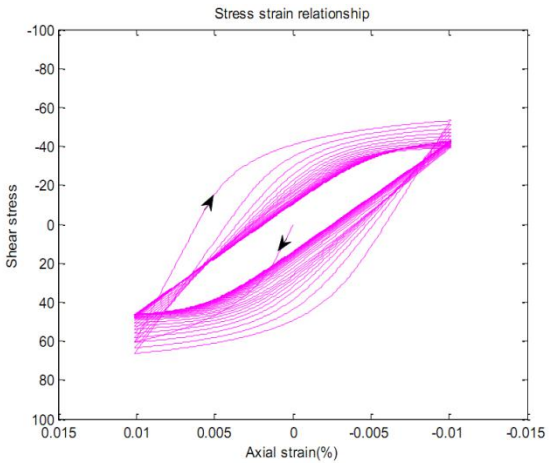

(c) Predicted using $\nu = 0.15$ (d) Predicted using $\nu = 0.10$

Figure 5.37 Measured and predicted stress strain relationship

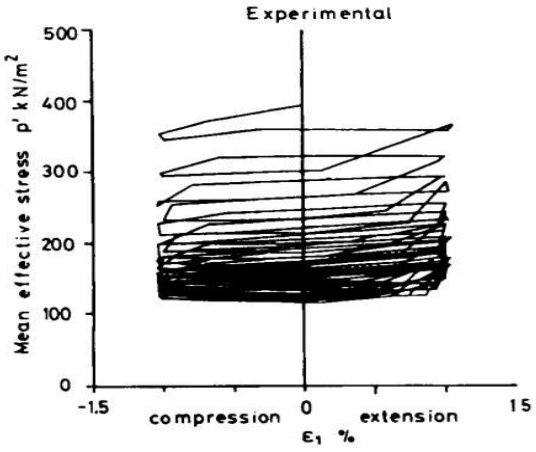

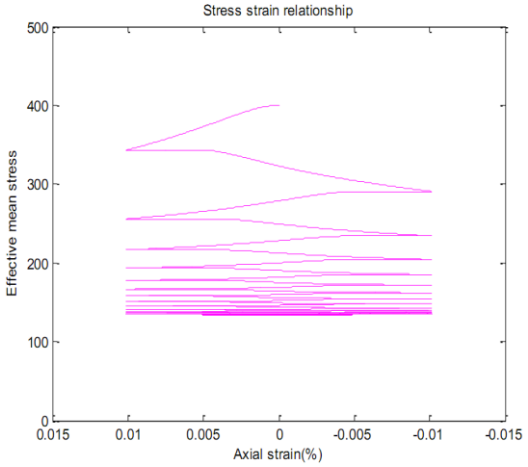

(a) Measured data (b) Predicted using $G = 8000kPa$

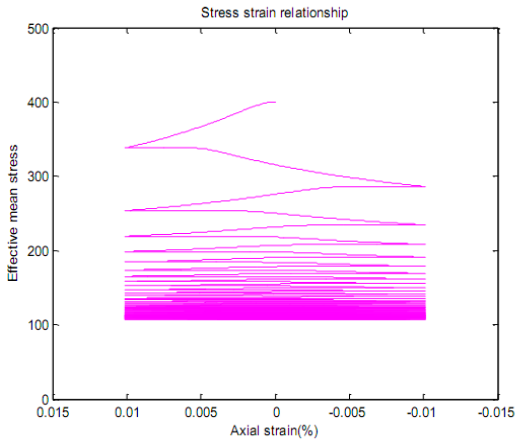

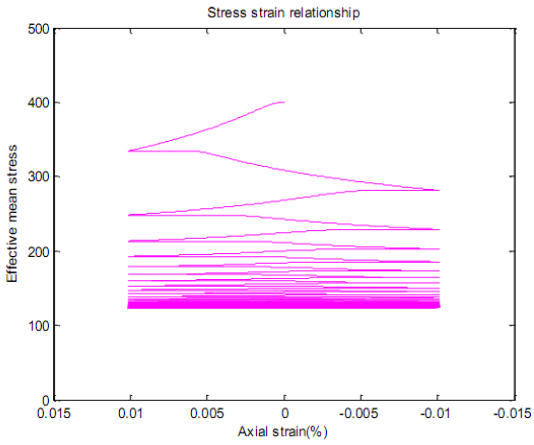

(c) Predicted using $\nu = 0.15$ (d) Predicted using $\nu = 0.10$

Figure 5.38 Measured and predicted effective mean stress

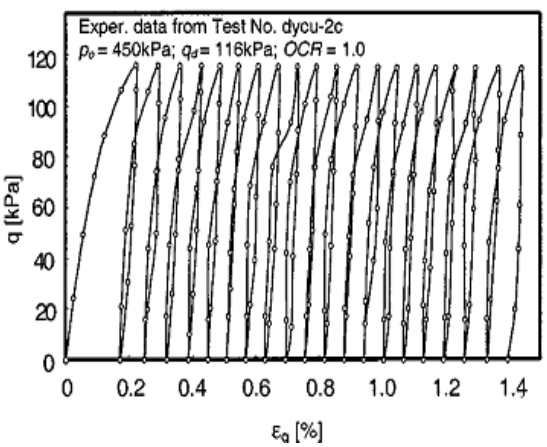

(a) Stress loop

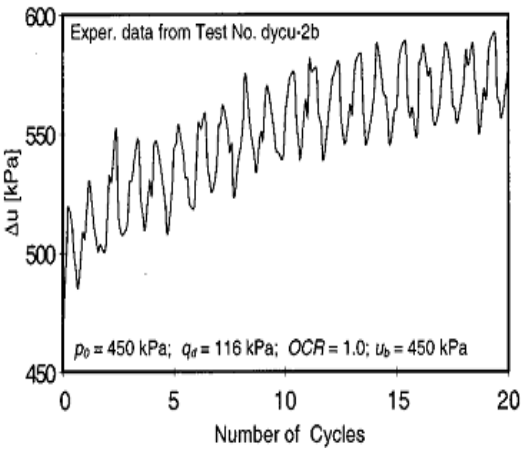

(b) Excess pore pressure

Figure 5.39 Measured data

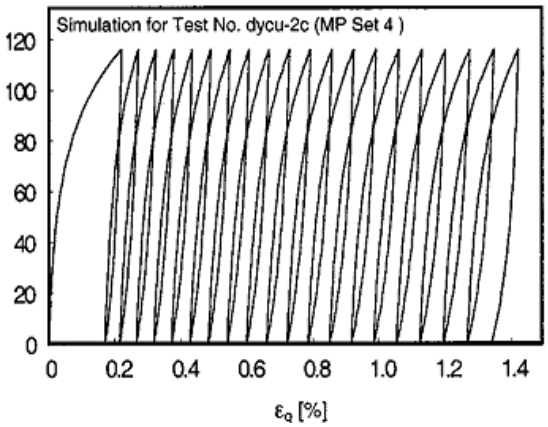

(a) Stress loop

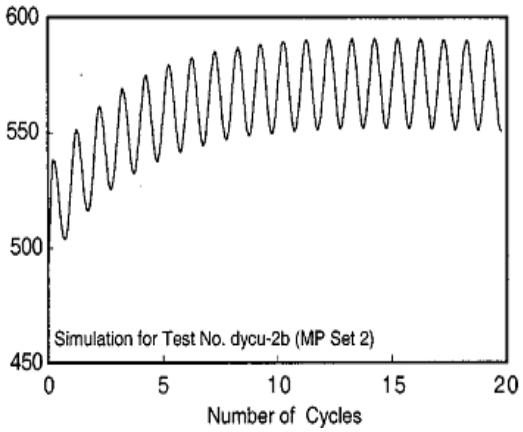

(b) Excess pore pressure

Figure 5.40 Predicted by Li and Hum (2002)

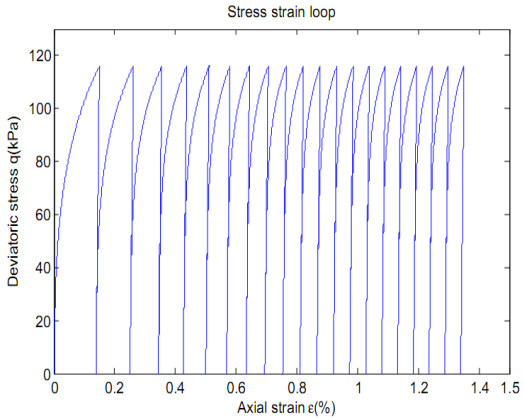

(a) Stress loop

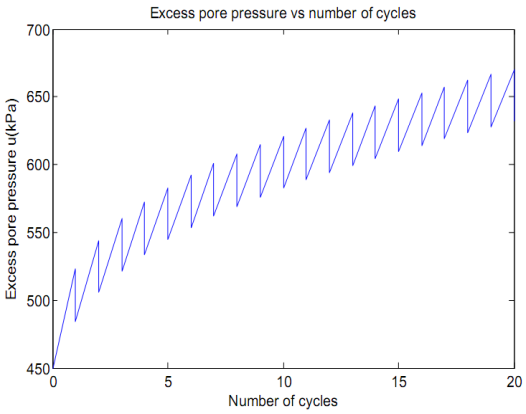

(b) Excess pore pressure

Figure 5.41 Predicted by AZ-Cam clay model

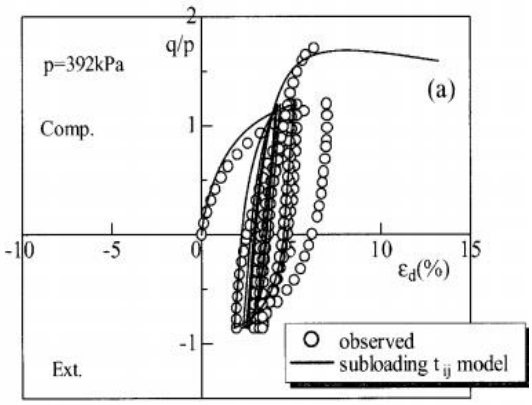

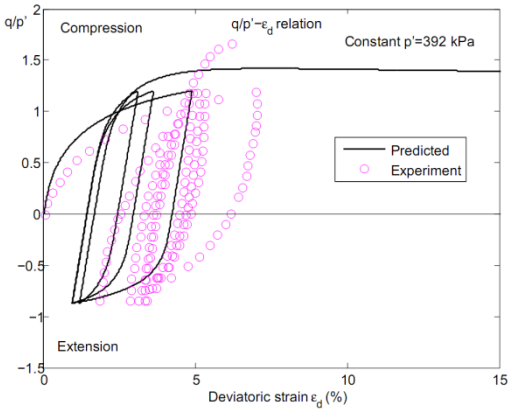

(a) t_{ij} model-stress-strain curve (b) AZ-Cam clay model-stress-strain curve

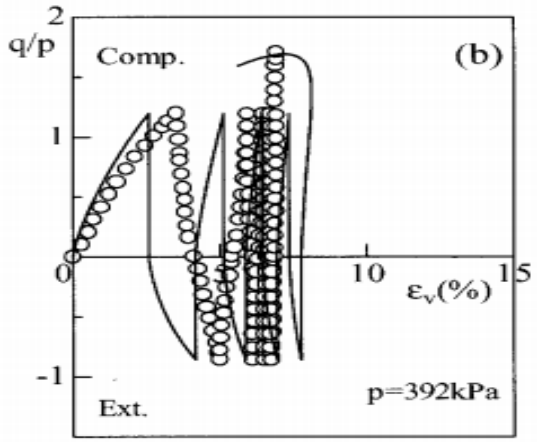

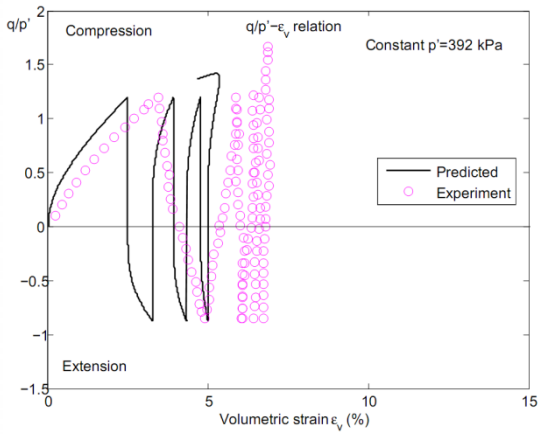

(c) t_{ij} model-volumetric behavior (d) AZ-Cam clay model-volumetric behavior

Figure 5.42 Cyclic *CICP* (constant load level) test on NC Fujinomori clay

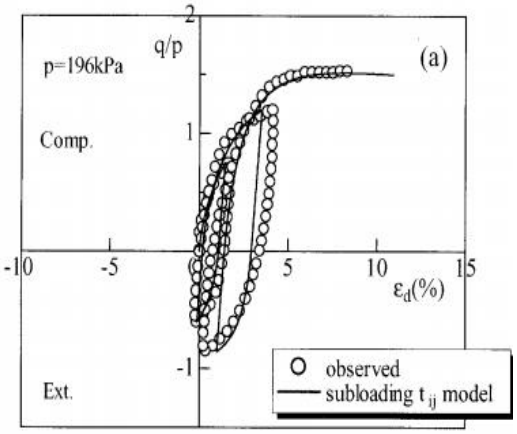

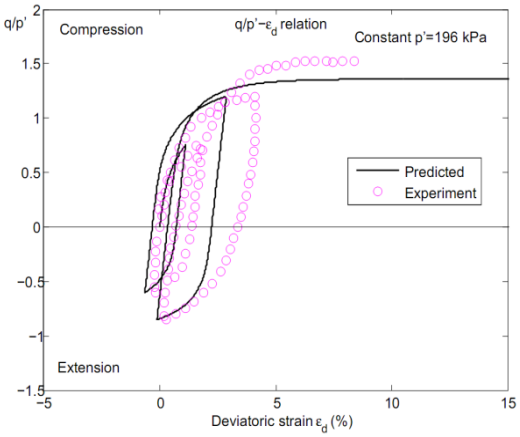

(a) t_{ij} model-stress strain curve (b) AZ-Cam clay model-stress strain curve

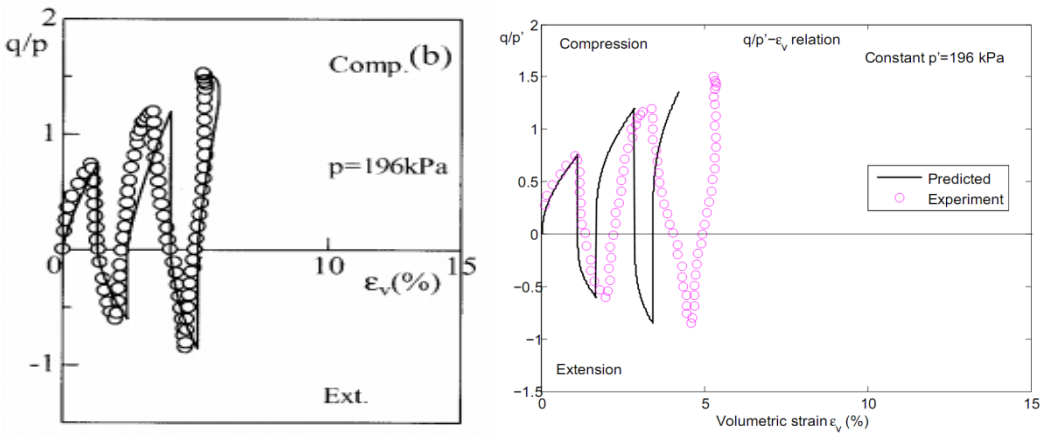

(c) t_{ij} model-volumetric behavior (d) AZ-Cam clay model-volumetric behavior

Figure 5.43 Cyclic *CICP* (varied load level) test on NC Fujinomori clay

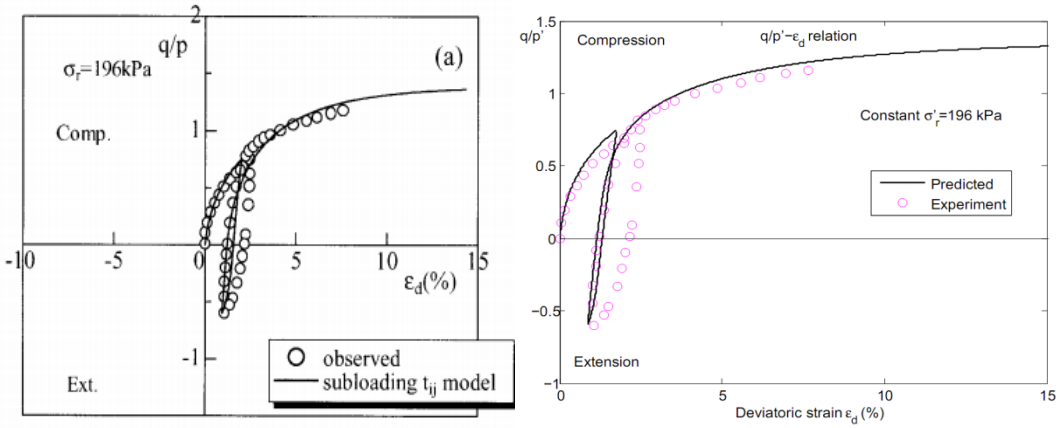

(a) t_{ij} model-stress strain curve (b) AZ-Cam clay model-stress strain curve

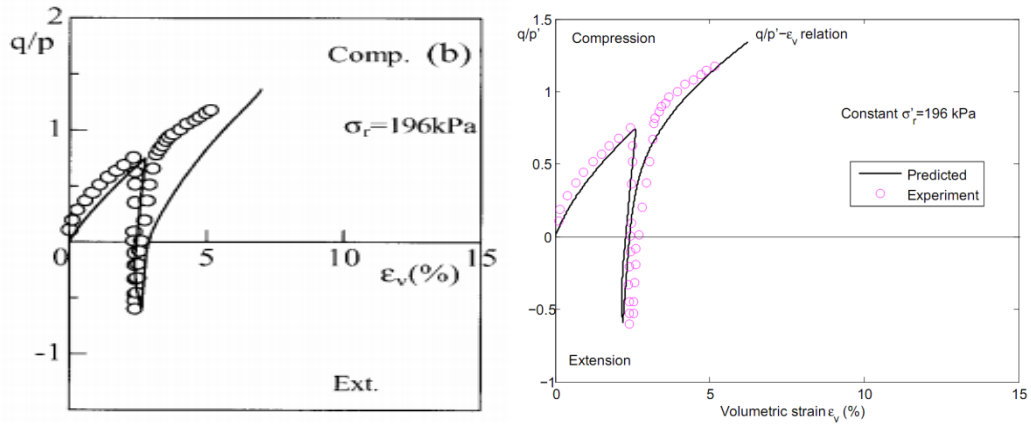

(c) t_{ij} model-volumetric behavior (d) AZ-Cam clay model-volumetric behavior

Figure 5.44 Cyclic *CID* test on NC Fujinomori clay

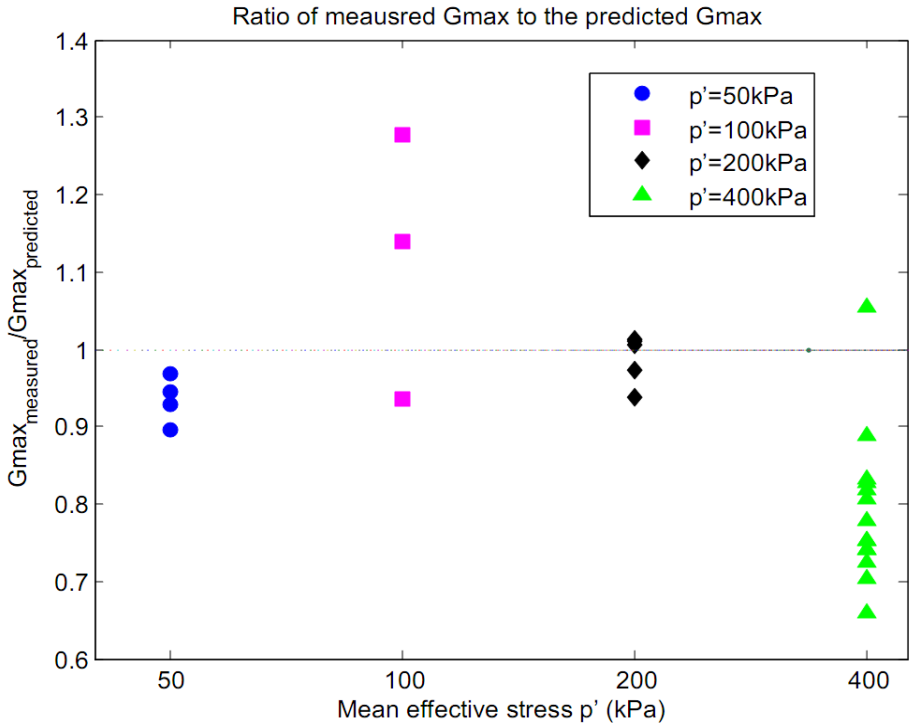

Figure 5.45 Measured G_{max} and predicted G_{max}

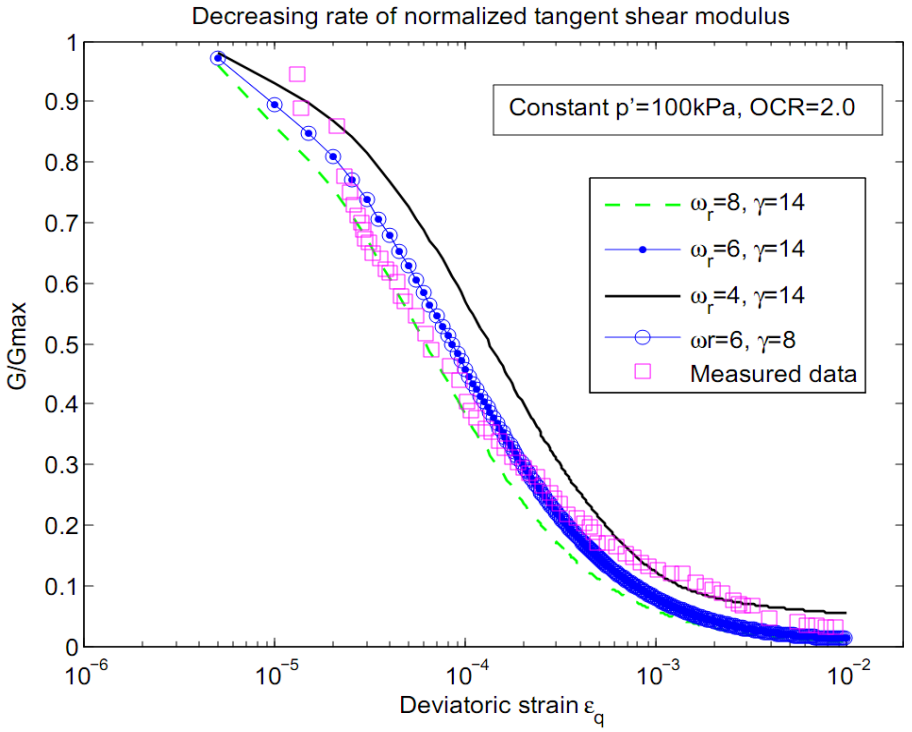

Figure 5.46 Determination of ω_r

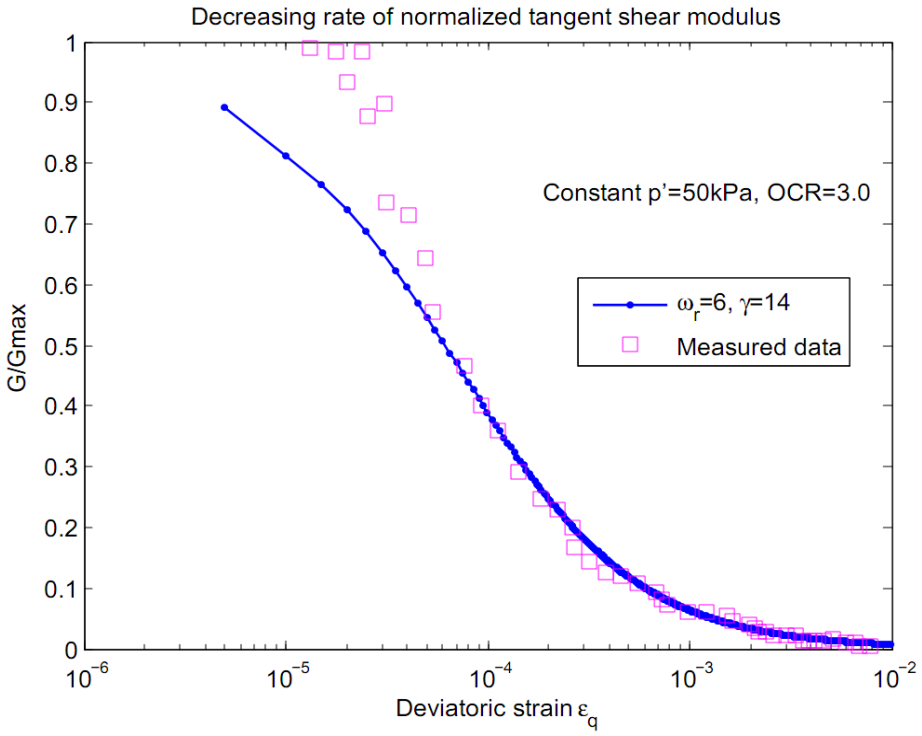

Figure 5.47 Determination of γ

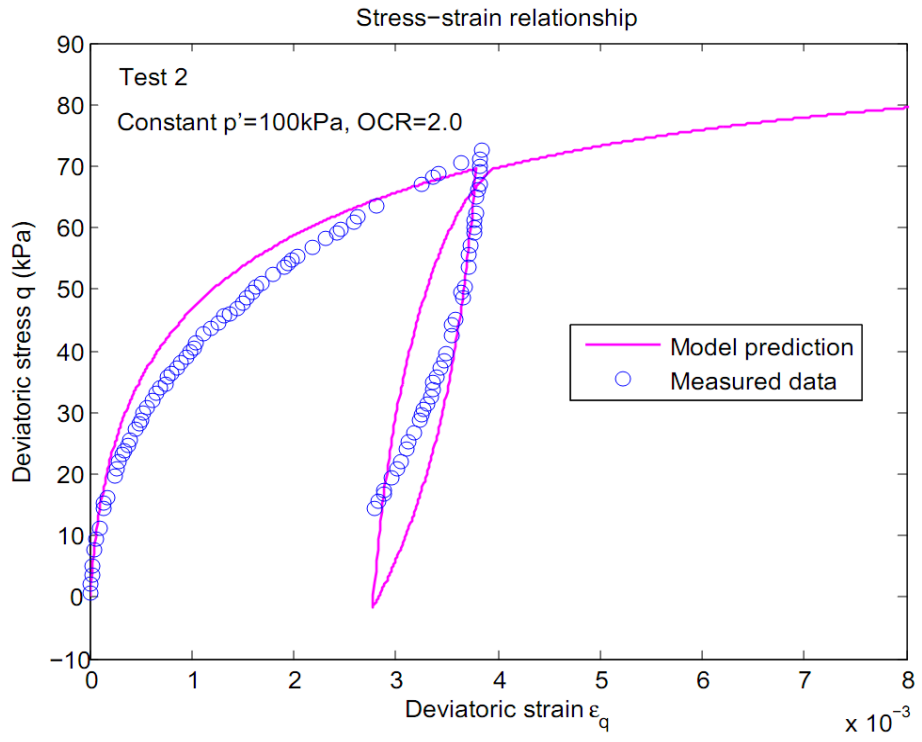

Figure 5.48 Simulation of Test 2 after Dasari (1996)

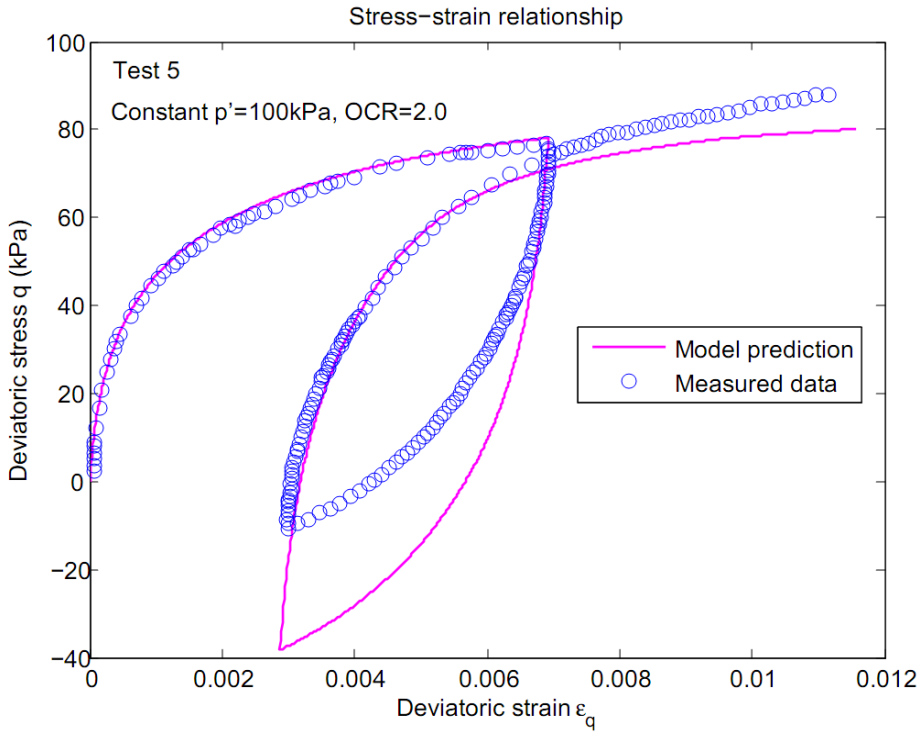

Figure 5.49 Simulation of Test 5 after Dasari (1996)

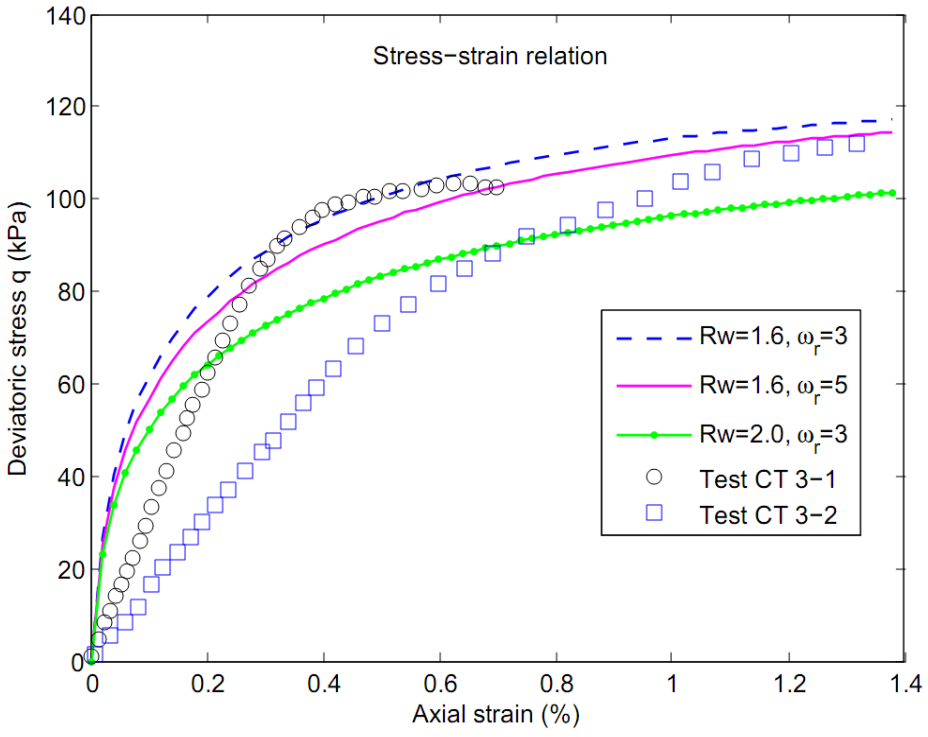

Figure 5.50 Determination of R_w and ω_r

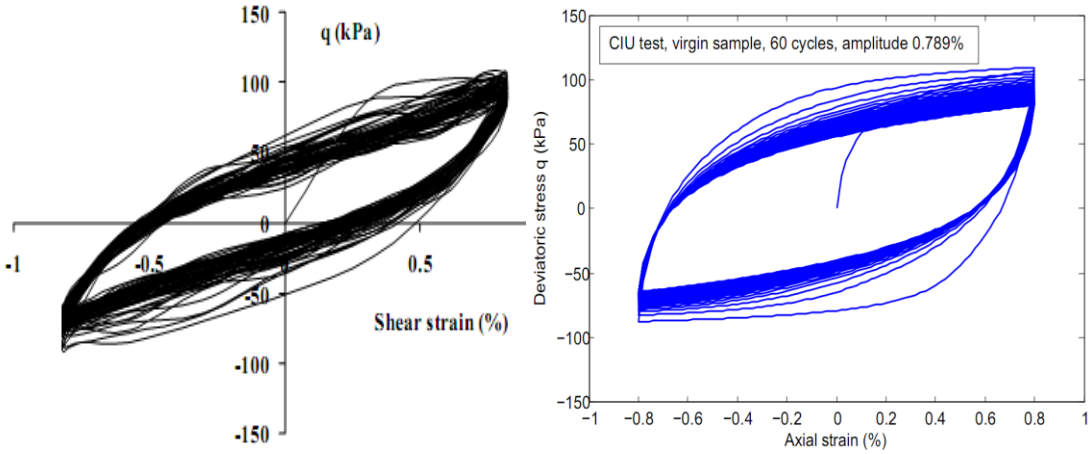

(a) Measured data (b) AZ-Cam clay model prediction

Figure 5.51 Comparison of stress strain loops

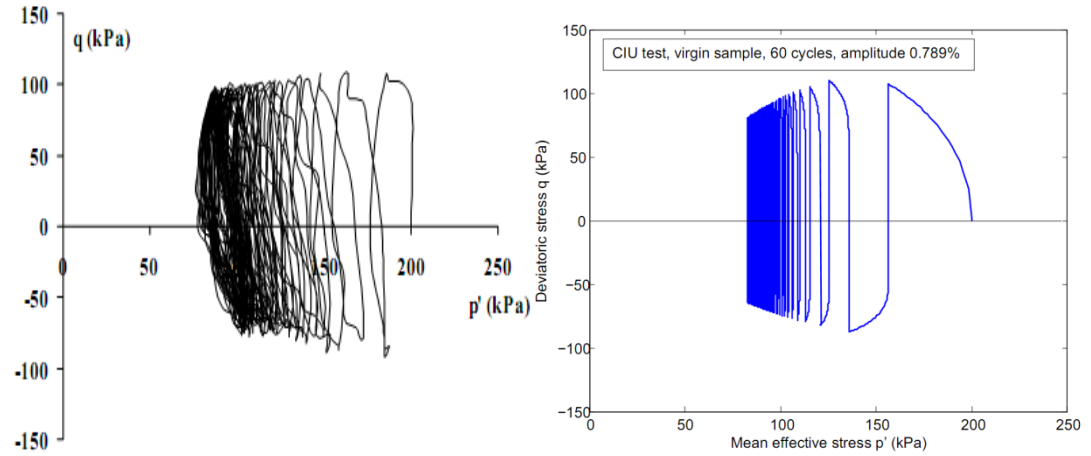

(a) Measured data (b) AZ-Cam clay model prediction

Figure 5.52 Comparison of effective stress path

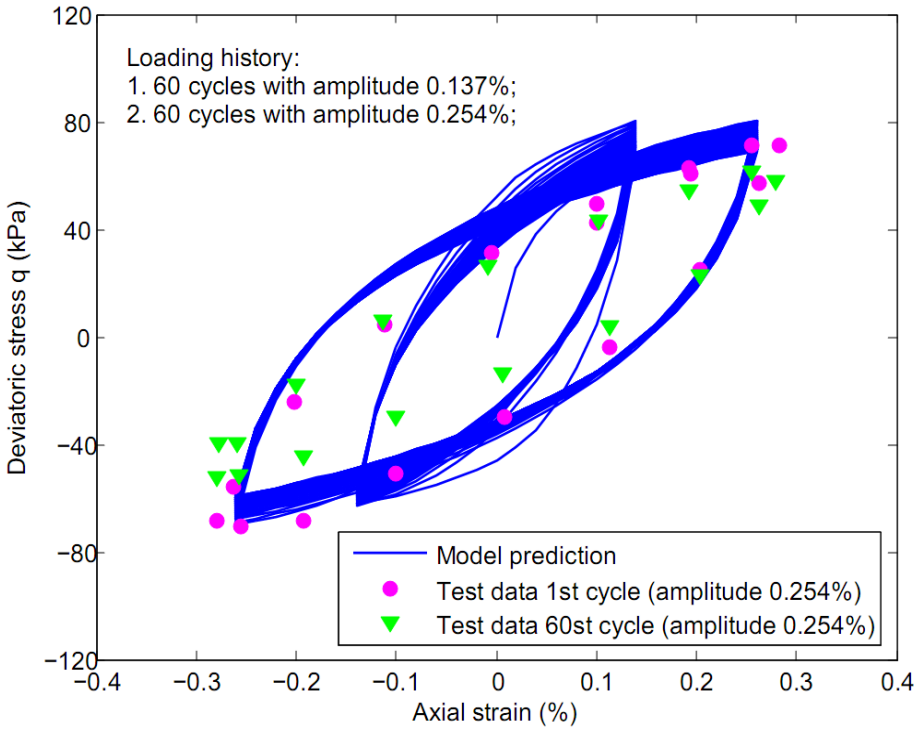

Figure 5.53 Comparison of multi-stage cyclic test

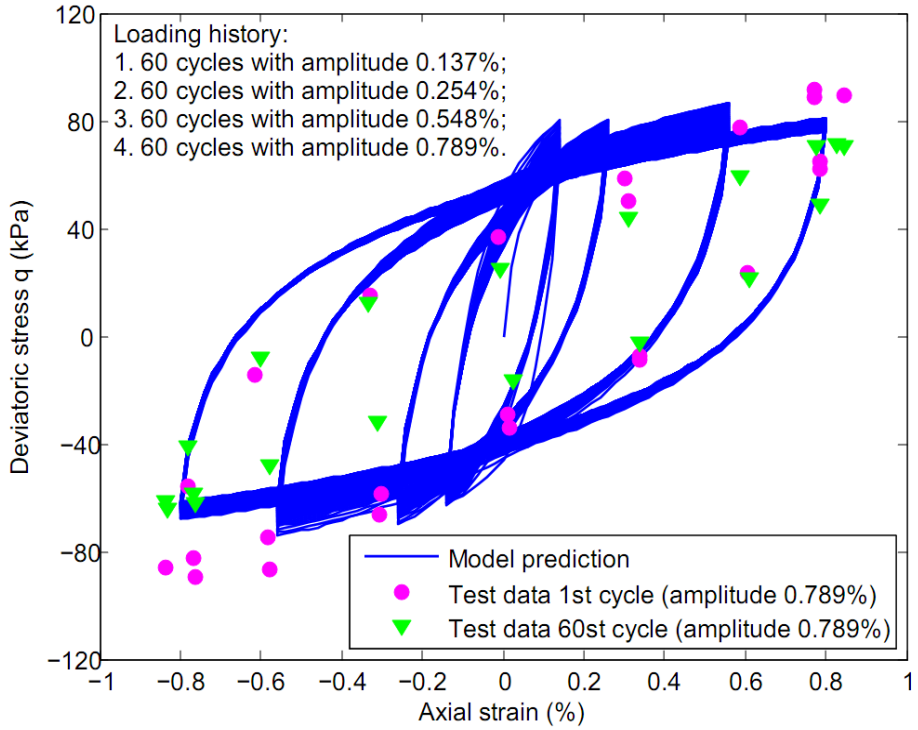

Figure 5.54 Comparison of multi-stage cyclic test

Chapter 6 **Prediction of the response of well conductor subjected to lateral loading using the AZ-Cam clay model**

6.1 Introduction

Single element simulation is useful to evaluate the capabilities of a constitutive model. However, the proposed constitutive model cannot be fully accepted before thorough evaluation in the application in boundary value problems is conducted. This chapter simulates the response of a well conductor subjected to lateral loading using the proposed AZ-Cam clay model. The results from both monotonic loading and cyclic loading (limited number of loading cycles) will be presented. Predictions from other common models frequently used in the Geotechnical Engineering will also be presented together with the measured data from corresponding centrifuge tests.

6.2 Centrifuge model tests description

The centrifuge tests carried out in C-CORE geotechnical centrifuge center were reported by Jeanjean (2009).

6.2.1 Model dimensions and test set up

The soil used in those tests was fine Alwhite kaolin clay, which was designed to be lightly overconsolidated. The detailed properties of basic Alwhite kaolin clay are summarized in Table 6.1 (C-CORE, 2005; Jeanjean, 2009).

The kaolin cake in the centrifuge was constructed in two lifts, separated by a 5mm thick sand drainage layer to accelerate the consolidation of the clay. The sand layer was approximately 215mm below the final clay surface. Clearance holes in the sand

layer were placed at the predesigned locations to accommodate the conductor to be installed and the PCPT tests to be conducted. The clay was reconstituted from slurry and mixed at approximately one-half atmosphere. The clay sample was pre-consolidated to about 95% of its effective vertical stress prior to the centrifuge test in order to reduce the in-flight consolidation time. The interpreted undrained shear strength profile from the PCPT tests, the submerged density profile, the *OCR* profile and the maximum elastic shear modulus profile are shown in Figure 6.1 after Jeanjean (2009, 2012) and Templeton (2009). It is noted that the method used to interpret the undrained shear strength from the PCPT tests is not described in the papers.

The model well conductor (steel) had an outer diameter of 19.05mm and 1.22mm wall thickness. In the centrifuge model tests, the length of the model conductor was limited by the depth of the sample container strong box. The total embedded model conductor length in the current study was 421mm, which was the maximum that could be accommodated with the existing 500mm deep test container. The tip of the conductor was simply resting on the clay bottom with no additional treatment. The model conductor was pushed-in closed-ended into slightly undersized pre-augered hole prior to each test (the pre-augered hole was 15.87mm in diameter). The applied load location was approximately 91mm above the mudline with no moment restriction. The model conductor before and after installation are shown in Figure 6.2.

A scale factor of 1:48 was used at 48 gravities. The embedded prototype length of the conductor was thus 20.2m with an outer diameter of 0.91m and 50.8mm wall thickness. The applied load location was thus about 4.3m above the clay surface in prototype scale.

6.2.2 Loading sequence in the centrifuge tests

Two sets of centrifuge tests are simulated in the current study. The first set is the monotonic loading test. The free head conductor was pushed laterally just over about 1 diameter. The second set of test is the cyclic loading test, which was carried on free head conductor with displacement-control, the maximum and minimum lateral displacement was 0.175m and 0.035m (in prototype scale), respectively.

6.3 FE model description

6.3.1 Basic model description

The commercial software ABAQUS is used for the FE analysis conducted in the current study. All the description in this section is based on the prototype scale of the conductor. The analysis is quasi-static, thus any results obtained are time-independent. The basic geometry of the model is shown in Figure 6.3. Following the symmetric conditions, only a half model is used in the FE analysis. It is better to simulate the boundary condition of the FE model the same as the boundary condition in the centrifuge test. However, the horizontal dimension of the container used in the centrifuge test is not available. Thus the model geometry includes finite elements up to 40 outer diameters of the conductor in the horizontal direction following Templeton (2009). The solid continuum element with 8-node with reduced-integration (C3D8R) is used to simulate the soil. The same element is used to model the conductor with an elastic-perfect plastic material model with von Mises failure criterion. The yield strength of the steel is 414MPa. The conductor is modeled down to a depth of 20.2m below the clay surface, which is the prototype length of the conductor. The bottom of

the conductor and soil is fixed at all degrees of freedom to facilitate the build-up of the initial stress of the soil.

6.3.2 Soil constitutive model

Various soil constitutive models are used to predict the lateral response of the conductor. The Tresca model is elastic-perfect plastic with yield stress taken as the undrained shear strength. The undrained shear strength is interpreted from the PCPT test and is referred to the *DSS* test. Considering the different time period for peak strain in the *DSS* test and the centrifuge test, an empirical equation was used by Jeanjean (2009) to consider the loading rate effect. Thus the undrained shear strength interpreted from the PCPT test was increased by 27% to consider the loading rate effect for the FE analysis. Resonance column tests reported by Templeton (2009) showed that the ratio of $G_{\max}$ to the loading rate adjusted undrained shear strength was about 550. Thus the $G_{\max}$ profile is obtained from the loading rate adjusted undrained shear strength as shown in Figure 6.1 (d). The elastic shear modulus in the Tresca model thus takes this $G_{\max}$ profile. The *OCR* profile in Figure 6.1 (c) is designated in the MCC model by assigning the initial void ratio in the ABAQUS through a subroutine. All the above models (except for the Tresca model) take the soil effective Poisson's ratio as 0.25. For the Tresca model, the analysis is conducted through the total stress analysis. Thus the undrained condition is ensured by the incompressibility of the soilwhich is simulated using a soil Poisson's ratio of 0.495. For the AZ-Cam clay model, the basic critical state parameters are presented in Table 6.1. In the general stress space, Mohr-Coulomb criterion is used to determine the critical state stress ratio and M is expressed in the form of Equation 4.1 as

$$\frac{M(\theta)}{\sqrt{3}} = \frac{0.4}{\left[1+0.384\sin(3\theta)\right]^{0.3}} \qquad 6.1$$

Experiments carried out by Atkinson & Richardson (1985) suggested that as far as cohesive soils were concerned, flow seemed to be associated. However, the experimental

study of Lewin & Burland (1970) and Wong & Mitchell (1975) showed quite clearly that the flow rules were non-associated. Thus it is hard to determine the flow rule in the current study due to the limited soil data. If associated flow rule is used with $M(\theta)$ expressed in Equation 6.1, the Lode's angle at the critical state in the plane strain condition will be either $+30^\circ$ or -30°. This is unrealistic as most soils fail with Lode's angle lies between $-10^\circ \sim -25^\circ$ (Potts & Zdravkovic, 1999). It is thus appropriate to use non-associate flow rule in the current study. Randolph & Wroth (1981) assumed the failure Lode's angle was zero under plane strain condition to analyze the stress state along the shaft of the pile. For simplicity, non-associated flow rule is used and the failure Lode's angle in plane strain condition is assumed to be zero in the current study. Thus the plastic potential is a circle in the deviatroic plane, which is also adopted by Mita (2002).

As the triaxial testing data on Alwhite kaolin clay is unavailable, it is thus not able to determine R_w, T and β. Thus the MCC yield surface is used as the bounding surface on the wet side, resulting in $R_w = 2.0$. The clay in the centrifuge was lightly overconsolidated. Since T and β are only applicable to heavily OC clay, which was concentrated on the first upper 2m. Besides, the stresses at the upper 2m are relatively small, assuming typical values of T and β would thus be expected to have a minor effect. Thus $T = 0.9$ and $\beta = 0.5$ will be used in the present study for whole range of Lode's angle.

It is well known that the G_{max} depends on the mean effective stress (Viggiani & Atkinson, 1995; Potts & Zdravkovic, 1999; Clayton, 2011). Thus it is appropriate to express the measured value of G_{max} in the form of Equation 2.11 to associate the G_{max} to the mean effective stress. Similar approach was used by Dasari (1996) in a small strain Cam clay model and Subhadeep (2009) in a hyperbolic model. Besides, from the cyclic modeling of view, it is inappropriate to fix the value of the G_{max} during the analysis. Because in the AZ-Cam clay model formulation, the clay behavior immediately after a loading reversal is almost elastic and the shear modulus takes the value of G_{max}. However, this value of G_{max} may be different from the G_{max} value at the initial loading due to the change of p' during the cyclic loading. Similar simulation to allow the G_{max} to change with the p' under cyclic loading can be seen from Dasari (1996) and Papadimitriou & Bouckovalas (2002).

However, it is difficult to match the G_{max} profile in Figure 6.1 (d) if Equation 2.11 is used. This is because the *OCR* value at the deeper depth is almost normally consolidated and the exponent of p' in Equation 2.11 cannot exceed 1.0 (Clayton, 2011). As the comparison of p-y curves, which will be presented below, concentrated on the upper 10 diameters of clay, Equation 2.11 is thus used to match the G_{max} profile in the upper 10m. However, it is noted the predicted global load-displacement response may be softer due to the deviation of the used G_{max} from measured value. This issue will be further discussed below. Thus the G_{max} used in the current study is obtained from Equation 6.2 and can be seen from Figure 6.4.

$$\frac{G_{max}}{p_r} = 100\left(\frac{p'}{p_r}\right)OCR^{0.7} \qquad 6.2$$

No information is available to determine γ. As discussed in Chapter 5, the model prediction is insensitive to γ. Thus γ is taken as a typical value from the simulation in Chapter 5 of 4. The decreasing rate of shear modulus ω_r is obtained from the parametric study of CK_0UDSS test reported by Jeanjean (2009). As can be seen from Figure 6.5, the normalized stress-strain curves are relatively insensitive to the value of ω_r, thus $\omega_r = 6$ will be used in the current study. The shakedown parameter is assumed to be zero as the number of loading cycles is relatively small. Table 6.2 summarizes the parameters used in the current study for the AZ-Cam clay model.

6.3.3 Initial stresses and analysis type

In ABAQUS, the initial stresses of soil have to be assigned. Based on Figure 6.2 (b), equivalent effective unit weight with $5.74kN/m^3$ for the upper 10m layers and $6.40kN/m^3$ for the rest part is used in the ABAQUS analysis. The initial stress is assumed to take the common form as follows

$$\sigma'_h = K_{nc} OCR^{\sin(\phi')} \sigma'_v \qquad 6.3$$

where K_{nc} is assumed to be $K_{nc} = 1 - \sin(\phi')$. Thus Equation 6.3 gives the initial lateral stress as

$$\sigma'_h = 0.64 OCR^{0.36} \sigma'_v \qquad 6.4$$

The installation process of the conductor will not be simulated in the current study, and the conductor is assumed to be wished-in-place for all the analyses. The loading is assumed to be fully undrained. The undrained loading could be achieved by running coupled fluid-solid analysis (Transient type) in ABAQUS with zero flow at all the boundary conditions. Accordingly, the default pore-fluid element (with additional degree of pore pressure) in ABAQUS will be used. However, for the simulation using

the Tresca model, it is not necessary to do so as the analysis is conducted under total stress, and no information on pore pressure will be available.

In all the analyses, the interface between the pile and soil is tied (share the same nodes at the interface) that the pile and soil share the same nodes at the interface. Thus no separation is allowed during loading and unloading process. It is noted that it is better to introduce contact analysis in the interface between the soil and the conductor to allow the separation of the soil and the conductor. However, it is beyond the ability of ABAQUS to run coupled fluid-solid analysis with UMAT when the contact pair is introduced. An alternative method is that by modifying the UMAT, a very large bulk modulus of water (compared to the bulk modulus of soil skeleton) is introduced to simulate the undrained condition. Under this condition, the analysis is conducted through total stress analysis in ABAQUS, but the constitutive law is still based on the effective stress. Thus it is possible to run ABAQUS with UMAT and contact analysis. However, this method suffers from convergence problem during cyclic loading in the current study. Thus there may be limitations within the implementation of the model in the current study.

6.4 Mesh size and element type sensitivity study

As linear solid element is used to model the soil and the conductor, the size of elements immediately adjacent to the conductor should be relatively fine in order to obtain relatively accurate result. It is thus necessary to conduct mesh sensitivity study to make sure the mesh size is fine enough to obtain reliable results. Three types of mesh sizes are used in the current study to address the effect of mesh size: 1) coarse mesh; 2) medium mesh; 3) fine mesh as can be seen from Figure 6.6 to Figure 6.8. For coarse mesh, the well conductor and soil are divided into 12 equal parts

circumferentially (half model). One layer of elements is used to simulate the wall thickness in the radial direction. Immediately adjacent to the conductor (up to 2 outer diameters of the conductor), 4 layers of elements are used in the radial direction, beyond which, the mesh size gradually increases, with maximum size ratio of 25 and totally 5 layers of elements in radial. In the vertical direction, for upper 10m, the mesh size increases gradually with maximum size ratio of 10 and totally 10 layers of elements. From 10m to 20.2m below the clay surface, 6 layers of elements with equal size in vertical direction are used. For the medium mesh, the mesh of the conductor remains the same, the number of elements in the radial direction is doubled comparing to the coarse mesh. The number of elements in the vertical direction is doubled comparing to the coarse mesh for the upper 10m. The rest remains the same. For the fine mesh, two layers of elements are used to model the conductor wall thickness. The number of elements in the radial direction is doubled comparing to the medium mesh. The number of elements in the vertical direction is doubled comparing to the medium mesh in the vertical direction. The rest remains the same as the medium mesh.

Figure 6.9 presents the lateral load-displacement curves at the conductor head. All the predictions use 8 nodes brick element with reduced-integration (C3D8R). As can been seen, relatively large discrepancy exists between the predicted response using the coarse mesh and the fine mesh. However, the predicted response between the medium mesh and the fine mesh is quite small. It is thus safe to conclude that using the medium mesh is able to obtain relatively accurate result. To further refine the mesh size of the fine mesh will be inefficient to improve the accuracy compared to the increased computational time. Therefore, the fine mesh is appropriate in order to achieve accurate results.

A number of continuum element types are available in ABAQUS. As the current study excludes contact and impact analysis, generally the second-order elements (20 nodes) provide higher accuracy than the first-order elements (8 nodes) (ABAQUS, 2011). Second-order reduced-integration elements in ABAQUS/Standard generally yield more accurate results than the corresponding fully integrated elements. However, for first-order elements, the accuracy achieved with full versus reduced integration is largely dependent on the nature of the problem (ABAQUS, 2011). Simulation carried out on a cantilever beam shows the results consistent with the ABAQUS manual as shown in Figure 6.10 (the geometry and the mesh of the cantilever beam is the same as the conductor described above, but the material model is linear elastic) and first-order elements with reduced integration can achieve good accuracy for bending related problems.

Figure 6.11 shows the conductor head lateral load-displacement response using different element types (Tresca model). As can be seen, 8 nodes brick element (first order) with full-integration (C3D8) predicts a much stiffer response than other elements. The prediction is improved by refining the mesh size. However, the predicted response is still stiffer compared to other types of elements. Thus C3D8 element is not appropriate to simulate the lateral response of the conductor. The predictions using reduced-integration lie closely, whether the element is 8 nodes or 20 nodes (second order). For the medium mesh, C3D8R element predicts a slightly stiffer response than the 20 nodes brick element with reduced integration (C3D20R). For the fine mesh, the prediction from C3D8R element is almost the same the corresponding C3D20R element. Considering the computational time, it is thus appropriate to use C3D8R element with fine mesh or to use C3D20R element with medium mesh.

For the MCC model and the AZ-Cam clay model, the simulation is conducted through the effective stress, and the undrained condition is simulated through the coupled fluid-solid analysis with zero flow at the boundary condition. Thus, the volume change of the whole model is zero. It is thus not appropriate to use 20 nodes brick element with full-integration (C3D20) as this type of element will suffer from the volumetric locking for incompressible elasto-plastic material (ABAQUS, 2011). For C3D20R element, if the strains exceed 20% to 40%, the volumetric locking will also occur for incompressible elasto-plastic material (ABAQUS, 2011).

Based on the above discussion, it is thus appropriate to use C3D8R element with fine mesh to simulate the lateral response of the conductor, and all the results in the following contents are based on this type of element and mesh size.

6.5 Other simulation from the literature

Templeton (2009) simulated the above centrifuge test under monotonic loading using the commercial software ABAQUS. The conductor was modeled with an elastic-perfect plastic material model with von Mises criterion. The yield stress is $414MP_a$. The constitutive model for soil is a semi-empirical elastic-plastic work hardening model with Mises yield. The elastic region is taken at below 10% of the ultimate strength, beyond which it is elastic-plastic. The input S_u profile is the same as the value used in the Tresca model in the current study, which is the loading rate adjusted S_u interpreted from the PCPT test reported by Jeanjean (2009) as shown in Figure 6.15. The input elastic shear modulus takes the profile of the $G_{\max}$, which is the same as the value used in the Tresca model in the current study as shown in Figure 6.1 (d). The analysis was conducted using a total stress method. However, only the predicted p-y curves for the centrifuge test under the monotonic loading are reported by Templeton

(2009). The predicted conductor head load-displacement response under monotonic loading and the prediction under the cyclic loading were not presented in the paper.

Templeton (2009) also conducted a FE analysis of a real offshore site problem under cyclic loading, which is quite similar to the above centrifuge problem (in the prototype scale). The geometry of the FE model and the soil constitutive model of the two problems are the same. The size and the material parameters of the conductor are the same. The input S_u in the FE model for this real offshore site problem was obtained from the *DSS* test, but the author did not present the *DSS* test data in the paper.

6.6 Prediction of the response under monotonic loading

6.6.1 Head response

Simulation is carried out for a free head conductor subjected to lateral 1m displacement. Figure 6.12 shows the deformations of the soil and the conductor. Caution should be paid on the reliability of results from the large deformation. However, this issue is beyond the scope of the current study. As can be seen from Figure 6.12 (b), the conductor is approaching yield due to the large lateral displacement. The maximum von Mises stress is about $408MP_a$, which occurs at about 6m (about 7 diameters of the conductor) below the clay surface. Thus the conductor remains in the elastic zone. From Figures 6.11 (c)-(f), the soil in front of the conductor is pushed upward and compressed away from the side of the conductor. Meanwhile, the soil at the back of the conductor flows downward, and the surrounding soil flows into the back of the conductor. The soil in front and at the back of the conductor flows horizontally in the same direction with the displacement of the conductor. However, the soil at the side of the conductor flows horizontally backward. The predicted soil

flow mechanism is quite realistic when compared to the flow mechanism observed in the centrifuge test as can be seen from Figure 6.13.

Figure 6.14 shows the predicted and measured load-displacement curves at the conductor head. The prediction of API (soft clay option) depends on the S_u profile. The S_u profile is rather sensitive to the estimation methods as shown in Figure 6.15. The S_u profile interpreted from the PCPT test from Jeanjean (2009) and the one calculated from the AZ-Cam clay model were used in the API calculation using USFOS (USFOS, 2012).

The results from the numerical studies all over predict the lateral ultimate capacity of the conductor as measured from the centrifuge test (the result from API will ultimate exceed the measured value beyond 1m, which has not been shown). Although the p-y curves from the AZ-Cam clay model agree well with p-y curves from the centrifuge data (as will be shown in the next section), the predicted head response differs significantly from the measured head response. Further, the prediction from the AZ-Cam clay model agrees quite well with the centrifuge test up to lateral displacement of 0.2m. For the Tresca model, the predicted response agrees well with the centrifuge result up to 0.4m. Besides, the centrifuge deduced p-y curves all show a much higher strength than the API p-y curves. However, the predictions from the API method show a higher global strength. This contradicting problem may need further discussion.

The deviation from the model prediction to the measured data may result from the large deformation of the soil. Besides, as the interface between the soil and the conductor is tied in the FE model, thus no separation is allowed. This tie simulation

may give a stiffer response, which may be another reason for the deviation of the prediction to the measured data at large deformation.

For the AZ-Cam clay model, it is noted that the input G_{max} is smaller than the measured value 10m below from the clay surface. The adopted smaller G_{max} may give a softer response. As shown in Figure 6.16, at small head lateral displacement (for example, 0.25m), the deflection of the conductor 10m below the clay surface is almost negligible, thus the effect of smaller G_{max} used in the FE model could be neglected. However, at larger head lateral displacement (for example, 0.5m), the conductor deflection 10m below the clay surface cannot be neglected. Thus the current prediction of load-displacement response may be softer than the one used with the measured G_{max} profile.

The above predictions are largely model-dependent. The API method predicts lowest lateral load compared to other models. The prediction from the total stress analysis with the Tresca model lies above the API method. Predicted response from the MCC model and the AZ-Cam clay model lie closely, where the AZ-Cam clay model gives a slightly lower lateral strength at the later stage and a high stiffness at the early stage.

6.6.2 P-y curves

The p-y curves obtained from the centrifuge test were based on the classical beam theory that the pressure p could be obtained from double differentiate the moment profile. The moment profile was obtained from discrete measurements of local strain along the conductor. The lateral displacement y could be obtained from double integration of moment profile combining the specific boundary condition at the

conductor head and conductor tip. 6^{th} order polynomial curve was used by Jeanjean (2009) to match the moment profile. The lateral displacement y in the numerical study could be obtained directly from the output of ABAQUS. The lateral pressure p is calculated by dividing the outer diameter of the conductor from total node force (the node force integrated from the stress at the integral points of an element) at the specific depth. Figure 6.17 shows the p-y curves from the centrifuge test and the predicted values from other models.

As can be seen from Figure 6.17, the prediction from Templeton (2009) agrees quite well with the centrifuge test result for all the presented p-y curves. For the AZ-Cam clay model, the general agreement between the prediction and the test result is satisfactory, but the model under predicts the limiting pressure at depth 1.5 diameters and 11.5 diameters below the clay surface. As can be seen from Figure 6.12 and Figure 6.13, the FE model predicts a weldge failure mechanism in the shallow depth, which is consistent with the failure mechanism assumed in API (2000). However, it remains unknown whether a weldge formed in the centrifuge test. Thus it is difficult to explain the deviation in the shallow depth. For the MCC model, within expectation, it over predicts the ultimate pressure. As no small strain stiffness is specified in the MCC model, the model under predicts the stiffness at initial stage. API predicts a rather low stiffness and the ultimate pressure when compared to the test result.

Thus in assessing the fatigue life of the well conductor, the much stiffer p-y curves obtained from the AZ-Cam clay model indicate the lateral displacement at the well conductor head would be significantly lower than the value predicted by the API method. Thus based on the current numerical studies, the stress in the well conductor may be over predicted by the API method, resulting relatively larger cyclic damage to

the conductor. Therefore, the fatigue life predicted by the API method may be overly conservative based on the current numerical study.

6.7 Prediction of the response under cyclic loading

6.7.1 Displacement control cyclic loading

Figure 6.18 and Figure 6.19 show the MCC model prediction and the AZ-Cam clay model prediction on displacement control cyclic loading, respectively. Loading lasts for 10 numbers of cycles with the maximum lateral displacement of 0.175m and the minimum of 0.035m. Compared to the centrifuge test result as in Figure 6.20, the AZ-Cam clay model could realistically simulate the hysteretic behavior in the cyclic loading as well as the softening behavior. However, as the unloading process of the MCC model is purely elastic and the elastic modulus remains the same during unloading, the MCC model is not able to predict the hysteretic behavior in cyclic loading and the softening will not occur.

Figure 6.21 shows the cyclic p-y curves at various depths. As can be seen, under displacement control cyclic loading, the cyclic degradation is quite significant that the pressure decreases with loading cycles. Besides, the degradation is much more severe for shallow depth than for deeper depth as the cyclic amplitude is much larger for shallow depth than deeper depth.

6.7.2 Load control cyclic loading

The centrifuge test data on the load control cyclic loading are not available from Jeanjean (2009). As stated earlier, the FE simulation of the centrifuge test under the cyclic loading is not available from Templeton (2009), but he reported the FE simulation results of the real offshore site problem under load control cyclic loading,

and the FE model for the centrifuge study and real offshore site problem is quite similar as described in section 6.5. Besides, a typical S_u profile in the analysed offshore site was provided by Templeton (2009) as shown in Figure 6.15, but the author did not explicitly point out whether he used this typical S_u profile in the FE analysis and whether this typical S_u profile was obtained from the *DSS* test. As can be seen from Figure 6.15, the typical S_u profile is close to the S_u calculated from the proposed AZ-Cam clay model. Thus the prediction on the cyclic loading for the real offshore site problem in Templeton (2009) is used to qualitative compare the response from the proposed model for the centrifuge problem due to the similarity of the two problems. It is noted that it may be unfair to directly compare the response from the real offshore site problem to the response obtained in the current study for the centrifuge problem. Thus the comparison only focuses on the response trend instead of the detail.

Generally, the hysteretic behavior is reproduced quite well by both models. However, the predicted stiffness from the AZ-Cam clay model is significantly lower than the value predicted by Templeton (2009) as can be seen from Figures 6.19 (a)-(d). This deviation may result from the different S_u value of the real offshore site problem and the centrifuge problem.

Figure 6.23 shows the cyclic p-y curves obtained from load control cyclic loading using the AZ-Cam clay model. As can be seen, the curves follow the Masing's rule, which is explicitly specified in the model formulation. The accumulated deformation is not obvious and generally the conductor is able to reach or approach the previous maximum load level at the same displacement, thus the degradation is not severe, if any.

6.8 Summary

This chapter presents the predictions of the response of a well conductor in soft clay subjected to lateral loading using various soil constitutive models. For monotonic loading, the predicted conductor head load-displacement response agrees well up to 0.2m with the centrifuge test by the AZ-Cam clay model. At larger displacement, the AZ-Cam clay model, the MCC model and the Tresca model all over predicted the response. The API method (soft clay option) predicts a much softer response than the measured value at smaller displacement. The predicted p-y curves from the AZ-Cam clay model agree quite satisfactory with the centrifuge tests. However, the MCC model largely over predicts the response and the API method under predicts the response. The p-y curves both from centrifuge test and numerical prediction using the AZ-Cam clay model show a much stiffer response than from the API method. Thus the actual stress in the well conductor under cyclic loading may be lower compared to the prediction following the API method. Therefore, the fatigue life may be under predicted by the API method.

For displacement control cyclic loading, the AZ-Cam clay model is able to predict the softening and the hysteretic behavior of the conductor. The predicted head response agrees reasonably well with the centrifuge test result. For load control cyclic loading, the stiffness predicted by the AZ-Cam clay model is much smaller than the value predicted by Templeton (2009). However, both models predict the hysteretic behavior well. For symmetric loading, the predicted response almost follows the Masing's rule. The above comparisons reveal that the AZ-Cam clay model is able to predict the salient behavior of the conductor in clay. Thus the model could be used to reasonably predict the boundary value problem, both under monotonic loading and cyclic loading with relatively small number of loading cycles.

Table 6.1 Summary of Alwhile kaolin properties (C-CORE, 2005; Jeanjean, 2009)

Property	Value
Material	Alwhile (Speswhile) kaolin
G_s (specific gravity)	2.64
λ	0.25
κ	0.05
N	3.58
M	0.8
K_0	0.64
c_v (consolidation coefficient)	$1 mm^2/\sec$
Strength ratio, $S_u/\sigma'_v = \alpha(OCR)^n$	$\alpha = 0.19, n = 0.67$
Liquid limit (LL)	58%
Plastic limit (PL)	32%
Plasticity index	26

Table 6.2 Model constants for the AZ-Cam clay model

N	λ	κ	M	R_w	R_d
3.58	0.25	0.05	$\frac{M(\theta)}{\sqrt{3}} = \frac{0.4}{\left[1+0.384\sin(3\theta)\right]^{0.3}}$	2.0	2.0
γ	β	T	$G_{\max}$	ω_r	k
4	0.5	0.9	$\frac{G_{\max}}{p_r} = 100\left(\frac{p'}{p_r}\right)OCR^{0.7}$	6.0	0

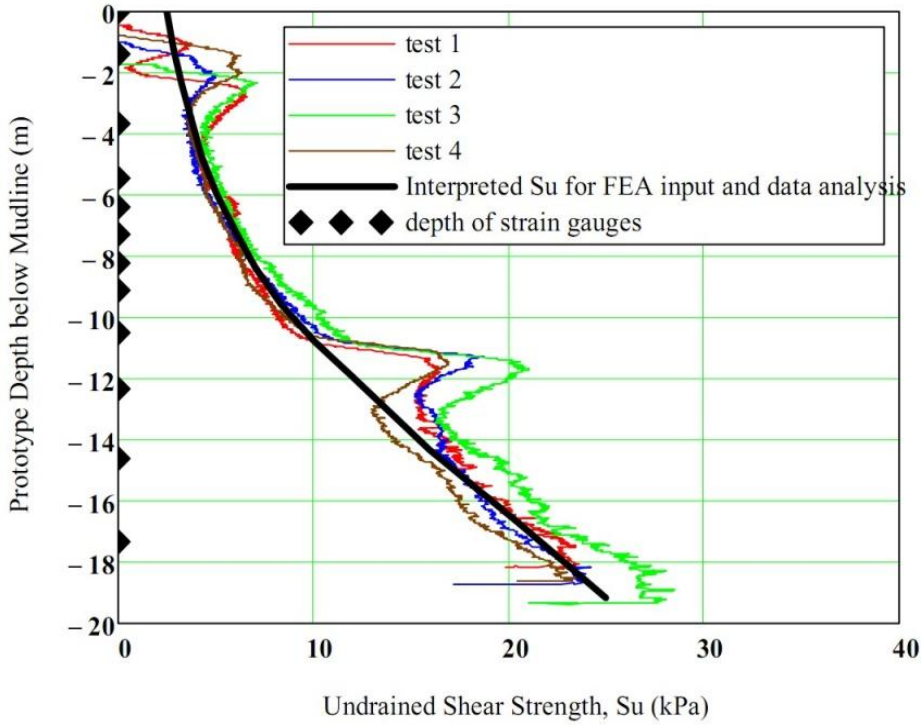

(a) Undrained shear strength S_u profile (Jeanjean, 2009)

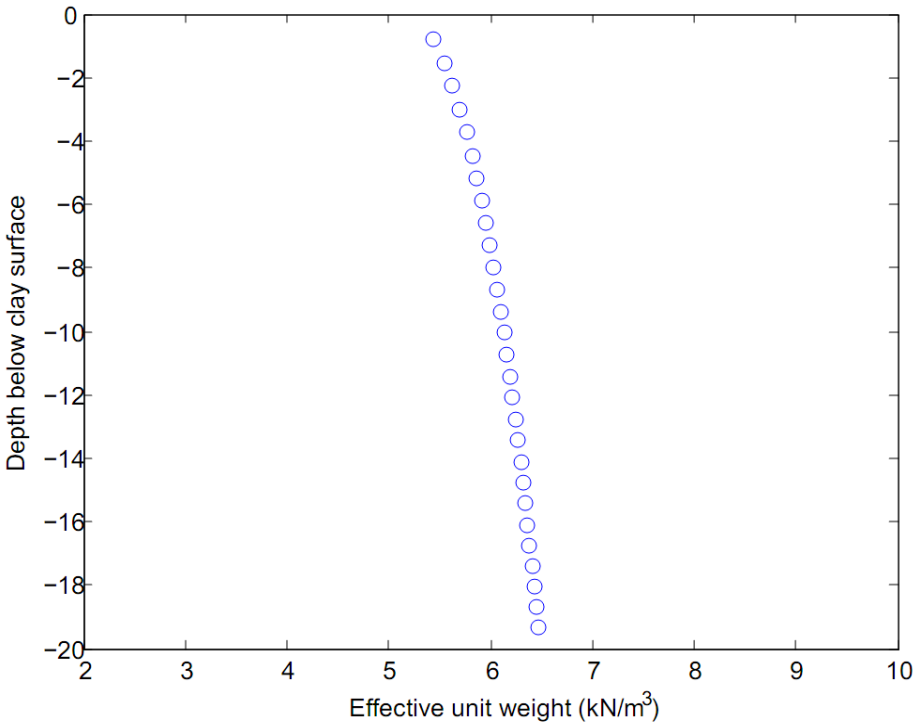

(b) Submerged density profile (Jeanjean, 2012)

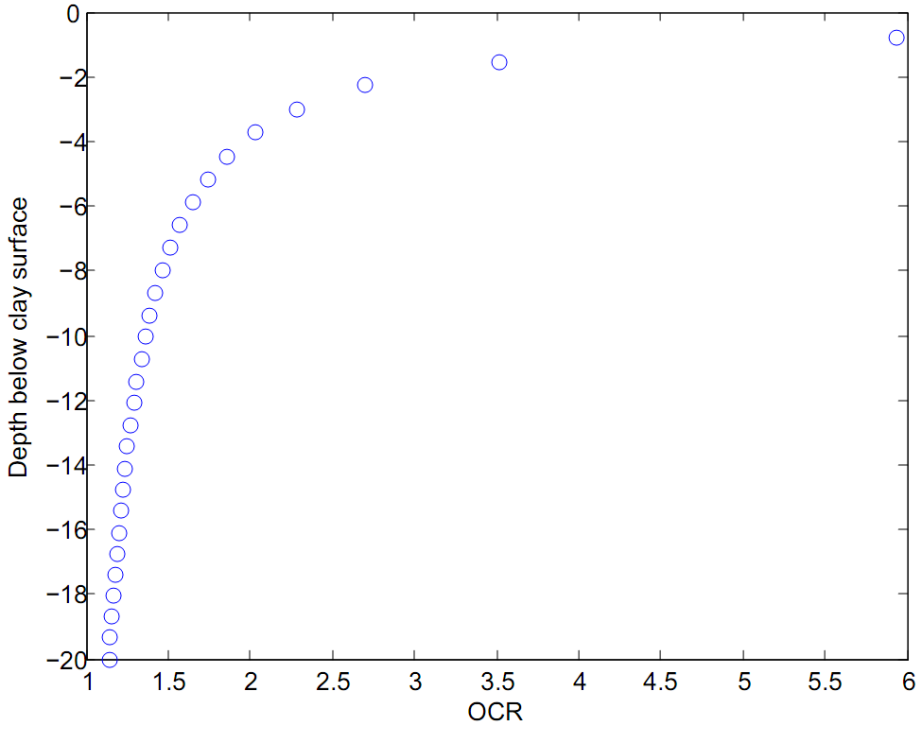

(c) *OCR* profile (Jeanjean, 2012)

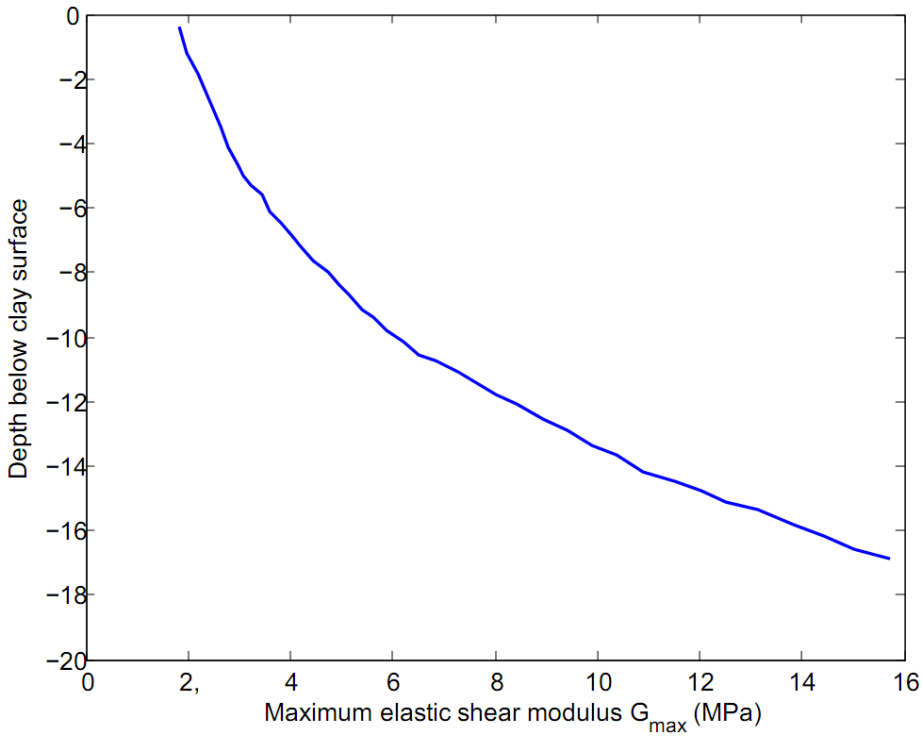

(d) Distribution of G_{max} reported by Templeton (2009)

Figure 6.1 Clay information in the centrifuge test

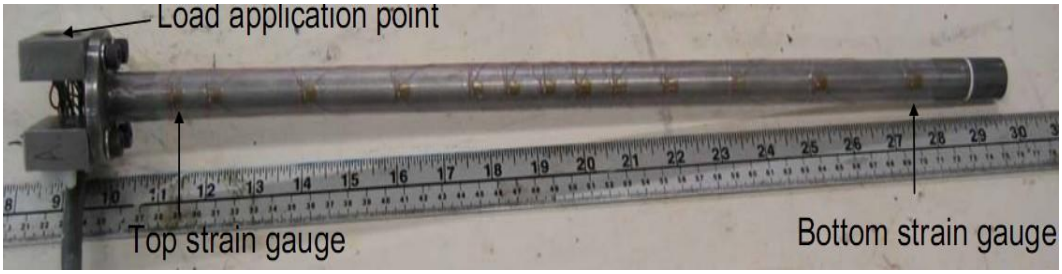

(a) Conductor model used in the centrifuge test

(b) Pre-augered hole (c) Set up in the centrifuge test

Figure 6.2 Model conductor in the centrifuge test (Jeanjean, 2009)

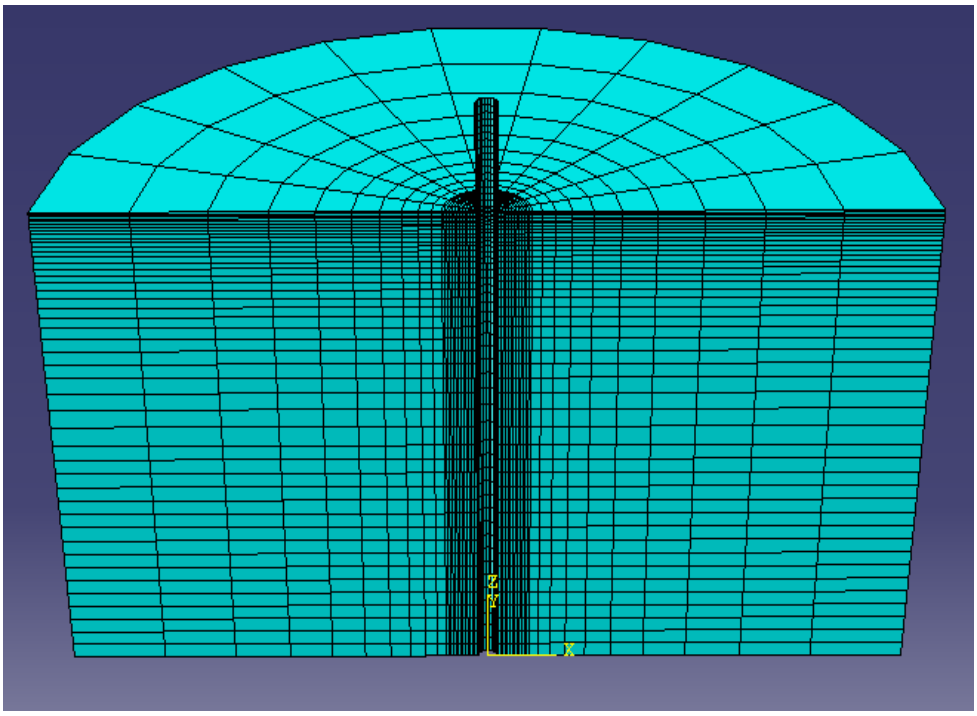

Figure 6.3 Geometry of the model used in ABAQUS

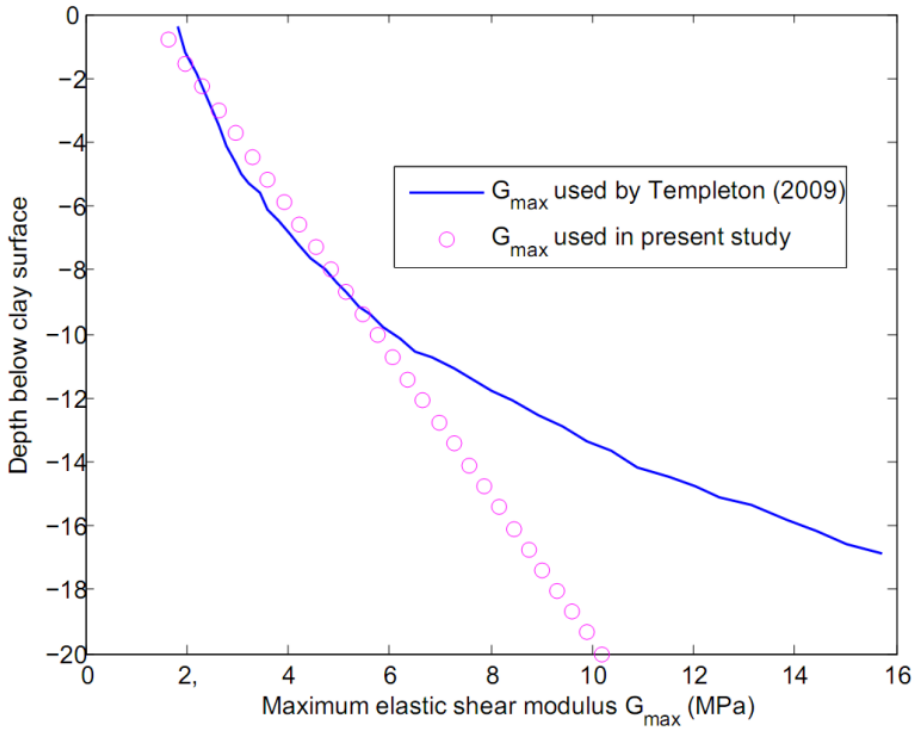

Figure 6.4 G_{max} used in current study

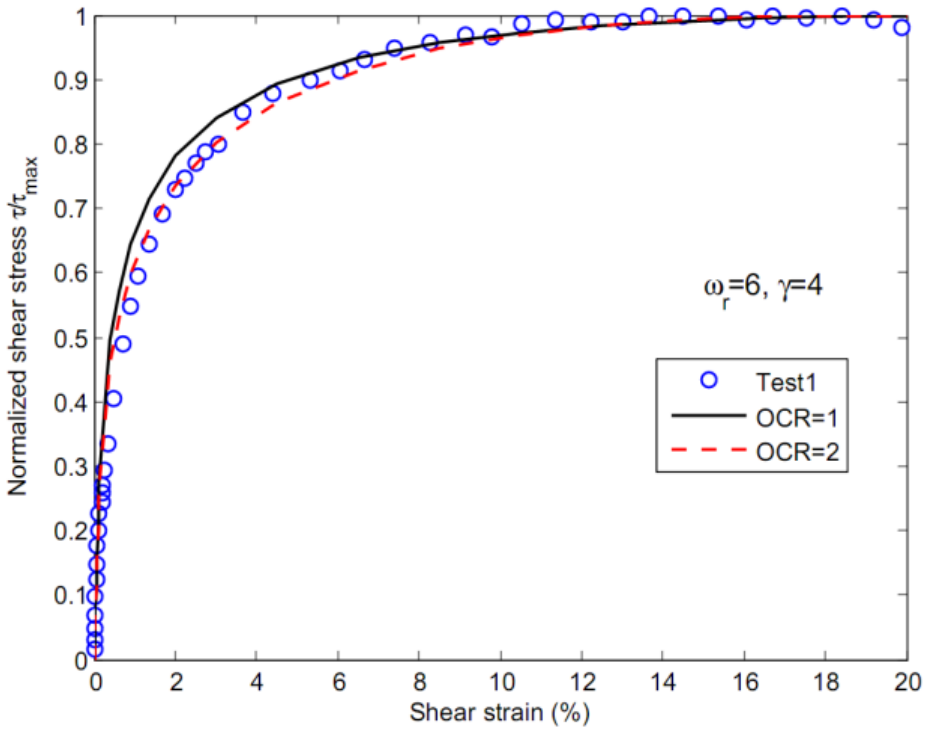

(a) $\omega_r = 6, \gamma = 4$

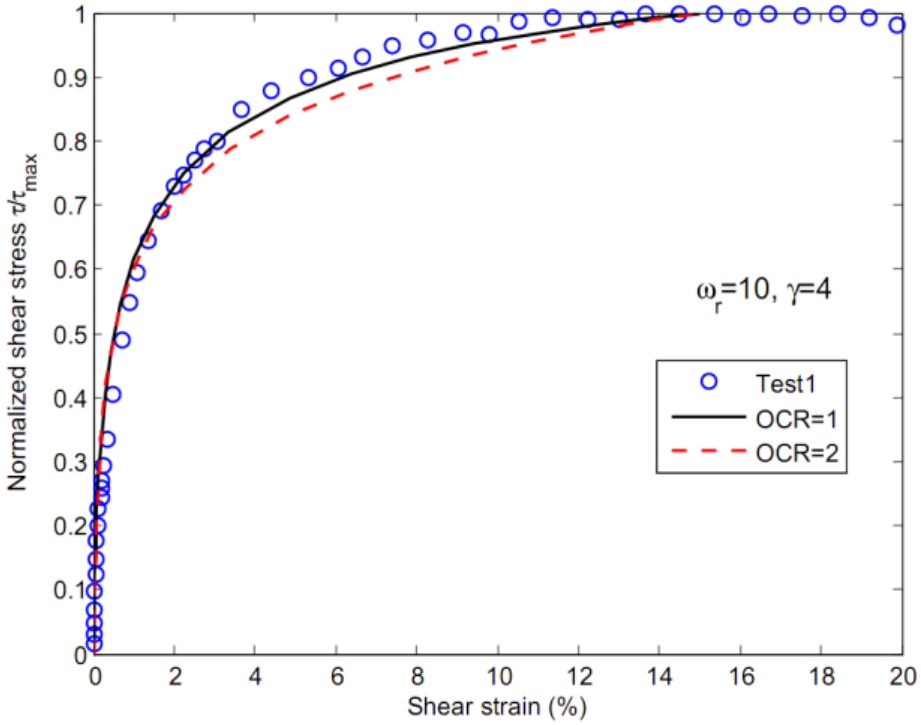

(b) $\omega_r = 10, \gamma = 4$

Figure 6.5 Stress-strain curves in CK_0UDSS test

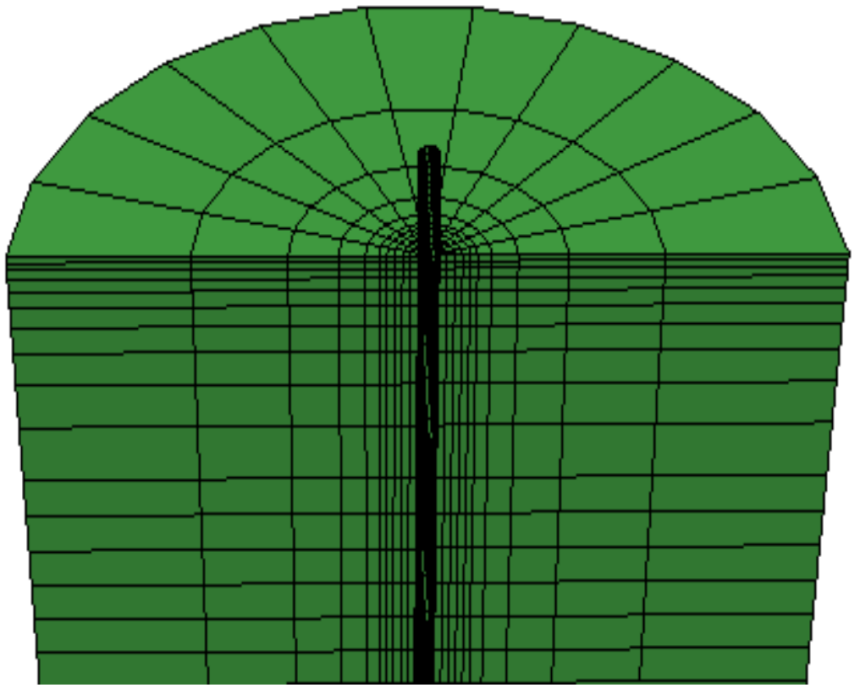

Figure 6.6 Coarse mesh

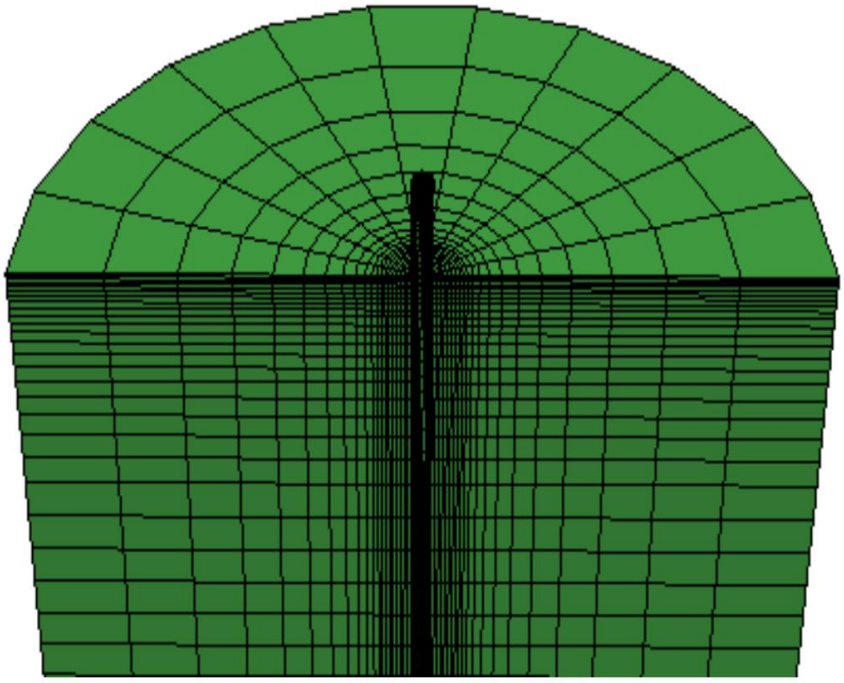

Figure 6.7 Medium mesh

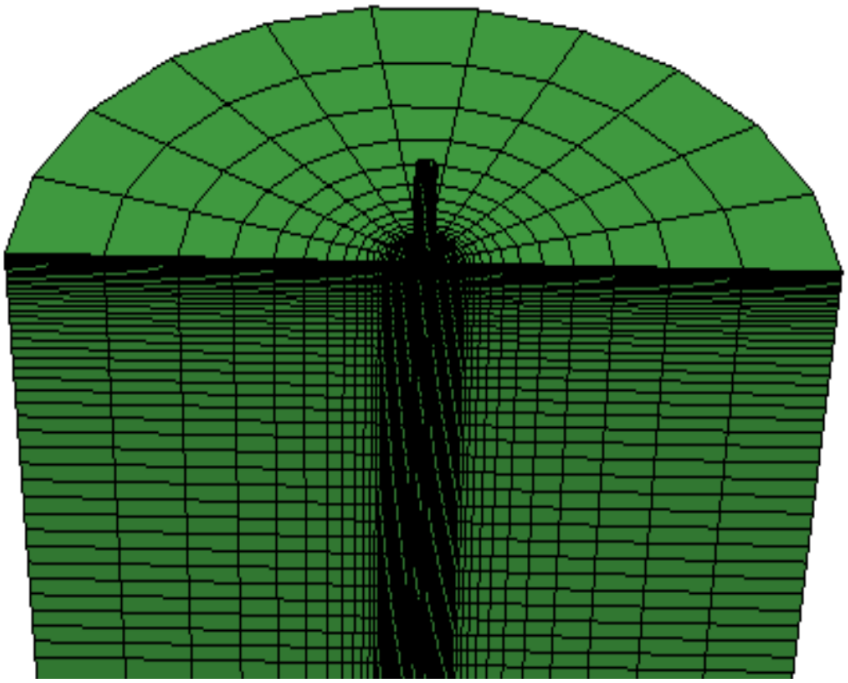

Figure 6.8 Fine mesh

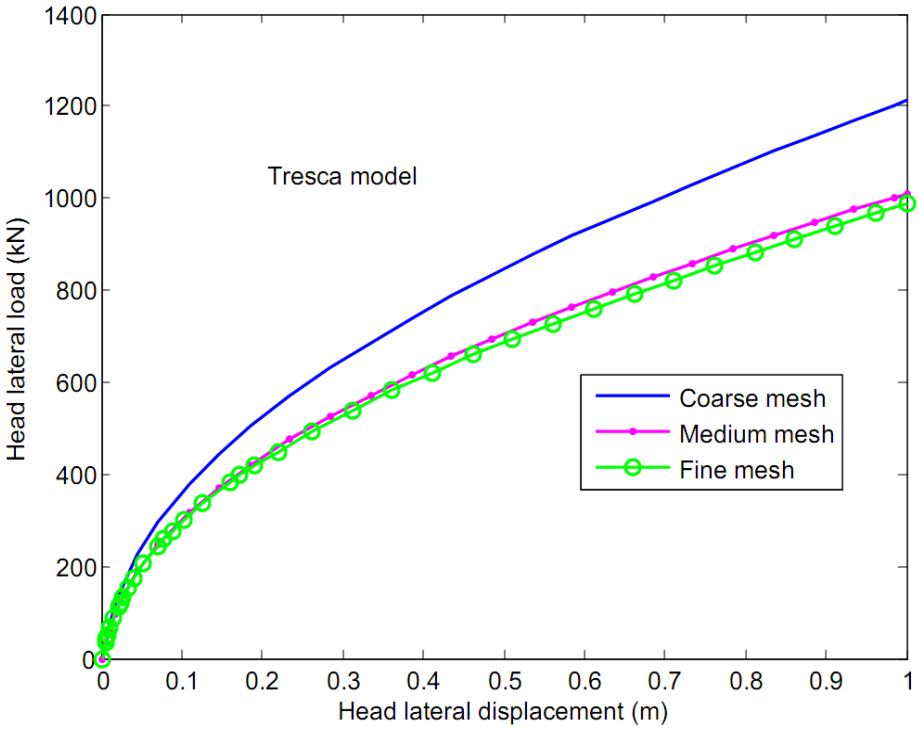

(a) Tresca model prediction

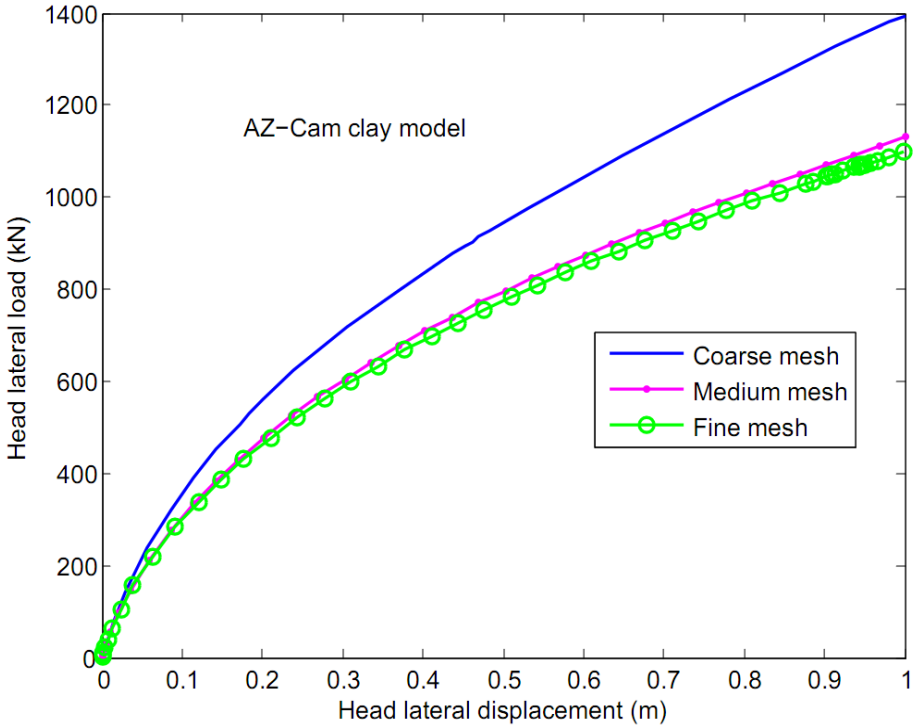

(b) AZ-Cam clay model prediction

Figure 6.9 Mesh sensitivity study-head response

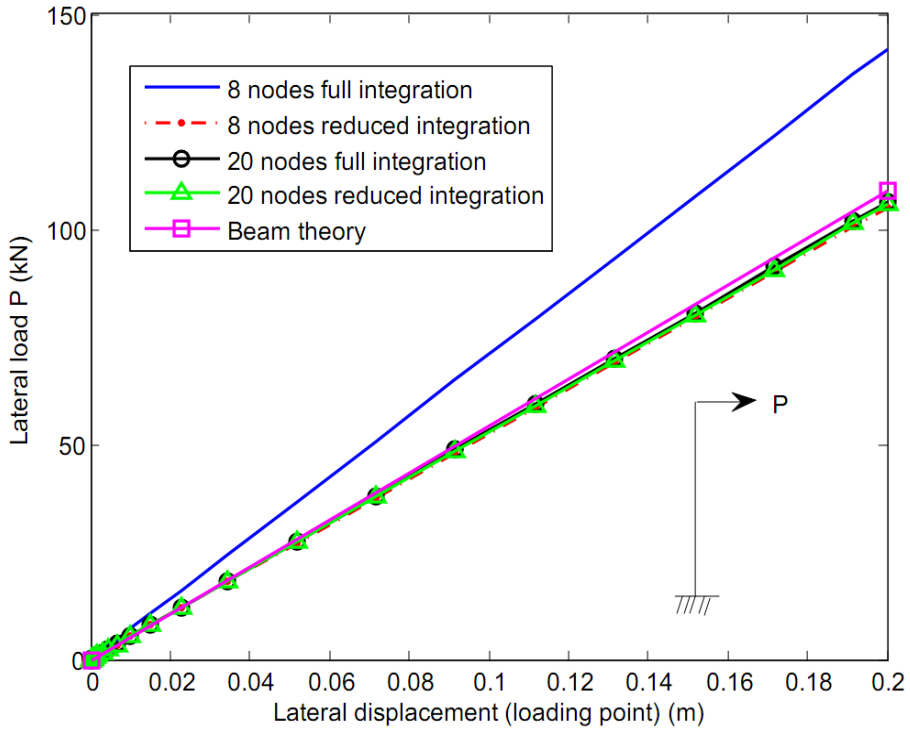

Figure 6.10 Accuracy of different element types

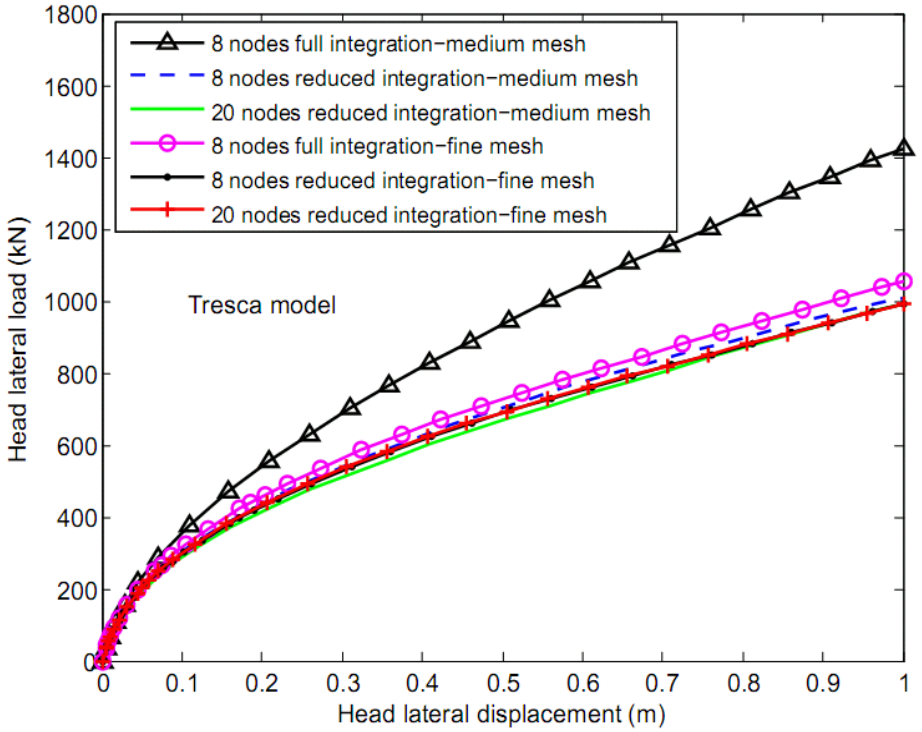

Figure 6.11 Element type study-head response

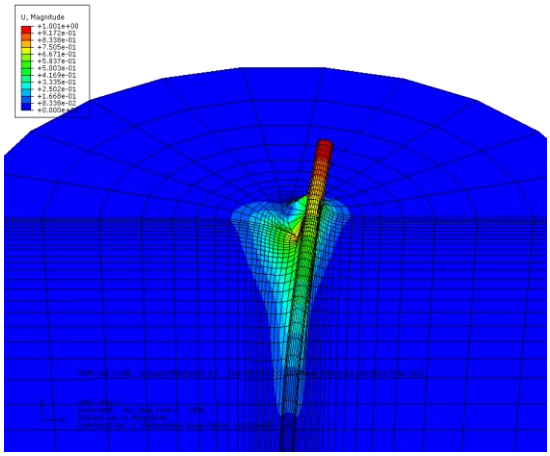

(a) Deformation of soil and conductor

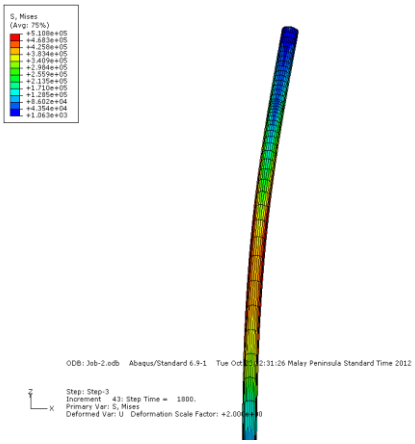

(b) Yielding of the conductor

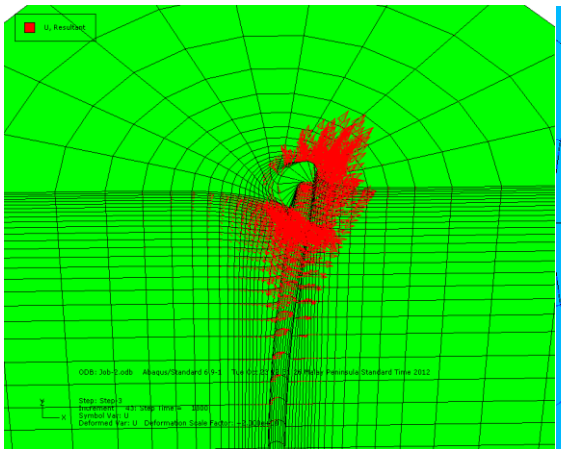

(c) Displacement vector of soil

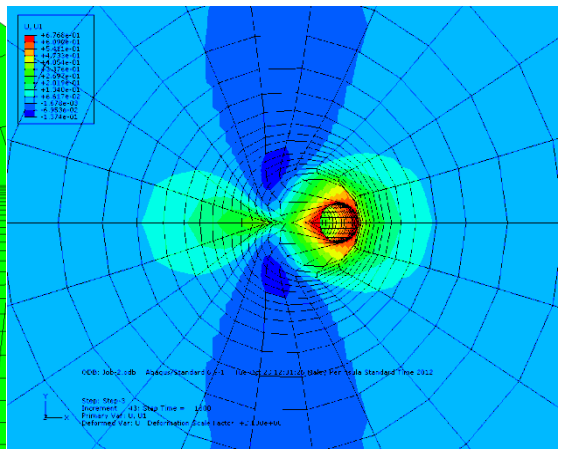

(d) Soil displacement contour-X direction

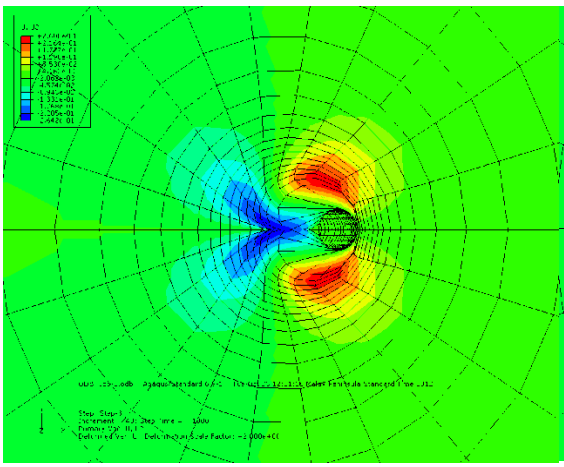

(e) Soil displacement contour-Y direction

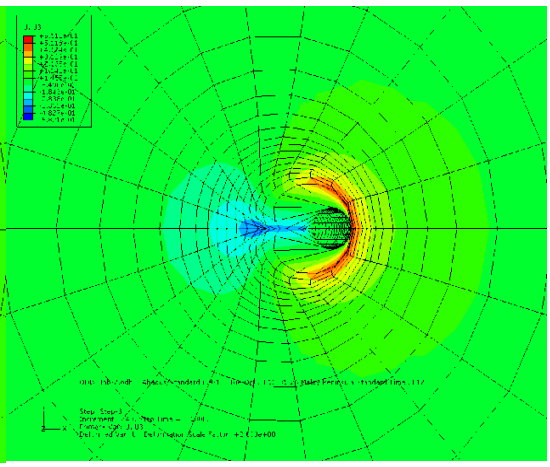

(f) Soil displacement contour-Z direction

Figure 6.12 Deformation of soil and conductor at the end of the analysis

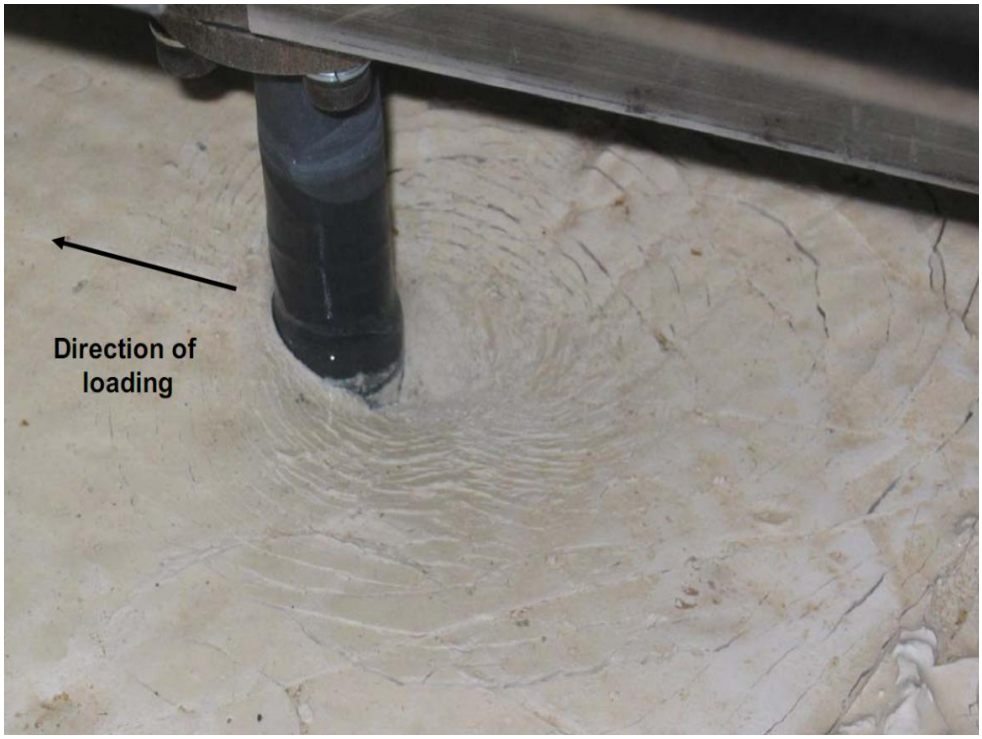

Figure 6.13 Observed deformation of soil (Jeanjean, 2009)

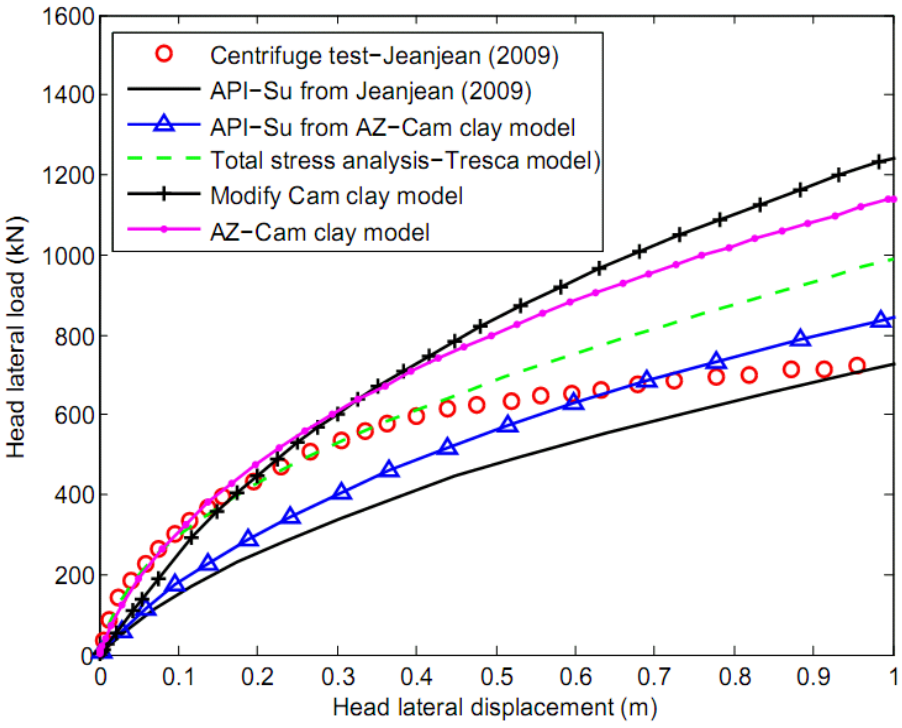

Figure 6.14 Predicted and measured head load-displacement curves

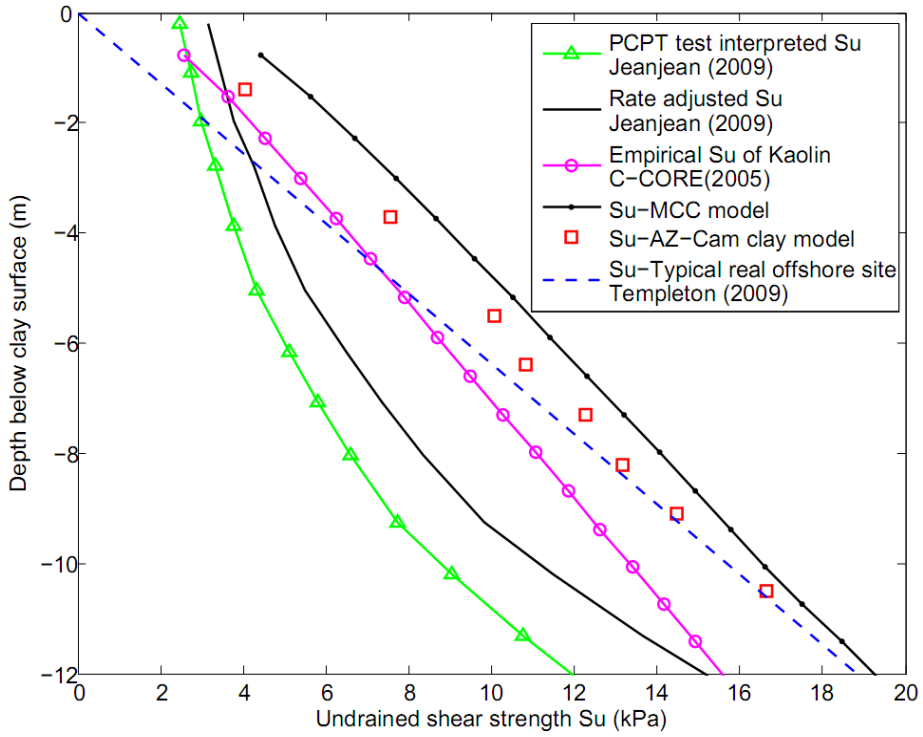

Figure 6.15 S_u profile based on different estimation methods

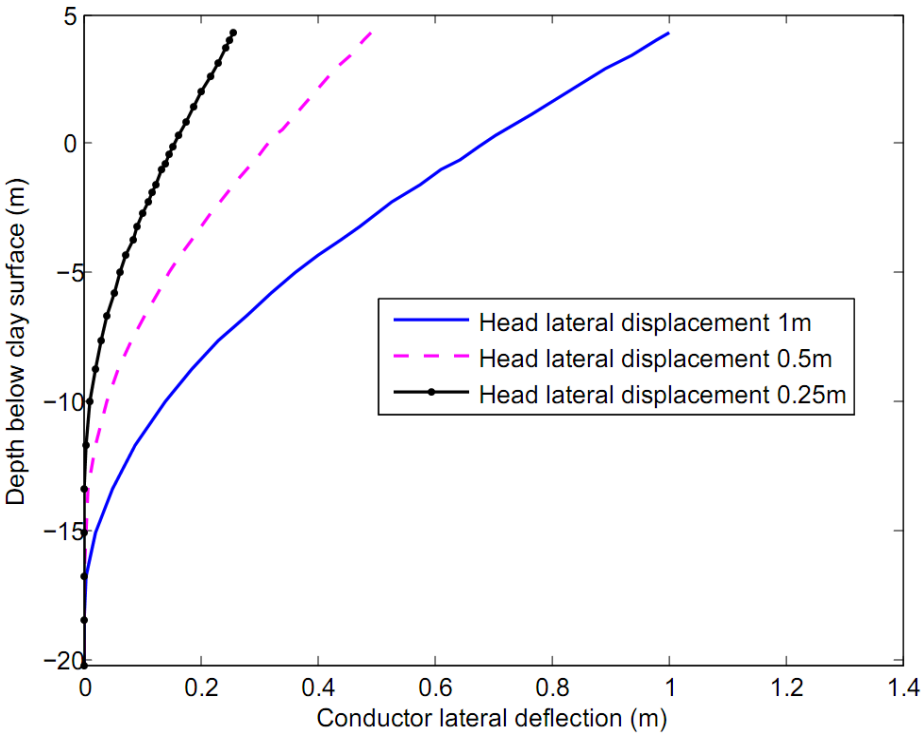

Figure 6.16 Conductor lateral deflections at various head lateral displacement

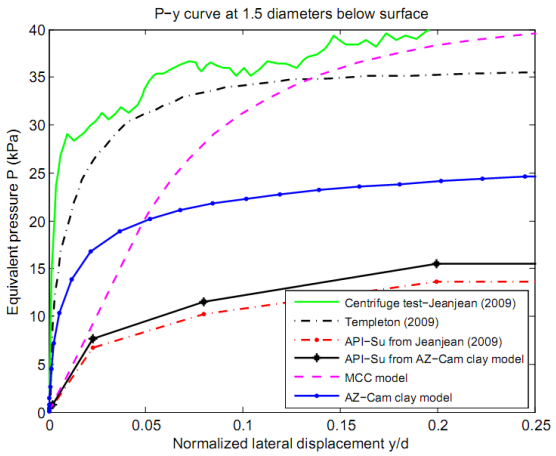

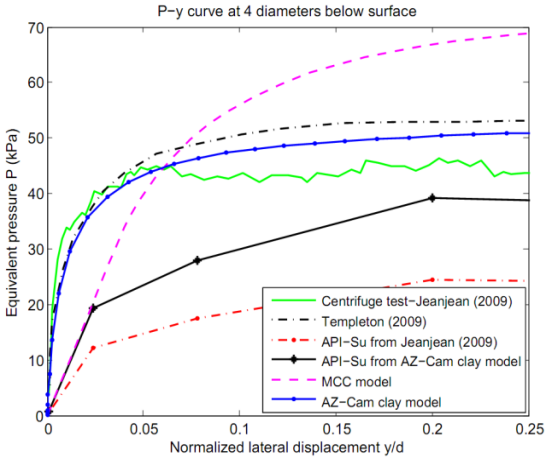

(a) 1.5 diameters below surface (b) 4 diameters below surface

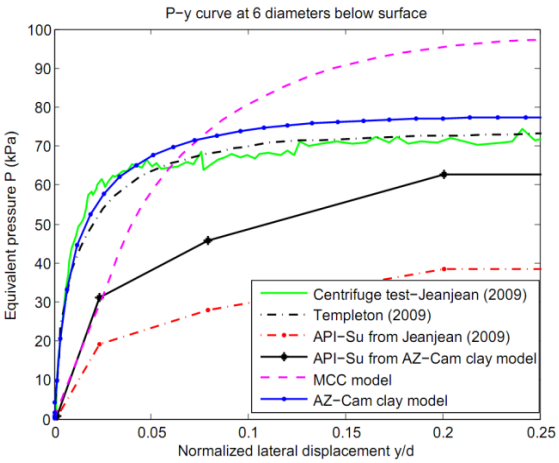

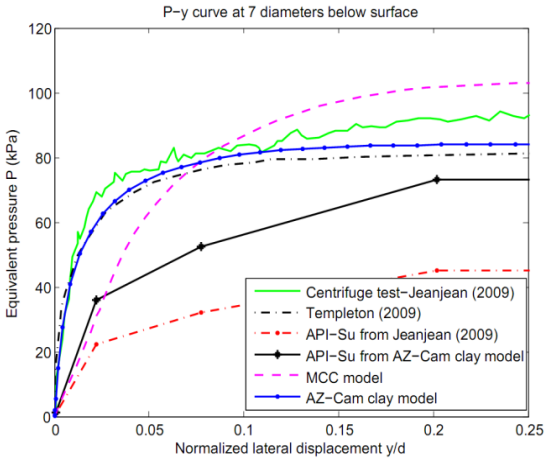

(c) 6 diameters below surface (d) 7 diameters below surface

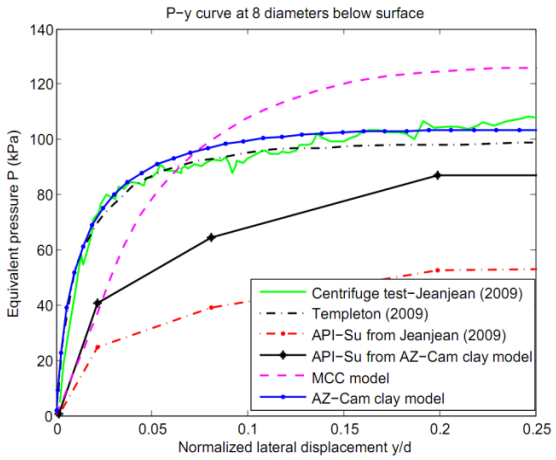

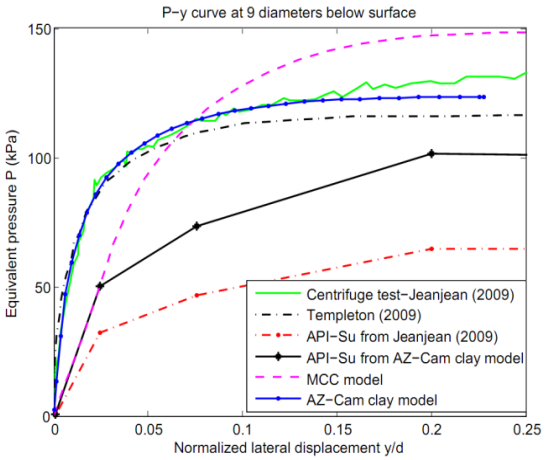

(e) 8 diameters below surface (f) 9 diameters below surface

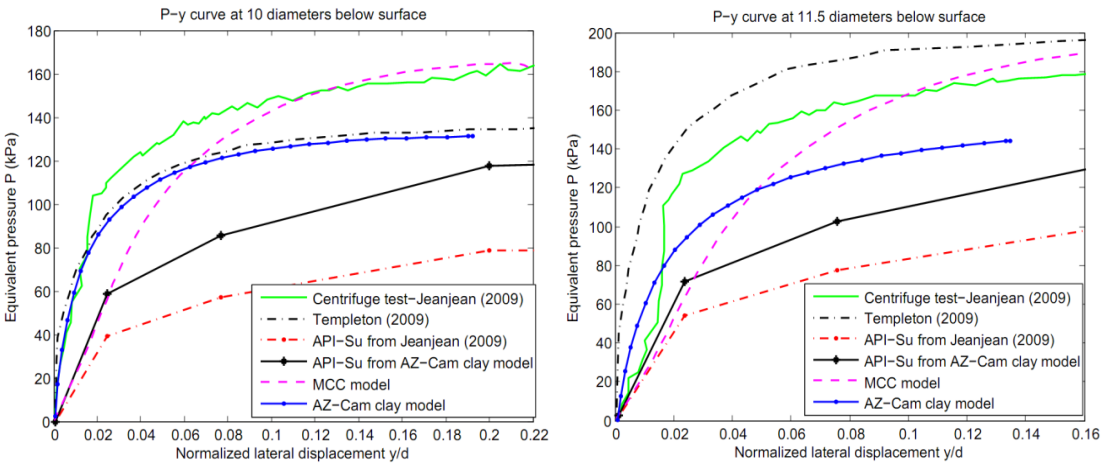

(g) 10 diameters below surface (h) 11.5 diameters below surface

Figure 6.17 Comparisons of the P-y curves

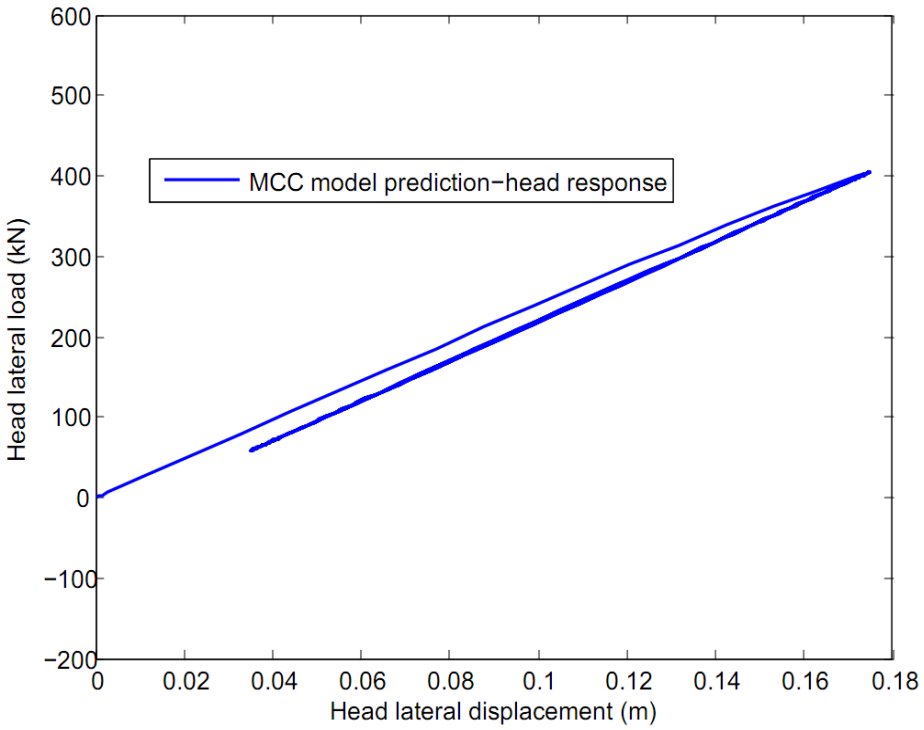

Figure 6.18 The MCC prediction

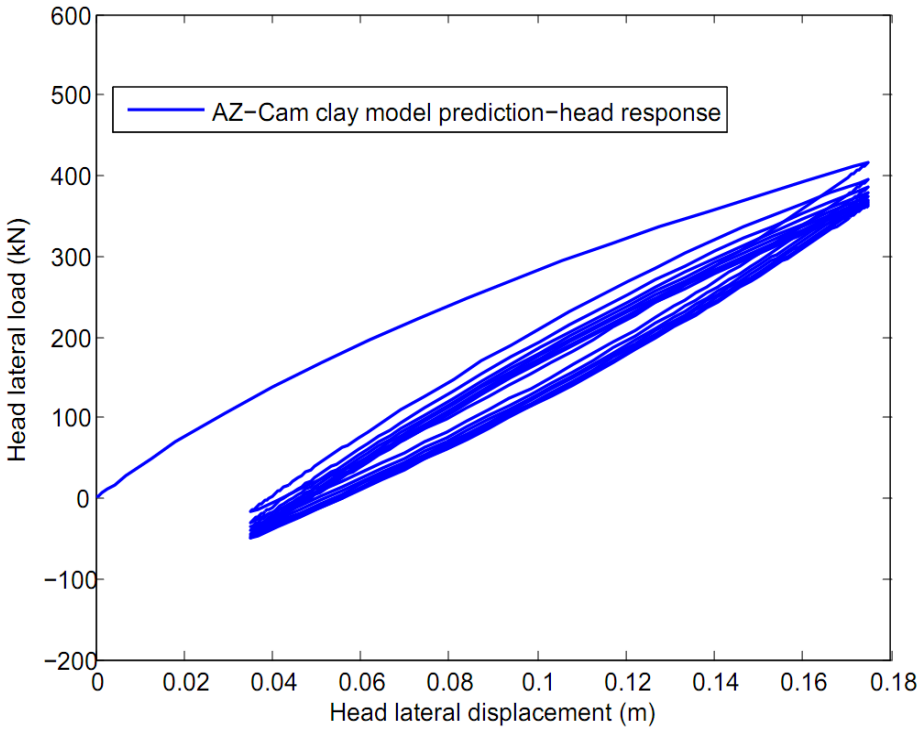

Figure 6.19 The AZ-Cam clay model prediction

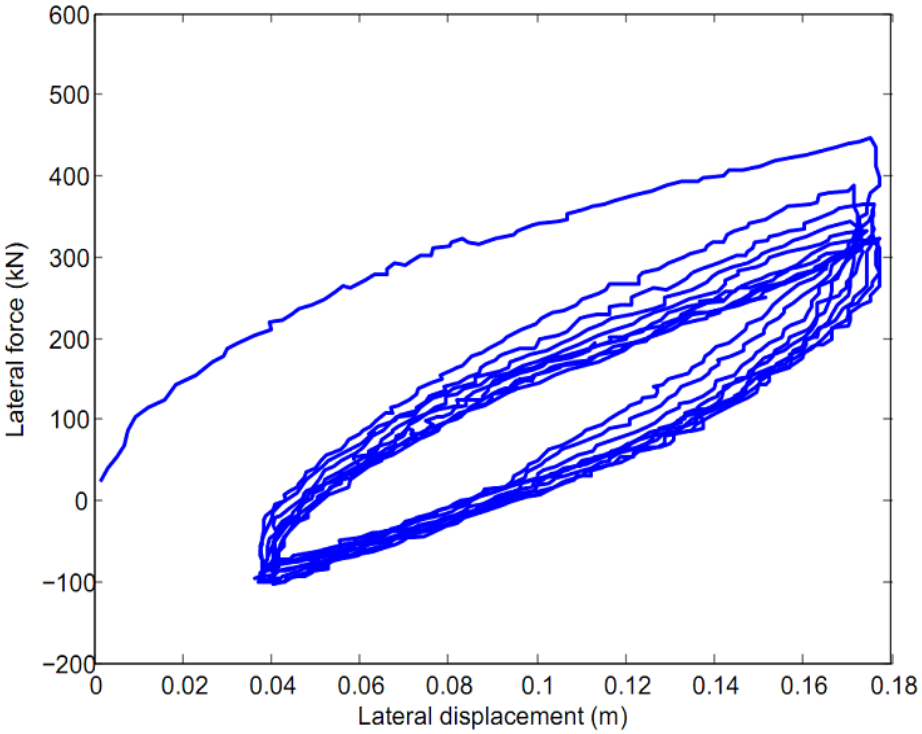

Figure 6.20 Measured data after Jeanjean (2009)

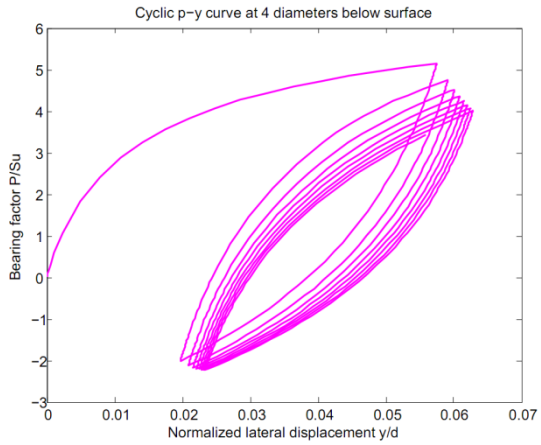

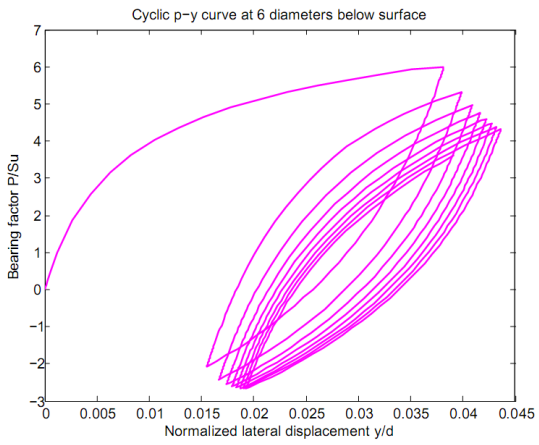

(a) 4 diameters below surface (b) 6 diameters below surface

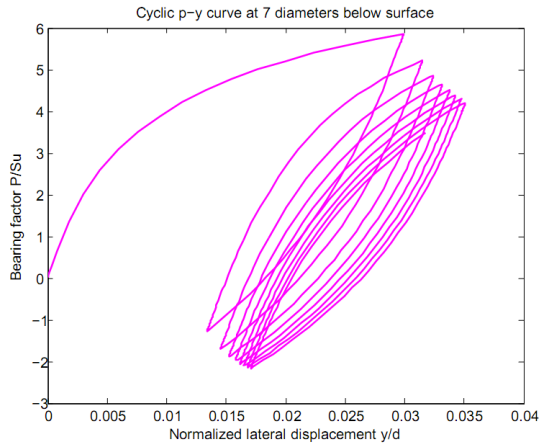

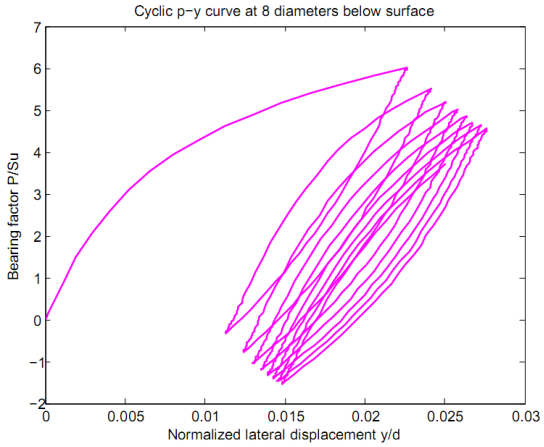

(c) 7 diameters below surface (d) 8 diameters below surface

Figure 6.21 Cyclic p-y cures under displacement control

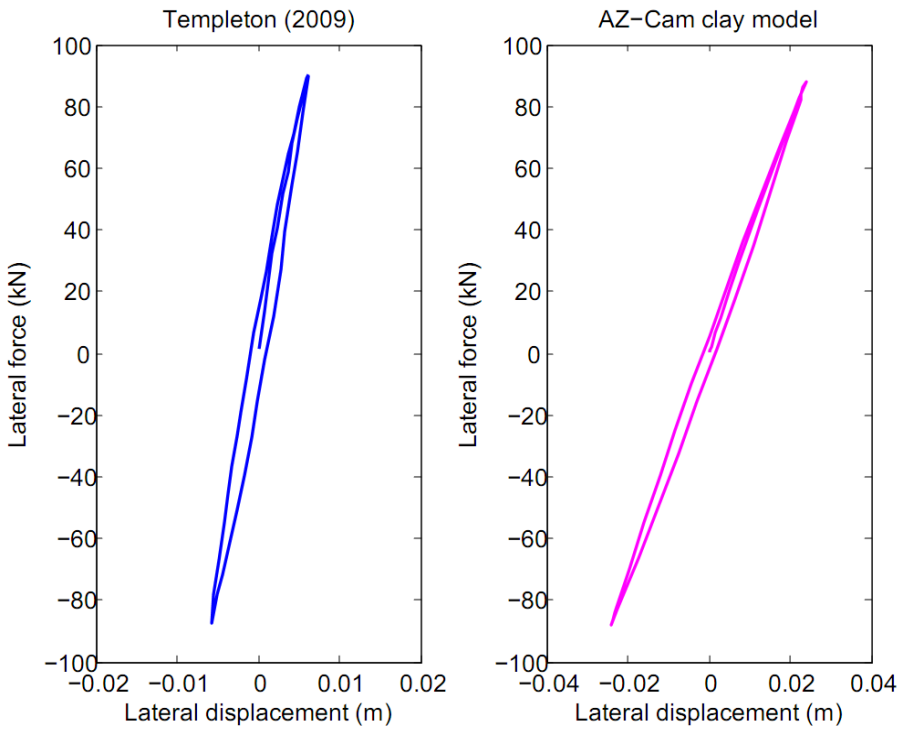
Templeton (2009)
AZ−Cam clay model
Lateral force (kN)
Lateral displacement (m)
100
80
60
40
20
0
−20
−40
−60
−80
−100
−0.02
−0.01
0
0.01
0.02
−0.04
−0.02
0.02
0.04

(a)

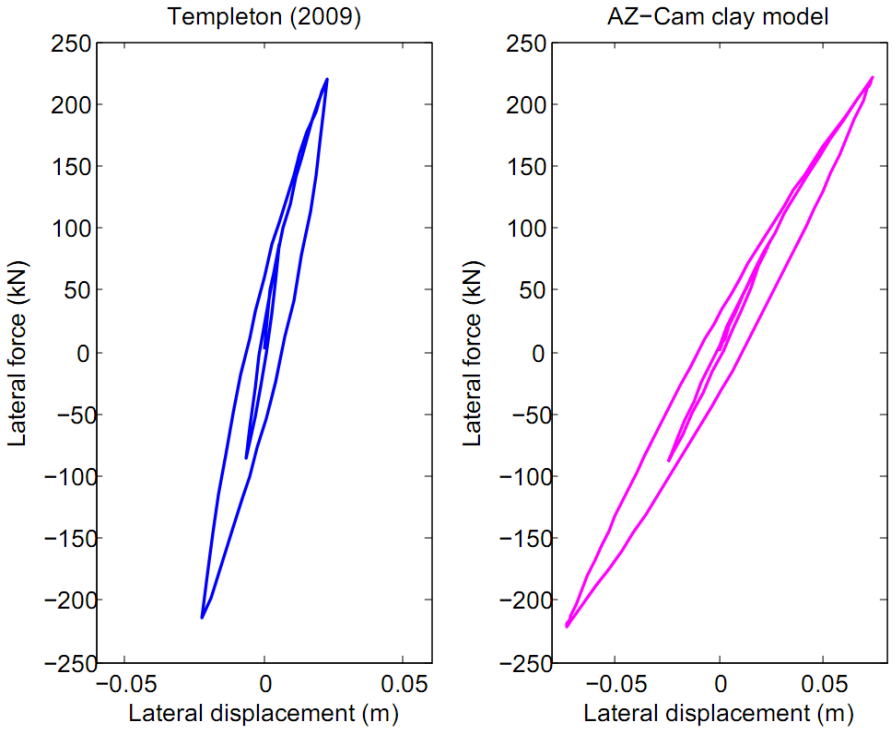
Templeton (2009)
AZ−Cam clay model
Lateral force (kN)
Lateral displacement (m)
250
200
150
100
50
0
−50
−100
−150
−200
−250
−0.05
0
0.05

(b)

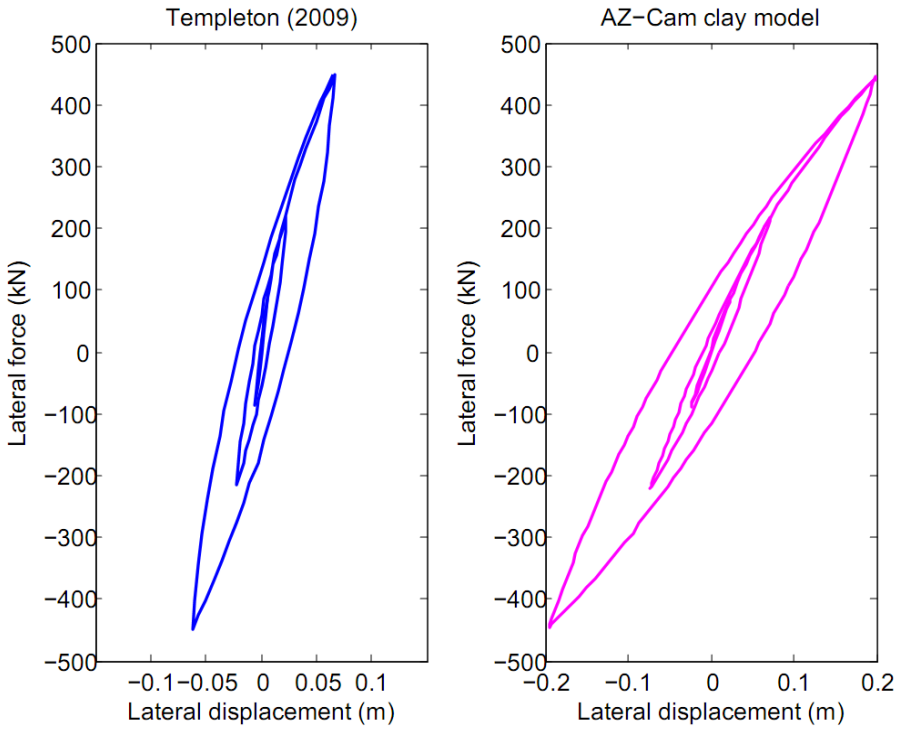

(c)

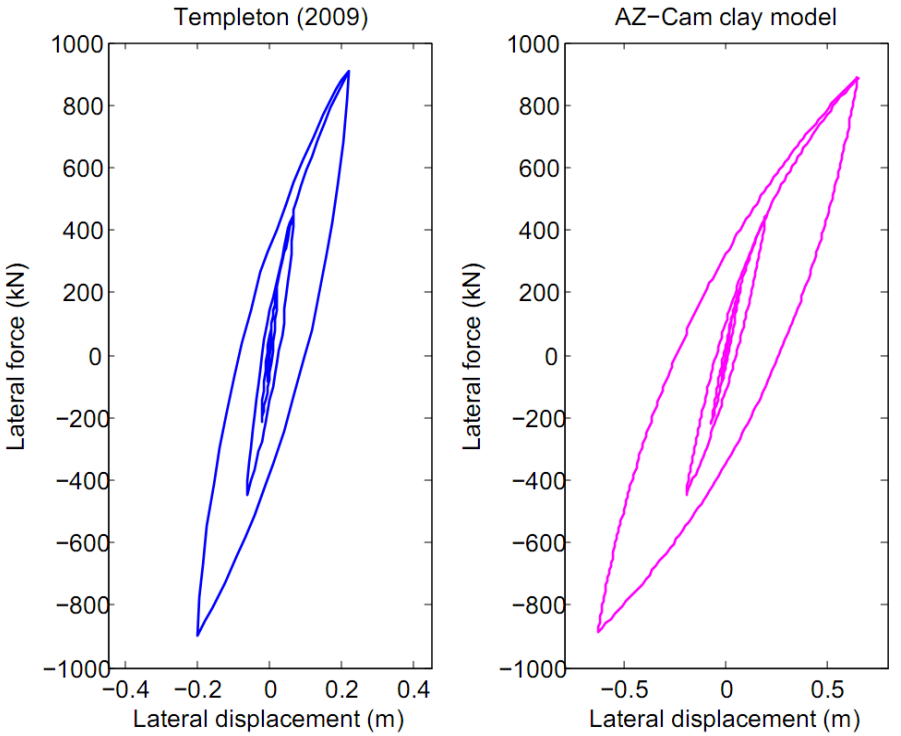

(d)

Figure 6.22 Comparison of head load-displacement curves

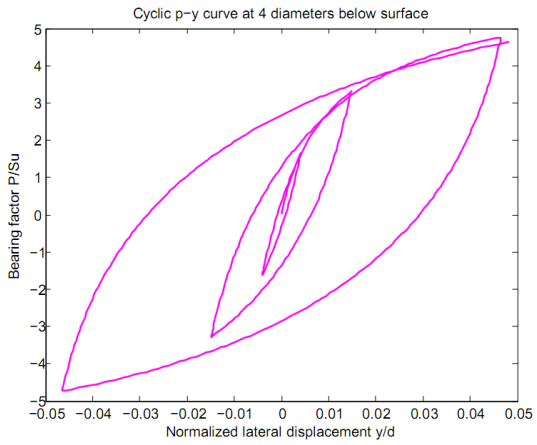

(a) 4 diameters below surface

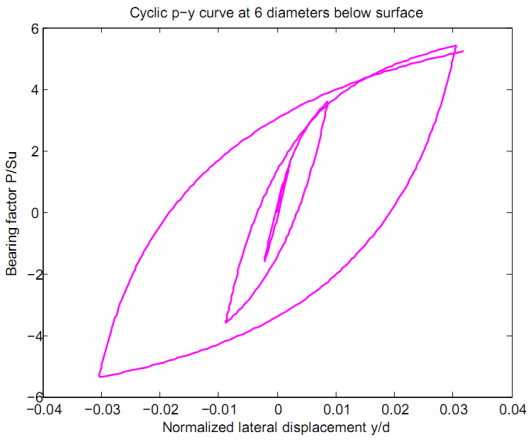

(b) 6 diameters below surface

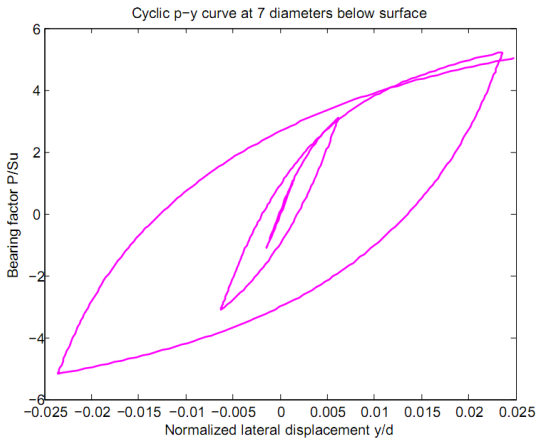

(c) 7 diameters below surface

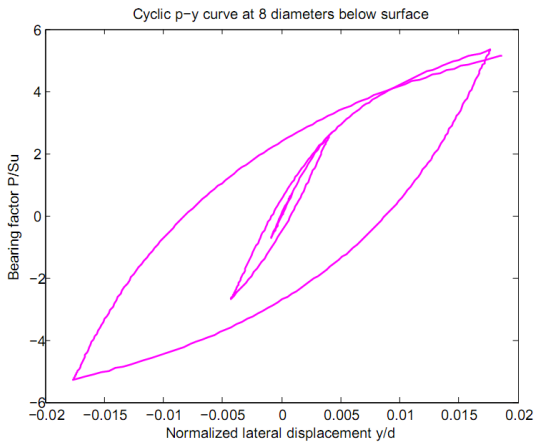

(d) 8 diameters below surface

Figure 6.23 Cyclic p-y cures under load control

Chapter 7 **Conclusions and recommendations**

7.1 Conclusions

The basic critical state models provide a rational framework for understanding soil behavior. A summary of the findings in this thesis is as follows:

1) The proposed AZ-Cam clay model retains the simplicity of the basic critical state models. To smoothen out the degradation of stiffness, the bounding surface concept is used. In order to govern the peak strength of heavily OC clay under drained shearing, rather than a straight Hvorslev line, a curved line is adopted in the current study as the failure line on the dry side in $v-\ln p'$ space based on the extensive test data of Atkinson (2007). To better model the undrained shear strength of heavily OC clay, the original CSL of the basic critical state models is repositioned in $v-\ln p'$ space. Therefore, the peak strength and the undrained shear strength of heavily OC clays can be predicted quite satisfactorily.
2) For single element tests, comprehensive comparisons of model predictions with laboratory test data are conducted on various clays (kaolin clay, Fujinomori clay and BBC) under various loading conditions. For monotonic loading, the model predictions on kaolin clay and Fujinomori clay are quite satisfactory, which demonstrate the capability of the model. The model is unable to predict the softening behavior of NC and lightly OC BBC which exhibits significant anisotropy. However, the agreement for heavily OC BBC is acceptable, even in CK_0UDSS tests, which is different from the triaxial shearing modes. Although the prediction of BBC is relatively unsatisfactory due to the isotropic assumption of the model, the failure envelope introduced does enhance the ability of the AZ-Cam

clay model in simulating heavily OC clays while retaining the simplicity of the model. The predicted variations of normalized undrained shear strength ratio and peak strength ratio with *OCRs* for various types of clays under different shearing modes show reasonable agreement which further verify the capability of the proposed model.

3) For cyclic loading, by using a constant Poisson's ratio, the model predicted effective stress path matches the test data of Wroth & Loudon (1967) quite well, although the model is unable to predict the plastic strain occurred during the unloading process of in the fifth cycle. Further, the model simulates the cyclic behavior of Fujinomori clay quite satisfactory by using a constant Poisson's ratio. By incorporating small strain stiffness and the Masing's rule as well as Pyke's extensions, the model can predict the salient hysteretic behavior of Gualt clay reported by Dasari (1996). The model can also predict the softening behavior of kaolin clay quite well in the multi-stage cyclic loading.
4) For boundary value problems, a well conductor in soft clay subjected to lateral loading is simulated by the proposed soil model and other common soil models. For monotonic loading, the predicted head load-displacement curve differs significantly among different soil constitutive models. Thus the predicted response of the well conductor is rather sensitive to the soil model employed. The predicted conductor head load-displacement response agrees well up to 0.2m with the centrifuge test by the AZ-Cam clay model. At larger displacement, the AZ-Cam clay model, the MCC model and the Tresca model all over predicted the response. The predicted p-y curves from the AZ-Cam clay model agree reasonably well with the centrifuge tests. However, the API method significantly under predicts the

stiffness in the initial loading and the ultimate strength at large deformation. Therefore, the fatigue life predicted by the API method may be overly conservative.

5) For cyclic loading, the AZ-Cam clay model is able to predict the softening and the hysteretic behavior of the conductor in cyclic displacement control loading. The predicted head response agrees reasonably well with the centrifuge test result. For load control cyclic loading, the stiffness predicted by the AZ-Cam clay model is smaller than the value predicted by Templeton (2009) using a total stress elastic-hardening soil model. However, both models predict the hysteretic behavior very well.

7.2 Recommendations

Along with above listed advantages of the proposed model, there are several limitations in the current study. Thus some recommendations for future work are listed as follows:

1) More high-quality triaxial test data are required to fully justify the ultimate strength parameter *T* introduced in the current study. *T* reflects a basic assumption made in the current study that the critical state of heavily OC clay will lie to the left of the original CSL of basic critical state models in $v-\ln p'$ space. To test this assumption, high-quality *CIU* tests on heavily OC clay should be carried out. However, as heavily OC clay will exhibit strain-softening when drainage occurs, if local drainage occurs in the undrained shearing, localized shearing band may form within the sample. The shear band will make the soil sample a boundary value problem. Thus the information after the formation of the shear band could not be used to test the constitutive relations. It is thus critical to control the drainage condition in *CIU* test.

2) Theoretical efforts should be directed to solve the negative Poisson's ratio problem when incorporating the small strain stiffness, although the effect of negative Poisson's ratio is negligible based on the current study. As the bulk modulus adopted in the current study is the same as that in basic critical state models, if the shear modulus takes the value at very small strain at initial loading, the Poisson's ratio will be negative in the very small stain region. With the increasing of strain or stress level, the shear modulus will decrease, thus the Poisson's ratio will become positive. A negative Poisson's ratio is theoretically acceptable and it seems to have little effect on the predicted behavior in the current study. Further research should be paid on this issue. A possible way is to adopt a very large bulk modulus in the very small strain region. However, the simulation and measurement of the bulk modulus in the very small strain region will inevitably introduce additional model parameters and add testing complexity.

3) Continued effects should be directed on the elastic shear modulus under the cyclic loading. As discussed previously, the hysteretic behavior of clay under the cyclic loading is rather sensitive to the choice of the shear modulus. A constant shear modulus may not be easy to choose in a boundary value problem if the cyclic strain level is unknown. A constant Poisson's ratio is theoretically unacceptable if the bulk modulus follows the formula in the basic critical state models. Incorporating $G_{\max}$ together with the Masing' rule works reasonably, but cannot capture the whole behavior under the cyclic loading. For example, the Masing's rule used in the current study under predicts the decreasing of shear stress in the unloading process. Thus the predicted damping is much larger than the test data of Subhadeep (2009).

4) The proposed model can only predict the isotropic cyclic behavior of NC to lightly OC clay. For heavily OC clay, both theoretical modeling and test data are needed to further improve the model. For intact soil, which exhibit significant anisotropy, more sophisticated anisotropic model will be needed.
5) For the boundary value problem, more field cases should be employed to further verify the proposed model. The major purpose of the proposed model is to better simulate the peak strength and ultimate strength of heavily OC clay, but the soil in the centrifuge test simulated in the current study is lightly OC clay. Therefore, it is meaningful to further simulate the boundary value problem consisting of heavily OC clay by using the proposed AZ-Cam clay model.

Reference

ABAQUS (2011). *User manual* Hibbit, Karlsson & Sorensen, Inc.

Abbo, A. J. & Sloan, S. W. (1996). An automatic load stepping algorithm with error control. *International Journal for Numerical Methods in Engineering*, **39**, No. 10: 1737-1759.

Abdulhadi, N. O. (2009). *An experimental investigation into the stress-dependent mechanical behavior of cohesive soil with application to wellbore instability*.

Achmus, M., Kuo, Y. S. & Abdel-Rahman, K. (2009). Behavior of monopile foundations under cyclic lateral load. *Computers and Geotechnics*, **36**, No. 5: 725-735.

Al-Tabbaa, A. (1987). *Permeability and stress-strain response of speswhite kaolin*, Cambridge University, UK.

Al-Tabbaa, A. (1987). *Permeability and stress-strain response of speswhite kaolin*, PhD Thesis, Cambridge University, UK.

Al-Tabbaa, A. & Wood, D. M. (1989). An experimentally based 'bubble' model for clay. *Int. Conf. Num. Models Geomech, NUMOG III*, Balkema. pp. 91-99.

Andersen, K. H. (2009). Bearing capacity under cyclic loading - offshore, along the coast, and on land. The 21st Bjerrum Lecture presented in Oslo, 23 November 2007. *Canadian Geotechnical Journal*, **46**, No. 5: 513-535.

API-RP2A (2000). Recommended practice for planning, designing, and constructing fixed offshore platforms: working stress design.

Atkinson, J. (2007). Peak strength of overconsolidated clays. *Geotechnique*, **57**, No. 2: 127-135.

Atkinson, J. H. & Bransby, P. L. (1978). *The mechanics of soils. An introduction to critical state soil mechanics*. McGraw-Hill, London.

Atkinson, J. H. & Richardson, D. (1987). The effect of local drainage in shear zones on the undrained strength of overconsolidated clay. *Geotechnique*, **37**, No. 3: 393-403.

Atkinson, J. H. & Sallfors, G. (1991). Experimental determination of stress-strain-time characteristics in laboratory and in situ tests. *Proceedings of the 10th European Conference on Soil Mechanics and Foundation Engineering,*, Florence. pp. 915-956.

Bailey, W. A. (1961). *Effects of salt on the shear strength of Boston blue clay*.

Banerjee, P. K. & Stipho, A. S. (1978). Associated and non-associated constitutive relations for undrained behavior of isotropic soft clays. *Int. J. Numer. Anal. Mech. Geomech.*, **2**, No. 1: 35-56.

Banerjee, P. K. & Stipho, A. S. (1979). Elastoplastic model for undrained behavior of heavily overconsolidated clays. *Int. J. Numer. Anal. Mech. Geomech.*, **3**, No. 1: 97-103.

Been, K. & Jefferies, M. G. (1985). A state parameter for sands. *Geotechnique*, **35**, No. 2: 99-112.

Bensari, J. E. (1984). *Stress-strain characteristics from undrained and drained triaxial tests on resedimented Boston blue clay*.

Borja, R. I. & Lee, S. R. (1990). Cam clay plasticity. 1. Implicit integration of elastoplastic constitutive relations. *Computer Methods in Applied Mechanics and Engineering*, **78**, No. 1: 49-72.

Burland, J. B. & Symes, M. (1982). A simple axial displacement gauge for use in the triaxial apparatus. *Geotechnique*, **32**, No. 1: 62-65.

Burland, J. B., Rampello, S., Georgiannou, V. N. & Calabresi, G. (1996). A laboratory study of the strength of four stiff clays. *Geotechnique*, **46**, No. 3: 491-514.

Buscarnera, G., Dattola, G. & di Prisco, C. (2011). Controllability, uniqueness and existence of the incremental response: A mathematical criterion for elastoplastic constitutive laws. *International Journal of Solids and Structures*, **48**, No. 13: 1867-1878.

Byrne, B. W. (2000). *Investigations of Suction Caissons in Dense Sand*, Oxford University, UK.

C-CORE (2005). *Centrifuge modeling of cyclically loaded conductors in clay: Tests 1-4*, Report R-04-100-293.

Casagrande, A. (1936). Characteristics of cohesionless soils affecting the stability of slopes and earth fills. *J. Boston Soc. Civ. Engrs*, **23**, No. 1: 13-32.

Chen, W. E. & Mizuno, E. (1990). *Nonlinear analysis in soil mechanics*. Elsevier Science Publishing Co Inc, New York, USA.

Clayton, C. R. I. (2011). Stiffness at small strain: research and practice. *Geotechnique*, **61**, No. 1: 5-37.

Costa-Filho, L. M. & Vaughan, P. R. (1980). Discussion on "A computer model for the analysis of ground movements in London clay" by Simpson et al. (1979). . *Geotechnique*, **30**, No.: 336-339.

Crouch, R. S. & Wolf, J. P. (1994). Unified 3D critical state bounding surface plasticity model for soils incorporating continuous plastic loading under cyclic path. I: Constitutive relations. *Int. J. Numer. Anal. Mech. Geomech.*, **18**, No. 11: 735-758.

Dafalias, Y. F. (1975). *On cyclic and anisotropic plasticity: i) a general model including material behaviour under stress reversals; ii) anisotropic hardening for initially orthotropic materials*, University of California at Berkeley, USA.

Dafalias, Y. F. & Herrmann, L. R. (1982). Bounding surface formulation of soil plasticity. In *Soil mechanics - transient and cyclic loads*. Edited by G. N. Pande and O. C. Zienkiewrcz, Wilcy Chichester. pp. 253-282.

Dasari, G. R. (1996). *Modeling of the variation of soil stiffness during sequential construction*, PhD Thesis, Cambridge University, UK.

Dasari, G. R. (1996). *Modeling of the variation of soil stiffness during sequential construction*, Cambridge University, UK.

de Saint-Venant, B. (1870). Memoire sur I'etablissement des equations differentielles des mouvements interieurs operes dans les corps solides ductiles au dela des limites ou I'elasticite pourrait les ramener a leur premier etat. *C.R. Acas. Sci. (Paris)*, **70**, No.: 473-480.

Demello, V. F. B. (1977). Reflections on design decisions of practical significance to embankment dams. *Geotechnique*, **27**, No. 3: 279-355.

Dowell, M. & Jarratt, P. (1972). The 'Pegasus' method for computing the root of an equation. *BIT*, **12**, No.: 503-508.

Drucker, D. C., Gibson, R. E. & Henkel, D. J. (1957). Soil mechanics and work hardening theories of plasticity. *Trans. ASCE*, **122**, No.: 338-346.

Fayad, P. (1986). *Aspects of the volumetric and undrained behavior of Boston blue clay*.

Fayad, P. (1986). *Aspects of the volumetric and undrained behavior of Boston blue clay*. SM Thesis, Massachusetts Institute of Technology, USA.

Gens, A. (1982). *Stress-strain and strength characteristics of a low plasticity clay*, Imperial College, London, UK.

Goh, T. L. (2003). *Stabilization of an excavation by an embedded improved soil layer*, National University of Singapore, Singapore.

Grammatikopoulou, A. (2004). *Development, implementation and application of kinematic hardening models for overconsolidated clays* University of London (Imperial College) UK.

Hardin, B. O. (1978). The nature of stress-strain behavior for soils. *In* Proc. Spec. Cod. Earthquake Eng. Soil Dyn., ASCE, Pasadena, pp. 3-90.

Hardin, B. O. & Black, W. L. (1968). Vibration modulus of nornally consolidated clay. *ASCE, JSMFD*, **94**, No. SM2: 353-368.

Hardin, B. O. & Drnevich, V. P. (2002). Shear modulus and damping in soils: Design equations and curves. *Geotechnical Special Publication*, **118**, No.: 1459-1484.

Hashiguchi, K. (1980). Constitutive equations of elastoplastic materials with elastic-plastic transition. *Journal of Applied Mechanics-Transactions of the Asme*, **47**, No. 2: 266-272.

Hashiguchi, K. (1989). Subloading surface model in unconventional plasticity. *International Journal of Solids and Structures*, **25**, No. 8: 917-945.

Hashiguchi, K. & Ueno, M. (1977). Elasto-plastic laws of granular materials. *9th ICSMFE*

Tokyo. pp. 73-82.

Henkel, D. J. (1959). The relationships between the effective stresses and water content in saturated clays. *Geotechnique*, **9**, No. 2: 41-54.

Henkel, D. J. (1959). The Relationships Between the Strength, Pore-Water Pressure, and Volume-Change Characteristics of Saturated Clays. *Geotechnique*, **9**, No. 3: 119-135.

Henkel, D. J. (1960). The relationships between the effective stresses and water content in saturated clays. *Geotechnique*, **10**, No. 2: 41-54.

Hill, R. (1950). *The Mathematical Theory of Plasticity*. Clarendon Press, Oxford.

Hoek, E. & Brown, E. T. (1980). *Underground excavation in rock*, Institution of Mining and Metallurgy, London.

Houlsby, G. T. (1982). A derivation of the small strain theory of plasticity from thermomechanics. *In* Int. Conf. Deform. and Flow of Granular Mat., Delft, pp. 109-118.

Houlsby, G. T. (1985). The use of a variable shear modulus in elastic-plastic models for clays. *Computers and Geotechnics,* **1**, No.: 3-13.

Houlsby, G. T., Wroth, C. P. & Wood, D. M. (1982). Predictions of the results of laboratory tests on a clay using a critical state model. *In* Proc. int. workshop on constitutive behaviour of soils, Grenoble, Balkema (Rotterdam), pp. 99-121.

Hueckel, T. & Nova, R. (1979). Some hysteresis effects of the behavior of geologic media. *International Journal of Solids and Structures*, **15**, No. 8: 625-642.

Hvorslev, M. J. (1936). Physical components of the shear strength of saturated clays. *Proceedings, ASCE Research Conference on the Shear Strength of Cohesive Soils, Boulder, Co.*, pp. 169-273.

Ishibashi, I. & Zhang, X. (1993). Unified dynamic shear moduli and damping ratios of sand and clay. *Soils and Foundations*, **33**, No. 1: 182-191.

Iwan, W. D. (1967). On a class of models for the yielding behaviour of continuous and composite systems. *Journal of Applied Mechanics,* **34**, No. 3: 612-&.

Jeanjean, P. (2009). Re-assessment of P-Y curves for soft clays from centrifuge testing and finite element modeling. Offshore Technology Conference, OTC 18005.

Jeanjean, P. (2012). Personal email communication.

Kavvadas, M. (1982). *Non-linear consolidation around driven piles in clay*, Massachusetts Institute of Technology

USA.

Krieg, R. D. (1975). Practical 2 surface plasticity theory. *Journal of Applied Mechanics-Transactions of the ASME*, **42**, No. 3: 641-646.

Kuntsche, K. (1982). Tests on clay. *In* Proc. Int.. Workshop on Constitutive Behavior of Soils, Grenoble.

Ladd, C. C., Foott, R., Ishihara, K., Schlosser, F. & Poulos, H. G. (1977). Stress-deformation and strength characteristics, state-of-the-art report. *9th ICSMFE*, Tokyo. pp. 421-494.

Lade, P. V. (1977). Elasto-plastic stress-strain theory for cohesionless soil with curved yield surfaces. *International Journal of Solids and Structures*, **13**, No. 11: 1019-1035.

Lade, P. V. & Duncan, J. M. (1978). Elastoplastic stress-strain theory for cohesionless soil. *Journal of the Geotechnical Engineering Division-Asce*, **104**, No. 1: 139-141.

Lade, P. V. & Nelson, R. B. (1987). Modeling the elastic behavior of granular materials. *International Journal for Numerical and Analytical Methods in Geomechanics*, **11**, No. 5: 521-542.

Leblanc, C., Houlsby, G. T. & Byrne, B. W. (2010). Response of stiff piles in sand to long-term cyclic lateral loading. *Geotechnique*, **60**, No. 2: 79-90.

Lesny, K. & Hinz, P. (2007). Investigation of monopile behaviour under cyclic lateral loading. *Proc.of 6th Int. Conf 'Offshore Site Investigation and Geotechnics'*, London, UK. pp. 383-390.

Lewin, P. I. & Burland, J. B. (1970). Stress-probe experiments on saturated normally consolidated clay. *Geotechnique*, **20**, No. 1: 38-&.

Li, T. & Meissner, H. (2002). Two-surface plasticity model for cyclic undrained behavior of clays. *Journal of Geotechnical and Geoenvironmental Engineering*, **128**, No. 7: 613-626.

Love, A. E. H. (1963). *A treatise on the mathematical theory of elasticity*. Dover, New York.

Manzanal, D., Merodo, J. A. F. & Pastor, M. (2011). Generalized plasticity state parameter-based model for saturated and unsaturated soils. Part 1: Saturated state. *International Journal for Numerical and Analytical Methods in Geomechanics*, **35**, No. 12: 1347-1362.

Marsland, A. (1971). Laboratory and in-situ measurements of the deformation moduli of London Clay. *Proceedings of Symposium on the interaction of structure and foundation*, University of Birmingham. pp. 7-17.

Masing, G. (1926). Eigenspannungen and verfestigung heim Messing, Proc. 2nd Int. Congr. Appl. Mech., Zurich.

Matsuoka, H. & Nakai, T. (1974). Stress-deformation and strength characteristics under three different principal stress. *In* Proc. JSCE, 232, pp. 59-70. .

McDowell, G. R. & Hau, K. W. (2004). A generalised Modified Cam clay model for clay and sand incorporating kinematic hardening and bounding surface plasticity. *Granular Matter*, **6**, No. 1: 11-16.

Melan, E. (1938). Zur plastizitat des raumlichen Kontinuums. *Ing. Arch.*, **9**, No.: 116-125.

Mita, K. A. (2002). *Constitutive testing of soil on the dry side of critical state*, National University of Singapore, Singapore.

Mita, K. A. (2002). *Constitutive testing of soil on the dry side of critical state*, PhD Thesis, National University of Singapore, Singapore.

Mita, K. A., Dasari, G. R. & Lo, K. W. (2004). Performance of a three-dimensional Hvorslev-modified Cam clay model for overconsolidated clay. *ASCE, Int. J. Geomech.*, **4**, No. 4: 296-309.

Mroz, Z. (1967). On description of anisotropic work hardening. *Journal of the Mechanics and Physics of Solids*, **15**, No. 3: 163-&.

Mroz, Z., Norris, V. A. & Zienkiewicz, O. C. (1978). Anisotropic hardening model for soils and its application to cyclic loading. *International Journal for Numerical and Analytical Methods in Geomechanics*, **2**, No. 3: 203-221.

Mroz, Z., Norris, V. A. & Zienkiewicz, O. C. (1979). Application of an anisotropic hardening model in the analysis of elastoplastic deformation of soils. *Geotechnique*, **29**, No. 1: 1-34.

Mroz, Z., Norris, V. A. & Zienkiewicz, O. C. (1981). Anisotropic, critical state model for soils subjected to cyclic loading. *Geotechnique*, **31**, No. 4: 451-469.

Nakai, T. (1989). Isotropic hardening elastoplastic model for sand considering the stress path dependency in three-dimensional stresses. *Soils and Foundations*, **29**, No. 1: 119-137.

Nakai, T. & Matsuoka, H. (1986). Generalized elastoplastic constitutive model for clay in three-dimensional stresses. *Soils and Foundations*, **26**, No. 3: 81-98.

Nakai, T. & Hinokio, M. (2004). A simple elastoplastic model for normally and overconsolidated soils with unified material parameters (vol 44, pg 53, 2004). *Soils and Foundations*, **44**, No. 5: 49-49.

Nakai, T. & Hinokio, M. (2004). A simple elastoplastic model for normally and overconsolidated soils with unified material parameters. *Soils Found.*, **44**, No. 5: 49-49.

Papadimitriou, A. G. & Bouckovalas, G. D. (2002). Plasticity model for sand under small and large cyclic strains: a multiaxial formulation. *Soil Dynamics and Earthquake Engineering*, **22**, No. 3: 191-204.

Parry, R. H. G. (1958). Triaxial compression and extension tests on remoulded saturated clay. *Geotechnique* **10**, No. 4: 166-180.

Parry, R. H. G. (1960). Triaxial compression and extension tests on remoulded saturated clay. *Geotechnique* **10**, No. 4: 166-180.

Pastor, M., Zienkiewicz, O. C. & Leung, K. H. (1985). Simple model for transient soil loading in earthquake analysis II Non-associative models for sands. *International Journal for Numerical and Analytical Methods in Geomechanics*, **9**, No. 5: 477-498.

Pastor, M., Zienkiewicz, O. C. & Chan, A. H. C. (1990). Generalized plasticity and the modelling of soil behaviour. *International Journal for Numerical and Analytical Methods in Geomechanics*, **14**, No. 3: 151-190.

Pestana, J. M. & Whittle, A. J. (1999). Formulation of a unified constitutive model for clays and sands. *Int. J. Numer. Anal. Mech. Geomech.*, **23**, No. 12: 1215-1243.

Pestana, J. M. & Whittle, A. J. (1999). Formulation of a unified constitutive model for clays and sands. *International Journal for Numerical and Analytical Methods in Geomechanics*, **23**, No. 12: 1215-1243.

Pestana, J. M., Whittle, A. J. & Gens, A. (2002). Evaluation of a constitutive model for clays and sands: Part II - Clay behaviour. *Int. J. Numer. Anal. Mech. Geomech.*, **26**, No. 11: 1123-1146.

Plaxis (2011). *User manual*. Plaxis.

Potts, D. M. & Ganendra, D. (1994). An evaluation of substepping and implicit stress point algorithms. *Computer Methods in Applied Mechanics and Engineering*, **119**, No. 3-4: 341-354.

Potts, D. M. & Zdravkovic, L. (1999). *Finite element analysis in geotechnical engineering -Theory*. Thomas Telford.

Potts, D. M. & Zdravkovic, L. (1999). *Finite element analysis in geotechnical engineering - Theory*. Thomas Telford.

Prevost, J. H. (1976). Undrain stress-strain-time behaviour of clays. *ASCE, JGED*, **102, GT12**, No.: 1245-1259.

Prevost, J. H. (1977). Mathematical modelling of monotonic and cyclic undrained clay behaviour. *International Journal for Numerical and Analytical Methods in Geomechanics*, **1**, No. 2: 195-216.

Prevost, J. H. (1978). Plasticiy theory for soil stress-strain behavior. *Journal of the Engineering Mechanics Division-ASCE*, **104**, No. 5: 1177-1194.

Pyke, R. (1979). Nonlinear soil models for irregular cyclic loadings. *Journal of the Geotechnical Engineering Division-ASCE*, **105**, No. 6: 715-726.

Randolph, M. F. & Wroth, C. P. (1981). Application of the failure state in undrained simple shear to the shaft capacity of driven piles. *Geotechnique*, **31**, No. 1: 143-157.

Randolph, M. F., Carter, J. P. & Wroth, C. P. (1979). Driven piles in clay - the effects of installation and subsequent consolidation. *Geotechnique*, **29**, No. 4: 361-393.

Roscoe, K. H. & Burland, J. B. (1968). On the generalized stress-strain behaviour of 'wet' clay. In *Eng. Plasticity*, Cambridge Univ. Press. pp. 535-609.

Schofield, A. N. & Wroth, C. P. (1968). *Critical state soil mechanics*. McGraw Hill, London.

Sloan, S. W. (1987). Substepping schemes for the numerical integration of elasto-plastic stress-strain relations. *International Journal for Numerical Methods in Engineering*, **24**, No. 5: 893-911.

St. John, H. D. (1975). *Field and theoretical studies of the behaviour of ground around deep excavations in London Clay*, University of Cambridge, UK.

Stallebrass, S. E. (1990). *Modelling the effect of recent stress history on the deformation of overconsolidated soils*, The City University, London, UK.

Stallebrass, S. E. & Taylor, R. N. (1997). The development and evaluation of a constitutive model for the prediction of ground movements in overconsolidated clay. *Geotechnique*, **47**, No. 2: 235-253.

Subhadeep, B. (2009). *Centrifuge and numerical modeling of soft clay-pile-raft foundations subjected to seismic shaking*, National University of Singapore, Singapore.

Templeton, J. S. (2009). Finite element analysis of conductor/seafloor interaction. Offshore Technology Conference, OTC 20197.

Terzaghi, K. (1936). The shearing resistance of saturated soil and the angle between the planes of shear. *1st ICSMFE*, Cambrudge, MA. pp. 54-56.

USFOS. (2012). User manual [online]. Available from http://www.usfos.no/.

Vaneekelen, H. A. M. (1980). Isotropic yield surfaces in 3 dimensions for use in soil mechanics. *Int. J. Numer. Anal. Mech. Geomech.*, **4**, No. 1: 89-101.

Vaneekelen, H. A. M. (1980). Isotropic yield surfaces in 3 dimensions for use in soil mechanics. *International Journal for Numerical and Analytical Methods in Geomechanics*, **4**, No. 1: 89-101.

Vaneekelen, H. A. M. & Potts, D. M. (1978). BEHAVIOR OF DRAMMEN CLAY UNDER CYCLIC LOADING. *Geotechnique*, **28**, No. 2: 173-196.

Viggiani, G. & Atkinson, J. H. (1995). Stiffness of fine-grained soil at very small strains. *Geotechnique*, **45**, No. 2: 249-265.

von Mises, R. (1928). Mechanik der plastischen Formaenderung von Kristallen. *Z. angew. Math. Meek,*, **8**, No.: 161-185.

Whitman, R. V., Holt, R. J. & Murphy, V. J. (1969). Discussion of paper by Hardin and Black. *ASCE, JSMFD*, **95**, No. SM2: 656-659.

Whittle, A. J. (1987). *Aconstitutive model for overconsolidated clays with application to the cyclic loading of friction piles*, Massachusetts Institute of Technology, USA.

Whittle, A. J. (1987). *Aconstitutive model for overconsolidated clays with application to the cyclic loading of friction piles*, PhD Thesis, Massachusetts Institute of Technology, USA.

Whittle, A. J. (1987). *Aconstitutive model for overconsolidated clays with application to the cyclic loading of friction piles*. PhD Thesis, Massachusetts Institute of Technology, USA.

Whittle, A. J. (1993). Evaluation of a constitutive model for overconsolidated clays. *Geotechnique*, **43**, No. 2: 289-313.

Wong, P. K. K. & Mitchell, R. J. (1975). Yielding and plastic flow of sensitive cemented clay. *Geotechnique*, **25**, No. 4: 763-782.

Woods, R. D. (1978). Measurement of dynamic soil properties. *Proceedings, ASCE Speciality Conference on Earthquake Engineering and Soil Dynamics*, Pasadena, Ca., pp. 91-178.

Wroth, C. P. (1984). The interpretation of insitu soil tests. *Geotechnique*, **34**, No. 4: 449-489.

Wroth, C. P. & Loudon, P. A. (1967). The correlation of strains within a family of triaxial tests on overconsolidated samples of kaolin. *Proc.,Geotechnical Conf.*, Olso, Norway. pp. 159-163.

Wroth, C. P. & Houlsby, G. T. (1980). A critical state model for predicting the behaviour of clays. *In* Proc. Workshop on Limit equilibrium, plasticity and generalized stress-strain in geotechnical engineering, Montreal, pp. 592-627.

Wroth, C. P. & Houlsby, G. T. (1985). Soil mechanics – property characterization and analysis procedures. *In* Proc. 11th Int. Conf. SMFE, (1), San Fransisco, pp. 1-55.

Yu, H. S. (1998). CASM: A unified state parameter model for clay and sand. *International Journal for Numerical and Analytical Methods in Geomechanics*, **22**, No. 8: 621-653.

Yu, H. S. (2006). *Plasticity and geomechanics*. Springer, USA.

Yu, H. S., Khong, C. & Wang, J. (2007). A unified plasticity model for cyclic behaviour of clay and sand. *Mechanics Research Communications*, **34**, No. 2: 97-114.

Zienkiewicz, O. C. & Naylor, D. J. (1973). Finite element studies of soils and porous media. In *Lect. Finite Elements in Continuum Mechanics*. Edited by Oden and d. Arantes, UAH press. pp. 459-493.

Zienkiewicz, O. C., Leung, K. H. & Pastor, M. (1985). Simple model for transient soil loading in earthquake analysis I Basic model and its application. *International Journal for Numerical and Analytical Methods in Geomechanics*, **9**, No. 5: 453-476.

Zienkiewicz, O. C., Leung, K. H. & Pastor, M. (1985). Simple model for transient soil loading in earthquake analysis I: Basic model and its application. *Int. J. Numer. Anal. Mech. Geomech.*, **9**, No. 5: 453-476.

Zienkiewicz, O. C., Taylor, R. L. & Zhu, J. Z. (2005). *The finite element method: Its basis and fundamentals-Sixth edition*. Elsevier Butterworth-Heinemann.

Zytynski, M., Randolph, M. F., Nova, R. & Wroth, C. P. (1978). Modeling unloading-reloading behavior of soils. *International Journal for Numerical and Analytical Methods in Geomechanics*, **2**, No. 1: 87-93.

Appendix A Classical theory of elasto-plasticity

A.1 Stress and strain variables

A.1.1 Stress definition

Following Chen & Mizuno (1990) and Grammatikopoulou (2004), stress is defined as a second order tensor which contains nine components as follows:

$$\boldsymbol{\sigma} = \begin{bmatrix} \sigma_x & \tau_{xy} & \tau_{xz} \\ \tau_{yx} & \sigma_y & \tau_{yz} \\ \tau_{zx} & \tau_{zy} & \sigma_z \end{bmatrix} \tag{A.1}$$

where σ denotes the normal stress, τ denotes the shear stress and the subscripts denote the direction and surface where the stress acts. Generally following equation holds for shear stress as

$$\tau_{ij} = \tau_{ji} \tag{A.2}$$

where i, j refers to x, y, z. Therefore only six independent components are required to fully define the stress state. The stress tensor in Equation A.1 thus can be simplified into a column vector as follows:

$$\{\sigma\} = \left(\sigma_x, \sigma_y, \sigma_z, \tau_{xy}, \tau_{yz}, \tau_{zx}\right)^T \tag{A.3}$$

A.1.2 Strain definition

In a similar way to define the stress, the strain is also a second order tensor defined by nine components as follows:

$$\boldsymbol{\varepsilon} = \begin{bmatrix} \varepsilon_x & \frac{1}{2}\gamma^s_{xy} & \frac{1}{2}\gamma^s_{xz} \\ \frac{1}{2}\gamma^s_{yx} & \varepsilon_y & \frac{1}{2}\gamma^s_{yz} \\ \frac{1}{2}\gamma^s_{zx} & \frac{1}{2}\gamma^s_{zy} & \varepsilon_z \end{bmatrix} \quad \text{A.4}$$

where ε denotes the normal strain, γ^s denotes the engineering shear strain and the subscripts denote corresponding direction and surface. Similarly, since $\gamma^s_{xy} = \gamma^s_{yx}$, $\gamma^s_{yz} = \gamma^s_{zy}$ and $\gamma^s_{zx} = \gamma^s_{xz}$, only six components are required to fully determine the strain state. Equation A.4 is thus simplified into a column vector as follows:

$$\{\varepsilon\} = \left(\sigma_x, \sigma_y, \sigma_z, \gamma_{xy}, \gamma_{yz}, \gamma_{zx}\right)^T \quad \text{A.5}$$

A.1.3 Stress invariants

From the geotechnical engineering point, a typical and suitable choice of three stress invariants is provided as follows:

Mean stress:

$$p = \frac{1}{3}(\sigma_x + \sigma_y + \sigma_z) \quad \text{A.6}$$

Deviatoric stress:

$$J = \left(\frac{1}{2}(\mathbf{s}:\mathbf{s})\right)^{1/2} = \left(\sigma_x - p\right)^2 + \left(\sigma_y - p\right)^2 + \left(\sigma_z - p\right)^2 + 2\tau^2_{xy} + 2\tau^2_{yz} + 2\tau^2_{zx} \quad \text{A.7}$$

or $q = \sqrt{3}J$ A.8

Lode's angle:

$$\theta = -\frac{1}{3}\sin^{-1}\left(\frac{3\sqrt{3}}{2}\frac{\det(\mathbf{s})}{\left(\left(\frac{1}{2}(\mathbf{s}:\mathbf{s})\right)^{1/2}\right)^{3}}\right) \quad \text{A.9}$$

where **:** is the tensor scalar product, $\det(\bullet)$ is the determinant of a tensor, and **s** denotes the deviatoric stress tensor as follows

$$\mathbf{s} = \begin{bmatrix} \sigma_x - p & \tau_{xy} & \tau_{xz} \\ \tau_{yx} & \sigma_y - p & \tau_{yz} \\ \tau_{zx} & \tau_{zy} & \sigma_z - p \end{bmatrix} \quad \text{A.10}$$

A.1.4 Strain invariants

As the material response can be divided manually into the volumetric response and deviatoric shear response, two corresponding strain invariants are as follows:

Volumetric strain:

$$\varepsilon_v = \varepsilon_x + \varepsilon_y + \varepsilon_z \quad \text{A.11}$$

Deviatoric strain:

$$E_d = \left[2(\mathbf{e_s}:\mathbf{e_s})\right]^{1/2} = \left[2\left(\varepsilon_x - \frac{\varepsilon_v}{3}\right)^2 + 2\left(\varepsilon_y - \frac{\varepsilon_v}{3}\right)^2 + 2\left(\varepsilon_z - \frac{\varepsilon_v}{3}\right)^2 + \gamma_{xy}^2 + \gamma_{yz}^2 + \gamma_{zx}^2\right]^{1/2} \quad \text{A.12}$$

or $\varepsilon_s = \frac{1}{\sqrt{3}} E_d$ A.13

where $\mathbf{e_s}$ represents the deviatoric components of the strain tensor defined as follows:

$$\mathbf{e_s} = \begin{bmatrix} \varepsilon_x - \frac{\varepsilon_v}{3} & \frac{1}{2}\gamma_{xy} & \frac{1}{2}\gamma_{xz} \\ \frac{1}{2}\gamma_{yx} & \varepsilon_y - \frac{\varepsilon_v}{3} & \frac{1}{2}\gamma_{yz} \\ \frac{1}{2}\gamma_{zx} & \frac{1}{2}\gamma_{zy} & \varepsilon_z - \frac{\varepsilon_v}{3} \end{bmatrix} \quad \text{A.14}$$

When a material element undergoes deformation, the work done by the external loads is independent of the choice of reference axes. Thus the internal energy obtained by multiplying the stress and strain invariants should also be independent of the reference axes. The choice of strain invariant is based on this criterion, which obviously depends on the proper choice of stress invariants as well. The incremental work which obtained by multiplying the stress and strain state can be expressed as follows:

$$dE^w = \{\sigma\}^T \{d\varepsilon\} \quad \text{A.15}$$

where E^w is the energy in the material element, 'd' represents the small change or 'incremental' as will be used throughout this thesis.

Alternatively, the incremental energy can be expressed as follows:

$$dE^w = pd\varepsilon_v + JdE_d \quad \text{A.16}$$

$$dE^w = pd\varepsilon_v + qd\varepsilon_s \quad \text{A.17}$$

The first term of the right hand of Equation A.16 (or Equation A.17) is the incremental energy resulted from the volumetric response, the second term of the right hand of Equation A.16 and Equation A.17 represents the incremental energy resulted from the deviatroic shear response. From the definitions of deviatroic stress and strain, Equation

A.16 and Equation A.17 actually are identical as long as deviatoric stress J corresponds to deviatoric strain E_d and deviatoric stress q corresponds to deviatoric strain ε_s.

A.2 Key concepts of plastic theory

In order to evaluate the plastic strain completely, following Yu (2006), Mita (2002) and Grammatikopoulou (2004), conventional plastic theory requires three main ingredients: yield condition, plastic flow rule and the hardening rule. All of those three ingredients will be discussed in the following sections.

A.2.1 Yield criterion

Under any possible stress combination, the yield criterion separates the elastic zone, where the material behaves purely elastically from the elasto-plastic zone, where the material undergoes both elastic and plastic strains. Mathematically, the yield surface can be specified as a yield function F, which is a function of stress state $\{\sigma\}$ and the hardening parameters $\{k\}$:

$$F\left(\{\sigma\},\{k\}\right)=0 \qquad \text{A.18}$$

The behavior of the material thus can be determined from the yield function. When $F<0$ stress state remains in the yield surface, the behavior is purely elastic; $F=0$ stress state remains on the yield surface, the behavior is elasto-plastic; $F>0$ theoretically impossible stress state.

A.2.2 Flow rule

The flow rule is employed to determine the plastic strain increments. The most widely used theory is to assume there exists a plastic potential in the general stress space, whose outward normal vector at the current stress state represents the plastic strain increment vector. The flow rule is thus can be expressed as the following formula (von Mises, 1928; Melan, 1938; Hill, 1950):

$$\left\{d\varepsilon^p\right\} = \Lambda\left\{\frac{\partial P\left(\{\sigma\},\{m\}\right)}{\partial\sigma}\right\} \qquad \text{A.19}$$

where $\left\{d\varepsilon^p\right\}$ is the plastic strain increment vector, Λ is a unknown non-negative scalar. P is the plastic potential and is specified as

$$P\left(\{\sigma\},\{m\}\right) = 0 \qquad \text{A.20}$$

where $\{m\}$ are immaterial since only the differentials of the plastic potential to the stress components are required in the flow rule.

If the plastic potential is assumed to be the same the yield function, $P\left(\{\sigma\},\{m\}\right) = F\left(\{\sigma\},\{k\}\right)$, then the flow rule is associated and a normality condition applies; however, if the plastic potential is different from the yield function, $P\left(\{\sigma\},\{m\}\right) \neq F\left(\{\sigma\},\{k\}\right)$, then the flow rule is non-associated.

Two things have to be noted in Equation A.19. One is Equation A.19 only determines the relative magnitude of the plastic strain increment. As the scalar Λ remains unknown at this stage, the actual plastic strain increments will not be known until Λ is solved. The other is that when Equation A.19 holds, an implicit assumption

of coaxial assumption is satisfied. Coaxial assumption states that principal axes of plastic strain increments coincide with those of the stress. This assumption is based on the observation of de Saint-Venant (1870) for metals, and has been the foundation of almost all the plasticity models used in engineering, although it may not be valid for soils (Yu, 2006).

A. 2.3 Hardening rule

The hardening of a material is a process that involves the yield surface changing in size, location or shape or even the combination of those changes with the loading history (often measured by accumulated plastic strains or the total plastic work per volume) (Hill, 1950). The hardening rule thus describes the evolution of the yield surface in the course of plastic strain or plastic work through affecting the hardening parameters $\{k\}$. The three most widely used hardening rules are presented in the follows:

(i) Isotropic hardening rule. Under isotropic hardening rule, the centre of the yield position will remain statuary in the stress space, while the size will expand or contract isotropically.

(ii) Kinematic hardening rule. It assumes that the yield surface translates in the stress space while the shape and the size remain unchanged. This is consistent with the Bauschinger effect observed in the uniaxial tension-compression test.

(iii) Mixed hardening rule. The mixed hardening rule combines the features of isotropic hardening and kinematic hardening.

A.3 Elastic matrix

The general elastic matrix relates the increments of stress to increments of strains can be expressed as follows:

$$\{d\sigma\} = \left[D^e\right]\{d\varepsilon\} \tag{A.21}$$

where $\{d\sigma\}$ is the total stress increment vector and $\{d\varepsilon\}$ is the total strain increment vector. $\left[D^e\right]$ represents the elastic matrix, the superscript e denotes elastic and $[\bullet]$ represents the expression is a matrix. It has to been noted that although Equation A.21 is specified here for the increments of elastic stress and elastic strain, this expression is still valid when the material behaves elasto-plastically as long as the total strain increment was substitute by the elastic strain increment accordingly.

From the engineering point, the elastic matrix is a six by six symmetric matrix. Following generalized Hooke's law, if the elastic matrix contains 21 material constants, the material is called linear anisotropic material (Chen & Mizuno, 1990). By introducing fully isotropic condition, the number of material constants can be reduced to two. Chen & Mizuno (1990) specifies the linear isotropic elastic matrix (as linearity and isotropicity always hold in the present study for elastic behavior, the linear isotropic elastic matrix is called elastic matrix for short) as follows:

$$\left[D^e\right] = \begin{bmatrix} \lambda_L + 2\mu & \lambda_L & \lambda_L & 0 & 0 & 0 \\ \lambda_L & \lambda_L + 2\mu & \lambda_L & 0 & 0 & 0 \\ \lambda & \lambda_L & \lambda_L + 2\mu & 0 & 0 & 0 \\ 0 & 0 & 0 & \mu & 0 & 0 \\ 0 & 0 & 0 & 0 & \mu & 0 \\ 0 & 0 & 0 & 0 & 0 & \mu \end{bmatrix} \tag{A.22}$$

where λ_L, μ are called Lame's constants. Alternatively, the elastic matrix can be specified in terms of more frequently used parameters Young's modulus E and Possion's ratio ν as follows:

$$\left[D^e\right] = \frac{E}{(1+\nu)(1-2\nu)} \begin{bmatrix} 1-\nu & \nu & \nu & 0 & 0 & 0 \\ \nu & 1-\nu & \nu & 0 & 0 & 0 \\ \nu & \nu & 1-\nu & 0 & 0 & 0 \\ 0 & 0 & 0 & \frac{1-2\nu}{2} & 0 & 0 \\ 0 & 0 & 0 & 0 & \frac{1-2\nu}{2} & 0 \\ 0 & 0 & 0 & 0 & 0 & \frac{1-2\nu}{2} \end{bmatrix} \quad \text{A.23}$$

For geotechnical purpose, as soil often undergoes volumetric strain, and behaves quite differently under isotropic mean stress and deviatoric stress, it is convenient to define the elastic matrix in terms of elastic shear modulus G and the bulk modulus K as follows:

$$\left[D^e\right] = \begin{bmatrix} K+\frac{4}{3}G & K-\frac{2}{3}G & K-\frac{2}{3}G & 0 & 0 & 0 \\ K-\frac{2}{3}G & K+\frac{4}{3}G & K-\frac{2}{3}G & 0 & 0 & 0 \\ K-\frac{2}{3}G & K-\frac{2}{3}G & K+\frac{4}{3}G & 0 & 0 & 0 \\ 0 & 0 & 0 & G & 0 & 0 \\ 0 & 0 & 0 & 0 & G & 0 \\ 0 & 0 & 0 & 0 & 0 & G \end{bmatrix} \quad \text{A.24}$$

Equation A.22, A.23 and A.24 can be inter-related. Mathematically, any two parameters from the above six can fully determine the elastic matrix. The relations between the six elastic parameters are specified as follows:

$$E = \frac{\mu\left(3\lambda_L + 2\mu\right)}{\lambda_L + \mu} \quad \text{A.25}$$

$$\nu = \frac{\lambda_L}{2\left(\lambda_L + \mu\right)} \quad \text{A.26}$$

$$G = \frac{E}{2\left(1+\nu\right)} \quad \text{A.27}$$

$$K = \frac{E}{3\left(1-2\nu\right)} \quad \text{A.28}$$

A.4 Formulation of elasto-plastic matrix

Providing the three key aspects of plastic theory in section A.2 and the elastic matrix in section A.3, these four ingredients can thus be employed to form the elasto-plastic matrix following Chen & Mizuno (1990) and Potts & Zdravkovic (1999).

Following the conventional method, the stress-strain relationship is specified through an incremental way in the form of Equation A.29:

$$\left\{d\sigma\right\} = \left[D^{ep}\right]\left\{d\varepsilon\right\} \quad \text{A.29}$$

where $\left[D^{ep}\right]$ represents the elasto-plastic matrix, the superscript *ep* denotes the elasto-plastic, as opposed to the purely elastic behavior.

The total strain increments vector $\left\{d\varepsilon\right\}$ can be split into two parts as follows:

$$\left\{d\varepsilon\right\} = \left\{d\varepsilon^e\right\} + \left\{d\varepsilon^p\right\} \quad \text{A.30}$$

where $\{d\varepsilon^e\}$ denotes the elastic strain increments vector and $\{d\varepsilon^p\}$ denotes the plastic strain increments vector.

Combining Equation A.21 and Equation A.30, the total stress increments can be expressed as follows:

$$\{d\sigma\} = [D^e]\left(\{d\varepsilon\} - \{d\varepsilon^p\}\right) \quad \text{A.31}$$

The incremental plastic strains can be evaluated from the flow rule. Substitute Equation A.19 into Equation A.31 yields:

$$\{d\sigma\} = [D^e]\{d\varepsilon\} - \Lambda[D^e]\left\{\frac{\partial P}{\partial \sigma}\right\} \quad \text{A.32}$$

As the parameter Λ remains unknown, additional work has to be done to determine Λ.

When the material is elasto-plastic, further loading should meet the consistency condition. Mathematically, the consistency condition can be expressed as follows:

$$dF\left(\{\sigma\},\{k\}\right) = 0 \quad \text{A.33}$$

Using the chain rule of differentiation gives:

$$dF = \left\{\frac{\partial F}{\partial \sigma}\right\}^T \{d\sigma\} + \left\{\frac{\partial F}{\partial k}\right\}^T \{dk\} = 0 \quad \text{A.34}$$

The hardening parameters $\{k\}$ are related to the plastic strains as follows:

$$\{dk\} = \left[\frac{\partial k}{\partial \varepsilon^p}\right]\{d\varepsilon^p\} \quad \text{A.35}$$

Substitute Equation A.35 into Equation A.34 yields

$$dF = \left\{\frac{\partial F}{\partial \sigma}\right\}^T \{d\sigma\} + \left\{\frac{\partial F}{\partial k}\right\}^T \left[\frac{\partial k}{\partial \varepsilon^p}\right] \{d\varepsilon^p\} = 0 \qquad \text{A.36}$$

Combining Equation A.19 gives

$$dF = \left\{\frac{\partial F}{\partial \sigma}\right\}^T \{d\sigma\} + \Lambda \left\{\frac{\partial F}{\partial k}\right\}^T \left[\frac{\partial k}{\partial \varepsilon^p}\right] \left\{\frac{\partial P}{\partial \sigma}\right\} = 0 \qquad \text{A.37}$$

The scalar quantity Λ is thus obtained as

$$\Lambda = \frac{1}{H} \left\{\frac{\partial F}{\partial \sigma}\right\}^T \{d\sigma\} \qquad \text{A.38}$$

where H denotes the hardening modulus (or plastic modulus) as follows:

$$H = -\left\{\frac{\partial F}{\partial k}\right\}^T \left[\frac{\partial k}{\partial \varepsilon^p}\right] \left\{\frac{\partial P}{\partial \sigma}\right\} \qquad \text{A.39}$$

Having determined the unknown scalar quantity Λ, combine Equation A.32 and Equation A.39 gives another expression of Λ as

$$\Lambda = \frac{\left\{\frac{\partial F}{\partial \sigma}\right\}^T \left[D^e\right] \{d\varepsilon\}}{H + \left\{\frac{\partial F}{\partial \sigma}\right\}^T \left[D^e\right] \left\{\frac{\partial P}{\partial \sigma}\right\}} \qquad \text{A.40}$$

Equation A.32 thus can be further modified by substituting Equation A.40 into it as

$$\{d\sigma\} = \left[D^e\right] \{d\varepsilon\} - \frac{\left[D^e\right] \left\{\frac{\partial P}{\partial \sigma}\right\} \left\{\frac{\partial F}{\partial \sigma}\right\}^T \left[D^e\right]}{H + \left\{\frac{\partial F}{\partial \sigma}\right\}^T \left[D^e\right] \left\{\frac{\partial P}{\partial \sigma}\right\}} \{d\varepsilon\} \qquad \text{A.41}$$

After a simple manipulation of Equation A.41, the elasto-plastic matrix is obtained as follows:

$$\left[D^{ep}\right]=\left[D^{e}\right]-\frac{\left[D^{e}\right]\left\{\frac{\partial P}{\partial \sigma}\right\}\left\{\frac{\partial F}{\partial \sigma}\right\}^{T}\left[D^{e}\right]}{H+\left\{\frac{\partial F}{\partial \sigma}\right\}^{T}\left[D^{e}\right]\left\{\frac{\partial P}{\partial \sigma}\right\}} \quad \text{A.42}$$

A.5 Loading and unloading conditions

Three possible states exist as loading, unloading and neutral loading. The criterion has to be specified to distinguish loading, unloading and neutral loading. A universal criterion to determine the loading and unloading for all materials (both strain hardening and strain softening) was provided by Pastor *et al.* (1990) and Manzanal *et al.* (2011) as follows:

Unloading: $dF=\left\{\frac{\partial F}{\partial \sigma}\right\}^{T}\left\{d\sigma^{e}\right\}<0$ A.43

Neutral loading: $dF=\left\{\frac{\partial F}{\partial \sigma}\right\}^{T}\left\{d\sigma^{e}\right\}=0$ A.44

Loading: $dF=\left\{\frac{\partial F}{\partial \sigma}\right\}^{T}\left\{d\sigma^{e}\right\}>0$ A.45

where $\left\{d\sigma^{e}\right\}$ is the elastic stress increment vector if the material behaves purely elastic under the giving strain increments and can be determined as follows:

$$\left\{d\sigma^{e}\right\}=\left[D^{e}\right]\{d\varepsilon\} \quad \text{A.46}$$

Appendix B Solving nonlinear equations in ABAQUS

In ABAQUS, one of the essential parts is to solve a set of simultaneous equations in the form

$$\mathbf{Ku} = \mathbf{P} \qquad \text{B.1}$$

where $\mathbf{K}$ is the global stiffness matrix, $\mathbf{u}$ is the global nodal displacements vector and $\mathbf{P}$ is the global load vector.

For linear problems, $\mathbf{K}$ would remain constant during the solution. It is thus quite straight forward to solve Equation B.1. As long as $\mathbf{K}$ is non-singular, the solution of Equation B.1 will be unique. However, in a nonlinear analysis, the solution cannot be obtained by solving a single system of linear equations, as would be done in a linear problem. Therefore, ABAQUS/Standard breaks the simulation into a number of increments (In Abaqus/Standard, the concept of time increment is used, as the concept of 'time' is not essential in solve nonlinear equations in the current study, for simplicity, the concept of time has been ignored) (ABAQUS, 2011). Equation B.1 is thus expressed in an incremental form as

$$\mathbf{K}^i d\mathbf{u}^i = d\mathbf{P}^i \qquad \text{B.2}$$

where the superscript i indicates ith increment.

The Newton-Raphson method is used in Abaqus/Standard to solve each load increment. For each increment, the initial global stiffness $\mathbf{K}_0^i$ (where the subscript indicates the number of iteration), which is evaluated from stress and/or strain states at the beginning of each increment is used to predict the incremental displacement vector $d\mathbf{u}_1^i$ due to the increment of load vector $d\mathbf{P}^i$. The internal force vector $\mathbf{I}_1^i$ is thus

possible to be defined from $d\mathbf{u}_1^i$ (the determination of $\mathbf{I}^i$ would be explained later). A residual load vector $\mathbf{R}_1^i$ is thus can be evaluated as

$$\mathbf{R}_1^i = \mathbf{P}^i - \mathbf{I}_1^i \qquad \text{B.3}$$

For a nonlinear problem, each component (every degree of freedom in the model) of $\mathbf{R}_1^i$ will seldom be zero after each increment. Thus additional iterations are needed. The residual load vector $\mathbf{R}_1^i$ is thus used instead of $d\mathbf{P}^i$ to evaluate additional incremental displacement vector $d\mathbf{u}_2^i$ in the second iteration, and a similar procedure is followed to evaluated the residual load vector $\mathbf{R}_2^i$ after the second iteration. Thus generally, the iteration procedure in each increment can be summarized as

$$\mathbf{K}_{j-1}^i d\mathbf{u}_j^i = d\mathbf{R}_{j-1}^i \qquad \text{B.4}$$

$$\mathbf{R}_j^i = \mathbf{P}^i - \mathbf{I}_j^i \qquad \text{B.5}$$

where the subscript j indicates the number of iteration. $d\mathbf{R}_0^i = d\mathbf{P}^i$.

In Abaqus/Standard, by default, the global stiffness matrix will be updated based on the stress and/or strain states at the start of the *ith* increment. Thus the Newton-Raphson method is used. However, if $\mathbf{K}_0^i$ remains the same during increments, or sometimes even a stiffness evaluated from a linear elastic assumption is used during each increment, then the method is the modified Newton-Raphson method. This is because the direct solution of Equation B.1 is always problematic due to the variation of global stiffness $\mathbf{K}$ during the solution. Therefore, an initial solution should be estimated based on a specified global stiffness $\mathbf{K}$ (for example, the global stiffness obtained by assuming the problem is linear elastic). As long as this estimated initial

solution is within the zone of attraction (Zienkiewicz *et al.*, 2005), the satisfied solution could be reached after certain iterations. The basic philosophy of using the modified Newton-Raphson method is that updating global stiffness in each incremental process may be time-consuming. A constant global stiffness employed may be possible to reduce computational time. However, it is a trade-off process rather than a golden rule. Because as a constant global stiffness employed will increase the number of iterations, especially for highly nonlinear problems. Thus the relative efficiency of the Newton-Raphson method and the modified Newton-Raphson is rather problem-dependent (e.g. nonlinearity of the material and the degree of freedom). Besides, the stress point algorithm used to integrate constitutive model will also affect the relative efficiency. A schematic representation of the Newton-Raphson method and the modified Newton-Raphson is shown in Figure B.1.

As for a nonlinear problem, the numerical iterative solution generally will not reach the exact solution. Thus certain criteria should be specified to terminate the iteration process whatever the iterative solution converges to the exact solution or the solution becomes divergent. In Abaqus/Standard, two criteria are used to terminate the iteration process when the solution converges. (i) Each component of the residual load vector is less than a tolerance value, by default of 0.5% and (ii) Each component of incremental load vector in the last iteration is small relative to the total corresponding incremental displacement, by default, the fraction is 1%. Both of these criteria must be satisfied before a solution is said to have converged for each increment. If the solution from an iteration is not converged, Abaqus/Standard performs another iteration. However, if after a certain number (by default is 16) of iteration the solution is still not converged, Abaqus/Standard reduce the incremental load vector $d\mathbf{P}^i$ (by default 25% of the previous value).

The internal load vector $\mathbf{I}_j^i$ after *jth* iteration is obtained as follows. The predicted incremental displacement vector after *jth* iteration $d\mathbf{u}_j^i$ is used to evaluate the corresponding incremental strains at each integral point following standard FE procedures. The constitutive model is then integrated along the incremental strain path to update the stress states before the next iteration. $\mathbf{I}_j^i$ is thus obtained from integrating the updated stress states in the whole domain. The essential part of this process is integrating the constitutive model (stress point algorithm). The stress point algorithm used in the current study is described in Chapter 4.

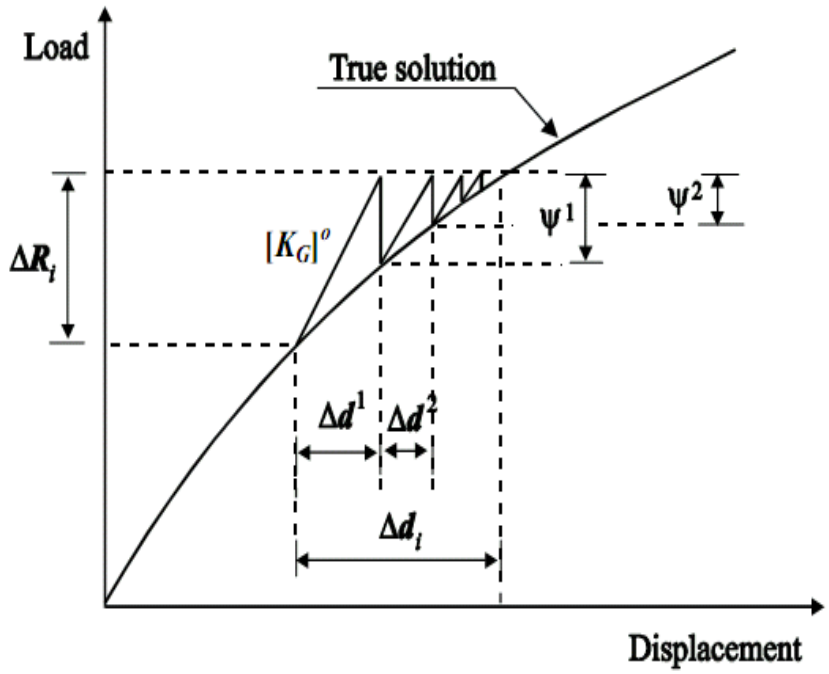

Figure B.1 Representation of the Newton-Raphson method (Potts & Zdravkovic, 1999)

Appendix C Common stress point algorithms

The most commonly used stress point algorithms are sub-stepping algorithm, which is essentially explicit proposed by Sloan (1987) and the return algorithm, which is essentially implicit as proposed by Borja & Lee (1990). In both sub-stepping and return algorithms, the objective is to integrate the constitutive equations along an incremental strain path. While the magnitudes of the strain increment are known, the manner in which they vary during the increment is not. It is therefore not possible to integrate the constitutive equations without making an additional assumption. Each stress point algorithm makes a different assumption and that influences the accuracy of the solution obtained (Potts & Zdravkovic, 1999).

C.1 Sub-stepping algorithm

In this algorithm, the incremental strains are divided into a number of sub-steps. Within each sub-step, the strains are a proportion of total incremental strains. A salient feature of sub-stepping algorithm is thus that the size of each sub-step can vary even automatically according to certain error control criterion (Sloan, 1987). Combining with Euler, modified Euler or Runge-Kutta scheme, the constitutive equations can be integrated with high accuracy. A major assumption made in this algorithm is that in each sub-step, the ratio between the strain components is the same as those in the total incremental strains. Hence the strains are said to vary proportionally over the increment. As in a practical problem, the strain may not vary proportionally. This assumption affects the accuracy of this algorithm and restrains the incremental size of strains.

C.2. Return algorithm

In this approach, the plastic strains over the increment are calculated from the stress conditions corresponding to the end of the increment. The problem is that these stress conditions are unknown. Hence the algorithm is implicit in nature (Potts & Zdravkovic, 1999). Iterative sub-algorithm is often employed to ensure convergence and to satisfy the constitutive behavior. It is thus possible to obtained stress changes in a single step. However, a major assumption made by this implicit method is that the plastic strains are calculated based on the stress state at the end of increment. If the plastic flow direction remains the same during the increment, then the return algorithm is exactly accurate. However, for a general problem, the plastic flow direction will depend on the current stress and/or strain states and evolve as a function of the changing stress/strain state. Thus the plastic strains evaluated from the stress state at the end of the increment are theoretically unacceptable and some errors inevitably introduced, which restrains the incremental size of strains.

C.3. Comparison of the two algorithms

Potts & Ganendra (1994) performed a comparison of these two types of stress point algorithm and concluded that both algorithms could give accurate results. But, of the two, the sub-stepping algorithm is better. Another advantage of sub-stepping algorithm is that it is quite flexible and can easily deal with more advanced constitutive models used in geotechnical engineering with extremely robust error control. For the return algorithm, although in theory can accommodate complex constitutive models, it involves some extremely complicated mathematics. This means considerable effort is required to include a new or modified model (Potts & Zdravkovic, 1999).

Appendix D UMAT for the AZ-Cam clay model in ABAQUS

```
CCCCCCCCCCCCCCCCCCCCCCCCCCCCCCCCCCCCCCCCCCCCCCCCCCCCCCCCCCCCCCCCCCCCCCCCCCCCC
C23456******************************************************************CCCCC
CCC10 ************  USER DEFINED MODEL USED IN ABAQUS            *******CCCCC
CCC10 ************  AZ-CAM CLAY MODEL-FOR CENTRIFUGE SIMULATION  *******CCCCC
CCCCC1************  COMPRESSION IS NEGATIVE                      *******CCCCC
CCCCCCCCCCCCCCCCCCCCCCCCCCCCCCCCCCCCCCCCCCCCCCCCCCCCCCCCCCCCCCCCCCCCCCCCCCCCC
C
      SUBROUTINE UMAT(STRESS,STATEV,DDSDDE,SSE,SPD,SCD,
     1 RPL,DDSDDT,DRPLDE,DRPLDT,
     2 STRAN,DSTRAN,TIME,DTIME,TEMP,DTEMP,PREDEF,DPREDEF,CMNAME,
     3 NDI,NSHR,NTENS,NSTATV,PROPS,NPROPS,COORDS,DROT,PNEWDT,
     4 CELENT,DFGRD0,DFGRD1,NOEL,NPT,LAYER,KSPT,KSTEP,KINC)
C
      INCLUDE ’ABA_PARAM.INC’
      CHARACTER*80 CMNAME
      DIMENSION STRESS(NTENS),STATEV(NSTATV),
     1 DDSDDE(NTENS,NTENS),
     2 DDSDDT(NTENS),DRPLDE(NTENS),
     3 STRAN(NTENS),DSTRAN(NTENS),TIME(2),PREDEF(1),DPRED(1),
     4 PROPS(NPROPS),COORDS(3),DROT(3,3),DFGRD0(3,3),DFGRD1(3,3)
C
C     ELASTIC MATRIX==EELM,PLASTIC MATRIXI==EPLM
C     ELASTO-PLASTIC MATRIX==DDSDDE
C     EDS_E==THE ELASTIC STRESS INCREMENT
C     EDS_PR==THE TRIED TOTAL STRESS INCREMENT
C     EDS_EP==ELASO-PLASTIC STRESS INCREMENT
C     EDSTA==STRAIN INCREMENT CAUSING PURELY ELASTIC STRESS
C     EPDSTA==STRAIN INCREMENT CAUSING ELASO-PLASTIC STRESS
C     SN_R=STRAIN AT STRESS REVERSAL
C     SS_R=STRESS AT STRESS REVERSAL
C     STRAN1=STRAIN AFTER THE INCREMENT
C
      DIMENSION  EELM(6,6),EELPLM(6,6),EF_DIR(6),EP_DIR(6),
     +           EDS_E(6),EDS_PR(6),EDS_EP(6),
     +           EDSTA(6),EPDSTA(6),ESS_PRE(6),
     +           SN_R(6),SS_R(6),STRAN1(6),SS_R0(6),ESS_RR(6),
     +           ESS_NN(6),DPD(6,6),ESTN_RE(6),SS_ACC(6),SS_LU(6)
C
      PARAMETER (TOL=1.0D-4,Y_TOL=1.0D-4)
C
C     Y_TOL IS THE TOLENCE FOR THE YIELD FUNCTION
C     1-LAMDA,2-KAPPA,3-M,3-G(OR SPECIFIED AS MUII)
C     4-X,5-Y,6-Z FOR M IN DEVIATROIC PLANE
C     7-YP,8-ZP FOR THE PLASTIC POTENTIAL
C
CCCCCCCCCCCCCCCCCCCCCCC
      ELAMDA=0.25
      EKAPPA=0.05
```

```
      EG_MU=-0.25
      EX=0.4
      EY=-0.384
      EZ=0.3
      EYP=0
      EZP=1.0
      ERW=2.0
      ERD=2.0
      EXT=0.9
      EYT=0
      EZT=1
      EXB=0.5
      EYB=0.0
      EZB=1.0
      EGAMMA=4.0
      EGAM_L=4.0
      EMR=10.0
      EW1=1.0
      EW2=6.0
      EKK=0.0
      EKW_FA=0.0
C
CCCCCCCCCCCCCCCCCCCCCCCCCCCCCCCCCCCCCCCCCCCCCCCCCCCCCCCCCCCCCCCCCCCCCCCCCCCC
C     V=STATEV(1),Pco=STATEV(2),INDEX=TO CONTROL THE VARIATION OF OCR
C     EQ=GENERALIZED STRAIN LENGTH, USED FOR CHECKING STRESS REVERSAL
C     EREI=STRAIN COMPONENT AT LATEST STRESS REVERSAL
C     ERSI=STRESS COMPONENT AT LATEST STRESS REVERSAL
C     NUMBER=NUMBER OF STRESS REVERSAL
C     SS_ACC IS USELESS, NO MEANING
C
      EV=STATEV(1)
      EPC=STATEV(2)
      ELEN=STATEV(3)
      DO I=1,6
      SN_R(I)=STATEV(3+I)
      SS_R(I)=STATEV(9+I)
      SS_R0(I)=STATEV(17+I)
      ESTN_RE(I)=STATEV(26+I)
      SS_ACC(I)=STATEV(32+I)
      SS_LU(I)=STATEV(38+I)
      ENDDO
      NUMBER=STATEV(16)
      NLU=STATEV(45)
      EINTA_MAX=STATEV(17)
      EVVP=STATEV(24)
      EPPW=STATEV(25)
      EGOCR=STATEV(26)
C
      DO I=1,6
      DO J=1,6
      DPD(J,I)=0
      END DO
      END DO
C
```

```
      DO I=1,3
      DO J=1,3
      DPD(J,I)=1.0
      END DO
      END DO
C
      IF (TIME(2).EQ.0.0 ) THEN
C
      DO I=1,6
      SS_ACC(I)=STRESS(I)
      SS_LU(I)=STRESS(I)
      ENDDO
C
      DO I=1,6
      SS_R(I)=STRESS(I)
      SN_R(I)=STRAN(I)
      SS_R0(I)=STRESS(I)
      ENDDO
      ELEN=0.0
      NUMBER=1
      NLU=1
      EINTA_MAX=0.0
      EVVP=0.0
      EGOCR=1.0
C
      EDEPTH=61.0-COORDS(3)
      IF (EDEPTH .LE.3.0 ) THEN
      EOCR=-0.459*EDEPTH**3+3.49*EDEPTH**2-9.35*EDEPTH+11.3
      ELSEIF (EDEPTH .LE.20.0) THEN
      EOCR=4.92*(1.0D-5)*EDEPTH**4-0.00282*EDEPTH**3+0.0598*EDEPTH**2
     +    -0.583*EDEPTH+3.53
      ELSE
      EOCR=1.1
      ENDIF
C
      IF (EOCR .LT.1.0) THEN
      EOCR=1.0
      ENDIF
C
      IF (EOCR .GT.6.0) THEN
      EOCR=6.0
      ENDIF
C
      EGOCR=EOCR
C
      EK_NC=0.64
C
      DO I=4,6
      ESS_PRE(I)=STRESS(I)
      ENDDO
C
      ESS_PRE(3)=EOCR*STRESS(3)
      ESS_PRE(2)=EK_NC*ESS_PRE(3)
      ESS_PRE(1)=EK_NC*ESS_PRE(3)
```

```
C
      EP=0.0
      ESS=0.0
      EJ=0.0
      ETHETA=0.0
      EDETS=0.0
C
      CALL ES_INV(ESS_PRE,EP,ESS,EJ,ETHETA,EDETS)
      EPC_B=CAL_PC_SUB(ERW,ERD,EX,EY,EZ,EP,EJ,ETHETA)
      CALL ES_INV(STRESS,EP,ESS,EJ,ETHETA,EDETS)
C
      EDEPTH=61.0-COORDS(3)
      IF (EDEPTH .LE.20.0 ) THEN
      EV=-6.5*(1.0D-5)*EDEPTH**3+0.0031*EDEPTH**2-0.062*EDEPTH+3.05
      ELSE
      EV=2.53
      ENDIF
C
      EPC=EPC_B
C
      ENDIF
C
      DO I=1,6
      STRESS(I)=SS_ACC(I)
      ENDDO
C
      IF (TIME(2).LE.2.0 ) THEN
      EKW_FA=0.0
      ELSE
      EKW_FA=0.0
      ENDIF
C
      DO I=1,3
      STRESS(I)=STRESS(I)+EPPW
      END DO
C
C     FIRST TO CHECKING WHETHER STRESS REVERSAL OCCURED
C
      EP=(STRESS(1)+STRESS(2)+STRESS(3))/3.0
      EP_R0=(SS_R0(1)+SS_R0(2)+SS_R0(3))/3.0
C
      DO I=1,6
      ESS_RR(I)=SS_R0(I)/EP_R0
      ESS_NN(I)=STRESS(I)/EP
      ENDDO
      EINTAS=0
      DO I=1,3
      EINTAS=EINTAS+0.5*((ESS_NN(I)-1)-(ESS_RR(I)-1))**2
      ENDDO
      DO I=4,6
      EINTAS=EINTAS+(ESS_NN(I)-ESS_RR(I))**2
      ENDDO
      EINTA=EINTAS**0.5*1.732
C
```

```
C     STRESS REVERSAL OCCURS WHEN EQ STARTS TO DECREASE
C     LU=1 STRESS REVERSAL OCCURS; LU=0 DOES NOT OCCUR
C
      ESND=0
      DO I=1,6
      ESND=ESND+(ESTN_RE(I)-STRAN(I))**2
      END DO
      ESND=ESND**0.5
C
      ELENR=ELEN
      IF (ESND.GE.1D-10) THEN
C
C    ELENR---THE STRAIN LENGTH FROM THE LAST LOAD REVERSAL
C    ELEN1---THE STRAIN LENGTH FROM THE ORIGION
C
      DO I=1,6
      STRAN1(I)=STRAN(I)+DSTRAN(I)
      ENDDO
C
      EV_R=(SN_R(1)+SN_R(2)+SN_R(3))/3.0
      EV_RR=(STRAN1(1)+STRAN1(2)+STRAN1(3))/3.0
C
      ELEN_SQ=0
      DO I=1,3
      ELEN_SQ=ELEN_SQ+2.0*((STRAN1(I)-EV_RR)-(SN_R(I)-EV_R))**2
      ENDDO
      DO I=4,6
      ELEN_SQ=ELEN_SQ+(STRAN1(I)-SN_R(I))**2
      ENDDO
C
      ELENR=ELEN_SQ**0.5
C
      IF (ELENR.GE.ELEN) THEN
      LU=0
      ELSEIF (ELEN.EQ.0) THEN
      LU=0
      ELSE
      LU=1
      DO I=1,6
      SN_R(I)=STRAN(I)
      SS_R(I)=STRESS(I)
      ENDDO
      NUMBER=NUMBER+1
      ELENR=0
      ENDIF
C
      ENDIF
C
      IF (TIME(2).LE.2.0 ) THEN
      ELEN=0.0
      ELENR=0.0
      NUMBER=1
      DO I=1,6
      SN_R(I)=0
```

```
      SS_R(I)=STRESS(I)
      ENDDO
C
      ENDIF
C
      EP=0.0
      ESS=0.0
      EJ=0.0
      ETHETA=0.0
      EDETS=0.0
C
      CALL ES_INV(STRESS,EP,ESS,EJ,ETHETA,EDETS)
      EPC_SUB=CAL_PC_SUB(ERW,ERD,EX,EY,EZ,EP,EJ,ETHETA)
C
C     DETERMINE THE ELASTIC MATRIX
C
      DO I=1,6
      DO J=1,6
      EELM(J,I)=0.0
      EELPLM(J,I)=0.0
      END DO
      END DO
C
C     1 REPRESENTS THE TANGENT SLOPE, 2 STANDS FOR THE SECANT SLOPE
      CALL EL_M(EELM,EV,EKAPPA,EG_MU,STRESS,DSTRAN,1,ELAMDA,
     +          EMR,EW1,EW2,SS_R,NUMBER,EINTA,EINTA_MAX,LU,SS_R0,EGOCR)
C
      IF (ABS(EPC_SUB/EPC-1.0).LT.(TOL)) THEN
      EPC_SUB=EPC
      ENDIF
C
C     DETERMINE THE DIRECTION TO THE CURRENT SURFACE FOR LOADING/UNLOADING
C
      DO I=1,6
      EF_DIR(I)=0.0
      END DO
C
      CALL EFP_DI(EF_DIR,EX,EY,EZ,EYP,EZP,EPC_SUB,STRESS,1,ERW,ERD)
C
CCCCCCCCCCCCCCCCCCCCCCCCCCCCCCCCCCCCCCCCCCCCCCCCCCCCCCCCCCCCCCCCCCCCCCCCCCCCCC
C     TO SPECIFY THE CRITERIA FOR LOADING AND UNLOADING
C     ECRI_LU==THE CRITERIA FOR LOADING AND UNLOADING
C     YIELD SURFACE VALUE,TO CHECK WHETHER YIELD OR NOT
C     ALPHA==THE ELASTIC PORTION OF STRAIN
C     EDSTRESSE==THE ELASTIC STRESS INCREMENT (BASED ON TANGENT STIFF)
C                CAN ONLY BE USED TO EVAULATE THE LOADING/UNLOADING
C     EDSTRESS_PRE==THE ELASTIC STRESS INCREMENT (BASED ON SECANT
C                STIFF),THE ACCURATE STRESS INCREMENT
C     EDSTRESS_ELPL==THE ELASTO-PLASTIC STRESS INCREMENT
C
      DO I=1,6
      EDS_E(I)=0.0
      EDS_PR(I)=0.0
      EDS_EP(I)=0.0
```

```
      END DO
C
      DO I=1,6
      DO J=1,6
      EDS_E(J)=EDS_E(J)+EELM(J,I)*DSTRAN(I)
      END DO
      END DO
C
      ECR_LU=0.0
      DO I=1,6
      ECR_LU=ECR_LU+EF_DIR(I)*EDS_E(I)
      END DO
C
      IF (ECR_LU.LE.0.0) THEN
C
CCCCCCCCCCCCCCCCCCCCCC  UNLOADING    CCCCCCCCCCCCCCCCCCCCCCCCCCCCCCCCCCCCCCCC
C     THE UNLOADING WILL ALWAYS BE ELASTIC
C     CALCULATE THE TRIED STRESS INCREMENT
C     TO DETERMINE THE SECANT ELASTIC MATRIX
C     TO DETERMINE THE SECANT BULK MODULUS
C
      NLU=0
C
      CALL C_EEST(STRESS,DSTRAN,EDS_PR,EV,EPC,ELAMDA,EKAPPA,EX,EY,EZ,
     +      EYP,EZP,EG_MU,TOL,ERW,ERD,EXT,EYT,EZT,EXB,EYB,EZB,EGAMMA,
     +      EGAM_L,NUMBER,SS_R,EMR,EW1,EW2,EINTA,EINTA_MAX,LU,SS_R0,
     +      EVVP,EKK,EKW_FA,EPPW,EGOCR,TIME,NOEL)
C
      DO I=1,6
      STRESS(I)=STRESS(I)+EDS_PR(I)
      END DO
C
C     THE ABOVE IS TRUE FOR THE END OF INCREMENT IS ELASTIC
C     TO CHECK WHETHER YIELD OR NOT AT THE END OF INCREMENT
C
      EYIELD=Y_SUR(STRESS,EX,EY,EZ,EPC_SUB,ERW,ERD)
C
      IF(EYIELD.GT.Y_TOL*10) THEN
C     THE END OF INCREMENT IS PLASTIC
C     BE CAREFUL,  THE STRESS HERE IS ALREADY ADD THE ELASTIC
C     STRESS INCREMENT
C
      EALFA=C_ALFA(EDS_PR,STRESS,EX,EY,EZ,EPC_SUB,DSTRAN,EV,EKAPPA,
     +              EG_MU,ERW,ERD,ELAMDA,EMR,EW1,EW2,SS_R,NUMBER,EINTA,
     +              EINTA_MAX,LU,SS_R0,EGOCR)
C
C     EDSTRAN==THE ELASTIC PART OF STRAIN INCREMENT
C
      DO I=1,6
      EDSTA(I)=EALFA*DSTRAN(I)
      EPDSTA(I)=(1.0-EALFA)*DSTRAN(I)
      STRESS(I)=STRESS(I)-EDS_PR(I)
C     RETURN THE STRESS STATUS BEFORE THE STRESS INCREMENT
      END DO
```

```
C
      CALL C_EEST(STRESS,EDSTA,EDS_PR,EV,EPC,ELAMDA,EKAPPA,EX,EY,EZ,
     +       EYP,EZP,EG_MU,TOL,ERW,ERD,EXT,EYT,EZT,EXB,EYB,EZB,EGAMMA,
     +       EGAM_L,NUMBER,SS_R,EMR,EW1,EW2,EINTA,EINTA_MAX,LU,SS_R0,
     +       EVVP,EKK,EKW_FA,EPPW,EGOCR,TIME,NOEL)

C
      DO I=1,6
      STRESS(I)=STRESS(I)+EDS_PR(I)
C     THE STRESS STATUS IS ON THE YIELD SURFACE
      END DO
C
C     TO RESERVE PC, SO CAN BE USED IN DRAG SUBROUTINE
      EPC_RE=EPC
C
      CALL C_EPST(STRESS,EPDSTA,EDS_EP,EV,EPC,ELAMDA,EKAPPA,EX,EY,EZ,
     +       EYP,EZP,EG_MU,TOL,ERW,ERD,EXT,EYT,EZT,EXB,EYB,EZB,EGAMMA,
     +       EGAM_L,NUMBER,SS_R,EMR,EW1,EW2,EINTA,EINTA_MAX,LU,SS_R0,
     +       EVVP,EKK,EKW_FA,EPPW,EGOCR,TIME,NOEL,SS_LU)
C
      DO I=1,6
      STRESS(I)=STRESS(I)+EDS_EP(I)
      END DO
C
      EYIELD=Y_SUR(STRESS,EX,EY,EZ,EPC,ERW,ERD)
C
      IF (EYIELD .GT.Y_TOL*10) THEN
      CALL DRAG_Y(STRESS,EPC,EV,ELAMDA,EKAPPA,EG_MU,
     +       EX,EY,EZ,EYP,EZP,TOL,ERW,ERD,EPC_RE,EMR,EW1,EW2,SS_R,
     +       NUMBER,EINTA,EINTA_MAX,LU,SS_R0,EGOCR)
      ENDIF
C
      CALL ES_INV(STRESS,EP,ESS,EJ,ETHETA,EDETS)
C
      EBETA=EXB/(1+EYB*SIN(3.0*ETHETA))**EZB
      ETT=EXT/(1+EYT*SIN(3.0*ETHETA))**EZT
      EG_THE=EX/(1+EY*SIN(3.0*ETHETA))**EZ
C
      IF (EP.GE.(ETT*2.0*EPC/(2.0+ERW))) THEN
C
      EFAIL_S=EJ/EG_THE/EP-(1+EBETA*LOG(2.0*ETT*ABS(EPC/EP)/(2.0+ERW)))
C
      IF (EFAIL_S .GT.0) THEN
      CALL FAIL_CORR(STRESS,EPC,EP,EXT,EYT,EZT,EXB,EYB,EZB)
      ENDIF
C
      ENDIF
C
C     UPDATE THE JACOBIAN MATRIX---FOR UNLOADING ENDED WITH PLASTIC
      CALL EL_PLM(EELPLM,EX,EY,EZ,EYP,EZP,EPC,STRESS,EV,ELAMDA,EKAPPA,
     +              EG_MU,EF_DIR,ERW,ERD,EXT,EYT,EZT,EXB,EYB,EZB,EGAMMA,
     +              EGAM_L,NUMBER,SS_R,EMR,EW1,EW2,EINTA,EINTA_MAX,LU,
     +              SS_R0,EVVP,EKK,EGOCR,TIME,NOEL,SS_LU)
C
```

```
      DO I=1,6
      DO J=1,6
      DDSDDE(J,I)=EELPLM(J,I)
      END DO
      END DO
C
      EKW=-EV*(STRESS(1)+STRESS(2)+STRESS(3))/3.0/EKAPPA*EKW_FA
C
      DO I=1,6
      DO J=1,6
      DDSDDE(J,I)=DDSDDE(J,I)+EKW*DPD(J,I)
      END DO
      END DO
C
      DO I=1,3
      STRESS(I)=STRESS(I)-EPPW
      END DO
C
      ELSE
C
C     UPDATE THE JACOBIAN MATRIX---FOR UNLOADING PURELY ELASTIC
      CALL EL_M(EELM,EV,EKAPPA,EG_MU,STRESS,DSTRAN,1,ELAMDA,
     +           EMR,EW1,EW2,SS_R,NUMBER,EINTA,EINTA_MAX,LU,SS_R0,EGOCR)
      DO I=1,6
      DO J=1,6
      DDSDDE(J,I)=EELM(J,I)
      END DO
      END DO
C
      EKW=-EV*(STRESS(1)+STRESS(2)+STRESS(3))/3.0/EKAPPA*EKW_FA
C
      DO I=1,6
      DO J=1,6
      DDSDDE(J,I)=DDSDDE(J,I)+EKW*DPD(J,I)
      END DO
      END DO
C
      DO I=1,3
      STRESS(I)=STRESS(I)-EPPW
      END DO
C
      ENDIF
C
C
      ELSE
C
CCCCCCCCCCCCCCCCCCCCCC  LOADING    CCCCCCCCCCCCCCCCCCCCCCCCCCCCCCCCCCCCCCCCCCCC
C     THE LOADING IS ALWAYS PLASTIC
C
      NLU_PRE=1
      IF (NLU_PRE.EQ.NLU) THEN
      NLU=NLU_PRE
      ELSE
      NLU=NLU_PRE
```

```
      DO I=1,6
      SS_LU(I)=STRESS(I)
      ENDDO
      ENDIF
C
      EPC_RE=EPC
C
      CALL C_EPST(STRESS,DSTRAN,EDS_EP,EV,EPC,ELAMDA,EKAPPA,EX,EY,EZ,
     +       EYP,EZP,EG_MU,TOL,ERW,ERD,EXT,EYT,EZT,EXB,EYB,EZB,EGAMMA,
     +       EGAM_L,NUMBER,SS_R,EMR,EW1,EW2,EINTA,EINTA_MAX,LU,SS_R0,
     +       EVVP,EKK,EKW_FA,EPPW,EGOCR,TIME,NOEL,SS_LU)
C
C
      DO I=1,6
      STRESS(I)=STRESS(I)+EDS_EP(I)
      END DO
C
      EYIELD=Y_SUR(STRESS,EX,EY,EZ,EPC,ERW,ERD)
C
      IF (EYIELD .GT.Y_TOL*10) THEN
      CALL DRAG_Y(STRESS,EPC,EV,ELAMDA,EKAPPA,EG_MU,
     +       EX,EY,EZ,EYP,EZP,TOL,ERW,ERD,EPC_RE,EMR,EW1,EW2,SS_R,
     +       NUMBER,EINTA,EINTA_MAX,LU,SS_R0,EGOCR)
      ENDIF
C
      CALL ES_INV(STRESS,EP,ESS,EJ,ETHETA,EDETS)
C
      EBETA=EXB/(1+EYB*SIN(3.0*ETHETA))**EZB
      ETT=EXT/(1+EYT*SIN(3.0*ETHETA))**EZT
      EG_THE=EX/(1+EY*SIN(3.0*ETHETA))**EZ
C
      IF (EP.GE.(ETT*2.0*EPC/(2.0+ERW))) THEN
C
      EFAIL_S=EJ/EG_THE/EP-(1+EBETA*LOG(2.0*ETT*ABS(EPC/EP)/(2.0+ERW)))
C
      IF (EFAIL_S .GT.0) THEN
      CALL FAIL_CORR(STRESS,EPC,EP,EXT,EYT,EZT,EXB,EYB,EZB)
      ENDIF
C
      ENDIF
C
C     UPDATE THE JACOBIAN MATRIX---FOR UNLOADING ENDED WITH PLASTIC
      CALL EL_PLM(EELPLM,EX,EY,EZ,EYP,EZP,EPC,STRESS,EV,ELAMDA,EKAPPA,
     +              EG_MU,EF_DIR,ERW,ERD,EXT,EYT,EZT,EXB,EYB,EZB,EGAMMA,
     +              EGAM_L,NUMBER,SS_R,EMR,EW1,EW2,EINTA,EINTA_MAX,LU,
     +              SS_R0,EVVP,EKK,EGOCR,TIME,NOEL,SS_LU)
C
      DO I=1,6
      DO J=1,6
      DDSDDE(J,I)=EELPLM(J,I)
      END DO
      END DO
C
      EKW=-EV*(STRESS(1)+STRESS(2)+STRESS(3))/3.0/EKAPPA*EKW_FA
```

```
C
      DO I=1,6
      DO J=1,6
      DDSDDE(J,I)=DDSDDE(J,I)+EKW*DPD(J,I)
      END DO
      END DO
C
      DO I=1,3
      STRESS(I)=STRESS(I)-EPPW
      END DO
C
      ENDIF
C
      IF (EINTA.GT.EINTA_MAX) THEN
      EINTA_MAX=EINTA
      ENDIF
C
      DO I=1,6
      ESTN_RE(I)=STRAN(I)
      ENDDO
C
      DO I=1,6
      SS_ACC(I)=STRESS(I)
      ENDDO
C
C     UPDATE STATE VARIABLES
      STATEV(1)=EV
      STATEV(2)=EPC
C
      STATEV(3)=ELENR
      DO I=1,6
      STATEV(3+I)=SN_R(I)
      STATEV(9+I)=SS_R(I)
      STATEV(17+I)=SS_R0(I)
      STATEV(26+I)=ESTN_RE(I)
      STATEV(32+I)=SS_ACC(I)
      STATEV(38+I)=SS_LU(I)
      STATEV(45)=NLU
      ENDDO
      STATEV(16)=NUMBER
      STATEV(17)=EINTA_MAX
      STATEV(24)=EVVP
      STATEV(25)=EPPW
      STATEV(26)=EGOCR
C
      RETURN
      END
C
CCCCCCCCCCCCCCCCCCCCCCCCCCCCCCCCCCCCCCCCCCCCCCCCCCCCCCCCCCCCCCCCCCCCCCCCCCCCC
CCCCCCC   THE FOLLOWING ARE THE USER DEFINED SUBROUTINES    CCCCCCCCCCCCCCCCC
CCCCCCCCCCCCCCCCCCCCCCCCCCCCCCCCCCCCCCCCCCCCCCCCCCCCCCCCCCCCCCCCCCCCCCCCCCCCC
C
CCCCCCCCCCCCCCCCCCCCCCCCCCCCCCCCCCCCCCCCCCCCCCCCCCCCCCCCCCCCCCCCCCCCCCCCCCCCC
CCCCCCCC    DRAG THE STRESS POINT TO THE FAILURE SURFACE     CCCCCCCCCCCCCCCC
```

```
CCCCCCCCCCCCCCCCCCCCCCCCCCCCCCCCCCCCCCCCCCCCCCCCCCCCCCCCCCCCCCCCCCCCCCCCCCCCC
C
      SUBROUTINE FAIL_CORR(STRESS,EPC,EPF,EXT,EYT,EZT,EXB,EYB,EZB)
C
      INCLUDE ’ABA_PARAM.INC’
C
      DIMENSION STRESS(6),STR_M(6)
C
      EREDU=0.99
      ED_REDU=0.01
C
      DO WHILE (EREDU .GT.0)
C
      DO I=1,6
      STR_M(I)=STRESS(I)*EREDU
      ENDDO
C
      EP=0
      ESS=0
      EJ=0
      ETHETA=0
      EDETS=0
C
      CALL ES_INV(STR_M,EP,ESS,EJ,ETHETA,EDETS)
C
      EBETA=EXB/(1+EYB*SIN(3.0*ETHETA))**EZB
      ETT=EXT/(1+EYT*SIN(3.0*ETHETA))**EZT
      EG_THE=EX/(1+EY*SIN(3.0*ETHETA))**EZ
C
      EFEXC=EJ/EP/EG_THE-(1+EBETA*LOG(2.0*ETT*ABS(EPC/EPF)/(2.0+ERW)))
C
      IF (EFEXC.LE.0) THEN
      EXIT
      ENDIF
C
      EREDU=EREDU-ED_REDU
C
      ENDDO
C
      DO I=1,6
      STRESS(I)=STRESS(I)*EREDU
      ENDDO
C
      RETURN
      END
CCCCCCCCCCCCCCCCCCCCCCCCCCCCCCCCCCCCCCCCCCCCCCCCCCCCCCCCCCCCCCCCCCCCCCCCCCCCC
C
CCCCCCCCCCCCCCCCCCCCCCCCCCCCCCCCCCCCCCCCCCCCCCCCCCCCCCCCCCCCCCCCCCCCCCCCCCCCC
CCCCCCCC    GET THE DISTANCE FROM THE ORIGION TO THE STRESS POINT  CCCCCCCCCC
CCCCCCCCCCCCCCCCCCCCCCCCCCCCCCCCCCCCCCCCCCCCCCCCCCCCCCCCCCCCCCCCCCCCCCCCCCCCC
C
      FUNCTION CAL_PC_SUB(ERW,ERD,EX,EY,EZ,EP,EJ,ETHETA)
C
      INCLUDE ’ABA_PARAM.INC’
```

```
C
      EG_THE=EX/(1+EY*SIN(3.0*ETHETA))**EZ
      EAW=2.0*EG_THE/ERW
      EBW=2.0*EG_THE/(2.0+ERW)
      EAD=2.0*EG_THE/ERD
      EBD=2.0*EG_THE/(2.0+ERW)
C
      IF (EJ.LE.ABS(EG_THE*EP))  THEN
C
      IF (ERW .EQ.2.0) THEN
      CAL_PC_SUB=EP+EJ**2/EP/EG_THE**2
      ELSE
C     BE CAREFUL, THIS IS DIFFERENT FROM THE MATLAB
      CAL_PC_SUB=(-EAW**2*EBW*EP/EG_THE-SQRT(ABS(EAW**2*EBW
     +           **2*EP**2+EJ**2*(EG_THE**2-EAW**2)*EBW**2/EG_THE**2)))
     +           /((EG_THE**2-EAW**2)/EG_THE**2*EBW**2)
      ENDIF
C
      ELSE
C
      IF (ERD .EQ.2.0) THEN
      CAL_PC_SUB=(EP+EJ**2/EP/EG_THE**2)*(2.0+ERW)/4.0
      ELSE
      CAL_PC_SUB=(-EAD**2*EBD*EP/EG_THE-SQRT(ABS(EAD**2*EBD
     +           **2*EP**2+EJ**2*(EG_THE**2-EAD**2)*EBD**2/EG_THE**2)))
     +           /((EG_THE**2-EAD**2)/EG_THE**2*EBD**2)
C
      ENDIF
C
      ENDIF
C
      RETURN
      END
CCCCCCCCCCCCCCCCCCCCCCCCCCCCCCCCCCCCCCCCCCCCCCCCCCCCCCCCCCCCCCCCCCCCCCCCCC
C
CCCCCCCCCCCCCCCCCCCCCCCCCCCCCCCCCCCCCCCCCCCCCCCCCCCCCCCCCCCCCCCCCCCCCCCCCC
CCCCCCCC    DRAG THE STRESS POINT TO THE YIELD SURFACE     CCCCCCCCCCCCCCCCCC
CCCCCCCCCCCCCCCCCCCCCCCCCCCCCCCCCCCCCCCCCCCCCCCCCCCCCCCCCCCCCCCCCCCCCCCCCC
C
      SUBROUTINE DRAG_Y(STRESS,EPC,EV,ELAMDA,EKAPPA,EG_MU,
     +            EX,EY,EZ,EYP,EZP,TOL,ERW,ERD,EPC_RE,EMR,EW1,EW2,SS_R,
     +            NUMBER,EINTA,EINTA_MAX,LU,SS_R0,EGOCR)
C
      INCLUDE 'ABA_PARAM.INC'
C
      DIMENSION EST_BE(6),EF_DIR(6),EP_DIR(6),
     +           EELM(6,6),STRESS(6),SS_R(6),SS_R0(6)
C
C
      ETOL=1.0D-3
C
      EY_VAL=Y_SUR(STRESS,EX,EY,EZ,EPC,ERW,ERD)
C
      IF ((EY_VAL).GT.(ETOL)) THEN
```

```
C
      IN=1
C
C     SEE POTTS(1999) PAGE 285
      DO WHILE (.TRUE.)
C
      DO I=1,6
      EST_BE(I)=STRESS(I)
      EF_DIR(I)=0.0
      EP_DIR(I)=0.0
      END DO
C
      DO I=1,6
      DO J=1,6
      EELM(J,I)=0.0
      END DO
      END DO
C
      CALL EFP_DI(EF_DIR,EX,EY,EZ,EYP,EZP,EPC_RE,EST_BE,1,ERW,ERD)
C
      CALL EFP_DI(EP_DIR,EX,EY,EZ,EYP,EZP,EPC_RE,EST_BE,2,ERW,ERD)
C
      CALL EL_M(EELM,EV,EKAPPA,EG_MU,EST_BE,DSTRAN,1,ELAMDA,
     +           EMR,EW1,EW2,SS_R,NUMBER,EINTA,EINTA_MAX,LU,SS_R0,EGOCR)
C
C     TO CALCULATE THE COEFFICIENT OF THE PLASTIC STRAIN
C
      EB1=0.0
      DO I=1,6
      DO J=1,6
      EB1=EB1+EF_DIR(J)*EELM(J,I)*EP_DIR(I)
      END DO
      END DO
C
      EP=(EST_BE(1)+EST_BE(2)+EST_BE(3))/3.0
C
      EPX=2.0/(2.0+ERW)*EPC
      IF (EP.LE.EPX) THEN
      EB2=(8.0/ERW**2*(EP-2.0*EPC/(2.0+ERW))*(-2.0/(2.0+ERW))
     +      -8.0*EPC/(2.0+ERW)**2)*EV*(-EPC)/(ELAMDA-EKAPPA)
     +      *8.0/ERW**2*(EP-2.0*EPC/(2.0+ERW))
C
      ELSE
C
      EB2=(8.0/ERD**2*(EP-2.0*EPC/(2.0+ERW))*(-2.0/(2.0+ERW))
     +      -8.0*EPC/(2.0+ERW)**2)*EV*(-EPC)/(ELAMDA-EKAPPA)
     +      *8.0/ERD**2*(EP-2.0*EPC/(2.0+ERW))
C
      ENDIF
C
      IF (ABS(EB1-EB2).LT.ETOL) EXIT
C
      ECOEFF=EY_VAL/(EB1-EB2)
C
```

```
C     CORRECT THE STRESS
C
      DO I=1,6
      DO J=1,6
      STRESS(J)=STRESS(J)-ECOEFF*EELM(J,I)*EP_DIR(I)
      END DO
      END DO
C
C     CORRECT PC
      EPX=2.0/(2.0+ERW)*EPC
      IF (EP.LE.EPX) THEN
      EPC=EPC+ECOEFF*EV*(-EPC)*(8.0/ERW**2*(EP-2.0*EPC/(2.0+ERW)))
     +    /(ELAMDA-EKAPPA)
C
      ELSE
C
      EPC=EPC+ECOEFF*EV*(-EPC)*(8.0/ERD**2*(EP-2.0*EPC/(2.0+ERW)))
     +    /(ELAMDA-EKAPPA)
C
      ENDIF
C
C     CORRECT PC
C     EPC=EPC+ECOEFF*EV*(-EPC)*(2*EP-EPC)/(ELAMDA-EKAPPA)
C
      EY_VAL=Y_SUR(STRESS,EX,EY,EZ,EPC,ERW,ERD)
      IF (ABS(EY_VAL).LE.ETOL) EXIT
C
      IF (IN.GE.3) EXIT
C
      IN=IN+1
C
      END DO
C
      ENDIF
C
      RETURN
      END
CCCCCCCCCCCCCCCCCCCCCCCCCCCCCCCCCCCCCCCCCCCCCCCCCCCCCCCCCCCCCCCCCCCCCCCCCCCCCCCCCCCCCCCCCCCCCCCCCCCCCCCC
C
CCCCCCCCCCCCCCCCCCCCCCCCCCCCCCCCCCCCCCCCCCCCCCCCCCCCCCCCCCCCCCCCCCCCCCCCCCCCCCCCCCCCCCCCCCCCCCCCCCCCCCCC
CCCCCCCC CALCULATE THE STRESS INCREMENT FROM EL-PL_MATRIX  CCCCCCCCCCCCCCCCCCC
CCCCCCCCCCCCCCCCCCCCCCCCCCCCCCCCCCCCCCCCCCCCCCCCCCCCCCCCCCCCCCCCCCCCCCCCCCCCCCCCCCCCCCCCCCCCCCCCCCCCCCCC
C
      SUBROUTINE C_EPST(STRESS,DSTRAN,EDS_EP,EV,EPC,ELAMDA,
     +                  EKAPPA,EX,EY,EZ,EYP,EZP,EG_MU,TOL,ERW,ERD,
     +                  EXT,EYT,EZT,EXB,EYB,EZB,EGAMMA,EGAM_L,NUMBER,
     +                  SS_R,EMR,EW1,EW2,EINTA,EINTA_MAX,LU,SS_R0,
     +                  EVVP,EKK,EKW_FA,EPPW,EGOCR,TIME,NOEL,SS_LU)
C
      INCLUDE 'ABA_PARAM.INC'
C
      DIMENSION ESTRS1(6),ESTRS2(6),ESTRS(6),EF_DIR(6),
     +          EELPLM(6,6),STRESS(6),DSTRAN(6),EDS_EP(6),SS_R(6),
     +          SS_R0(6),TIME(2),EDS_IN(6),STRS_JF(6),EELM(6,6),
```

```
     +            SS_LU(6)
C
C      TO RESERVE THE VOLUME
       EV_R=EV
C
       EP22=0
       ESS22=0
       EJ22=0
       ETHETA22=0
       EDETS22=0
C
       EP=0
       ESS=0
       EJ=0
       ETHETA=0
       EDETS=0
C
       DO I=1,6
       ESTRS(I)=STRESS(I)
       EF_DIR(I)=0.0
       EDS_IN(I)=0.0
       STRS_JF(I)=0.0
       END DO
C
       DO I=1,6
       DO J=1,6
       EELPLM(J,I)=0.0
       EELM(J,I)=0.0
       END DO
       END DO
C
       EDD=0
       EDD_MAX=0
       DO I=1,6
       EDD=ABS(DSTRAN(I))
       IF (EDD.GT.EDD_MAX) THEN
       EDD_MAX=EDD
       ENDIF
       ENDDO
C
       NN=1
       NK=1
       DO NN=1,1000
       EDUP=EDD_MAX/NN
       IF (EDUP.LT.0.005) THEN
       NK=NN
       EXIT
       ENDIF
       ENDDO
C
       ET=0.0
       ETOL=1.0D-4
       ETOLE=1.0D-2
C
```

```
      KTOTLE=1
C
      DO WHILE (ABS(ET-1.0) .GT. ETOL)
C
      IF (KTOTLE .GE. 40) THEN
      EXIT
      ENDIF
C
      EDT1=(1.0)/NK
      EDT2=1-ET
      IF (EDT1.GT.EDT2) THEN
      EDT_P=EDT2
      ELSE
      EDT_P=EDT1
      ENDIF
C
      CALL ES_INV(STRESS,EP,ESS,EJ,ETHETA,EDETS)
      EBETA=EXB/(1+EYB*SIN(3.0*ETHETA))**EZB
      ETT=EXT/(1+EYT*SIN(3.0*ETHETA))**EZT
      EG_THE=EX/(1+EY*SIN(3.0*ETHETA))**EZ
C
      IF (EP.LE.(ETT*2.0*EPC/(2.0+ERW))) THEN
      EPF=EP
      EJF=-EG_THE*EPF
      ELSE
      EPF=EP
      EJF=EG_THE*ABS(EPF)*(1+EBETA*LOG(2.0*ETT*ABS(EPC/EPF)/(2.0+ERW)))
      ENDIF
C
      CALL EL_M(EELM,EV,EKAPPA,EG_MU,STRESS,DSTRAN,1,ELAMDA,
     +           EMR,EW1,EW2,SS_R,NUMBER,EINTA,EINTA_MAX,LU,SS_R0,EGOCR)
C
      DO I=1,6
      EDS_IN(I)=0.0
      STRS_JF(I)=0.0
      END DO
C
      DO I=1,6
      DO J=1,6
      EDS_IN(J)=EDS_IN(J)+EELM(J,I)*DSTRAN(I)*EDT_P
      END DO
      END DO
C
      DO I=1,6
      STRS_JF(I)=STRESS(I)+EDS_IN(I)
      END DO
C
      CALL ES_INV(STRS_JF,EP,ESS,EJ,ETHETA,EDETS)
C
      EJ_RATIO=EJ/EJF
C
      IF (EJ_RATIO.LT.1.0) THEN
      EDT=EDT_P
      ELSE
```

```
      EDT=EDT_P*0.1/EJ_RATIO
      ENDIF
C
      CALL ES_INV(STRESS,EP,ESS,EJ,ETHETA,EDETS)
C
      KCOUNT=1
C
      DO WHILE (.TRUE.)
C
C     FIRST CALCULATE THE STRESS INCREMENT
C     CALCULATE THE MEAN STRESS P
C
      CALL ES_INV(STRESS,EP22,ESS22,EJ22,ETHETA22,EDETS22)
      EPC_S=CAL_PC_SUB(ERW,ERD,EX,EY,EZ,EP22,EJ22,ETHETA22)
C
      CALL EL_PLM(EELPLM,EX,EY,EZ,EYP,EZP,EPC,STRESS,EV,ELAMDA,EKAPPA,
     +            EG_MU,EF_DIR,ERW,ERD,EXT,EYT,EZT,EXB,EYB,EZB,EGAMMA,
     +            EGAM_L,NUMBER,SS_R,EMR,EW1,EW2,EINTA,EINTA_MAX,LU,
     +            SS_R0,EVVP,EKK,EGOCR,TIME,NOEL,SS_LU)
C
      DO I=1,6
      ESTRS1(I)=STRESS(I)
      END DO
C
      DO I=1,6
      DO J=1,6
      ESTRS1(J)=ESTRS1(J)+EELPLM(J,I)*EDT*DSTRAN(I)
      END DO
      END DO
C
      EP1=(STRESS(1)+STRESS(2)+STRESS(3))/3.0
C
      EDP1=(ESTRS1(1)+ESTRS1(2)+ESTRS1(3))/3.0-EP1
C     TO DETERMINE THE ELASTIC VOLUMETRIC STRAIN
C
      ESTR_V1=-EKAPPA/EV*EDP1/EP1
C
C     TO DETERMINE THE PLASTIC VOLUMETRIC STRAIN
      EPSV1=(DSTRAN(1)+DSTRAN(2)+DSTRAN(3))*EDT-ESTR_V1
      EVVP1=EVVP+ABS(EPSV1)
C     TO DETERMINE THE HARDENING PARAMETER
      EPC1=EPC+EV/(ELAMDA-EKAPPA)*(-EPC)*EPSV1
      EV1=EV*(1.0+(DSTRAN(1)+DSTRAN(2)+DSTRAN(3))*EDT)
      EKW=-EKW_FA*EV*EP1/EKAPPA
      EPPW1=EPPW-EKW*((DSTRAN(1)+DSTRAN(2)+DSTRAN(3))*EDT)
C
C     SECOND CALCULATE THE STRESS INCREMENT
C     CALCULATE THE MEAN STRESS P
C
      CALL ES_INV(ESTRS1,EP22,ESS22,EJ22,ETHETA22,EDETS22)
      EPC_S1=CAL_PC_SUB(ERW,ERD,EX,EY,EZ,EP22,EJ22,ETHETA22)
C
      EY_VAL=Y_SUR(ESTRS1,EX,EY,EZ,EPC1,ERW,ERD)
      IF (EY_VAL.GT.1.0D-2) THEN
```

```
      CALL DRAG_Y(ESTRS1,EPC1,EV1,ELAMDA,EKAPPA,EG_MU,
     +      EX,EY,EZ,EYP,EZP,TOL,ERW,ERD,EPC_RE,EMR,EW1,EW2,SS_R,
     +      NUMBER,EINTA,EINTA_MAX,LU,SS_R0,EGOCR)
      ENDIF

      CALL EL_PLM(EELPLM,EX,EY,EZ,EYP,EZP,EPC1,ESTRS1,EV1,ELAMDA,EKAPPA,
     +            EG_MU,EF_DIR,ERW,ERD,EXT,EYT,EZT,EXB,EYB,EZB,EGAMMA,
     +            EGAM_L,NUMBER,SS_R,EMR,EW1,EW2,EINTA,EINTA_MAX,LU,
     +            SS_R0,EVVP1,EKK,EGOCR,TIME,NOEL,SS_LU)
C
      DO I=1,6
      ESTRS2(I)=ESTRS1(I)
      END DO
C
      DO I=1,6
      DO J=1,6
      ESTRS2(J)=ESTRS2(J)+EELPLM(J,I)*EDT*DSTRAN(I)
      END DO
      END DO
C
      EP2=(ESTRS1(1)+ESTRS1(2)+ESTRS1(3))/3.0
C
      EDP2=(ESTRS2(1)+ESTRS2(2)+ESTRS2(3))/3.0-EP2
C
C     TO DETERMINE THE ELASTIC VOLUMETRIC STRAIN
C
      ESTR_V2=-EKAPPA/EV1*EDP2/EP2
C     TO DETERMINE THE PLASTIC VOLUMETRIC STRAIN
      EPSV2=(DSTRAN(1)+DSTRAN(2)+DSTRAN(3))*EDT-ESTR_V2
      EVVP2=EVVP+ABS(EPSV2)
C     TO DETERMINE THE HARDENING PARAMETER
      EPC2=EPC1+EV1/(ELAMDA-EKAPPA)*(-EPC1)*EPSV2
      EKW=-EKW_FA*EV1*EP2/EKAPPA
      EPPW2=EPPW-EKW*((DSTRAN(1)+DSTRAN(2)+DSTRAN(3))*EDT)
C
      CALL ES_INV(ESTRS2,EP22,ESS22,EJ22,ETHETA22,EDETS22)
C
      EPC_S2=CAL_PC_SUB(ERW,ERD,EX,EY,EZ,EP22,EJ22,ETHETA22)
C
      EY_VAL=Y_SUR(ESTRS2,EX,EY,EZ,EPC2,ERW,ERD)
      IF (EY_VAL.GT.1.0D-2) THEN
      CALL DRAG_Y(ESTRS2,EPC2,EV1,ELAMDA,EKAPPA,EG_MU,
     +      EX,EY,EZ,EYP,EZP,TOL,ERW,ERD,EPC_RE,EMR,EW1,EW2,SS_R,
     +      NUMBER,EINTA,EINTA_MAX,LU,SS_R0,EGOCR)
      ENDIF
C
C     THE ERROR CONTROL IS SPECIFIED AS THE NORM OF THE STRESS
C     VECTOR AND PC
C
      ENORS=0.0
      ENORS1=0.0
      ENORS2=0.0
      DO I=1,6
      ENORS=ENORS+STRESS(I)**2
```

```
      ENORS1=ENORS1+ESTRS1(I)**2
      ENORS2=ENORS2+ESTRS2(I)**2
      END DO
      ENORS=ENORS**0.5
      ENORS1=ENORS1**0.5
      ENORS2=ENORS2**0.5
C
      IF (ENORS.EQ.0) THEN
      ER_ST=0.0
      ER_PC=0.0
      ELSE
      ER_ST=ABS(0.5*(ENORS2-ENORS1)/ENORS)
      ER_PC=ABS(0.5*(EPC2-EPC1)/EPC)
      ENDIF
C
      IF (ER_ST.LE.ETOLE .AND.ER_PC .LE.ETOLE) THEN
      DO I=1,6
      STRESS(I)=0.5*(STRESS(I)+ESTRS2(I))
      END DO
      EPC=0.5*(EPC+EPC2)
      EVVP=0.5*(EVVP1+EVVP2)
      EV=EV1
      EPPW=0.5*(EPPW1+EPPW2)
      ET=ET+EDT
      EXIT
C
      ELSEIF (KCOUNT.GE.3.OR.KTOTLE.EQ.19) THEN
      DO I=1,6
      STRESS(I)=0.5*(STRESS(I)+ESTRS2(I))
      END DO
      EPC=0.5*(EPC+EPC2)
      EVVP=0.5*(EVVP1+EVVP2)
      EV=EV1
      EPPW=0.5*(EPPW1+EPPW2)
      ET=ET+EDT
      EXIT
C
      ELSE
C
      IF (ER_ST .GT.ER_PC) THEN
      ER_MAX=ER_ST
      ELSE
      ER_MAX=ER_PC
      END IF
      EDT1=EDT*0.8*(TOL/ER_MAX)**0.5
      EDT2=EDT*0.25
C
      IF (EDT1 .GT. EDT2) THEN
      EDT=EDT1
      ELSE
      EDT=EDT1
      ENDIF
C
      END IF
```

```
C
      KCOUNT=KCOUNT+1
C
      END DO
C
      KTOTLE=KTOTLE+1
C
      END DO
C
      DO I=1,6
      EDS_EP(I)=STRESS(I)-ESTRS(I)
      STRESS(I)=ESTRS(I)
      END DO
C
      EV=EV_R*(1.0+(DSTRAN(1)+DSTRAN(2)+DSTRAN(3)))
C
      RETURN
      END
CCCCCCCCCCCCCCCCCCCCCCCCCCCCCCCCCCCCCCCCCCCCCCCCCCCCCCCCCCCCCCCCCCCCCCCCCCCCCC
C
CCCCCCCCCCCCCCCCCCCCCCCCCCCCCCCCCCCCCCCCCCCCCCCCCCCCCCCCCCCCCCCCCCCCCCCCCCCCCC
CCCCCCCC CALCULATE THE STRESS INCREMENT PURELY ELASTIC     CCCCCCCCCCCCCCCCCC
CCCCCCCCCCCCCCCCCCCCCCCCCCCCCCCCCCCCCCCCCCCCCCCCCCCCCCCCCCCCCCCCCCCCCCCCCCCCCC
C
      SUBROUTINE C_EEST(STRESS,DSTRAN,EDS_EP,EV,EPC,ELAMDA,
     +            EKAPPA,EX,EY,EZ,EYP,EZP,EG_MU,TOL,ERW,ERD,
     +            EXT,EYT,EZT,EXB,EYB,EZB,EGAMMA,EGAM_L,NUMBER,
     +            SS_R,EMR,EW1,EW2,EINTA,EINTA_MAX,LU,SS_RO,
     +            EVVP,EKK,EKW_FA,EPPW,EGOCR,TIME,NOEL)
C
      INCLUDE 'ABA_PARAM.INC'
C
      DIMENSION ESTRS1(6),ESTRS2(6),ESTRS(6),EF_DIR(6),
     +           STRESS(6),DSTRAN(6),EDS_EP(6),SS_R(6),
     +           SS_RO(6),TIME(2),EDS_IN(6),STRS_JF(6),EELM(6,6)
C
C     TO RESERVE THE VOLUME
      EV_R=EV
C
      EP22=0
      ESS22=0
      EJ22=0
      ETHETA22=0
      EDETS22=0
C
      EP=0
      ESS=0
      EJ=0
      ETHETA=0
      EDETS=0
C
      DO I=1,6
      ESTRS(I)=STRESS(I)
      EF_DIR(I)=0.0
```

```
      EDS_IN(I)=0.0
      STRS_JF(I)=0.0
      END DO
C
      DO I=1,6
      DO J=1,6
      EELM(J,I)=0.0
      END DO
      END DO
C
      EDD=0
      EDD_MAX=0
      DO I=1,6
      EDD=ABS(DSTRAN(I))
      IF (EDD.GT.EDD_MAX) THEN
      EDD_MAX=EDD
      ENDIF
      ENDDO
C
      NN=1
      NK=1
      DO NN=1,1000
      EDUP=EDD_MAX/NN
      IF (EDUP.LT.0.001) THEN
      NK=NN
      EXIT
      ENDIF
      ENDDO
C
      ET=0.0
      ETOL=1.0D-4
      ETOLE=1.0D-2
C
      KTOTLE=1
C
      DO WHILE (ABS(ET-1.0) .GT. ETOL)
C
      IF (KTOTLE .GE. 100) THEN
      EXIT
      ENDIF
C
      EDT1=(1.0)/NK
      EDT2=1-ET
      IF (EDT1.GT.EDT2) THEN
      EDT_P=EDT2
      ELSE
      EDT_P=EDT1
      ENDIF
C
      CALL ES_INV(STRESS,EP,ESS,EJ,ETHETA,EDETS)
      EBETA=EXB/(1+EYB*SIN(3.0*ETHETA))**EZB
      ETT=EXT/(1+EYT*SIN(3.0*ETHETA))**EZT
      EG_THE=EX/(1+EY*SIN(3.0*ETHETA))**EZ
C
```

```
      IF (EP.LE.(ETT*2.0*EPC/(2.0+ERW))) THEN
      EPF=EP
      EJF=-EG_THE*EPF
      ELSE
      EPF=EP
      EJF=EG_THE*ABS(EPF)*(1+EBETA*LOG(2.0*ETT*ABS(EPC/EPF)/(2.0+ERW)))
      ENDIF
C
      CALL EL_M(EELM,EV,EKAPPA,EG_MU,STRESS,DSTRAN,1,ELAMDA,
     +           EMR,EW1,EW2,SS_R,NUMBER,EINTA,EINTA_MAX,LU,SS_R0,EGOCR)
C
      DO I=1,6
      EDS_IN(I)=0.0
      STRS_JF(I)=0.0
      END DO
C
      DO I=1,6
      DO J=1,6
      EDS_IN(J)=EDS_IN(J)+EELM(J,I)*DSTRAN(I)*EDT_P
      END DO
      END DO
C
      DO I=1,6
      STRS_JF(I)=STRESS(I)+EDS_IN(I)
      END DO
C
      CALL ES_INV(STRS_JF,EP,ESS,EJ,ETHETA,EDETS)
C
      EJ_RATIO=EJ/EJF
C
      IF (KTOTLE.LT.4) THEN
      IF (EJ_RATIO.LT.1.0) THEN
      EDT=EDT_P
      ELSE
      EDT=EDT_P*0.8/EJ_RATIO
      ENDIF
      ELSE
      EDT=EDT_P
      ENDIF
C
      CALL ES_INV(STRESS,EP,ESS,EJ,ETHETA,EDETS)
C
C     FIRST CALCULATE THE STRESS INCREMENT
C     CALCULATE THE MEAN STRESS P
C
      CALL ES_INV(STRESS,EP22,ESS22,EJ22,ETHETA22,EDETS22)
      EPC_S=CAL_PC_SUB(ERW,ERD,EX,EY,EZ,EP22,EJ22,ETHETA22)
C
      CALL EL_M(EELM,EV,EKAPPA,EG_MU,STRESS,DSTRAN,1,ELAMDA,
     +           EMR,EW1,EW2,SS_R,NUMBER,EINTA,EINTA_MAX,LU,SS_R0,EGOCR)
C
      DO I=1,6
      ESTRS1(I)=STRESS(I)
      END DO
```

```
C
      DO I=1,6
      DO J=1,6
      ESTRS1(J)=ESTRS1(J)+EELM(J,I)*EDT*DSTRAN(I)
      END DO
      END DO
C
      DO I=1,6
      STRESS(I)=ESTRS1(I)
      END DO
C
      ET=ET+EDT
      KTOTLE=KTOTLE+1
C
      END DO
C
      DO I=1,6
      EDS_EP(I)=STRESS(I)-ESTRS(I)
      STRESS(I)=ESTRS(I)
      END DO
C
c       EV=EV_R*(1.0+(DSTRAN(1)+DSTRAN(2)+DSTRAN(3)))
C
      RETURN
      END
CCCCCCCCCCCCCCCCCCCCCCCCCCCCCCCCCCCCCCCCCCCCCCCCCCCCCCCCCCCCCCCCCCCCCCCCCCCCCC
C
CCCCCCCCCCCCCCCCCCCCCCCCCCCCCCCCCCCCCCCCCCCCCCCCCCCCCCCCCCCCCCCCCCCCCCCCCCCCCC
CCCCCCCC  TO CALCULATE THE ELASTIC PORTION OF STRAIN---ALPHA  CCCCCCCCCCCCCCC
CCCCCCCCCCCCCCCCCCCCCCCCCCCCCCCCCCCCCCCCCCCCCCCCCCCCCCCCCCCCCCCCCCCCCCCCCCCCCC
C
      FUNCTION C_ALFA(EDS_PR,STRESS,EX,EY,EZ,EPC,DSTRAN,EV,EKAPPA,EG_MU,
     +                 ERW,ERD,ELAMDA,EMR,EW1,EW2,SS_R,NUMBER,EINTA,
     +                 EINTA_MAX,LU,SS_R0,EGOCR)
C
C     FOR THE THIS STRESS, HAVE ALREADY ADDED THE STRESS INCREMENT
C     SHOULD BE PAID ATTENSION
C
      INCLUDE ’ABA_PARAM.INC’
C
      DIMENSION ESTRS0(6),ESTRS1(6),ESTRS(6),EELM(6,6),E_DSTAN(6),
     +           EDS_PR(6),STRESS(6),DSTRAN(6),SS_R(6),SS_R0(6)
C
C     ESTRESS0==ALPHA=0,ESTRESS1==ALPHA=1,ESTRESS==THE TRIED STRESS
C
      DO I=1,6
      DO J=1,6
      EELM(J,I)=0.0
      END DO
      END DO
C
      DO I=1,6
      ESTRS0(I)=STRESS(I)-EDS_PR(I)
      ESTRS1=STRESS(I)
```

```
      ESTRS(I)=ESTRS0(I)
      END DO
C
      DO I=1,6
      E_DSTAN(I)=0.5*DSTRAN(I)
      END DO
C
      CALL EL_M(EELM,EV,EKAPPA,EG_MU,ESTRS0,E_DSTAN,2,ELAMDA,
     +           EMR,EW1,EW2,SS_R,NUMBER,EINTA,EINTA_MAX,LU,SS_R0,EGOCR)
C
      DO I=1,6
      DO J=1,6
      ESTRS(J)=ESTRS(J)+0.5*EELM(J,I)*DSTRAN(I)
      END DO
      END DO
C
      ETOL=1.0D-2
      EALFA0=0.0
      EALFA1=1.0
      K=2
C
C     TO INSURE THE TWO END POINTS HAVE DIFFERENT SIGN
C
      DO WHILE (.TRUE.)
C
      EYSUR=Y_SUR(ESTRS,EX,EY,EZ,EPC,ERW,ERD)
      IF (EYSUR .LT.0.0) THEN
      EALFA0=0.5**(K-1)
      EXIT
C
      ELSE
C
      IF (K.GE.4) EXIT
C
      DO I=1,6
      E_DSTAN(I)=0.5**K*DSTRAN(I)
      END DO
C
      CALL EL_M(EELM,EV,EKAPPA,EG_MU,ESTRS0,E_DSTAN,2,ELAMDA,
     +           EMR,EW1,EW2,SS_R,NUMBER,EINTA,EINTA_MAX,LU,SS_R0,EGOCR)
C
      DO I=1,6
      ESTRS(I)=ESTRS0(I)
      END DO
C
      DO I=1,6
      DO J=1,6
      ESTRS(J)=ESTRS(J)+EELM(J,I)*E_DSTAN(I)
      END DO
      END DO
C
      ENDIF
C
      K=K+1
```

```
      END DO
C
      IF (K.GE.4) THEN
      C_ALFA=0.0
      ELSE
C
C     THE "PEGASUS" METHOD TO CALCULATE THE ROOT OF AN EQUATION
C     THE COMPUTATIONAL EFFICIENCY IS 1.642
C
      IN=1
C
      EF0=EYSUR
      EF1=Y_SUR(STRESS,EX,EY,EZ,EPC,ERW,ERD)
C
      DO WHILE (.TRUE.)
C
      EALFA2=(EF1*EALFA0-EF0*EALFA1)/(EF1-EF0)
C
      IF (IN.GE.3) THEN
      C_ALFA=EALFA2
      EXIT
      ENDIF
C
      DO I=1,6
      E_DSTAN(I)=EALFA2*DSTRAN(I)
      END DO
C
      CALL EL_M(EELM,EV,EKAPPA,EG_MU,ESTRS0,E_DSTAN,2,ELAMDA,
     +           EMR,EW1,EW2,SS_R,NUMBER,EINTA,EINTA_MAX,LU,SS_R0,EGOCR)
C
      DO I=1,6
      ESTRS(I)=ESTRS0(I)
      END DO
C
      DO I=1,6
      DO J=1,6
      ESTRS(J)=ESTRS(J)+EELM(J,I)*E_DSTAN(I)
      END DO
      END DO
C
      EF2=Y_SUR(ESTRS,EX,EY,EZ,EPC,ERW,ERD)
C
      IF (ABS(EF2).LE.ETOL) THEN
      C_ALFA=EALFA2
      EXIT
C
      ELSE IF (EF2*EF1.LT.0.0) THEN
      EALFA0=EALFA1
      EALFA1=EALFA2
      EF0=EF1
      EF1=EF2
      ELSE
      EALFA0=EALFA0
      EF0=EF0*EF1/(EF1+EF2)
```

```
      EALFA1=EALFA2
      EF1=EF2
      END IF
C
      IN=IN+1
C
      END DO
C
      ENDIF
C
      RETURN
      END
CCCCCCCCCCCCCCCCCCCCCCCCCCCCCCCCCCCCCCCCCCCCCCCCCCCCCCCCCCCCCCCCCCCCCCCCCCCCCCCCCCCCCCCCCCCCCCCCCCCCCCCCCCCC
C
CCCCCCCCCCCCCCCCCCCCCCCCCCCCCCCCCCCCCCCCCCCCCCCCCCCCCCCCCCCCCCCCCCCCCCCCCCCCCCCCCCCCCCCCCCCCCCCCCCCCCCCCCCCC
CCCCCCC    TO CHECK WHETHER OR NOT YIELDING OCCURS     CCCCCCCCCCCCCCCCCCCCCC
CCCCCCCCCCCCCCCCCCCCCCCCCCCCCCCCCCCCCCCCCCCCCCCCCCCCCCCCCCCCCCCCCCCCCCCCCCCCCCCCCCCCCCCCCCCCCCCCCCCCCCCCCCCC
C
      FUNCTION Y_SUR(STRESS,EX,EY,EZ,EPC,ERW,ERD)
C
      INCLUDE 'ABA_PARAM.INC'
C
      DIMENSION STRESS(6)
C
      EP=0.0
      ESS=0.0
      EJ=0.0
      ETHETA=0.0
      EDETS=0.0
C
      CALL ES_INV(STRESS,EP,ESS,EJ,ETHETA,EDETS)
C
      EPC_SUB=CAL_PC_SUB(ERW,ERD,EX,EY,EZ,EP,EJ,ETHETA)
C
      Y_SUR=(EPC-EPC_SUB)/ABS(EPC)
C
      RETURN
      END
CCCCCCCCCCCCCCCCCCCCCCCCCCCCCCCCCCCCCCCCCCCCCCCCCCCCCCCCCCCCCCCCCCCCCCCCCCCCCCCCCCCCCCCCCCCCCCCCCCCCCCCCCCCC
C
CCCCCCCCCCCCCCCCCCCCCCCCCCCCCCCCCCCCCCCCCCCCCCCCCCCCCCCCCCCCCCCCCCCCCCCCCCCCCCCCCCCCCCCCCCCCCCCCCCCCCCCCCCCC
CCCCCCCCCC   CALULATE THE EL_PLASTIC MATRIX   CCCCCCCCCCCCCCCCCCCCCCCCCCCCCCC
CCCCCCCCCCCCCCCCCCCCCCCCCCCCCCCCCCCCCCCCCCCCCCCCCCCCCCCCCCCCCCCCCCCCCCCCCCCCCCCCCCCCCCCCCCCCCCCCCCCCCCCCCCCC
C
      SUBROUTINE EL_PLM(EELPLM,EX,EY,EZ,EYP,EZP,EPC,
     +              STRESS,EV,ELAMDA,EKAPPA,EG_MU,EF_DIR,ERW,ERD,
     +              EXT,EYT,EZT,EXB,EYB,EZB,EGAMMA,EGAM_L,NUMBER,SS_R,
     +              EMR,EW1,EW2,EINTA,EINTA_MAX,LU,SS_RO,EVVP,EKK,EGOCR,
     +              TIME,NOEL,SS_LU)
C
      INCLUDE 'ABA_PARAM.INC'
C
      DIMENSION EB1(6),ENN(6,6),EDNN(6,6),EDNND(6,6),
     +            EP_DIR(6),EELM(6,6),EELPLM(6,6),EF_DIR(6),
```

```
     +            STRESS(6),DSTRAN(6),SS_R(6),ESS_RR(6),ESS_NN(6),
     +            SS_R0(6),TIME(2),SS_LU(6)
C
      ETOL=1.0D-4
C
      EP=0.0
      ESS=0.0
      EJ=0.0
      ETHETA=0.0
      EDETS=0.0
C
      CALL ES_INV(STRESS,EP,ESS,EJ,ETHETA,EDETS)
C
C     DETERMINE THE ELASTIC MATRIX
      DO I=1,6
      DO J=1,6
      EELM(J,I)=0.0
      END DO
      END DO
C
      DO I=1,6
      EF_DIR(I)=0.0
      EP_DIR(I)=0.0
      END DO
C
C     FOR ELPLM,ONLY NEED TANGENT STIFFNESS, SO STRAN CAN BE SPECIFIED
C     TO ANY VALUE
C
      DO I=1,6
      DSTRAN(I)=0.0
      END DO
C
      CALL EL_M(EELM,EV,EKAPPA,EG_MU,STRESS,DSTRAN,1,ELAMDA,
     +           EMR,EW1,EW2,SS_R,NUMBER,EINTA,EINTA_MAX,LU,SS_R0,EGOCR)
C
C     TO CALCULATE THE PLASTIC MODULUS H
C     COMPRESSION IS NEGATIVE
C     FIRST SHOULD CALCULATE THE DISTANCE TO THE BOUNDING SURFACE
C
C     FIRST IMAGY POINT
C
      CALL ES_INV(STRESS,EP,ESS,EJ,ETHETA,EDETS)
      EPC_S1=CAL_PC_SUB(ERW,ERD,EX,EY,EZ,EP,EJ,ETHETA)
      IF (ABS(EPC_S1).GT.ABS(EPC)) THEN
      EPC_S1=EPC
      ENDIF
C
      IF (ABS(EPC_S1/EPC-1.0).LT.(ETOL)) THEN
C
C     EPC=EPC_S1
      EPX=2.0/(2.0+ERW)*EPC
      IF (EP.LE.EPX) THEN
      EH=-EV/(ELAMDA-EKAPPA)*(-EPC)*(8.0/ERW**2*(EP-2.0*EPC/(2.0+ERW)))
     +    *(8.0/ERW**2*(EP-2.0*EPC/(2.0+ERW))*(-2.0/(2.0+ERW))
```

```
     +    -8.0*EPC/(2.0+ERW)**2)
C
      ELSE
      EH=-EV/(ELAMDA-EKAPPA)*(-EPC)*(8.0/ERD**2*(EP-2.0*EPC/(2.0+ERW)))
     +    *(8.0/ERD**2*(EP-2.0*EPC/(2.0+ERW))*(-2.0/(2.0+ERW))
     +    -8.0*EPC/(2.0+ERW)**2)
C
      ENDIF
C
      ELSE
C
      EP_B1=EPC/EPC_S1*EP
C
C     SECOND IMAGY POINT
      EBETA=EXB/(1+EYB*SIN(3.0*ETHETA))**EZB
      ET=EXT/(1+EYT*SIN(3.0*ETHETA))**EZT
      EG_THE=EX/(1+EY*SIN(3.0*ETHETA))**EZ
      IF (EP.LE.(ET*2.0*EPC/(2.0+ERW))) THEN
      EP_B2=2.0*EPC/(2.0+ERW)
      EPF=EP
      EJF=-EG_THE*EPF
      ELSE
      EPF=EP
      EJF=EG_THE*ABS(EPF)*(1+EBETA*LOG(2.0*ET*ABS(EPC/EPF)/(2.0+ERW)))
      IF (EJ.GT.EJF) THEN
C      EJF=EJ*1.05
      EJ=0.95*EJF
      ENDIF
      EPC_S2=CAL_PC_SUB(ERW,ERD,EX,EY,EZ,EPF,EJF,ETHETA)
      EP_B2=EPC/EPC_S2*EPF
C
      IF (ABS(EP_B2/(2.0*EPC/(2.0+ERW))-1).LT.(1D-3).OR.
     +    EP_B2.LT.2.0*EPC/(2.0+ERW)) THEN
      EP_B2=2.0*EPC/(2.0+ERW)
      ENDIF
      ENDIF
C
C     PLASTIC MODULUS-FIRST IMAGY POINT
      EPX=2.0/(2.0+ERW)*EPC
      IF (EP_B1.LE.EPX) THEN
      EH1=-EV/(ELAMDA-EKAPPA)*(-EPC)*(8.0/ERW**2
     +    *(EP_B1-2.0*EPC/(2.0+ERW)))*(8.0/ERW**2*(EP_B1-2.0
     +    *EPC/(2.0+ERW))*(-2.0/(2.0+ERW))-8.0*EPC/(2.0+ERW)**2)
      ELSE
      EH1=-EV/(ELAMDA-EKAPPA)*(-EPC)*(8.0/ERD**2
     +    *(EP_B1-2.0*EPC/(2.0+ERW)))*(8.0/ERD**2*(EP_B1-2.0
     +    *EPC/(2.0+ERW))*(-2.0/(2.0+ERW))-8.0*EPC/(2.0+ERW)**2)
      ENDIF
C
C     PLASTIC MODULUS-SECOND IMAGY POINT
      IF (EP.LE.(ET*2.0*EPC/(2.0+ERW))) THEN
      EH2=0
      ELSE
      EH2=-EV/(ELAMDA-EKAPPA)*(-EPC)*(8.0/ERD**2
```

```
     +    *(EP_B2-2.0*EPC/(2.0+ERW)))*(8.0/ERD**2*(EP_B2-2.0
     +    *EPC/(2.0+ERW))*(-2.0/(2.0+ERW))-8.0*EPC/(2.0+ERW)**2)
          ENDIF
C
          IF (EP.GE.0) THEN
          EROH1=3.0
          EROH2=3.0
          EROH=(1+EROH2**2/EG_THE**2)/(1+EROH1**2/EG_THE**2)
C         THIRD IMAGY POINT (VERTICAL PROJECTION ON THE BOUNDING SURFACE)
C         THE STRESS RATIO
          EROH3=3.0
          ELSE
          EROH1=-EJ/EP
          EROH2=-EJF/EPF
          EROH=(1+EROH2**2/EG_THE**2)/(1+EROH1**2/EG_THE**2)
          EROH3=EG_THE*SQRT(ABS((2.0/(2.0+ERW))**2*EPC**2-4.0/ERD**2
     +       *(EP-2.0*EPC/(2.0+ERW))**2))/(-EP)
          ENDIF
C
          IF (ABS(EROH3-EROH2).LE.ETOL) THEN
          EK=0.0
          ELSE
          EK=EROH*(EROH3-EROH1)/(EROH3-EROH2)
          ENDIF
C
C         PLASTIC MODULUS H
          ED_RAT=EPC/EPC_S1
C
          EP_R=(SS_LU(1)+SS_LU(2)+SS_LU(3))/3.0
C
          IF (ABS(EP_R).GT.ABS(EP)) THEN
          ECA1=1-ABS(EP)/ABS(EP_R)
          ELSE
          ECA1=1-ABS(EP_R)/ABS(EP)
          ENDIF
C
          DO I=1,6
          ESS_RR(I)=SS_LU(I)/EP_R
          ESS_NN(I)=STRESS(I)/EP
          ENDDO
          EJ_RS=0
          DO I=1,3
          EJ_RS=EJ_RS+0.5*((ESS_NN(I)-1)-(ESS_RR(I)-1))**2
          ENDDO
          DO I=4,6
          EJ_RS=EJ_RS+(ESS_NN(I)-ESS_RR(I))**2
          ENDDO
          EJ_R=EJ_RS**0.5
          IF (EJ_R.LT.ETOL) THEN
          EJ_R=ETOL
          ENDIF
          ECA2=EJ_R*1.732
C
          ECA_EQ=(ECA1**2+ECA2**2)**0.5
```

```
      IF (ECA_EQ.LE.ETOL)THEN
      ECA_EQ=ETOL
      ENDIF
      ECA=1.0/ECA_EQ
C
      ECOXI=(1+ECA*(1.0-1.0/ED_RAT))**EGAMMA

      EH=(EH1-EH2*EK)*ECOXI
C
      ENDIF
C
C     DETERMINE THE DIRECTION OF YIELD SURFACE
      CALL EFP_DI(EF_DIR,EX,EY,EZ,EYP,EZP,EPC_S1,STRESS,1,ERW,ERD)
C
C     DETERMINE THE DIRECTION OF PLASTIC POTENTIAL
      IF ((EY.EQ.EYP).AND.(EZ.EQ.EZP)) THEN
      DO I=1,6
      EP_DIR(I)=EF_DIR(I)
      END DO
C
      ELSE
C
      CALL EFP_DI(EP_DIR,EX,EY,EZ,EYP,EZP,EPC_S1,STRESS,2,ERW,ERD)
      END IF
C
      DO I=1,6
      EB1(I)=0.0
      END DO
C
      DO I=1,6
      DO J=1,6
      EB1(I)=EB1(I)+EF_DIR(J)*EELM(J,I)
      END DO
      END DO
C
      EB2=0.0
      DO I=1,6
      EB2=EB2+EB1(I)*EP_DIR(I)
      END DO
C
      EB=EB2+EH
C
      IF (ABS(EB).LT.(1D-10).AND.EB.GT.0) THEN
      EB=1D-10
      ELSEIF (ABS(EB).LT.(1D-10).AND.EB.LT.0) THEN
      EB=-1D-10
      ENDIF
C
      DO I=1,6
      DO J=1,6
      ENN(J,I)=EP_DIR(J)*EF_DIR(I)
      EDNN(J,I)=0.0
      EDNND(J,I)=0.0
      END DO
```

```
      END DO
C
      DO J=1,6
      DO I=1,6
      DO K=1,6
      EDNN(I,J)=EDNN(I,J)+EELM(I,K)*ENN(K,J)
      END DO
      END DO
      END DO
C
      DO J=1,6
      DO I=1,6
      DO K=1,6
      EDNND(I,J)=EDNND(I,J)+EDNN(I,K)*EELM(K,J)
      END DO
      END DO
      END DO
C
      DO I=1,6
      DO J=1,6
      EELPLM(J,I)=EELM(J,I)-EDNND(J,I)/EB
      END DO
      END DO
C
      RETURN
      END
CCCCCCCCCCCCCCCCCCCCCCCCCCCCCCCCCCCCCCCCCCCCCCCCCCCCCCCCCCCCCCCCCCCCCCCCCCCC
C
CCCCCCCCCCCCCCCCCCCCCCCCCCCCCCCCCCCCCCCCCCCCCCCCCCCCCCCCCCCCCCCCCCCCCCCCCCCC
CCCCCCC   CALULATE THE DIRECTION OF YIELD SURFACE   CCCCCCCCCCCCCCCCCCCCCCCCC
CCCCCCCCCCCCCCCCCCCCCCCCCCCCCCCCCCCCCCCCCCCCCCCCCCCCCCCCCCCCCCCCCCCCCCCCCCCC
C
      SUBROUTINE EFP_DI(EF_DIR,EX,EY,EZ,EYP,EZP,EPC,STRESS,KFP_V,
     +            ERW,ERD)
C
      INCLUDE 'ABA_PARAM.INC'
C
C     ST={SIGAMA_X-P,SIGAMA_Y-P,SIGAMA_Z-P,TOU_XY,TOU_XZ,TOU_YZ}
C     EQ_S(6)==THE DERIVATIVE OF Q TO S
C     EDS_S(6)==THE DERIVATIVE OF DET(S) TO S
C     EII(6)==TO CALCULATE THE SURFACE DIRECTION
C     ETRA(6,6)==TO CALCULATE THE SURFACE DIRECTION
C
      DIMENSION EQ_S(6),EDET_S(6),EII(6),ETRA(6,6),EF_DIR1(6),
     +           STRESS(6),EF_DIR(6)
C
      EP=0.0
      ESS=0.0
      EJ=0.0
      ETHETA=0.0
      EDETS=0.0
C
      DO I=1,6
      EDET_S(I)=0.0
```

```
      END DO
C
      IF (KFP_V.EQ.2) THEN
      EY0=EYP
      EZ0=EZP
      ELSE
      EY0=EY
      EZ0=EZ
      ENDIF
C
      CALL ES_INV(STRESS,EP,ESS,EJ,ETHETA,EDETS)
C
      EG_THE=EX/(1+EY*SIN(3.0*ETHETA))**EZ
C
      EPC=CAL_PC_SUB(ERW,ERD,EX,EY,EZ,EP,EJ,ETHETA)
C
C     EFP_VALUE=1,FOR YIELD SURFACE,=2,FOR PLASTIC POTENTIAL
C
      DO I=1,3
      EQ_S(I)=2*(STRESS(I)-EP)
      END DO
C
      DO I=4,6
      EQ_S(I)=4*STRESS(I)
      END DO
C
      EDET_S(1)=(STRESS(2)-EP)*(STRESS(3)-EP)-STRESS(6)**2
      EDET_S(2)=(STRESS(1)-EP)*(STRESS(3)-EP)-STRESS(5)**2
      EDET_S(3)=(STRESS(1)-EP)*(STRESS(2)-EP)-STRESS(4)**2
      EDET_S(4)=-2.0*(STRESS(3)-EP)*STRESS(4)+2.0*STRESS(5)
     +            *STRESS(6)
      EDET_S(5)=-2.0*(STRESS(2)-EP)*STRESS(5)+2.0*STRESS(4)
     +            *STRESS(6)
      EDET_S(6)=-2.0*(STRESS(1)-EP)*STRESS(6)+2.0*STRESS(4)
     +            *STRESS(5)
C
      EF_Q=0.5/EG_THE**2
C
      EF_THE=3.0*ESS*EZ0*EY0*(COS(3.0*ETHETA))/(1+EY0*SIN(3.0*ETHETA))
     +          /EG_THE**2
      EALFA1=EF_Q+EF_THE*0.6495*EDETS/COS(3.0*ETHETA)/EJ**5
      EALFA2=-EF_THE*0.866/COS(3.0*ETHETA)/EJ**3
C
C     PREMARY CACULATE DIRECTION, SHOULD BE FURTHER REVISED
C
      DO I=1,6
      EF_DIR(I)=EALFA1*EQ_S(I)+EALFA2*EDET_S(I)
      EII(I)=1.0
      EF_DIR1(I)=0.0
      END DO
C
      DO I=4,6
      EII(I)=0.0
      END DO
```

```
C
      DO I=1,6
      DO J=1,6
      ETRA(J,I)=0.0
      END DO
      END DO
C
      DO I=1,3
      DO J=1,3
      ETRA(J,I)=-1.0
      END DO
      ETRA(I,I)=2.0
      END DO
C
      DO I=4,6
      ETRA(I,I)=3.0
      END DO
C     THE ABOVE HAVE SPECIFIED EII AND ETRA
      DO I=1,6
      DO J=1,6
      EF_DIR1(J)=EF_DIR1(J)+1.0/3.0*ETRA(J,I)*EF_DIR(I)
      END DO
      END DO
C
      EPX=2.0/(2.0+ERW)*EPC
      IF(EP.LE.EPX) THEN
      DO I=1,6
      EF_DIR(I)=EF_DIR1(I)+8.0/3.0/ERW**2*(EP-EPC*2.0/(2.0+ERW))
     +          *EII(I)
      END DO
C
      ELSE
C
      DO I=1,6
      EF_DIR(I)=EF_DIR1(I)+8.0/3.0/ERD**2*(EP-EPC*2.0/(2.0+ERW))
     +          *EII(I)
      END DO
C
      ENDIF
C
      RETURN
      END
CCCCCCCCCCCCCCCCCCCCCCCCCCCCCCCCCCCCCCCCCCCCCCCCCCCCCCCCCCCCCCCCCCCCCCCCCCCCC
C
CCCCCCCCCCCCCCCCCCCCCCCCCCCCCCCCCCCCCCCCCCCCCCCCCCCCCCCCCCCCCCCCCCCCCCCCCCCCC
CCCCCCC      CALULATE THE ELASTIC MATRIX   CCCCCCCCCCCCCCCCCCCCCCCCCCCCCCCCCC
CCCCCCCCCCCCCCCCCCCCCCCCCCCCCCCCCCCCCCCCCCCCCCCCCCCCCCCCCCCCCCCCCCCCCCCCCCCCC
C
      SUBROUTINE EL_M(EELM,EV,EKAPPA,EG_MU,STRESS,DSTRAN,KS_T,ELAMDA,
     +                 EMR,EW1,EW2,SS_R,NUMBER,EINTA,EINTA_MAX,LU,SS_R0,
     +                 EGOCR)
C
      INCLUDE ’ABA_PARAM.INC’
C
```

```
      DIMENSION STRESS(6),DSTRAN(6),EELM(6,6),SS_R(6),
     +            ESS_RR(6),ESS_NN(6),SS_R0(6)
C     K-BULK MODULUS,G-SHEAR MODULUS
C     ES_T IS TO DETERMINE THE TANGENT OR SECANT ELASTIC MATRIX
C     1.0 IS TANGENT, OTHERS IS SECANT
      ETOL=1.0D-4
C
      EP=0.0
      ESS=0.0
      EJ=0.0
      ETHETA=0.0
      EDETS=0.0
C
      CALL ES_INV(SS_R,EP,ESS,EJ,ETHETA,EDETS)
C
      EP=0.0
      ESS=0.0
      EJ=0.0
      ETHETA=0.0
      EDETS=0.0
C
      CALL ES_INV(STRESS,EP,ESS,EJ,ETHETA,EDETS)
C
      EPSI_V=(DSTRAN(1)+DSTRAN(2)+DSTRAN(3))
C
      IF (KS_T.EQ.1) THEN
      EK=ABS(EV*EP/EKAPPA)
      ELSE
      EK=ABS(EV*EP/EKAPPA)
      ENDIF
C
      IF (EG_MU.GE.0.5) THEN
      EG=EG_MU
      ELSEIF (EG_MU .GT.0) THEN
      EG=1.5*(1-2.0*EG_MU)/(1+EG_MU)*EK
      ELSE
C
      IF (EGOCR.GT.2) THEN
      EGMAX=40.0*(ABS(EP))*EGOCR**0.7
      ELSE
      EGMAX=100.0*(ABS(EP))*EGOCR**0.7
      ENDIF
C
      EP_R=(SS_R(1)+SS_R(2)+SS_R(3))/3.0
      DO I=1,6
      ESS_RR(I)=SS_R(I)/EP_R
      ESS_NN(I)=STRESS(I)/EP
      ENDDO
      EJ_RS=0
      DO I=1,3
      EJ_RS=EJ_RS+0.5*((ESS_NN(I)-1)-(ESS_RR(I)-1))**2
      ENDDO
      DO I=4,6
      EJ_RS=EJ_RS+(ESS_NN(I)-ESS_RR(I))**2
```

```
      ENDDO
      EJ_R=EJ_RS**0.5*1.732
C
      IF (NUMBER .EQ.1) THEN
      EAA=2.0*EXP(EW2*EJ_R)/(1.0+EXP(EW1*EJ_R))
      ELSEIF ((EINTA .LE.EINTA_MAX)) THEN
      EAA=2.0*EXP(EW2*EJ_R/2.0)/(1.0+EXP(EW1*EJ_R/2.0))
      ELSE

      EP_R0=(SS_R0(1)+SS_R0(2)+SS_R0(3))/3.0
      DO I=1,6
      ESS_RR(I)=SS_R0(I)/EP_R0
      ESS_NN(I)=STRESS(I)/EP
      ENDDO
      EJ_RS=0
      DO I=1,3
      EJ_RS=EJ_RS+0.5*((ESS_NN(I)-1)-(ESS_RR(I)-1))**2
      ENDDO
      DO I=4,6
      EJ_RS=EJ_RS+(ESS_NN(I)-ESS_RR(I))**2
      ENDDO
      EJ_R=EJ_RS**0.5*1.732

      EAA=2.0*EXP(EW2*EJ_R)/(1.0+EXP(EW1*EJ_R))
      ENDIF
C
      EG=EGMAX/EAA
C
C       IF (EG .LT. (1.5*(1-2.0*ABS(EG_MU))/(1+ABS(EG_MU))*EK)) THEN
C       EG=1.5*(1-2.0*ABS(EG_MU))/(1+ABS(EG_MU))*EK
C       ENDIF
C
      ENDIF
C
      DO I=1,3
      DO J=1,3
      EELM(J,I)=EK-2.0/3.0*EG
      END DO
      EELM(I,I)=EK+4.0/3.0*EG
      END DO
C
      DO I=4,6
      EELM(I,I)=EG
      END DO
C
      RETURN
      END
CCCCCCCCCCCCCCCCCCCCCCCCCCCCCCCCCCCCCCCCCCCCCCCCCCCCCCCCCCCCCCCCCCCCCCCC
C
CCCCCCCCCCCCCCCCCCCCCCCCCCCCCCCCCCCCCCCCCCCCCCCCCCCCCCCCCCCCCCCCCCCCCCCCC
CCCCCCCCCCC   CACULATE THE STRESS INVARIANTS  CCCCCCCCCCCCCCCCCCCCCCCCCCCCCCC
CCCCCCCCCCCCCCCCCCCCCCCCCCCCCCCCCCCCCCCCCCCCCCCCCCCCCCCCCCCCCCCCCCCCCCCCC
C
      SUBROUTINE ES_INV(STRESS,EP,ESS,EJ,ETHETA,EDETS)
```

```
C
      INCLUDE ’ABA_PARAM.INC’
C
C     1-P,2-J,3-THETA,ESS=S:S=2*J**2
C     EDETS==THE DETERMINANT OF S
      DIMENSION STRESS(6)
C
      ETOL=1.0D-5
C
      EP=(STRESS(1)+STRESS(2)+STRESS(3))/3.0
C
      ESS=(STRESS(1)-EP)**2+(STRESS(2)-EP)**2+(STRESS(3)-EP)**2
     +     +2*STRESS(4)**2+2*STRESS(5)**2+2*STRESS(6)**2
C
      EJ=(0.5*ESS)**0.5
C
C     SIGMA_X=STRESS(1),SIGMA_Y=STRESS(2),SIGMA_Z=STRESS(3)
C     TOU_XY=STRESS(4),TOU_XZ=STRESS(5),TOU_YZ=STRESS(6)
C     EDETS==THE DETERMINANT OF S
      EDETS=(STRESS(1)-EP)*(STRESS(2)-EP)*(STRESS(3)-EP)
     +      +2*STRESS(4)*STRESS(5)*STRESS(6)
     +      -(STRESS(1)-EP)*STRESS(6)**2
     +      -(STRESS(2)-EP)*STRESS(5)**2
     +      -(STRESS(3)-EP)*STRESS(4)**2
C
      IF (EJ.LT.ETOL) THEN
      EJ=ETOL
      ESS=2.0*EJ**2
      ETHETA=0.0
C
      ELSE
      EXXX=1.5*1.73205*EDETS/EJ**3
      IF (EXXX.GT.1.0) THEN
      EXXX=1.0
      ELSEIF(EXXX.LT.-1.0) THEN
      EXXX=-1.0
      ENDIF
      ETHETA=-1.0/3.0*ASIN(EXXX)
      ENDIF

      IF (ABS(ETHETA-0.5235988).LT.ETOL) THEN
      ETHETA=0.5236
      ELSEIF (ABS(ETHETA+0.5235988).LT.ETOL) THEN
      ETHETA=-0.5236
      ENDIF
C
      RETURN
      END
CCCCCCCCCCCCCCCCCCCCCCCCCCCCCCCCCCCCCCCCCCCCCCCCCCCCCCCCCCCCCCCCCCCCCCCCCCCCC
```